NUMERICAL MODELLING OF ONSHORE WIND TURBINE GRAVITY FOUNDATIONS SUSCEPTIBLE TO CYCLIC SOIL DEGRADATION

by Steven Seymour

Supervised by A/Prof. Denis Kalumba

Department of Civil Engineering

University of Cape Town

January 2018

A Dissertation Submitted in Partial Fulfilment for the Degree of

Master of Science in Engineering specialising in Geotechnical Engineering

DECLARATION

I, Steven Seymour, submit this dissertation in partial fulfilment of the requirements for the degree of Master of Science in Engineering at the University of Cape Town.

I know the meaning of plagiarism and declare that all the work in the document, save for that which is properly acknowledged, is my own.

This dissertation has been submitted to the Turnitin module and I confirm that my supervisor has seen my report and any concerns revealed by such have been resolved with my supervisor.

Signed by candidate

Signed

31 January 2018

Date

Dedicated to Inês Portela

ACKNOWLEDGMENTS

First and foremost, I would like to express my gratitude and appreciation to my supervisor, Associate Professor Denis Kalumba, for his support, feedback and enthusiasm throughout the course of this project. Thank you for always being accessible and willing to assist when needed.

I am especially thankful to Dr Gabrielle Wojtowitz of *Aurecon*, for not only providing the resources and documents necessary to undertake this study, but for also suggesting this research topic initially.

My postgraduate studies would not have been possible without the financial assistance provided by the Wilhelm Frank Trust Master's Scholarship, for which I am thoroughly grateful. I would also like to acknowledge my undergraduate bursars, *Aurecon*, for allowing me the opportunity to pursue postgraduate research.

Lastly, thank you to my family, friends, and colleagues in the Geotechnical Engineering Research Group at the University of Cape Town, for the endless support throughout the completion of this work.

ABSTRACT

South Africa is currently one of the global leaders in emerging wind markets. This development has come about since the country adopted a new approach towards sustainable growth and development. However, wind turbine structures present unconventional and complex design challenges, largely because they are subject to highly fluctuating and irregular cyclic loads. Accordingly, one of the major uncertainties in the design of wind turbines is accurate prediction of the long-term performance of the foundation. In this regard, a particular issue relates to founding conditions comprised of softer or plastic soil layers, where the effects of cyclic degradation need to be taken into consideration during the design stage.

Cyclic degradation refers to the phenomenon in which the stiffness of soil decreases progressively when subjected to cyclic loading. This reduction in soil stiffness occurs due to deterioration of the soil microstructure, as well as accumulation of excess pore water pressure, with the extent of it being largely dependent on the shear strain level in the soil and the number of loading cycles. Accounting for the potential reduction in soil stiffness is crucial when dimensioning the foundation of a wind turbine, as wind turbines are dynamically sensitive structures, with their natural frequencies being dependent, *inter alia*, on the stiffness of the underlying soil. However, despite the possible implications of cyclic degradation, there is a present lack of guidance provided in design guidelines to explicitly incorporate it into design.

The primary objective of this study was to investigate the effect of cyclic soil degradation on the design of onshore wind turbine gravity foundations. This was undertaken by: (1) analysing a case study of a wind farm in South Africa, and quantifying the effect of cyclic degradation on the foundation design for three separate ground profiles; (2) performing a parametric study to identify key parameters controlling cyclic degradation in the context of wind turbine foundations.

Numerical modelling was undertaken to investigate these objectives, through the development of three-dimensional finite element models in the software package *RS*^{3} by *Rocscience*. The three ground profiles analysed were selected from the wind farm based on the presence of soils that were deemed susceptible to cyclic degradation, as well as to illustrate different scenarios in ground conditions. Using these ground profiles, it was demonstrated how appropriate ground moduli could be selected for design, such that they were representative of the time-related cyclic degradation. This was achieved by assessing the depth of influence of cyclic degradation in the numerical models, and applying a reduction factor to the soil stiffness within this depth in the evaluation of the minimum required foundation diameter.

Several parameters were varied in the parametric study. Regarding soil properties, the plasticity index, initial shear modulus G_0, and degradation shear strain threshold γ_{tv} were identified as having a significant effect in governing the extent of cyclic degradation. Furthermore, it was observed that altering the foundation diameter also had a considerable impact on the depth of influence of cyclic degradation, particularly for very soft profiles. Finally, an assessment of different load cases indicated that cyclic degradation may not only occur in rare conditions, but is also likely to accumulate in normal operating conditions during the lifetime of the structure. This emphasised the importance of accounting for cyclic degradation in design.

CONTENTS

Declaration i
Acknowledgments v
Abstract vii
Contents ix
List of Figures xiii
List of Tables xvii
Notation xix

Chapter 1 Introduction

1.1 Background 1
1.1.1 Wind energy in South Africa 2
1.1.2 Design challenges of wind turbine foundations 4
1.1.3 Cyclic soil degradation 5
1.2 Objectives 6
1.3 Scope 6
1.4 Potential Benefits of Research 7
1.5 Dissertation Structure 8

Chapter 2 Onshore Wind Turbines

2.1 Introduction 9
2.2 Historical Background 10
2.3 Modern Configurations 12
2.3.1 Primary components 14
2.3.2 Power generation and upscaling trends 24
2.4 Foundation Loading 27
2.4.1 Extreme loading 29
2.4.2 Fatigue loading 31
2.5 Foundation Design Requirements 37
2.5.1 Site investigation 38
2.5.2 Foundation stiffness 41
2.5.3 Ultimate limit state design checks 47
2.5.4 Serviceability limit state design checks 50

Chapter 3 Cyclic Loading of Soil

3.1 Introduction 53
3.2 Cyclic Loading Effects 54
3.3 Strain Dependent Behaviour 56
3.3.1 Stiffness 56
3.3.2 Damping 66
3.4 Constitutive Modelling 69
3.4.1 Elastoplastic framework 69
3.4.2 Models for cyclic loading 77

Chapter 4 Numerical Model Development

4.1 Introduction 87
4.2 Modelling Approach 88
4.2.1 Quasi-static versus dynamic analysis 88
4.2.2 Long-term versus short-term conditions 89
4.2.3 Modelling methodology 89
4.3 Constitutive Model 93
4.4 Site Characterisation 95
4.4.1 Wind climate 95
4.4.2 Site geology 97
4.4.3 Groundwater 97
4.4.4 Ground profiles 97
4.4.5 Material properties 102
4.4.6 Summary of ground models 105
4.5 Turbine Model and Loads 106
4.6 General Model Characteristics 108
4.6.1 Analysis stages 108
4.6.2 Boundaries and restraints 110
4.6.3 Foundation element 110
4.6.4 Groundwater and drainage conditions 114
4.6.5 Mesh generation and sensitivity analysis 115
4.7 Parametric Study 118
4.7.1 Plasticity index, initial shear modulus, and degradation threshold 118
4.7.2 Foundation size 121
4.7.3 Load magnitude 121

Chapter 5 Results and Discussions

5.1 Introduction 127
5.2 Ground Profile A 127
5.2.1 Depth of influence of degradation 128
5.2.2 Impact on foundation design 133
5.3 Ground Profile B 136
5.3.1 Depth of influence of degradation 136
5.3.2 Impact on foundation design 141
5.4 Ground Profile C 142
5.4.1 Depth of influence of degradation 143
5.4.2 Impact on foundation design 147
5.5 Parametric Study 149
5.5.1 Plasticity index, initial shear modulus, and degradation threshold 149
5.5.2 Foundation size 156
5.5.3 Load magnitude 158

Chapter 6 Conclusions and Recommendations

6.1 Introduction 161
6.2 Case Study 162
6.3 Parametric Study 163
6.4 Recommendations for Further Research 164

References 169

Appendix A: Calculation Method for Mass Ground Modulus

Appendix B: Calculation of Mass Ground Moduli and Minimum Required Foundation Diameters for Case Study

LIST OF FIGURES

Figure 1.1: Global cumulative installed wind capacity 1
Figure 1.2: South African wind farm locations for each REIPPPP bidding window 2
Figure 1.3 Cumulative installed wind capacity in South Africa 3
Figure 1.4: Diameter of wind turbine foundation versus cost 7
Figure 2.1: Historical development of the use of wind as a source of energy 11
Figure 2.2: Wind turbine classification according to axis of rotation 12
Figure 2.3: Components of a horizontal-axis wind turbine 14
Figure 2.4: Pitching of rotor blade to alter angle of attack 15
Figure 2.5: Horizontal-axis wind turbine rotor classification 16
Figure 2.6: Drivetrain configuration 17
Figure 2.7: Erection and transportation of tubular steel tower segments 18
Figure 2.8: Precast concrete towers at the Gouda Wind Farm 19
Figure 2.9: Concrete-steel hybrid tower with 133 m hub height 19
Figure 2.10: Common foundation types for onshore wind turbines 20
Figure 2.11: Construction of a circular gravity base foundation 21
Figure 2.12: Piling completed for a tower base at the Gouda Wind Farm 22
Figure 2.13: Rock anchor foundation 22
Figure 2.14: Prestressed concrete cylinder foundation 23
Figure 2.15: Increase in wind turbine size and generating capacity from 1980 to 2010 24
Figure 2.16: Power curve for a Vestas V112-3.0 MW wind turbine 26
Figure 2.17: Mean wind speed at 100 m above ground level 27
Figure 2.18: Simplified loading scheme of a wind turbine structure 30
Figure 2.19: Single degree-of-freedom system 31
Figure 2.20: Response of single degree-of-freedom system to harmonic excitation 34
Figure 2.21: Cyclic loading of an onshore wind turbine 35
Figure 2.22: Continuous surface wave system 39
Figure 2.23: Frequency spectrum for wind turbine dynamic loads and design choices 42
Figure 2.24: Plot of rotational stiffness versus lateral stiffness 43
Figure 2.25: Eccentric loading effects on foundation bearing pressure 48
Figure 2.26: Effective area of circular foundation 49
Figure 3.1: Modes of cyclic loading 54
Figure 3.2: Stress-strain relationship for hysteretic soils and definition of parameters 57
Figure 3.3: Conceptual shear modulus reduction curve with proposed strain thresholds for saturated clayey soils 58

Figure 3.4: Effect of plasticity index on shear modulus reduction curve 61
Figure 3.5: Effect of mean effective confining pressure on shear modulus reduction curve 62
Figure 3.6: Effect of cyclic degradation on shear modulus reduction curve 63
Figure 3.7: Relationship between degradation parameter t and γ_c for varying OCR and PI 64
Figure 3.8: Phenomenon of cyclic degradation and definition of parameters 65
Figure 3.9: Effect of plasticity index on damping curve..... 68
Figure 3.10: Constituents of an elastoplastic constitutive model..... 70
Figure 3.11: Hyperbolic stress-strain curve 71
Figure 3.12: Principal effective stress space and the three stress invariants..... 74
Figure 3.13: Hardening and softening mechanisms..... 75
Figure 3.14: Common failure surfaces in principal stress space..... 77
Figure 3.15: The effect of stress reversals on soil stiffness 78
Figure 3.16: Types of cyclic behaviour 79
Figure 3.17: Definition of reference shear strain 81
Figure 3.18: Application of extended Masing rules..... 82
Figure 3.19: Bounding surface model..... 84
Figure 4.1: Two of the soil-structure interaction problems for onshore wind turbines 88
Figure 4.2: Modelling methodology 91
Figure 4.3: Degraded backbone curves..... 94
Figure 4.4: Wind rose and wind speed distribution for Vredenburg mast at 100 m AGL..... 95
Figure 4.5: Wind rose and wind speed distribution within wind farm at 100 m AGL 96
Figure 4.6: Correlation between surface elevation and groundwater level..... 97
Figure 4.7: Ground Profile A 99
Figure 4.8: Ground Profile B 100
Figure 4.9: Ground Profile C 101
Figure 4.10: Trend of degradation shear strain threshold versus plasticity index 103
Figure 4.11: Correlation between SPT N-value and c_u for insensitive clays..... 104
Figure 4.12: Waveform of cyclical overturning moment 107
Figure 4.13: Analysis stages of finite element model..... 108
Figure 4.14: Model boundaries and restraints..... 110
Figure 4.15: Actual and simplified geometry of foundation element..... 111
Figure 4.16: Pressure distribution beneath a footing subjected to concentric vertical load..... 113
Figure 4.17: Application of loads on the foundation element..... 113
Figure 4.18: Refined element size versus strain depth..... 116
Figure 4.19: Cross-section of meshes used in mesh sensitivity analysis..... 117
Figure 4.20: Modified hyperbola modulus reduction curves for varying plasticity index 119

Figure 4.21: Thrust coefficient and calculated rotor thrust for Vestas V112-3.0 MW 124
Figure 5.1: Model of Ground Profile A 127
Figure 5.2: Shear strains after first loading cycle for Ground Profile A 128
Figure 5.3: Isosurface of γ_{td} after first loading cycle for Ground Profile A 129
Figure 5.4: Progression of γ_{td} isosurfaces for stiffness iterations 1-4 for Ground Profile A 130
Figure 5.5: Progression of γ_{td} isosurfaces for stiffness iterations 5-8 for Ground Profile A 132
Figure 5.6: Relationship between degradation parameter t and γ_c for varying PI 133
Figure 5.7: Degradation index versus number of loading cycles 134
Figure 5.8: Upper and lower bound stiffness profiles for Ground Profile A 135
Figure 5.9: Model of Ground Profile B 136
Figure 5.10: Shear strains after first loading cycle for Ground Profile B 137
Figure 5.11: Isosurface of γ_{td} after first loading cycle for Ground Profile B 137
Figure 5.12: Progression of γ_{td} isosurfaces for stiffness iterations 1-4 for Ground Profile B .. 139
Figure 5.13: Progression of γ_{td} isosurfaces for stiffness iterations 5-8 for Ground Profile B .. 140
Figure 5.14: Upper and lower bound stiffness profiles for Ground Profile B 141
Figure 5.15: Model of Ground Profile C 142
Figure 5.16: Shear strains after first loading cycle for Ground Profile C 143
Figure 5.17: Isosurface of γ_{td} after first loading cycle for Ground Profile A 144
Figure 5.18: Progression of γ_{td} isosurfaces for stiffness iterations 1-4 for Ground Profile C .. 145
Figure 5.19: Progression of γ_{td} isosurfaces for stiffness iterations 5-8 for Ground Profile C .. 146
Figure 5.20: Upper and lower bound stiffness profiles for Ground Profile C 147
Figure 5.21: Model used for parametric study 149
Figure 5.22: Variation in maximum depth of γ_{td} for PI = 15% 150
Figure 5.23: Shear strain isosurfaces corresponding to $\gamma_{td} \triangleq G/G_0 = 0.7$ for PI = 15% and various values of G_0 151
Figure 5.24: Shear strain isosurfaces corresponding to various values of γ_{td} for G_0 = 60 MPa and PI = 15% 152
Figure 5.25: Variation in maximum depth of γ_{td} for PI = 0% 153
Figure 5.26: Variation in maximum depth of γ_{td} for PI = 30% 154
Figure 5.27: Variation in maximum depth of γ_{td} for PI = 50% 154
Figure 5.28: Variation in maximum depth of γ_{td} for PI = 100% 155
Figure 5.29: Variation in maximum depth of assumed characteristic value of γ_{td} for varying PI and G_0 156
Figure 5.30: Variation in maximum depth of γ_{td} for different foundation diameters 157
Figure 5.31: Shear strain isosurfaces corresponding to different foundation sizes for $\gamma_{td} \triangleq G/G_0 = 0.7$, G_0 = 60 MPa and PI = 15% 158
Figure 5.32: Variation in maximum depth of γ_{td} for different load cases 159

Figure 5.33: Shear strain isosurfaces corresponding to different load cases for $\gamma_{td} \triangleq G/G_0 = 0.7$, $G_0 = 60$ MPa and PI = 15% 159
Figure 6.1: Proposed layout of instrumentation for experimental study..... 167

LIST OF TABLES

Table 2.1: Geotechnical design methodology for wind turbine gravity foundations 37
Table 2.2: Typical laboratory tests for wind turbine foundation design 40
Table 2.3: Foundation stiffness requirements for a Vestas V112-3.0 MW wind turbine 43
Table 2.4: Effect of soil type on degradation potential 46
Table 3.1: Effect of various increasing parameters on G_0 and G/G_0 of normally consolidated and moderately overconsolidated clays 60
Table 3.2: Effect of various increasing parameters on the damping ratio of normally consolidated and moderately overconsolidated clays 67
Table 4.1: Summary of ground models 105
Table 4.2: General specifications of the Vestas V112-3.0 MW wind turbine 106
Table 4.3: Foundation load cases for Vestas V112-3.0 MW wind turbine 106
Table 4.4: Extreme loads during normal operation for Vestas V112-3.0 MW foundation 107
Table 4.5: Material properties of foundation element 112
Table 4.6: Mesh dependency of shear strain depth 115
Table 4.7: Modified hyperbola parameters for varying plasticity index 119
Table 4.8: Assumed characteristic values of degradation threshold for varying PI 120
Table 4.9: Degradation shear strain threshold for various PI and $\gamma_{td} \triangleq G/G_0$ combinations 121
Table 4.10: Equivalent and mean fatigue loads for Vestas V112-3.0 MW foundation 122
Table 4.11: Summary of fatigue load case for Vestas V112-3.0 MW foundation 123
Table 4.12: Summary of site-specific load case for Vestas V112-3.0 MW foundation 125
Table 6.1: Summary of the effect of cyclic degradation on the wind turbine foundation design for the three ground profiles analysed in the case study 162

NOTATION

The selection of notation in this dissertation was based on standard nomenclature adopted in geotechnical engineering practice. However, some symbols have been selected to conform to other engineering or mathematical disciplines where applicable.

All acronyms and symbols are defined at appropriate places within the text, usually at their first occurrence. Occasionally, the same symbol may be used to represent more than one parameter, however the meaning should be unambiguous when read in context. The SI unit convention was adopted.

Acronyms

AGL	Above ground level
AMSL	Above mean sea level
API	American Petroleum Institute
ASCE	American Society of Civil Engineers
BSI	The British Standards Institution
CSSA	Concrete Society of Southern Africa
CSW	Continuous surface wave
DNV	Det Norske Veritas
DoE	Department of Energy
DPSH	Dynamic probe super heavy
FE	Finite element
GWEC	Global Wind Energy Council
HAWT	Horizontal-axis wind turbine
IEC	International Electrotechnical Commission
IRP	Integrated Resource Plan
OCR	Overconsolidation ratio
PI	Plasticity index
REIPPPP	Renewable Energy Independent Power Producer Procurement Programme
RS^3	Rock and Soil 3D analysis program
SANEDI	South African National Energy Development Institute
SANS	South African National Standards
SLS	Serviceability limit state
SPT	Standard penetration test
UCS	Unconfined compressive strength
ULS	Ultimate limit state
USA	United States of America
USD	United States dollar
VAWT	Vertical-axis wind turbine
WASA	Wind Atlas for South Africa

Symbols

$1P$	Rotor frequency
$3P$	Blade passing frequency
a	Modified hyperbola material parameter
A	Rotor swept area
A_{eff}	Effective foundation area
b	Modified hyperbola material parameter
B	Foundation width
B'	Effective foundation width
c	Cementation
c	Viscous damping coefficient
c'	Effective cohesion
c_u	Undrained shear strength
C_p	Power coefficient
C_t	Thrust coefficient
D	Dynamic amplification factor
e	Eccentricity
e	Void ratio
e_{ij}	Strain deviator
E	Elastic modulus
E_{mass}	Mass elastic modulus
F_0	Excitation load amplitude
F_{res}	Resulting shear force
F_z	Vertical force
G	Shear modulus
G_0	Initial shear modulus (=G_{max})
$G_{0(mass)}$	Mass small-strain shear modulus
G_1	Secant shear modulus after the first cycle
G_{mass}	Mass shear modulus
G_{max}	Maximum shear modulus (=G_0)
G_N	Secant shear modulus after N cycles
G_{sec}	Secant shear modulus
G_{tan}	Tangent shear modulus
H	Horizontal load
i_c, i_q, i_γ	Inclination factors
I	Influence factor
k	Spring constant
K_H	Lateral stiffness
K_R	Rotational stiffness
K_V	Vertical stiffness
K	Bulk modulus
K_0	Coefficient of lateral earth pressure at rest
m	Mass
M_{res}	Resulting bending moment
M_z	Torsion moment
N	Number of loading cycles
N	Standard penetration test resistance
N_c, N_q, N_γ	Bearing capacity factors
p'	Mean effective stress/ confining pressure
P	Power
q	Deviatoric stress
q'	Effective overburden pressure
q_u	Unconfined compressive strength
q_{ult}	Ultimate bearing capacity
Q	Load
Q_a	Average load

Q_{cy}	Cyclic load amplitude
Q_{max}	Maximum load
Q_{min}	Minimum load
s_c, s_q, s_γ	Shape factors
r	Ramberg-Osgood material parameter
R	Foundation radius
t	Degradation parameter
t	Time
t_g	Geologic age
T	Period
u	Displacement
$\dot{u}$	Velocity
$\ddot{u}$	Acceleration
u_c	Complementary solution
u_p	Particular solution
U	Wind speed
V	Vertical load
V_r	Rayleigh wave velocity
V_s	Shear wave velocity
ΔW	Energy loss per cycle
W	Total stored energy
α	Phase angle
α	Ramberg-Osgood material parameter
γ	Shear strain
γ'	Effective unit weight
$\dot{\gamma}$	Shear strain rate
γ_c	Cyclic shear strain
γ_r	Reference shear strain
γ_{sat}	Saturated unit weight
γ_{td}	Degradation shear strain threshold
γ_{tf}	Flow shear strain threshold
γ_{tl}	Linear shear strain threshold
γ_{tv}	Volumetric shear strain threshold
δ	Degradation index
ε	Normal strain
ε^e	Component of elastic strain
ε^p	Component of plastic strain
ε_q	Deviatoric strain
ζ	Damping ratio
θ	Lode's angle
ν	Poisson's ratio
ν_{mass}	Mass Poisson's ratio
ρ_a	Air density
ρ	Bulk density
σ	Total stress
$\sigma_{1,2,3}$	Total principal stresses
$\sigma'_{1,2,3}$	Effective principal stresses
σ_y	Yield stress
τ	Shear stress
τ_c	Cyclic shear stress
τ_f	Shear stress at failure
ϕ'	Angle of internal friction
ω	Excitation load frequency
ω_d	Damped natural frequency
ω_n	Natural frequency

Units

GN	Giganewton
GPa	Gigapascal
GWh	Gigawatt-hour
ha	Hectare
Hz	Hertz
kg	Kilogram
km	Kilometre
kN	Kilonewton
kPa	Kilopascal
kW	Kilowatt
m	Metre
mm	Millimetre
MN	Meganewton
MPa	Megapascal
MW	Megawatt
N	Newton
Pa	Pascal
rad	Radian
rpm	Revolutions per minute
s	Second
W	Watt

Chapter 1
INTRODUCTION

1.1 Background

Over recent decades, the renewable energy industry has experienced significant growth globally. This has been driven by emerging concerns about the finitude of the earth's fossil fuel reserves, the negative impact that burning such fuels has on the environment, and the urgent need for energy in expanding economies. Wind energy in particular has experienced a constant growth in installed capacity worldwide, as illustrated in Figure 1.1, having been spurred on by constant technological innovation and improved cost-competitiveness.

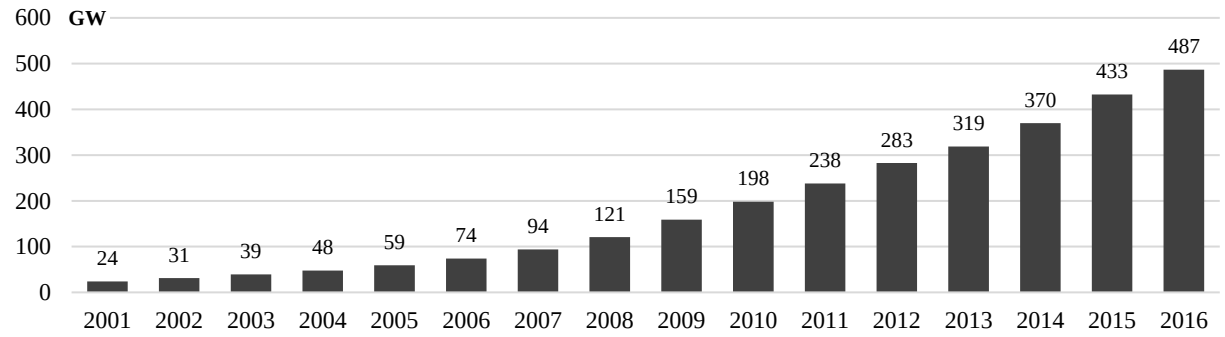

Figure 1.1: Global cumulative installed wind capacity
Data sourced from GWEC (2017)

Although wind power is present today in more than ninety countries, only nine of these have a capacity of more than 10 GW installed. As reported by the Global Wind Energy Council (GWEC, 2017), at the end of 2016 these included China (169 GW), the USA (82 GW), Germany (50 GW), India (29 GW), Spain (23 GW), UK (15 GW), France (12 GW), Canada (12 GW) and Brazil (11 GW). Although onshore wind energy is regarded as a mature industry in these markets, and several other markets around the world, it is still a relatively new technology in developing countries such as South Africa.

1.1.1 Wind energy in South Africa

The birth of the South African wind industry was brought about, in part, by the commitment of national policymakers to a reduction in South Africa's substantial carbon footprint (DoE, 2015). Historically, carbon emissions in South Africa have been disproportionally high due to a heavy reliance on coal for electricity generation, in combination with its economy being highly energy-intensive (Eberhard *et al.*, 2014). To curb this trend and place South Africa on a more sustainable path, the Department of Energy (DoE) has established long-term goals for renewable energy production, a significant component being wind energy. These goals have been specified in the Integrated Resource Plan (IRP), that was developed to outline the preferred electricity mix and delivery timeline with which to meet the country's electricity needs. The original edition of this document set a target to procure 8.4 GW of wind energy by 2030 (DoE, 2011), however it was revised in 2016 with a new target set of 37.4 GW to be installed by 2050 (DoE, 2016). Although the latter document is currently out for consultation and its implementation into policy is uncertain, it nonetheless indicates South Africa's intentions to move towards developing a significant wind industry.

In line with the goals stipulated by the IRP, the DoE has undertaken to accelerate private sector investment into renewable energy in South Africa through the implementation of the Renewable Energy Independent Power Producer Procurement Programme (REIPPPP) in August 2011. This programme comprises a competitive bidding process, whereby private investors have been able to invest in a variety of wind, solar, hydro, landfill gas and biomass energy projects. To date, four bid windows have been completed for the REIPPPP, with the locations of the wind energy projects from each illustrated in Figure 1.2.

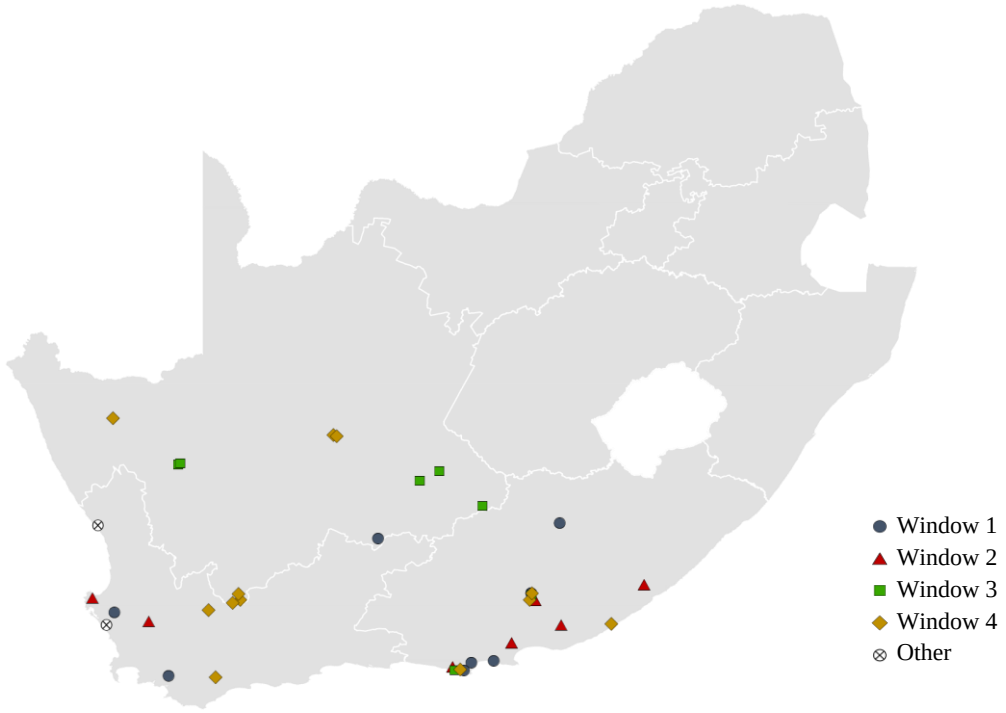

Figure 1.2: South African wind farm locations for each REIPPPP bidding window
Data sourced from The Energy Blog (2017)

All wind farms from bid windows one and two are fully operational, whereas those from window three are currently either fully operational, partially operational, or still under construction. This has resulted in the total installed wind capacity in South Africa rising from 10 MW in 2013 to 1471 MW at the end of 2016, as illustrated in Figure 1.3. The twelve wind farms from the fourth bidding window, comprising a total capacity of 1362 MW, are in the approval, planning, and financing stages (The Energy Blog, 2017), having been delayed due to political issues with the national utility provider Eskom.

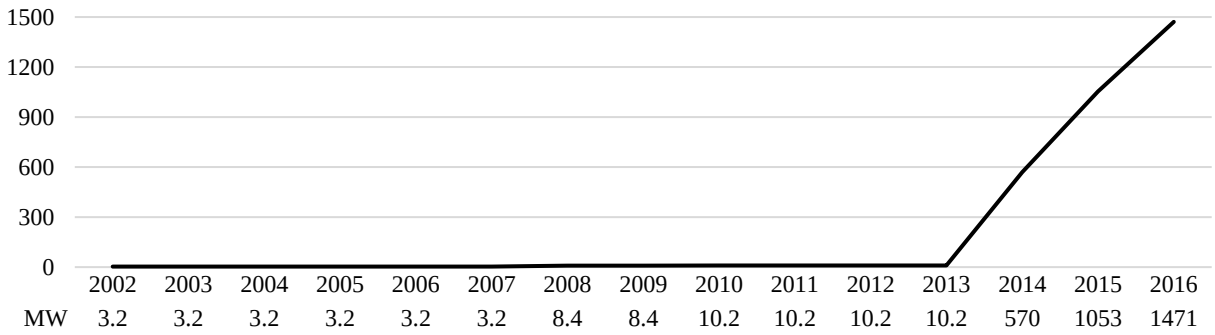

Figure 1.3 Cumulative installed wind capacity in South Africa

Data sourced from GWEC (2017)

The strong growth in South Africa's wind industry has placed it as one of the leading new wind markets globally (GWEC, 2017). A significant factor contributing to this is that the country's topographical and meteorological characteristics are highly suitable for wind energy development. A recent collaborative study, conducted in part by the Council for Scientific and Industrial Research, found that more than 80% of South Africa's land mass has enough wind resource for the establishment of economic wind farms with very high annual load factors of greater than 30% (Knorr *et al.*, 2016). This suggests that South Africa has ideal conditions to introduce a significant amount of wind power into its energy mix in a cost-effective way. This substantial wind energy potential, as well as South Africa's recent wind industry development and imminent growth based on the IRP goals, provided the motivation for this research.

As wind energy is a relatively new technology in South Africa, it is important from a design standpoint to identify areas of uncertainty that may require further research and understanding. Wind turbine foundation design is one such area, as there are several design challenges inherent to wind turbine substructures that are not encountered in conventional geotechnical engineering practice.

1.1.2 Design challenges of wind turbine foundations

The foundation of a wind turbine is responsible for transferring the forces emanating from the structure into the surrounding soil and rock. There are several foundation options available for doing so, with the most common being the gravity base. This consists of a wide, shallow footing that is constructed of reinforced concrete, in-situ, and primarily relies on its massive self-weight and soil overburden to provide stability against the overturning loads from the tower. Although many of the design concepts for such foundations resemble those of a conventional shallow footing, it must be acknowledged that wind turbine foundations are unique structures from both geotechnical and structural perspectives, largely due to the following key design challenges:

i) Wind turbines experience complex loading in the form of cyclic loads. These can be non-dynamic in nature, such as those produced externally by the wind and its turbulence, or they can be dynamic, such as the loads emanating internally from the mass and aerodynamic imbalances of the rotor, as well as blade shadowing effects. Each of these loads has unique characteristics in terms of the magnitude, frequency, and number of cycles applied to the foundation. Accordingly, the long-term performance of wind turbine foundations is an important consideration, however there is currently little guidance for designers in this regard.

ii) The loading on a wind turbine foundation is highly eccentric. That is, the ratio of the overturning moment to the total vertical force is relatively large. This is attributed to the fact that wind turbines are very tall and slender structures that are subjected to large wind thrusts at significant heights above ground level, the result of which is the generation of unconventionally large overturning moments at the base. As the magnitudes of these overturning moments are disproportionately higher than the vertical loads from the self-weight of the structure, extreme eccentricities of the resultant loads are developed.

iii) There currently does not exist a single standardised guideline or code that addresses all the necessary checks required to design a wind turbine foundation. Consequently, foundation designs to date have been based on various parts of available standards and guidelines (e.g. DNV/Risø, 2002; ASCE/AWEA, 2011; CFMS, 2011), on guidelines produced by wind turbine manufacturers themselves, or on the designer's own analysis models and methods. Typical regional design standards, such as the Eurocodes, are not sufficiently specialised to deal with the key design criteria inherent to wind turbine foundation design.

iv) Wind farm sites cover vast expanses of land, and thus the spacing between wind turbines is often considerably large. Consequently, there can be significant variability in founding conditions across them. Furthermore, a wide variety of soil conditions exist within South African wind energy corridors, with each presenting a different set of challenges and design drivers.

With respect to the challenge posed by cyclic loading, one of the major uncertainties in the design of wind turbines is the prediction of the long-term performance of the foundation. In this regard, there are two main long-term concerns:

i) Irregular and asymmetric cyclic loads can result in the accumulation of permanent plastic strain of the soil over time, thus inducing differential settlement of the foundation and leading to accumulated rotation of the wind turbine tower. The recommended maximum allowable differential settlement is generally in the order of 3 to 4.5 mm/m and is an important requirement specified by the turbine manufacturer, as it can impact all components of the wind turbine.

ii) Long-term cyclic loading of the foundation is likely to alter the stiffness of the underlying soil, thereby changing the natural frequency of the rotor-tower-foundation-soil system. In the case of strain-hardening soils such as loose to medium dense sand, the natural frequency is expected to increase, possibly due to densification, whereas for strain-softening soils such as normally consolidated clay, the natural frequency will likely decrease as a result of cyclic degradation. Thus, any significant change in stiffness may cause the first natural frequency of the system to coincide with the excitation frequencies, resulting in resonance problems.

The latter issue, specifically that of cyclic degradation, was the focus of this study.

1.1.3 Cyclic soil degradation

When fully saturated soil is subjected, in undrained conditions, to cyclic loading with moderate to large cyclic shear strain amplitude, its stiffness decreases with an increasing number of loading cycles. This phenomenon of stiffness reduction with cyclic loading is called *cyclic degradation*. This degradation occurs due to the deterioration of the soil microstructure, as well as the accumulation of excess pore water pressure, with the extent of degradation being largely dependent on the shear strain level of the soil and the number of loading cycles.

The importance of considering cyclic degradation in wind turbine foundation design stems from the fact that wind turbines are dynamically sensitive structures, in the sense that their natural frequencies are very close to the forcing frequencies of the wind, 1P (rotor frequency) and 3P (blade shadowing) loading. Accordingly, to avoid fatigue-inducing resonance of the structure, it is imperative that the natural frequency of the wind turbine system is designed to avoid these excitation frequencies. However, the natural frequency is dependent, *inter alia*, on the total stiffness of the wind turbine system, which in turn is a function of the tower stiffness, the foundation stiffness, and the stiffness of the underlying soil. As cyclic degradation causes the stiffness of the underlying soil to decrease over time, it will also decrease the natural frequency of the overall wind turbine system, and thus potentially cause it to coincide with the excitation frequencies.

Despite the potential consequences of cyclic degradation, it has not been explicitly incorporated into current methods of analysis in wind turbine foundation design. Rather, current guidelines

either briefly mention that the effects of cyclic degradation require consideration, without providing a practical means of doing so, or they specify a general rule of thumb, which is to prevent or highly restrict gapping (temporary upliftment of the footing base at its windward side) of the foundation under serviceability load conditions. Irrespective of this general requirement, the long-term performance of gravity foundations subjected to cyclic loading remains uncertain.

One approach to explicitly consider cyclic degradation in design is to select a ground modulus value that is representative of the time-related cyclic degradation. This relates to the fact that the stiffness of a wind turbine foundation is typically calculated assuming the soil to be an elastic half-space, or a semi-infinite continuum of soil idealised as an elastic material. Therefore, cyclic degradation of the soil can be accounted for by applying a reduction factor to the ground stiffness up to a certain depth below founding level. However, the depth to which the cyclic degradation occurs, as well as the amount of cyclic degradation, is uncertain and was the subject of this investigation.

1.2 Objectives

The primary objective of this research was to, through reviewing relevant literature and conducting numerical modelling, investigate the effect of cyclic soil degradation on the design of onshore wind turbine gravity foundations. In doing so, the following sub-objectives were developed:

i) By considering a case study of a wind farm in South Africa, model three separate ground profiles that are recognised as being susceptible to cyclic degradation, and quantify the effect of the degradation on the foundation design.

ii) Conduct a parametric study to evaluate the dependency of cyclic degradation on various input parameters, and therefore identify the key parameters that potentially require the most attention in wind turbine foundation design involving cyclic degradation.

1.3 Scope

This dissertation focused specifically on cyclic degradation of soil underlying wind turbine foundations, and the implications of such degradation on the foundation stiffness requirements only. Although several foundation types were discussed in the literature review, only shallow gravity base foundations were analysed in the numerical model, as this is the most prevalent wind turbine foundation type in South Africa. Additionally, the wind turbine analysed was that of a utility-scale, horizontal-axis wind turbine with a generating capacity of 3 MW and hub height of approximately 120 m, as this was deemed to be representative of the scale of modern wind turbines. This study was also solely limited to the onshore wind energy sector, as offshore wind turbines differ from onshore in the sense that different forces are applied to the structures and construction methods differ significantly. Nonetheless, several concepts were adapted from the offshore wind sector where applicable. Finally, the numerical modelling consisted of three-dimensional finite element models using quasi-static analyses, in contrast to dynamic analyses.

1.4 Potential Benefits of Research

The relatively high capital cost and repetitive nature of a large number of wind turbine foundations on similar founding conditions lend themselves to investing more effort into the design phase of the project, so as to ensure optimisation of the design with associated material and program savings. The incentive for wind turbine foundations to be designed economically is evident from Figure 1.4, which indicates that there is an exponential increase in total foundation cost as the diameter increases. Accordingly, a potential benefit of this research was to improve the understanding of large foundation behaviour subjected to cyclic loading, consequently reducing conservatism in design, and thus resulting in more economical foundation solutions.

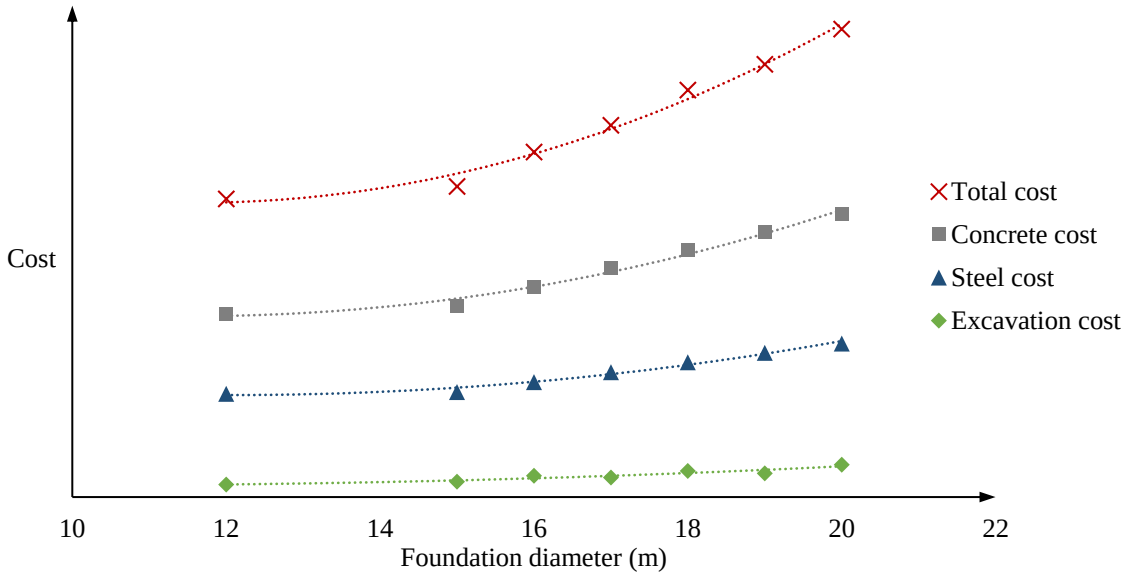

Figure 1.4: Diameter of wind turbine foundation versus cost

Data sourced from van der Spuy (2014)

A further potential benefit of this research related to the design life of wind turbine structures. Wind turbines are generally designed for a finite service life of 20 years (DNV GL, 2016a). However, they can be assessed for a lifetime extension of up to 25 to 30 years if it is justifiable from a technical and economic point of view. Therefore, by understanding the issues involved with the long-term behaviour of wind turbine foundations, and making provisions for this in the design stage, the service life of future turbines can potentially be prolonged.

1.5 Dissertation Structure

This dissertation consists of six chapters, followed by the references and appendices.

Chapter 1 provides background information and motivation for the research problem. The themes of the investigation are also defined, consisting of the objectives, scope and potential benefits.

Chapter 2 presents a review of literature regarding onshore wind turbine structures in general, as well as the methodology involved in wind turbine foundation design.

Chapter 3 comprises a further literature review on cyclic loading of soil, with emphasis placed on strain dependent behaviour, as well as constitutive modelling.

Chapter 4 details the development of the numerical model. This includes characterisation of the wind farm site used for the case study, as well as a description of the modelling approach and general model characteristics.

Chapter 5 presents the results of the numerical model analyses and foundation design evaluations for each of the ground profiles. The results of the parametric study are also discussed.

Chapter 6 describes the conclusions drawn from the study, and provides recommendations for further research.

Chapter 2
ONSHORE WIND TURBINES

2.1 Introduction

This chapter comprises a literature review of onshore wind turbine structures including several concepts relevant to the design of their foundations. The primary aim of this was to gain a sound understanding of the structure to be founded and the nature of the concomitant loads borne by the structure, as well as to provide insight into the foundation design methodology. However, prior to addressing the more technical aspects of this technology, the history of wind energy was briefly reviewed to highlight some of the major milestones in its overall development. The modern configurations of wind turbines were subsequently discussed, after which each of the major components of a horizontal-axis wind turbine were explored. Power generating capacities were also analysed, with an emphasis placed on the challenges that upscaling trends could have on the design of support structures in the future.

The loading regime of wind turbine foundations was an important consideration in this study. This was discussed with regards to two general load categories, namely that of extreme and fatigue loads. Finally, the design methodology for wind turbine foundations was reviewed. This comprised the requirements for site investigation, foundation stiffness, ultimate limit state design, and serviceability limit state design.

Although the literature review herein is considered comprehensive, reference can be made to Warren-Codrington (2013) for a more detailed review of wind turbine structures, as well as Mawer (2015) for an in-depth study into the geotechnical design of wind turbine foundations.

2.2 Historical Background

Wind energy has played a long and important role in the history of human civilisation, with modern wind turbines representing the culmination of several centuries of innovation in wind power technology. This innovation can be reviewed by dividing the history of wind energy into the following four overlapping time periods, as described by Beurskens (2014):

- **600-1890 – Classical period:** Whilst some authors maintain that the use of windmills originated approximately 3000 years ago in Egypt, the first reliable source of information documenting their existence is from the seventh century in Persia (Hau, 2013). The simple windmills from this era were used to convert wind energy into mechanical energy, such as for grinding grain, pumping water, and other agricultural applications. In Holland, windmills were also used to prevent the ocean from flooding low-lying land, such as those shown in Figure 2.1(a). This time period eventually ended with the advent of the steam engine, which had the convenience of being able to produce more power at will, and thus had a devastating effect on the number of windmills in operation.
- **1890-1930 – Development of electricity-generating wind turbines:** The development of electricity as a source of energy lead to the gradual adaption of windmills into wind turbines by connecting them to electrical dynamos. Scottish academic James Blyth was the first person accredited with this adaption in 1887, whose 10 m tall wind turbine with blades covered in sail cloth was used to power the lighting in his holiday home (Beurskens, 2014). His modified version of this wind turbine, in which he replaced the sail cloth blades with semi-cylindrical boxes, is shown in Figure 2.1(b). Interest in wind power continued with basic advances in the field of aerodynamics, until the decline after World War I (1914-1918) when fossil fuels became more freely available.
- **1930-1960 – First phase of innovation:** Various countries such as Denmark, the United States and Germany continued with the development of wind turbines during, and immediately after, World War II. This was spurred on by new research already conducted on aerodynamics and materials for manufacturing aircraft during the war, which was adapted to wind turbine technology. A particular landmark achievement was the development of the Smith-Putnam wind turbine in 1941, shown in Figure 2.1(c). At a generating capacity of 1.25 MW, it was the world's first megawatt-scale wind power plant, and the largest ever built for almost 40 years despite being decommissioned in 1945 (Divone, 2009). This innovation phase eventually came to an end due to the lack of financial means, the drop in price of fossil fuels, and the rise in popularity of nuclear power.
- **From 1973 – Second phase of innovation and mass production:** The 1973 oil crisis induced a very significant and sudden increase in the price of oil, which in turn stimulated a substantial amount of research and development in wind energy. Various configurations of prototype towers were being constructed and tested, with considerable advances in the disciplines of aerodynamics, structural dynamics and atmospheric sciences. By the last decade of the twentieth century the typical modern configurations of wind turbines started to emerge, with the very low carbon dioxide emissions being the main driver for the use of wind turbines.

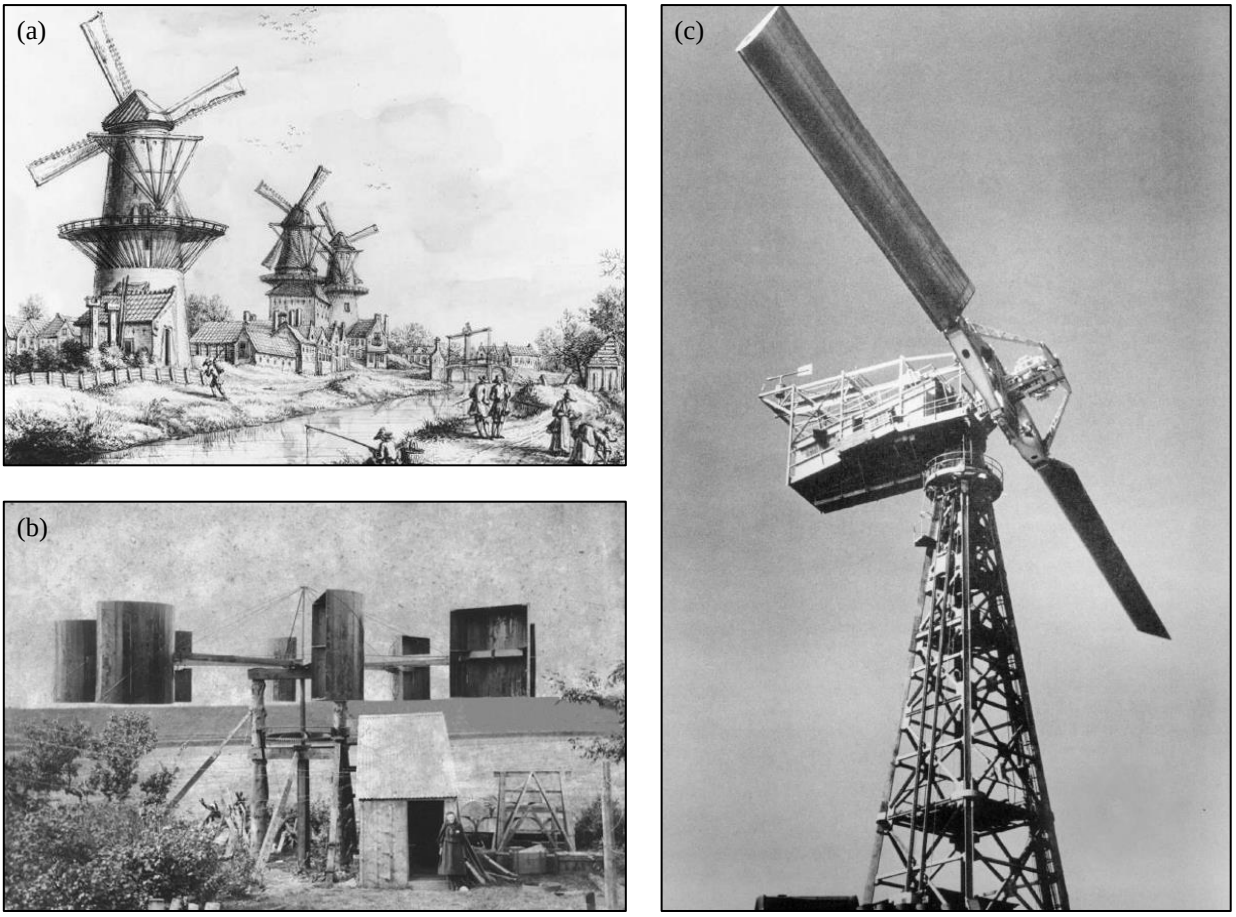

Figure 2.1: Historical development of the use of wind as a source of energy
(a) Dutch windmills in 1757 (Beurskens, 2014)
(b) James Blyth's modified vertical-axis machine in Marykirk, Scotland, in 1891 (Price, 2005)
(c) The 1.25 MW Smith-Putnam wind turbine in Vermont, USA, built in 1941 (Hau, 2013)

Today, wind is a mainstream source of energy supply and one of the fastest growing technologies in the world, with global investments estimated to total USD 3.6 trillion between 2014 and 2040 (GWEC, 2016). The worldwide wind power capacity had surged from less than 20 GW in 2000 to over 480 GW at the end of 2016, with more than half of this having been installed since 2011 (GWEC, 2017). This has prompted an emphasis on the configurations, mechanics and loading schemes of wind turbine structures, as even larger energy yields are sought.

2.3 Modern Configurations

The fundamental function of modern wind turbines is to convert the kinetic energy of the wind into electrical energy. To do so as efficiently as possible, several innovative configurations have emerged in recent decades. These configurations can either be classified according to their aerodynamic function, or more commonly with regards to their constructional design (Hau, 2013). Characterisation pertaining to the rotor's aerodynamic function is based on the fact that when air flows around an object, that object experiences two forces, namely lift and drag. As wind turbines are powered exclusively from either of these two forces, it follows that they can be classified as having either lift-type or drag-type rotors. On the other hand, classification based on constructional design is more practical as the orientation of a wind turbine's rotor axis to the ground is distinctly visible. In this regard, a wind turbine can be classified as a horizontal-axis wind turbine (HAWT) or a vertical-axis wind turbine (VAWT), examples of which are shown in Figure 2.2.

Figure 2.2: Wind turbine classification according to axis of rotation

(a) Horizontal-axis wind turbine (Hau, 2013)

(b) Vertical-axis wind turbine of the Darrieus type (Schaffarczyk, 2014)

HAWTs are characterised by having an axis of rotation that is parallel to the ground. They consist of a lift-type rotor, resembling that of an aircraft propeller, which is kept perpendicular to the flow of the wind. Significant advantages of this type of turbine include the ability to control rotor speed and power output by pitching the blades about their longitudinal axis; being able to aerodynamically optimise the rotor blade shape to achieve higher efficiency; the possibility of constructing taller towers to capture stronger winds at greater heights; high power density (the amount of energy that can be extracted per unit area of land); low cut-in wind speeds, and low cost per unit output (Tong, 2010; Hau, 2013). However, HAWTs are not without their disadvantages, such as the difficulty associated with the transportation and installation of the large tower segments and rotor blades; the high centre of gravity brought about by the heavy components situated at the top of the tower; and the fact that they are sensitive to the direction of the wind, which thus necessitates the addition of a yaw mechanism to constantly rotate the nacelle into the prevailing wind direction.

VAWTs are designed to have their blades rotate about a vertical axis that is perpendicular to the ground. Although they were initially built as drag-type rotors, engineers were eventually able to develop designs that utilised aerodynamic lift, which were identified as being much more efficient aerodynamically and in terms of material use. The most promising and thoroughly-researched VAWT concept for utility-scale energy production was the Darrieus rotor, pictured in Figure 2.2(b). These machines had two primary advantages, firstly that the rotor was able to accept wind from any direction without the need for a yaw mechanism, and secondly that the heavy mechanical and electrical components, such as the gearbox and generator, could be housed at ground level. However, they also had several disadvantages, the most prominent of which were their inability to self-start, not being able to control power output by pitching the rotor blades, not being able to turn away from the wind to avoid damage, reduced aerodynamic efficiency due to the blades creating downstream turbulence, having a limited maximum practical height, and low tip-speed ratio (Tong, 2010; Lynn, 2012; Hau, 2013). Consequently, there are currently no VAWTs that can compete with large HAWTs on a commercial scale, particularly considering that even the largest prototypes were built with rated powers of only about 0.5 MW. As a result, they currently make up a very small percentage of installed wind energy capacity worldwide.

This study focussed on HAWTs as they represent the wind turbine configuration dominating the wind energy industry today. The primary components of this type of wind turbine are subsequently described, followed by the loading regimes and foundation design requirements.

2.3.1 Primary components

The primary components of a HAWT include the rotor, nacelle, tower and foundation, the schematic arrangement of which is illustrated in Figure 2.3. In addition to this, there are several other mechanical and electrical components, such as the gearbox, generator and transformer, which all together are responsible for generating electricity and exporting it to the grid. As expected, designs differing from the standard concept are possible, however the basic features of each major component remain consistent and are subsequently described.

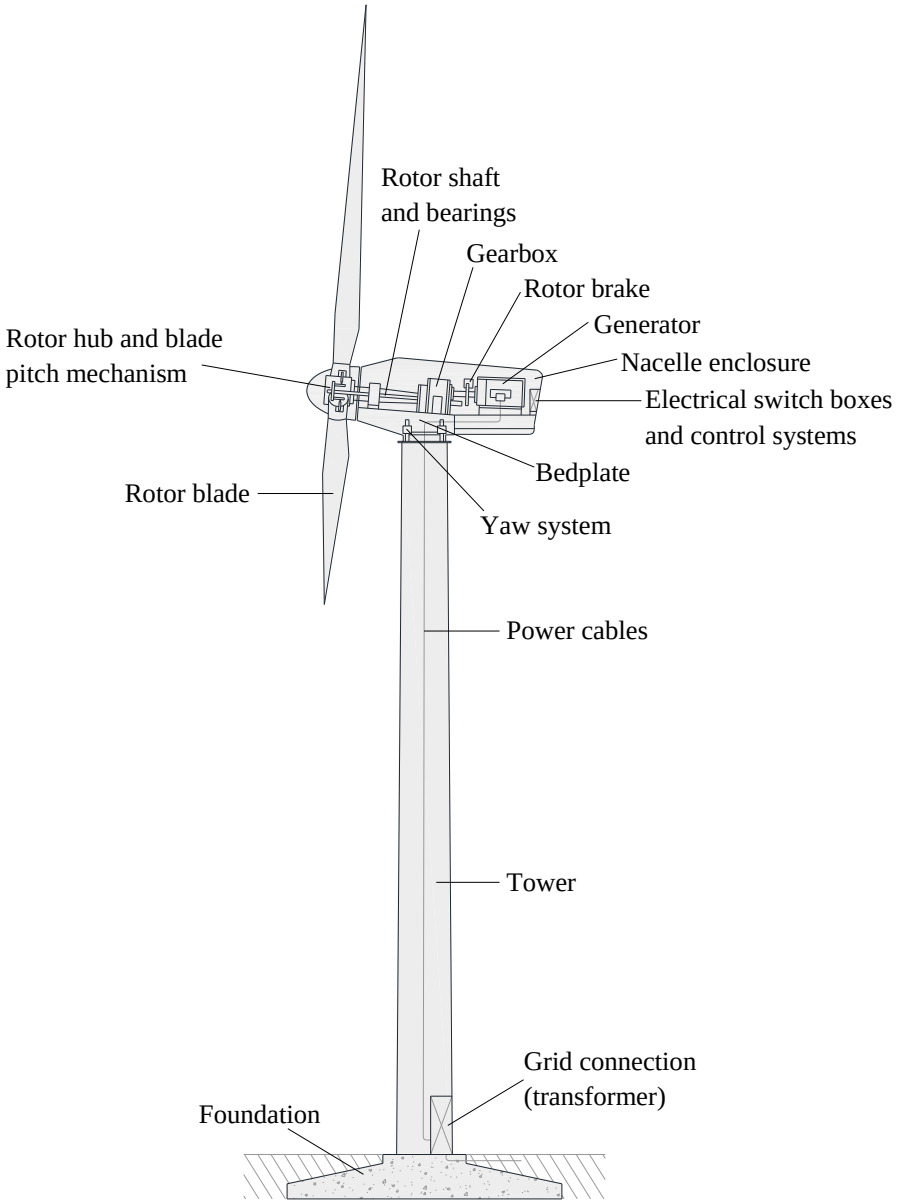

Figure 2.3: Components of a horizontal-axis wind turbine
Adapted from Hau (2013)

2.3.1.1 Rotor

As the name implies, the rotor consists of the rotating parts of the turbine, specifically the blades affixed to a central hub. These are considered to be the most important elements in determining the amount and efficiency of energy capture, as well as the magnitude of the static and dynamic loads that are transferred to the turbine (Viterna & Ancona, 2009). The blades are usually manufactured from a composite material, such as glass fibre reinforced plastic, for its high strength and low weight. They are also fabricated with a particular aerofoil profile that facilitates the generation of aerodynamic torque from the wind, thereby driving the turbine shaft which leads into the nacelle. Furthermore, a pitching mechanism is installed allowing the blades to rotate about their longitudinal axis and thus alter their angle of attack with respect to the wind. This is used to optimise power output when the wind speed is at the lower end of the spectrum, illustrated in Figure 2.4(a) where the lift force is increased by varying the pitch angle between 0º and approximately 30º. Conversely, it is also used to slow the rotor down in high wind speeds by pitching the blades between 70 º to 90 º as shown in Figure 2.4(b), thereby avoiding damage.

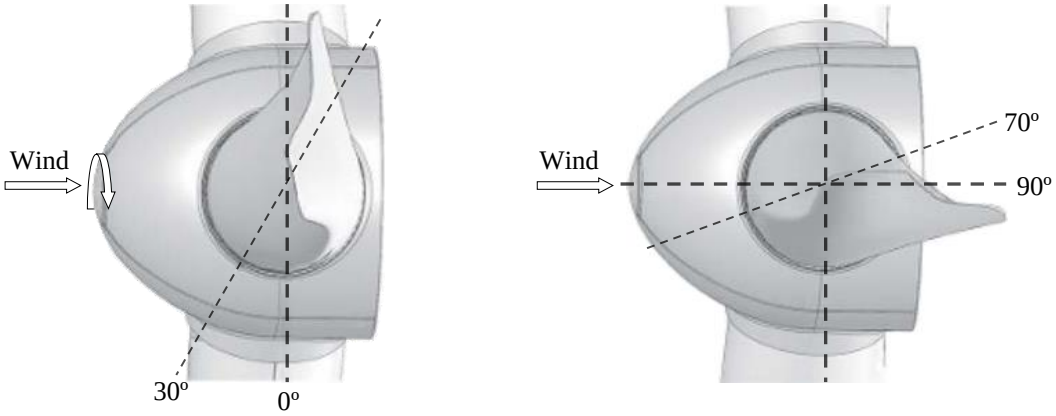

(a) Pitch angle 0º to 30º for normal operation (b) 70º for slow rotation; 90º for complete stop

Figure 2.4: Pitching of rotor blade to alter angle of attack

Adapted from Siegfriedsen (2014)

There are many ways in which HAWT rotors can be classified, some of which include:

- Number of blades. Wind turbine concepts with one and two blades have been developed in the past, having been predominantly justified due to their reduced cost and weight. However, the three-bladed design has been favoured in almost all modern installations due to the dynamically-symmetrical nature of its rotor, superior aerodynamic efficiency, and reduced visual impact.
- Upwind or downwind rotors. These terms denote the location of the rotor with respect to the tower, the difference of which is illustrated in Figure 2.5(a). Upwind rotors are those that face the wind directly, whereas downwind are those that face the opposite direction and are thus affected by wind shade from the tower. The majority of wind turbines today have upwind rotors.

- Rigid or teetered rotor hub. Teetered hubs allow the rotor blades to pivot through small teeter angles as shown in Figure 2.5(b), whereas rigid rotors do not. This feature has the effect of reducing the dynamic loads that are transferred to the rotor shaft. However, it is typically only required for rotors with two blades and not those with three, due to the unbalanced aerodynamic and yawing-induced cyclic loads that are produced (Spera, 2009).
- Rotor control. The rotor control system is responsible for ensuring that the rotational speed of the rotor is kept within a predefined range. In simplistic terms, there are three such systems (Bonnett, 2005): (1) passive stall regulation; (2) active stall regulation; and (3) pitch regulation.

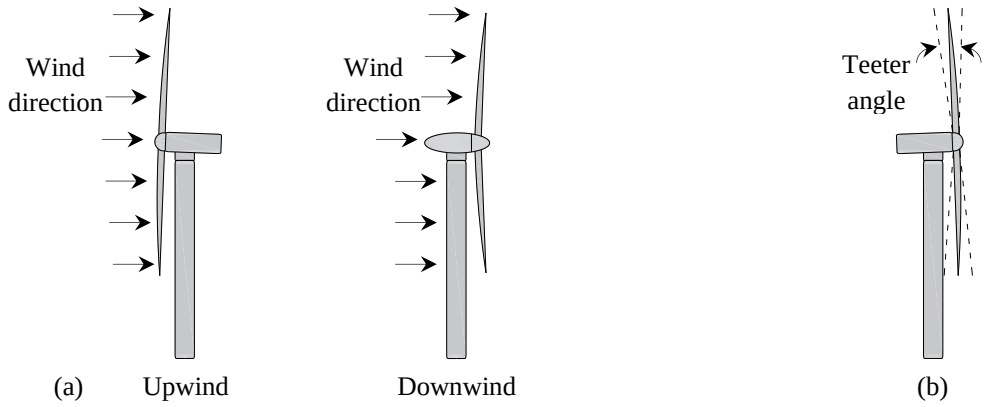

Figure 2.5: Horizontal-axis wind turbine rotor classification
(a) Distinction between upwind and downwind rotors
(b) Teetered hub design for a two-bladed rotor

2.3.1.2 Nacelle

The nacelle is the enclosed space at the top of the tower to which the rotor is connected. It has three main purposes, firstly to house the mechanical drivetrain and electrical equipment, secondly to allow the turbine to yaw so that the rotor can be orientated into the prevailing wind direction, and lastly to provide a counterweight for the weight of the rotor (Hemami, 2012).

The common mechanical components of the drivetrain are shown in Figure 2.6. The rotor shaft, otherwise referred to as the low-speed shaft, is supported by the main bearing and is directly connected to the hub. As a result, it has a slow rate of rotation of only tens of revolutions per minute (rpm). It is thus necessary to connect it to a gearbox to increase the rate to that which is more suitable for driving the generator, which is typically thousands of rpm on the high-speed shaft. This high-speed shaft leads into the generator, where the mechanical to electrical energy conversion takes place. A brake is also provided to prevent rotation of the shaft in various circumstances, such as maintenance, malfunctions or strong winds. The bedplate serves as a platform to which all of these components are mounted. Finally, the yaw drive system and tower head bearing allows the bedplate and nacelle to rotate with respect to the tower axis.

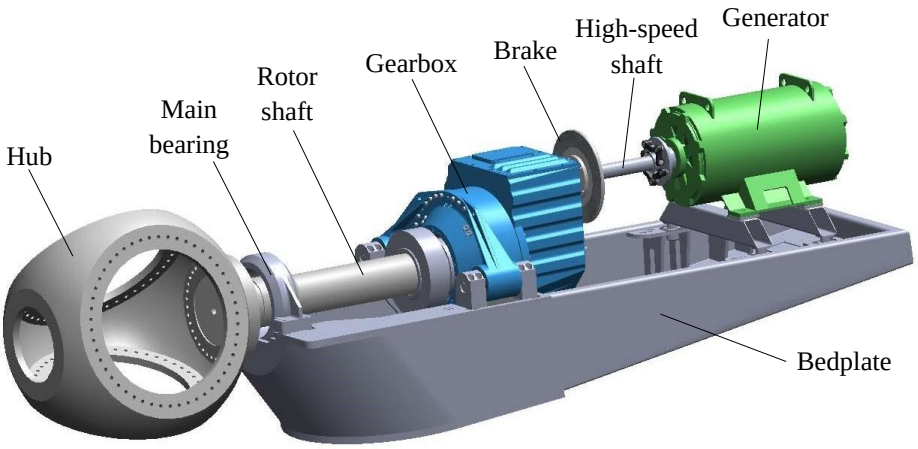

Figure 2.6: Drivetrain configuration
Adapted from Oyague (2009)

In addition to the drivetrain, the nacelle contains other equipment to assist with the functioning of the turbine. A pivotal piece of the nacelle is the controller, which is a computer system that is able to control the operation of the turbine and monitor performance. It is continually fed with measured data from various sensors, such as the anemometer for wind speed and the wind vane for wind direction. From this, the controller can regulate the pitch angle of the blades to control rotor speed, monitor the cut-in and cut-out wind speeds, conduct normal and emergency shutdowns, control the nacelle orientation using the yaw system, and so forth.

2.3.1.3 Tower

The tower supports the rotor and nacelle and provides the necessary elevation for the rotor to access strong and steady winds. It also enables access for maintenance workers to reach the nacelle, and protects the power and communication cables against adverse weather conditions. One of the most important considerations for the tower is the selection of an appropriate height. This is because, on one hand, as the tower height increases there is a corresponding increase in the specific energy yield of the turbine due to increased wind velocity, but on the other there is also a substantial increase in the difficulty and cost of transportation, assembly and erection of the tower. Therefore, the height of the tower requires optimisation and theoretically this would involve analysing where the two growth functions of energy yield and construction cost intersect. Nonetheless, the tower height is typically 1 to 1.5 times the diameter of the rotor (Manwell *et al.*, 2009), which generally translates to between 80-120 m for commercial turbines.

The materials used for the construction of the towers are steel and concrete. These have been arranged into several tower configurations in the past, the dimensioning of which is predominantly governed by strength and stiffness considerations. These considerations primarily include the buckling resistance of the walls in compression, the fatigue strength required to withstand the dynamic loads of the tower over its design life, and the stiffness requirements for tuning the natural frequency of the tower to prevent resonance (Burton *et al.*, 2011). With that, the most common tower configurations are discussed as follows:

i) **Tubular steel tower:** This is the most frequently used tower configuration for modern utility-scale wind turbines. It consists of three to four prefabricated sections of 20-30 m lengths, which are fashioned from rolled steel plates with flanges welded on either end. On site, they are lifted into place and bolted together as shown in Figure 2.7(a), making for simple and rapid construction. The towers are also tapered in diameter and shell thickness from top to bottom, thus saving on material costs and providing added strength at the base where it is needed. However, optimised tower dimensions are not usually possible, with the most significant factor driving the design being transportation logistics. Specifically, road obstructions such as overhead bridges often govern the maximum diameter of the tower base as indicated in Figure 2.7(b). In South Africa, this dimension is around 4.9 m as this is the stipulated minimum vertical clearance for a road overpass (SANRAL, 2002).

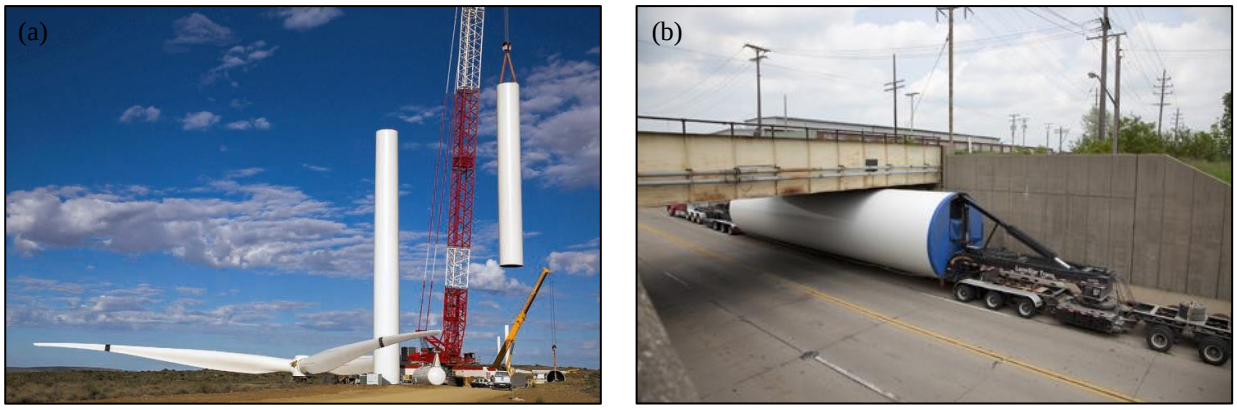

Figure 2.7: Erection and transportation of tubular steel tower segments
(a) Erection of tower (McGovern, 2017)
(b) Transportation logistics limiting tower base diameter (Smith & Myers, 2015)

ii) **Precast concrete tower:** Precast concrete towers are a viable alternative to steel towers for hub heights exceeding 100 m (Hau, 2013; Wagner & Mathur, 2013). This is largely on account of the fact that they are manufactured in prefabricated sections that are further separated into smaller segments, and thus the transportation problems associated with having a large diameter base are alleviated. The wall thickness of a concrete tower is also several times greater than that of a steel tower, with the advantages of reduced lateral deflections, higher tower natural frequencies, and less stability problems. However, the main disadvantage of this type of tower is the concrete's lack of tensile strength and thus the potential for cracking, a substantial issue considering the high bending stresses that are associated with large wind loads. This therefore necessitates the use of post-tensioning of the concrete segments, which can be an expensive and tedious process. South Africa's first wind farm to have concrete towers, the Gouda Wind Farm in the Western Cape (Figure 2.8), was connected to the national grid in 2015. For this project, the Concrete Society of Southern Africa (CSSA, 2016) states that the precast concrete segments for the towers and 95% of the associated raw materials were produced locally, providing a significant advantage over steel towers which typically have to be imported.

Figure 2.8: Precast concrete towers at the Gouda Wind Farm
Sourced from the CSSA (2016)

iii) **Concrete-steel hybrid tower:** Hybrid towers offer another alternative to wind turbine tower design with various configurations having been developed. The concept is for the tower to comprise of a combination of post-tensioned concrete in the lower portion and conventional steel in the upper portion as shown in Figure 2.9(a), which allows for capitalisation on the advantages of both materials. This makes the tower more economical due to the lower volume of steel required, less prone to resonance due to the higher natural frequencies, and overcomes the transportation limitations associated with the tower base diameter, as the slender concrete sections shown in Figure 2.9(b) are easily transportable. However, the post-tensioning requirement for the concrete remains a disadvantage.

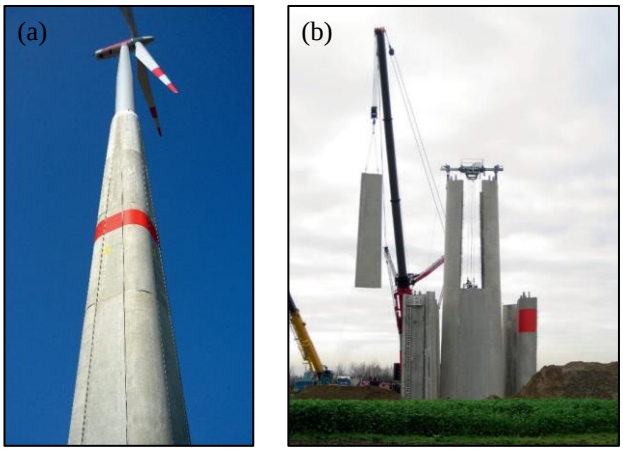

Figure 2.9: Concrete-steel hybrid tower with 133 m hub height
Sourced from de Vries (2010)

2.3.1.4 Foundation

The role of a wind turbine foundation is to transfer the forces emanating from the structure to the surrounding soil and rock. In doing so, it must keep the turbine upright and stable, particularly under extreme environmental conditions. The dimensions of the foundation are influenced by numerous factors, such as the type of turbine and its size, the ground conditions at the site, the weather conditions in the region, and the terrain topography. Therefore, unlike the rotor and nacelle which are supplied by the manufacturer in standard sizes, the design of the foundation is site-specific and most likely to vary across the vast expanse of a wind farm. There are also several foundation options available for onshore wind turbine structures, the most common of which are illustrated in Figure 2.10 and subsequently described.

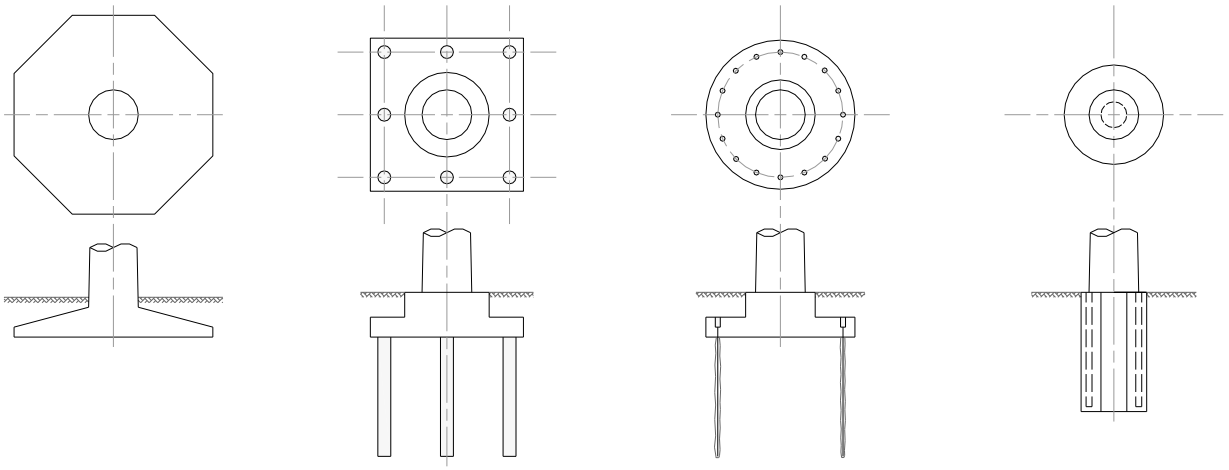

(a) Gravity base (b) Piles and pile cap (c) Rock anchors (d) Prestressed cylinder

Figure 2.10: Common foundation types for onshore wind turbines
Adapted from Bonnett (2005)

i) **Gravity base:** The gravity base is the standard foundation solution for onshore wind turbines. This is largely due to its cost-effectiveness, overall simplicity, and the fact that the design methods for such foundations are universally accepted and well understood. It consists of a wide, shallow footing that is constructed in-situ of reinforced concrete with an elevated central pedestal. An I-beam-ring or prestressed anchor bolt cage is embedded into the central pedestal, to which the tower is attached. As the name suggests, this type of foundation primarily relies on its massive self-weight and soil overburden to provide stability against the overturning loads from the tower.

   In the interest of minimising costs, designers often aim for the smallest foundation size possible that is yet large enough to satisfy all of the design constraints. This typically results in the following dimensions (Ntambakwa *et al.*, 2016):

   - Foundation diameter of 15 to 20 m
   - Pedestal diameter of 4.5 to 5.5 m

- Pedestal height of 2 to 3 m, tapering to 1 m or less at the outer edges of the foundation
- Foundation base embedment of 1 to 3 m below finished ground level

Furthermore, although the ideal shape of a gravity base foundation in plan is a circle (Figure 2.11) due to the constantly changing loading direction from the wind, complications with providing circular formwork often results in an octagonal or hexadecagonal shape being chosen instead. Occasionally the foundations are designed to be square in plan to simplify the shuttering and reinforcement further, however such foundations can be susceptible to stress concentrations at the corners.

Figure 2.11: Construction of a circular gravity base foundation
Sourced from van der Spuy (2014)

ii) **Piles and pile cap.** Pile foundations are able to transfer the loads of the wind turbine to greater depths should the conditions at a planned site require it. Examples of such conditions include cases where the top soil strata are not able to provide adequate bearing resistance for a conventional gravity base foundation, if there is inadequate stiffness to satisfy the serviceability limit states, when expansive or collapsible soils are present, if the foundation is subject to uplift from a high water table, and so forth. The piles are either driven into the ground or bored and cast in-situ, then connected with a concrete cap which distributes the load of the structure to all of the piles in the group. The loads applied at the head of each pile are transferred down its length and absorbed by the soil through a combination of axial and lateral pile resistance. The former is generated by wall friction and end-bearing resistance, and the latter by bending of the piles, each of which is mobilised when the pile is displaced relative to the soil.

This foundation solution has been implemented in South Africa for wind turbines located in unfavourable conditions, such as at the Gouda Wind Farm in the Western Cape where six of the forty-seven wind turbines were founded on piles. Each of these pile foundations,

one of which is pictured in Figure 2.12 prior to the casting of the pile cap, consisted of sixteen 750 mm diameter piles that were cast in-situ and designed to socket 3.0 m into the underlying rock (van Zyl, 2014).

Figure 2.12: Piling completed for a tower base at the Gouda Wind Farm
Sourced from van der Westhuizen (2015)

iii) **Rock anchors:** Foundations with rock anchors can be implemented at sites with relatively shallow bedrock, and consist of post-tensioned steel rods that are grouted into holes drilled deep into the rock (Figure 2.13). The loads are resisted by a combination of the tension in the rods and the bearing resistance beneath the concrete pad at the founding level. The advantage of this is that it allows the overall foundation size to be significantly reduced as less weight is required for counterbalance purposes, provided that the bearing capacity of the underlying soil is sufficiently high. However, the installation process requires specialist contractors, and consequently they are seldom used (Burton *et al.*, 2011).

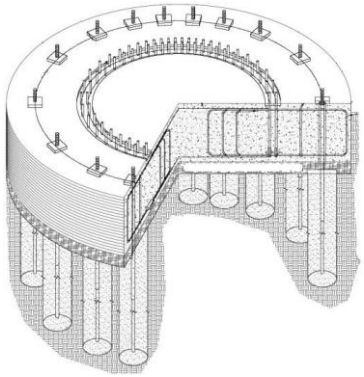

Figure 2.13: Rock anchor foundation
Sourced from Earth Systems Global (2009)

iv) **Prestressed cylinder:** The prestressed concrete cylinder foundation, also known as the *Patrick and Henderson* foundation after its inventors, is relatively simple to construct and can be an efficient and cost-competitive solution in suitable ground conditions. Initially during installation, it requires a deep hole to be excavated with a diameter in the order of ~5 m and depth ~8-12 m, and thus is only applicable to sites in which competent bedrock or non-collapsing soil is located near the ground surface, so as to prevent the side walls from caving in. Two concentric corrugated metal cylinders with different diameters are then placed into the excavated hole, and the annular space filled with concrete to form a concrete cylinder (Figure 2.14). Subsequently, the hollow interior is plugged at the base with concrete, backfilled with uncompacted soil, and capped with a structural slab. The anchor bolts of the wind turbine, which are embedded in the concrete cylinder as shown in Figure 2.14, are post-tensioned to ensure that the concrete remains in compression under all loading conditions. The horizontal loads and overturning moment are primarily resisted by the horizontal resistance of the soil that surrounds the pier, the wall friction, and to a lesser extent the bearing at the base. This type of foundation has been particularly successful in the USA (Bonnett, 2005) with the main advantage being the cost savings associated with the reduction in material usage.

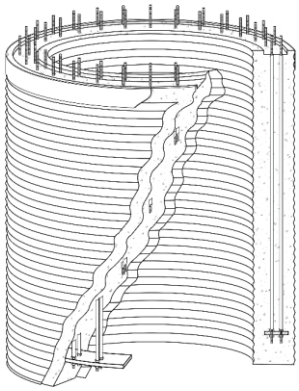

Figure 2.14: Prestressed concrete cylinder foundation
Sourced from Earth Systems Global (2009)

2.3.2 Power generation and upscaling trends

In recent decades, advances in wind engineering have brought about a continuous increase in power output capacities of utility-scale wind turbines. One of the most significant factors behind this has been the considerable upscaling of wind turbine structures that has occurred with regards to both rotor diameter and hub height. As indicated in Figure 2.15, this has resulted in the progression of the technology from machines with rated powers of 25 kW in the 1980s to the current commercial range of 2-3 MW. Although this range represents the typical power ratings of wind turbines sold by manufacturers today, even larger sizes have been achieved, albeit with added cost and logistical constraints. For instance, German company *Enercon* has developed the world's largest onshore wind turbine, the *E-126* model, which has a hub height of 135 m, rotor diameter of 127 m, and can generate up to 7.58 MW of power.

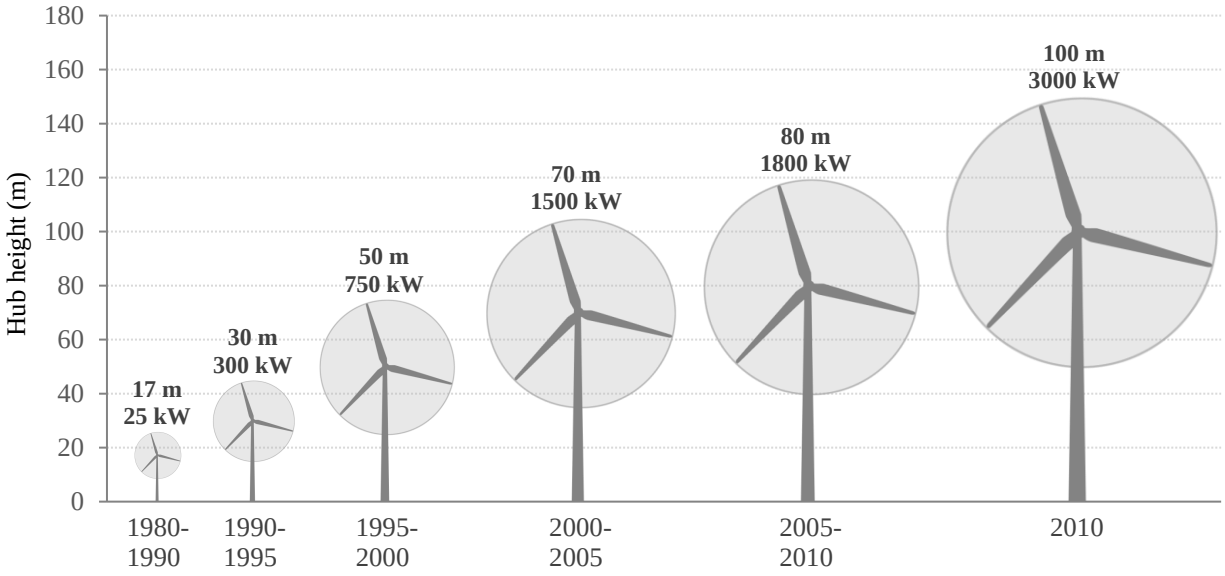

Figure 2.15: Increase in wind turbine size and generating capacity from 1980 to 2010
Adapted from Lantz *et al.* (2012)

The growth in the hub heights and rotor diameters of modern wind turbine structures can be explained through the principles of momentum theory in the field of fluid dynamics. A wind turbine operates by extracting the kinetic energy of a stream of moving air. By considering this airflow to be a cylindrical mass passing through the area of the rotor, the following well-known expression can be derived for the power output of a wind turbine:

$$P = \tfrac{1}{2} C_p \rho_a A U^3 \qquad \text{Eqn. 2.1}$$

Where P = power (W); C_p = power coefficient (unitless); ρ_a = air density (kg/m^3); A = rotor swept area (m^2); and U = wind speed (m/s).

It is evident from Equation 2.1 that there are four primary parameters that influence the power generated by a wind turbine, each of which is described below:

i) **Power coefficient:** This is a unitless value that is defined as the ratio between the power generated by the turbine to the total power contained in the wind resource. It is a product of the mechanical, electrical and aerodynamic efficiencies of the turbine. In the early 1920s, German physicist Albert Betz discovered that the maximum achievable value of the power coefficient is 16/27, or 59%, known as the *Betz limit*. This discovery, which was based on the fundamentals of fluid dynamics, and was independent of the precise design of the rotor, means that fundamentally a wind turbine cannot convert more than 59% of the kinetic energy in the wind into mechanical energy in the rotor. However, the Betz limit is considered to be an optimistic upper limit of the power coefficient and modern optimized wind turbines generally operate with a power coefficient of up to 0.5 (Hansen, 2015).

ii) **Air density:** As the kinetic energy of a moving body is directly proportional to its mass, it follows that the kinetic energy in the wind is dependent on the density of the air. The denser it is, the more energy can be extracted by the turbine, and vice versa. Furthermore, air density increases with decreasing altitude, temperature or humidity, with the differences in power generation being up to 10% or more between different sites or at the same site between summer and winter (Lynn, 2012).

iii) **Rotor swept area:** The power available from the wind is directly proportional to the cross-sectional area of the wind turbine's rotor. Therefore, it is also proportional to the square of the rotor radius, and thus doubling the rotor blade length increases the available power by a factor of four. However, although this indicates that increasing the blade length can produce a significant increase in energy yield, doing so has several implications. Some of these include the associated increase in blade stiffness required to maintain a minimum clearance between the blade tips and the tower, the variability of the wind velocity over the large area of the rotor, resulting in unbalanced fatigue loads, as well as added complications with transportation and installation (Tong, 2010).

iv) **Wind speed:** The relationship between wind speed and available power is cubic as shown in Equation 2.1, and therefore it has a significant impact on wind turbine design and performance. For instance, doubling the wind speed will increase the power available in the wind by a factor of eight, and an increase in wind speed of 26% will double the available power. It is because of this that greater hub heights are desirable, as taller towers lift the rotor into winds that are less turbulent, more consistent, and have greater speeds and hence energy.

Furthermore, wind turbines are designed to operate over a range of wind speeds. Evidence of this range is seen in a wind turbine's power curve, which is a graphic representation of its power output as a function of wind speed for a given air density. The power curve is provided by the turbine manufacturer in the form of a table or graph, an example of which is illustrated in Figure 2.16 for a Vestas V112-3.0 MW turbine. There are several characteristic wind speeds associated with this curve, defined below:

- Cut-in wind speed: The minimum wind speed at which the wind turbine starts to operate and produce useful power.
- Rated wind speed: The minimum wind speed at which the rated power is reached.
- Cut-out wind speed: The maximum wind speed at which the wind turbine is designed to produce power. At this wind speed the turbine shuts down to avoid damage.

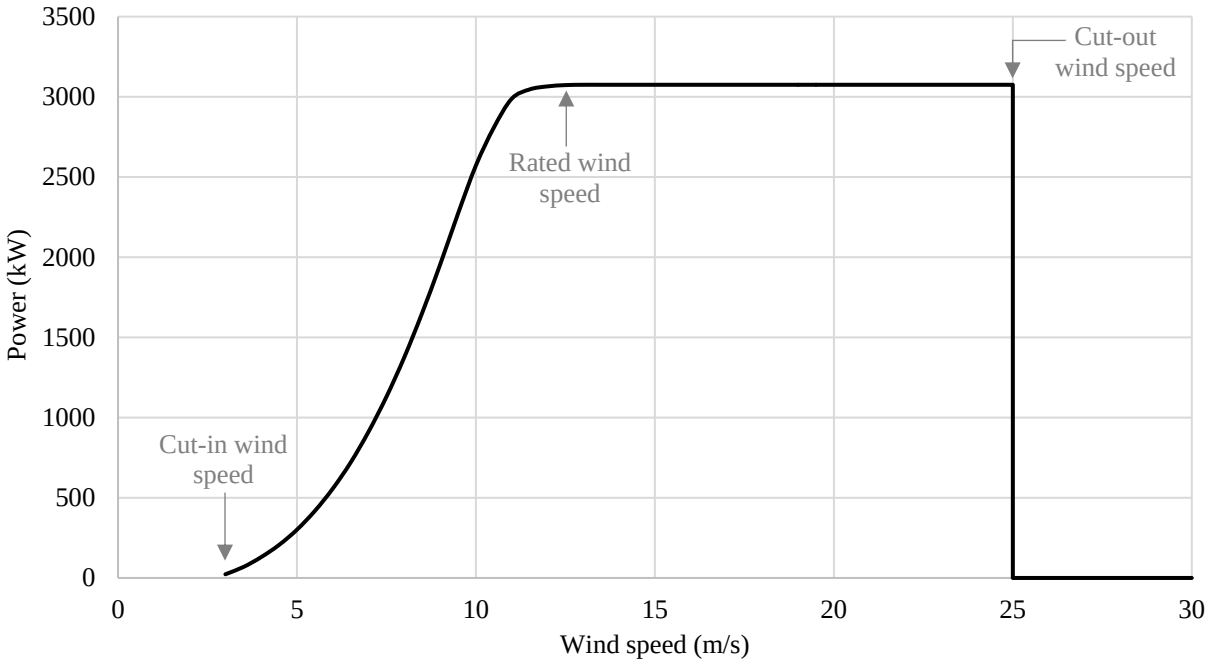

Figure 2.16: Power curve for a Vestas V112-3.0 MW wind turbine
Data sourced from Vestas (2010)

Although the rated power of a wind turbine represents the maximum amount of energy that it can produce per unit of time in ideal conditions, it does not provide an indication of how the turbine will perform over a longer timeframe due to wind variability. Therefore, in assessing the economics and feasibility of a proposed wind farm, it is more suitable to estimate its annual energy production. This is the amount of electrical energy delivered to the grid over a one year period, measured in units of energy rather than power, such as gigawatt-hours (GWh). In order to make such an estimate, accurate predictions of the wind speed and wind regime characteristics in the region of the wind farm are of fundamental importance. In South Africa, this information can be obtained from the Wind Atlas for South Africa (WASA) project, initiated by the Department of Energy in 2009 to provide authorities with the necessary information to conduct long-term planning of large-scale wind energy projects. The WASA project uses a combination of numerical modelling and data captured from wind masts around South Africa to produce high-resolution mapping and databases of the country's wind resources. Various aspects are included, such as mean wind speed, mean power density, terrain elevation, ruggedness index, 1:50 year ten-minute wind speed, 1:50 year gust speed, and so forth. The map of mean wind speed at an elevation of 100 m above ground level is shown in Figure 2.17.

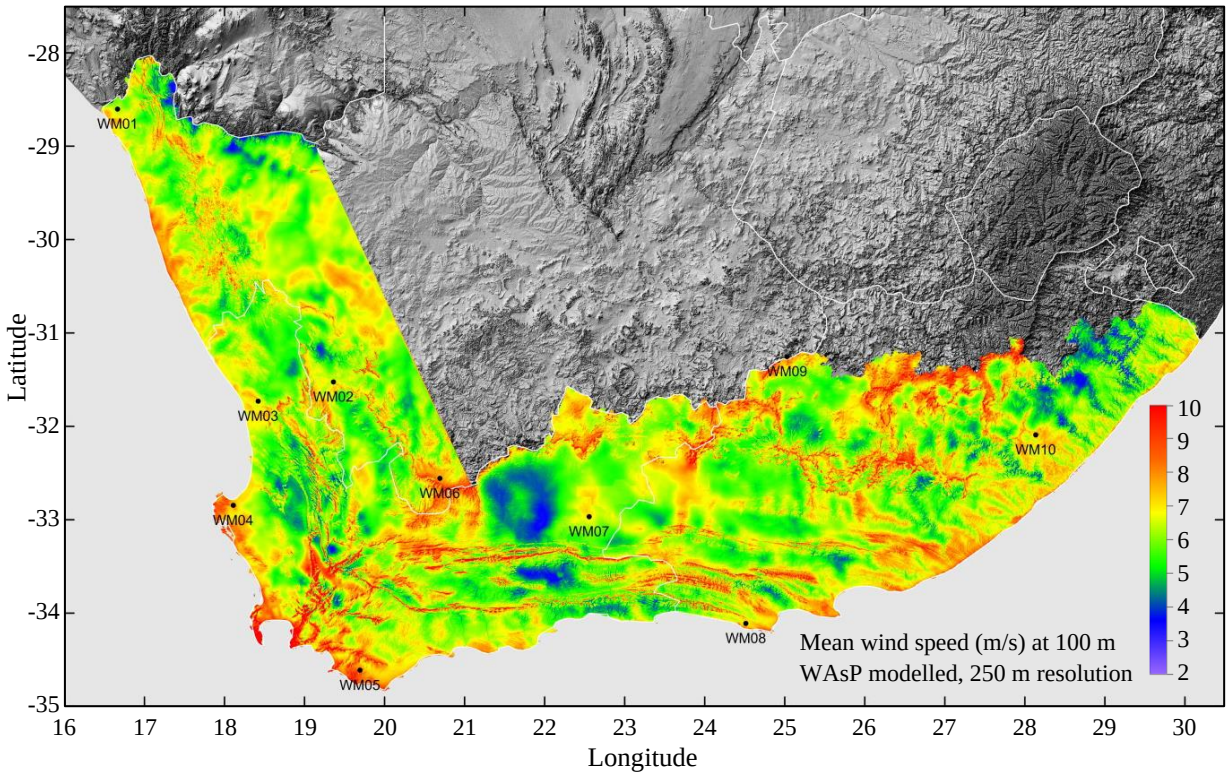

Figure 2.17: Mean wind speed at 100 m above ground level
Adapted from the SANEDI (2015)

As larger energy yields continue to be sought and the growth in height and rotor swept area of wind turbines progresses, there will be associated increases in the design loads that must be endured by the support structures. The tower of a wind turbine is essentially a wind loaded cantilever beam, and hence any increase in its overall height or loads at its tip (from the nacelle and rotor) will contribute to higher bending moments, as well as lateral and vertical forces, at the base. These factors will prompt a need for larger, more robust, and more expensive foundation solutions.

2.4 Foundation Loading

As part of the design process, a wind turbine must be analysed for the various loads it will experience during its design life. This task is undertaken by evaluating several load cases, each with a reasonable probability of occurrence, and each representing different combinations of design situations and external conditions. In doing so, the applied loads dictate the structural requirements of the various wind turbine components. The necessary resistance to be provided by the foundation system is also evaluated, as the loads acting on the rotor and substructure are ultimately transferred to the foundation.

The International Electrotechnical Commission Standard 61400-1 (IEC, 2005), which is an international standard for the design requirements of wind turbines, specifies that the following general load types should be considered in wind turbine design calculations:

i) **Gravitational and inertial loads:** These are static and dynamic loads acting on the wind turbine, which are dependent on mass, and result from gravity, vibration, rotation, and seismic activity. The gravitational loads comprise the dead weight of the components, and are simple to calculate relative to other load types. Examples of inertial loads include the centrifugal forces induced by rotation of the rotor, and the gyroscopic effects caused by yaw motion.

ii) **Aerodynamic loads:** Aerodynamic loads are generated by airflow interacting with the stationary and moving parts of the wind turbine, and can also be both static and dynamic in nature. This airflow is influenced by several factors, such as the average wind speed and turbulence across the rotor plane, the rotational speed of the rotor, the density of the air and the aerodynamic shapes of the wind turbine components. The most notable aerodynamic load is that which acts on the rotor blades to produce lift and drag forces, however aerodynamic drag forces on the tower and nacelle also require consideration.

iii) **Actuation loads:** These loads are generated by the operation and control of the wind turbine. They may be experienced in several forms, such as mechanical braking loads, yaw and pitch actuator loads, torque control from the generator, and so forth.

iv) **Other loads:** Miscellaneous loads, not included in the above categories, may occur and should be included where appropriate. Examples include wake effects, impact loads and ice loads.

Wind turbine loading is largely governed by the environmental conditions that surround the structure. However, in addition to this, the loading is also dependent on the state of operation of the wind turbine. Consequently, numerous load case permutations are stipulated by IEC 61400-1 (IEC, 2005) for analysis, with the primary operational states summarised as:

- **Power production:** The wind turbine is in normal operation and connected to the electrical grid. This is the state in which the structure will spend most of its serviceable life, whereby the rotor has a rotational frequency equal to, or less than, the design frequency.
- **Parked:** The rotor is stationary and hence no rotation-induced loads are experienced by the structure. The turbine may be put into a parked state when the environmental conditions are considered too extreme for safe operation. In this situation, the rotor blades are pitched into a feathered position, thereby considerably reducing the rotor thrust and thus the bending moment at the tower base.
- **Start-up and shut-down:** The wind turbine transitions from a standstill or idling situation to power production, or vice versa. These procedures initiate a change in rotor frequency.
- **Abnormal or fault states:** Situations in which the turbine is not operating as it should, such as over-speeding of the rotor, a control system fault, or a rotor emergency stop. These technical faults can subject the wind turbine to additional loads not covered by the other load cases.

In considering the load types and operational states mentioned above, it is important to recognise that wind turbine components, including the foundation, are ultimately designed for two loading scenarios: (1) extreme loads, and (2) fatigue loads. The former, also referred to as ultimate loads, correspond to the maximum loads that the component is required to sustain momentarily in the course of its lifetime. On the other hand, fatigue loads are cyclical in nature, much smaller in magnitude, and are associated with the long-term performance of the materials, which may weaken due to repeated variations in stress. These two loading scenarios are subsequently described with respect to the foundation design.

2.4.1 Extreme loading

Wind turbine foundations are designed to resist the infrequent application of the highest loads expected during the useful lifetime of the structure. It is typically these extreme loads, or the foundation stiffness requirements, that govern the final dimensions of the footing. In practice, wind turbine manufacturers provide a loading document, created in accordance with the IEC 61400-1 standard, that specifies the magnitudes of the extreme loads for the relevant load cases. The loads provided therein are turbine-specific and generated using highly specialised software capable of dynamic load simulations. The conditions under which these simulations take place correspond to a combination of different extreme wind events, such as extreme gusts, crosswinds and changes in wind direction, with their respective probabilities and resulting loads taken into consideration.

In selecting the load cases for design, it is common practice to distinguish between normal and extreme wind conditions on one hand, and between normal machine states and fault states on the other. With this, the following combinations are considered relevant (DNV/Risø, 2002):

- Normal wind conditions in combination with normal machine states
- Extreme wind conditions in combination with normal machine states
- Machine fault states in combination with appropriate wind conditions, which may include extreme wind conditions

The first load case corresponds to normal operating conditions and is thus applicable to the serviceability limit state, whereas the latter two occur rarely and are relevant to the ultimate limit state. As would be expected, the maximum extreme bending moment occurs for extreme wind conditions in combination with the abnormal operational state. However, as machine fault states arise infrequently, and are presumed to be uncorrelated with extreme wind conditions, a general assumption might be that the return period of both events occurring simultaneously is sufficiently high such that it is not analysed as a load case. However, IEC 61400-1 stipulates that if a correlation is found between an extreme external condition and a fault situation, then a realistic combination of the two should be considered as a design load case (IEC, 2005).

To facilitate the design and analysis of wind turbine foundations, the loads provided by the turbine manufacturers are simplified into vertical, horizontal and moment components. For

instance, the notation adopted by Vestas (2013) is illustrated in Figure 2.18, and includes the following simplified moments and forces:

- $\boldsymbol{M_{res}}$**:** Resulting bending moment
- $\boldsymbol{M_z}$**:** Simultaneous torsion moment
- $\boldsymbol{F_{res}}$**:** Simultaneous resulting shear force
- $\boldsymbol{F_z}$**:** Simultaneous vertical force

The resulting bending moment M_{res} is the combination of moment vectors in the x- and y-direction respectively, M_x and M_y, and similarly F_{res} is the resultant of vectors F_x and F_y. In some load reports, these components are stated separately and must be combined as vectors. The vertical force F_z is representative of the dead load of the wind turbine components, excluding the foundation, and also includes a small vertical component of the thrust.

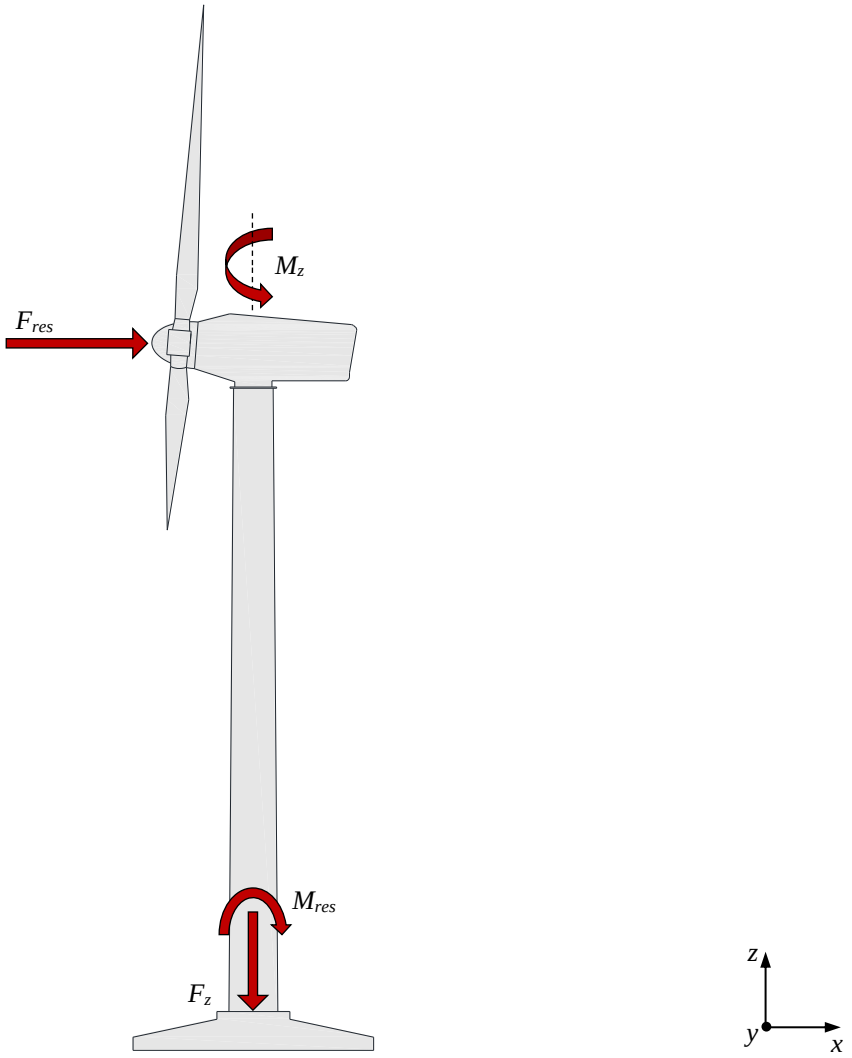

Figure 2.18: Simplified loading scheme of a wind turbine structure

2.4.2 Fatigue loading

Wind turbine structures present many difficult fatigue design problems. This is largely because they are relatively slender and flexible, subject to vibration and resonance, acted upon by loads which are nondeterministic, and are operated continuously in all types of conditions. Over a design life of 20 years or more, the continued rotation of the rotor, as well as alternating stochastic loads from the turbulence of the wind, lead to extraordinarily high cyclic load numbers. The persistent, alternating stresses induced by this loading can cause fatigue damage of the various materials after a period of time.

Onshore wind turbines experience different forms of cyclic loading, each of which has unique characteristics in terms of the magnitude, frequency, and number of cycles applied to the foundation. These cyclic loads are subsequently described. However, a key consideration in the context of this study is how these loads act from a dynamics point of view, and to explain this further, some background theory is first presented.

2.4.2.1 Concepts from basic dynamics

Dynamics is the study of systems whose behaviour varies over time. It follows that a fundamental aspect that differentiates a dynamic problem from a corresponding static problem is the time-varying nature of the load, as well as the time-varying response of the system. To illustrate this, a single degree-of-freedom system is considered, shown in Figure 2.19.

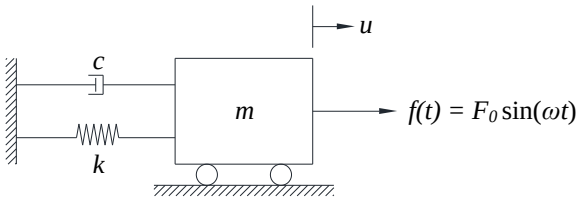

Figure 2.19: Single degree-of-freedom system

Figure 2.19 illustrates that the basic features of the system are (1) the mass, *m*, which possesses inertia and can have kinetic energy by virtue of its velocity of motion; (2) the damper, *c*, which is assumed to possess neither inertia nor elasticity, and represents the dissipation of energy from the system; (3) the spring, *k*, which possesses elasticity and can store potential energy by virtue of its deformation; and (4) the excitation force, *f(t)*, which is a function of time, *t*, and is the agent by which energy is introduced into the system. By taking equilibrium of forces in this system, Equation 2.2 is produced, known as the fundamental equation of motion. Note that the excitation force is assumed to be harmonic.

$$\underbrace{m\ddot{u}(t)}_{\text{Inertia term}} + \underbrace{c\dot{u}(t)}_{\text{Damping term}} + \underbrace{ku(t)}_{\text{Stiffness term}} = \underbrace{F_0 \sin(\omega t)}_{\text{Excitation force}} \qquad \text{Eqn. 2.2}$$

Where m = mass (kg); c = viscous damping coefficient (N·s/m); k = spring constant (N/m); $\ddot{u}$ = acceleration (m/s^2); $\dot{u}$ = velocity (m/s); u = displacement (m); F_0 = excitation load amplitude (N); ω = excitation load frequency (Hz); and t = time (s).

Equation 2.2 is a differential equation and its solution is the sum of two parts, the complementary solution (u_c) and the particular solution (u_p), as shown in Equation 2.3. The former represents the transient response of the system and corresponds to free vibration conditions in which there is an absence of any excitation (Eqn. 2.4), and the latter represents the steady-state response of the system to the applied load (Eqn. 2.5).

$$u(t) = u_c(t) + u_p(t) \qquad \text{Eqn. 2.3}$$

$$u_c(t) = e^{-\zeta\omega_n t}\left(A\sin(\omega_d t) + B\cos(\omega_d t)\right) \qquad \text{Eqn. 2.4}$$

$$u_p(t) = \frac{F_0}{k}\frac{1}{\sqrt{\left(1-\left(\omega/\omega_n\right)^2\right)^2 + \left(2\zeta\left(\omega/\omega_n\right)\right)^2}}\sin(\omega t - \alpha) \qquad \text{Eqn. 2.5}$$

Where u_c = complementary solution (m); u_p = particular solution (m); ζ = damping ratio (unitless); ω_n = natural frequency $= \sqrt{k/m}$ (Hz); A,B = coefficients determined from the initial conditions (m); ω_d = damped natural frequency (Hz); α = phase angle (radians); and other parameters previously defined.

The complementary solution dampens out after a limited number of cycles due to the exponential decay ($e^{-\zeta\omega_n t}$). Thus, the solution of interest is the particular solution as it continues indefinitely as long as the excitation force persists. It can be inferred from this solution (Eqn. 2.5) that the maximum response of the system occurs when $\sin(\omega t - \alpha)$ is equal to unity, as this is the maximum value possible. Therefore, by rearranging the equation, the formula for the dynamic amplification factor (D) can be derived, shown in Equation 2.6. This factor, otherwise referred to as the *magnification factor*, is important in dynamics because in physical terms it represents the ratio between the displacement of the steady-state response to that of the static displacement due to the peak value of the excitation force (F_0/k). For instance, a dynamic amplification factor of two indicates that the displacement caused by dynamic effects is double that of the static displacement.

In addition, Equation 2.7 shows the derived formula for the phase angle, α, which is indicative of the extent to which the response of the system lags behind the applied loading.

$$D = \frac{u_p(t)}{F_0/k} = \frac{1}{\sqrt{\left(1-\left(\omega/\omega_n\right)^2\right)^2 + \left(2\zeta\left(\omega/\omega_n\right)\right)^2}} \qquad \text{Eqn. 2.6}$$

$$\tan\alpha = \frac{2\zeta\left(\omega/\omega_n\right)}{1-\left(\omega/\omega_n\right)^2} \qquad \text{Eqn. 2.7}$$

Where D = dynamic amplification factor (unitless); ω/ω_n = frequency ratio (unitless); and other parameters previously defined.

The dynamic amplification factor and phase angle are better interpreted by plotting their variation with the frequency ratio for several different damping ratios, as illustrated in Figure 2.20(a) and (b) respectively. A close examination of this figure reveals that the time-dependent response of the system can be classified into the following three categories:

- $(\omega/\omega_n) << 1$: If the frequency ratio is very small and approaches a value of zero, as would be the case for a slowly-varying excitation frequency, then the dynamic amplification factor is close to unity and the phase angle close to zero. This implies that the response is similar to that of a static load and it is in phase with the excitation for all practical purposes. This is known as *quasi-static* behaviour, and is characterised by a negligible contribution of the inertia term in the equation of motion.
- $(\omega/\omega_n) >> 1$: On the other end of the spectrum, when the frequency ratio is very large such as for a rapidly-varying excitation frequency, the inertia term dominates the force equilibrium and the behaviour is that of wave propagation. The dynamic amplification factor quickly approaches zero, leading to a very small steady-state dynamic response. The phase angle tends towards 180º, which means that the force is out of phase with the system, for instance when the force acts to the right, the system displaces to the left.
- $(\omega/\omega_n) \approx 1$: If the excitation frequency coincides with the natural frequency, then the frequency ratio will be close to unity and the response will be that of resonance. In this condition, the displacement of the system is governed by damping as illustrated in Figure 2.20(a), and the inertia and stiffness forces are of comparable magnitude with each other. For small values of the damping ratio, there are very high dynamic amplification factors, and theoretically this factor would tend towards infinity for the case of zero damping. Furthermore, the response lags the excitation by 90º, and thus the displacement attains its peak as the force is zero.

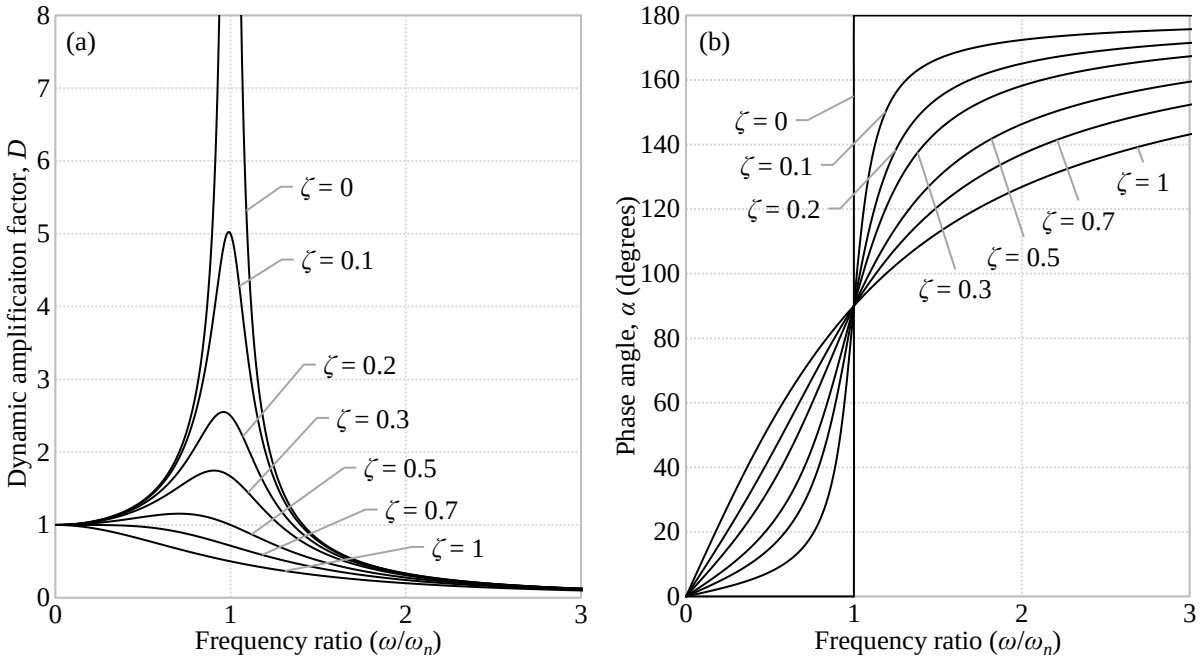

Figure 2.20: Response of single degree-of-freedom system to harmonic excitation
(a) Dynamic amplification factor versus frequency ratio for various amounts of damping
(b) Phase angle versus frequency ratio for various amounts of damping

The preceding background in dynamics served to provide insight into how the cyclical excitation loads acting on a wind turbine structure affect the time-dependent response of the system. A key aspect to note is that even though these loads act cyclically, this does not necessarily mean that they act dynamically, and this is dependent on the frequency of the loading.

2.4.2.2 Cyclic and dynamic loading

Cyclic loads are those which involve reversals of load about a mean level and which are periodic in nature. There are three primary cyclic loads transmitted to the foundation of an onshore wind turbine, each of which is outlined below, and illustrated in Figure 2.21 along with their typical waveforms.

i) The external load produced by the wind and its turbulence. This load is random with regards to both space and time, however it is often approximated as applying one-way cyclic loading to the foundation. It is generally regarded as being composed of a constant mean speed and a fluctuating component, or gust.

ii) Loading due to rotation of the rotor system, referred to as 1*P* loading. This is an internal load caused by vibration at the hub level due to the mass and aerodynamic imbalances of the rotor. It has a forcing frequency equal to the rotational frequency of the rotor, which for modern variable-speed machines is not a single frequency but rather a frequency band. For instance, the rotor of the Vestas V112-3.0 MW wind turbine has an operational interval

of 6.2 to 17.7 rpm (Vestas, 2010), which corresponds to a 1*P* frequency range of 0.10 to 0.30 Hz.

iii) Loading due to passing of the rotor blades, referred to as 3*P* loading for a three-bladed turbine, or 2*P* for a two-bladed. This is an internal load that is a result of blade shadowing effects, whereby the blades passing the front of the tower cause a momentary loss of wind load on the tower. The 3*P* forcing frequency is also a frequency band for a variable-speed turbine, with the frequencies being equal to three times that of the rotor frequency (1*P*). Therefore, for the Vestas V112-3.0 MW turbine, the 3*P* frequency range is 0.31 to 0.89 Hz.

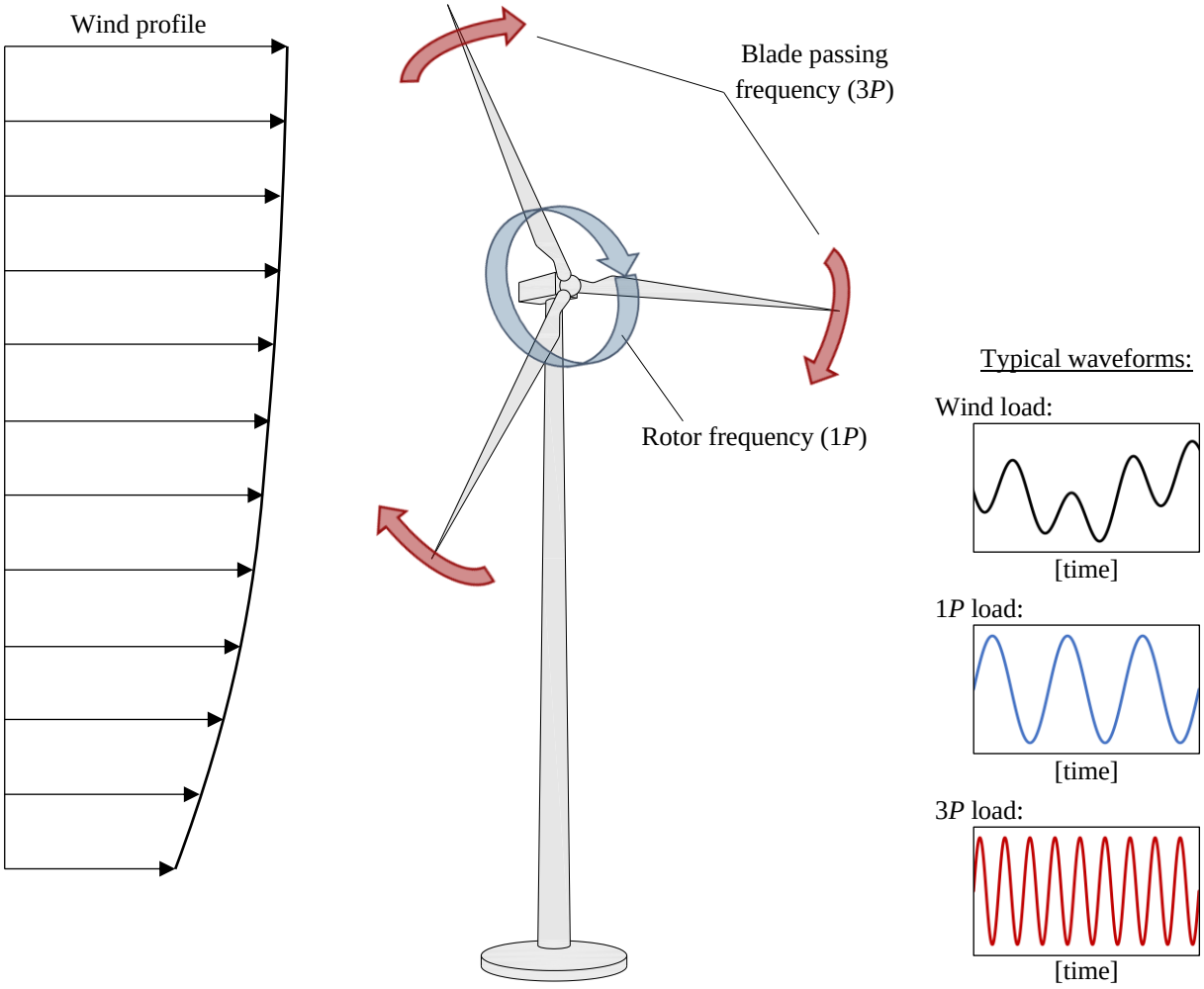

Figure 2.21: Cyclic loading of an onshore wind turbine
Adapted from Nikitas *et al.* (2016)

The amplitudes of the 1*P* and 3*P* cyclic loads are orders of magnitude lower than that of the cyclic wind loading. For instance, calculations conducted by Arany *et al*. (2014) for a particular model of offshore wind turbine indicate that the 1*P* loading may account for ~0.02% of the total bending moment at the mudline of the structure. It is further pointed out by Arany *et al*. (2014) that the 3*P* cyclic loading is effectively a load loss, and it is calculated that it may also be in the order of less than 1% of the total mudline bending moment.

Additionally, the 1*P* and 3*P* cyclic loads are considered to act dynamically as they have forcing frequencies in close resemblance to that of the natural frequency of the wind turbine system. This requires careful consideration in the foundation design process, as the stiffness of the foundation element and underlying soil influences the natural frequency of the system, potentially shifting the frequency ratio closer to a value of unity, and thus inducing resonance and associated fatigue related problems. This is discussed in further detail in §2.5.2.

On the other hand, the frequency of cyclic wind loading is more difficult to predict, and realistically it consists of quasi-static and dynamic components. In the offshore wind energy sector, several studies involving monopiles (e.g. Bhattacharya *et al.*, 2013; Lombardi *et al.*, 2013; Arany *et al.*, 2014; Guo *et al.*, 2015; Yu *et al.*, 2015) utilise wind spectrum models that predict very low wind frequencies, much below the 1*P* intervals. It is also reported in many of these studies that the dominant frequency of gusty wind is very low compared to waves, such as Adhikari and Bhattacharya (2012) who state that it is in the order of 0.02 Hz, as well as Lopez-Querol *et al.* (2017) who suggest that it is even lower with a frequency of 0.01 Hz. This general understanding is reiterated by Andresen (2015), who states that the frequency of wind loading is sufficiently low, such that even if the structure experiences dynamic amplification from this loading frequency, the inertia effects in the soil domain will be negligible and the cyclic load will be considered quasi-static. This is an important consideration when analysing the fatigue response of soil due to cyclic wind loading, as it indicates that conducting dynamic modelling is not a necessary undertaking, but rather quasi-static modelling is suitable. This is discussed in the context of the numerical model development for this study in §4.2.1.

2.5 Foundation Design Requirements

Wind turbine foundations have specific design requirements, which need to be accounted for, to ensure reliable operation of the turbine over a typical design life of 20 years. This involves two relatively independent but related design processes. First the geotechnical design, which is concerned with the behaviour and capacity of the soil in response to the structural loading, and second the structural design, which involves the detailing of the reinforced concrete structural element. In the case of a gravity base foundation, the geotechnical design process is used to determine the required bearing area, embedment depth and overall weight of the foundation. In doing so, several key design criteria inherent to wind turbine foundations need to be considered, however the majority of national building codes are not sufficiently specialized to deal with these criteria. Consequently, wind turbine foundation designs to date have been based on technical guidelines provided by the turbine manufacturers themselves (e.g. Vestas, 2011; General Electric, 2013), or the guideline developed by Det Nortske Veritas and the Risφ National Laboratory in Denmark, titled *Guidelines for design of wind turbines* (DNV/Risø, 2002). The general geotechnical design methodology for wind turbine foundations is summarised in Table 2.1, followed by a review of the most pertinent aspects thereof.

Table 2.1: Geotechnical design methodology for wind turbine gravity foundations

Adapted from Wojtowitz and Vorster (2014) and Mawer (2015)

Step 1: Site Investigation	**Step 2:** Initial Dimensioning	**Step 3:** Stiffness Requirements

• Determine design ground profile for wind turbine
  - Minimum of one boring per wind turbine location
• Conduct in-situ and laboratory tests to evaluate
  - Soil classification
  - Strength and stiffness parameters
• Determine representative geotechnical design parameters for each wind turbine location
	• Initial dimensions based on expected critical design criteria
	  - In poor quality soils, design likely to be controlled by stiffness requirements or bearing capacity
	  - In good quality soils, design likely to be controlled by overturning stability or limiting gapping
	• Or based on previous designs in the area, or manufacturer's guidelines
		• Calculate rotational and lateral foundation stiffness based on initial dimensions and verify that they meet manufacturer's requirements
		• Use appropriate stiffness reduction model to reduce G_0 to G based on expected strain levels ($\gamma \approx 10^{-3}$ to 10^{-2})
		• Account for effects of cyclic degradation in assessment of G if applicable

Step 4: ULS Checks	**Step 5:** SLS Checks	**Step 6:** Site Verification
• Check bearing capacity of ground profile • Check overturning stability • Check sliding resistance	• Check for gapping under normal operating and extreme conditions • Calculate vertical and differential settlement • Assess potential for local overstressing and the need for a contact layer	• Verify geotechnical conditions in foundation base excavations • Review design assumptions

2.5.1 Site investigation

A thorough site investigation is required to ensure that relevant geotechnical information and data are available at the various stages of the project. The aims of the investigation are to establish the soil, rock and groundwater conditions, to determine the properties of the soil and rock, and to gather additional relevant knowledge about the site. Ultimately, this provides the necessary information to undertake the detailed design of the foundation at each specific turbine position.

The starting point for a site investigation is a desk study of the regional geology, topography, hydrology, climate, vegetation and seismology. This provides a basis for selection of investigative methods and extent of the site investigation. An investigation programme can then be developed, consisting of a series of in-situ exploration methods and laboratory tests. Following this, the design ground profile and representative geotechnical design parameters can be derived for each wind turbine location.

2.5.1.1 In-situ soil exploration

An integral component of in-situ soil exploration is the drilling of boreholes. Boreholes provide the opportunity to obtain samples for visual description and index testing, which are the primary ways of determining soil stratigraphy. Boreholes also allow in-situ testing to be conducted for parameter determination; high quality undisturbed samples to be obtained using various push-in type samplers; and the installation of instrumentation such as piezometers for groundwater monitoring. As wind farm sites typically occupy very large expanses of land, and are thus likely to be highly variable with regards to founding conditions, at least one soil boring is generally recommended for each turbine location. For wind turbine gravity foundations, the minimum depth of each boring is usually taken to be equal to the largest lateral dimension of the footing. Borings are supplemented by the excavation of trial pits, which allow the stratigraphy to be assessed up to relatively shallow depths, and permit large soil samples to be obtained.

Various in-situ tests are conducted as part of the field investigation for wind farms. Numerous penetrometer tests are available, such as the standard penetration test (SPT), dynamic probe super heavy (DPSH) test, and cone penetration test. Of these, the SPT is widely used, largely due to its general acceptance and availability around the world. SPT results in boreholes provide an empirical qualitative guide to the in-situ engineering properties of cohesive and cohesionless soils, and provide soil samples for classification purposes. In Southern Africa, considerable use is also made of DPSH testing (Byrne *et al.*, 2008). The advantages of this test are its cost-effectiveness and rapid performance, however a significant disadvantage is that no soil sample is procured. In addition to penetrometer tests, other exploration and testing methods such as plate load tests, pressuremeter tests, and vane shear tests are also utilised for characterisation of strength and deformation properties of subsurface deposits. Furthermore, geotechnical investigations for wind turbines also generally include electrical resistivity testing for grounding system design, as well as for confirmation of the phreatic surface or perched water tables.

Geophysical testing can also be undertaken to supplement the in-situ investigation. This comprises non-intrusive methods in which a set of physical measurements relating to the underling soil and rock strata is made at ground surface or in boreholes. Several such methods

have been developed, however for site investigation of wind farms in South Africa, the continuous surface wave (CSW) test is frequently used.

The CSW test is a seismic technique for determining ground stiffness by measuring the velocity of Rayleigh wave propagation along the ground surface (Heymann, 2007). The specific output of this test is a profile of small-strain (initial) shear modulus (G_0) with depth. As illustrated in Figure 2.22, the layout of the CSW system consists of a shaker placed on the ground surface, which is connected to a signal generator and amplifier, as well as a series of geophones connected to a data acquisition system. The shaker induces a vertical sinusoidal force of known frequency onto the ground. High load frequencies produce short Rayleigh waves that penetrate to shallow depths, whereas low frequencies penetrate to greater depths, as indicated in Figure 2.22. Sweeping through a range of frequencies allows a Rayleigh wave velocity profile to be established. The radiated waves are detected by the linear array of geophones and recorded by the data acquisition system. The recorded data is subsequently processed to determine the wavelength and velocity of the Rayleigh wave (V_r) for each vibration frequency. The shear wave velocity (V_s) is then calculated using the relationship in Equation 2.8, and subsequently G_0 is calculated using Equation 2.9. Overall, this test method is cost-effective and quick, with a production rate of three to four profiles per day (Heymann, 2007). This is particularly appealing to wind farm site investigations considering the large number of foundations typically involved.

$$\frac{V_r}{V_s} \cong \frac{0.874+1.117\nu}{1+\nu} \qquad \text{Eqn. 2.8}$$

$$G_0 = \rho V_s^2 \qquad \text{Eqn. 2.9}$$

Where V_r = Rayleigh wave velocity (m/s); V_s = shear wave velocity (m/s); ν = Poisson's ratio (unitless); G_0 = initial shear modulus (Pa); and ρ = bulk density (kg/m^3).

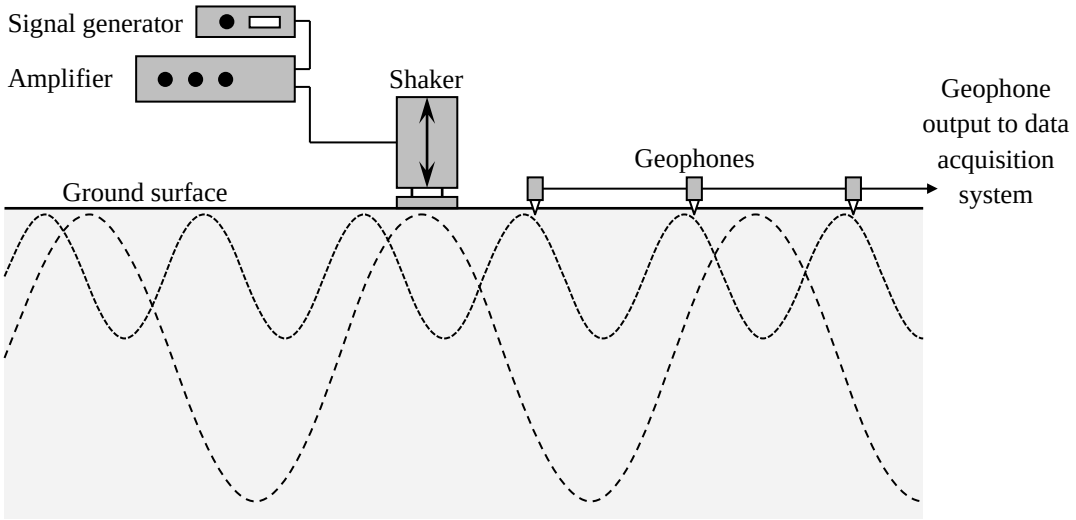

Figure 2.22: Continuous surface wave system
Adapted from Heymann (2007)

2.5.1.2 Laboratory tests

As part of the site investigation, appropriate laboratory testing should be conducted on the collected soil and rock samples to provide more reliable estimates of the geotechnical parameters. The extent of the testing should be sufficient to characterise all soil types and layers that may have an impact on the foundation design. A non-exhaustive list of laboratory tests generally recommended for wind turbine foundation design is presented in Table 2.2. In addition to these tests, geotechnical investigations for wind farms also typically include California Bearing Ratio testing for access road design, as well as thermal and electrical resistivity testing for electrical collection and grounding system design.

Table 2.2: Typical laboratory tests for wind turbine foundation design

Adapted from Ntambakwa *et al.* (2016)

Laboratory test	Properties measured
Soil index tests	Particle size distribution Moisture content Unit weight Atterberg limits Expansion/swelling index
Consolidation tests	Coefficient of consolidation Preconsolidation pressure Compression/swelling index
Proctor compaction tests	Optimum moisture content Maximum dry density of backfill material
Direct shear and triaxial tests	Cohesion and friction angle Undrained shear strength
Soil chemical tests	Soluble chloride and soluble sulfate Soil pH
Rock tests	Unconfined compressive strength Joint characteristics Rock mass classification

2.5.1.3 Geotechnical design parameters

Using the available in-situ and laboratory test data, characteristic values of design parameters can be derived. According to Wojtowitz and Vorster (2014), the geotechnical design parameters required for the design of onshore wind turbine gravity foundations consist of mass elastic modulus (E_{mass}), mass shear modulus (G_{mass}), mass small-strain shear modulus ($G_{0(mass)}$), Poisson's ratio (ν), angle of internal friction (ϕ'), undrained shear strength (c_u), vertical spring stiffness (K_V), rotational stiffness (K_R), and lateral stiffness (K_H).

The mass ground moduli E_{mass}, G_{mass}, and $G_{0(mass)}$ are essentially 'equivalent' moduli that represent the mobilised portion of the ground profile. Mass ground moduli are difficult to determine directly because the moduli E, G and G_0 differ between the various soil types and layers, and in the case of E and G are also dependent on the stress state of the soil. To estimate the mass ground moduli, the properties of each soil and rock layer within the ground profile need to be accounted for. Wojtowitz and Vorster (2014) suggest that the method developed by Fraser and Wardle (1976) can be adopted for doing so. Although this method was originally intended for rectangular rafts, Wojtowitz and Vorster (2014) propose that it can be used for circular wind turbine foundations by using an equivalent rectangular width determined from the diameter of the foundation.

The method proposed by Fraser and Wardle (1976) for calculating the mass ground modulus is detailed in Appendix A. To summarise, this method involves calculating the 'equivalent' isotropic modulus for a multi-layered ground profile by weighting the modulus of each layer according to its influence on settlement. This is done using an influence factor, which is large near the surface and decreases with depth. Accordingly, the soil near founding level with a larger influence factor has a larger contribution to the mass ground modulus, and soil at a greater depth has a smaller contribution. Using this or a similar method to calculate the mass ground modulus is crucial in the context of cyclic degradation because it allows the degradation to be quantified and reflected in the modulus, as discussed in §2.5.2.2.

2.5.2 Foundation stiffness

Foundation stiffness requirements for wind turbines are of very high importance and may govern the design of the foundation. This stems from the fact that wind turbine structures experience dynamic loading, and if the frequency of this loading coincides with the natural frequency of the structure, the phenomenon of resonance will occur. This is characterised by high-amplitude oscillations or vibrations of the structure, which can lead to large deflections and rotations, thus increasing the fatigue damage and ultimately diminishing the intended design life of the wind turbine. It is therefore imperative for design engineers to predict and calculate the natural frequency of wind turbine systems, so that it can be designed within certain frequency ranges to avoid resonance (Mawer *et al.*, 2017). However, the natural frequency is dependent, *inter alia*, on the total stiffness of the wind turbine system, which in turn is a function of the tower stiffness, the foundation stiffness, and the stiffness of the underlying soil. Therefore, to accurately calculate the natural frequency of the system, the foundation and underlying soil is not modelled as a rigid restraint, but rather their respective stiffness values are incorporated into the calculations.

The main working frequencies to be avoided are those corresponding to the 1P and 3P loads, plus and minus a 10% buffer for uncertainties. As illustrated in Figure 2.23, it follows that there are three natural frequency ranges that wind turbine structures can be designed for if resonance is to be avoided:

i) **Soft-soft:** This corresponds to a natural frequency less than the 1*P* frequency, which is achieved by designing a tower-foundation system with sufficiently low stiffness. Such systems have a degree of inherent risk and are often impractical as they lack the stiffness to resist other operational loads satisfactorily.

ii) **Stiff-stiff:** At the other end of the spectrum, stiff-stiff designs have very high stiffness and hence a natural frequency that exceeds the 3*P* frequency. This is a conservative approach and usually uneconomical due to the additional material requirements.

iii) **Soft-stiff:** Soft-stiff designs offer a compromise between the two previous options, in which the natural frequency lies between the 1*P* and 3*P* frequencies. This is typically the approach used for modern turbines as it is resource-efficient.

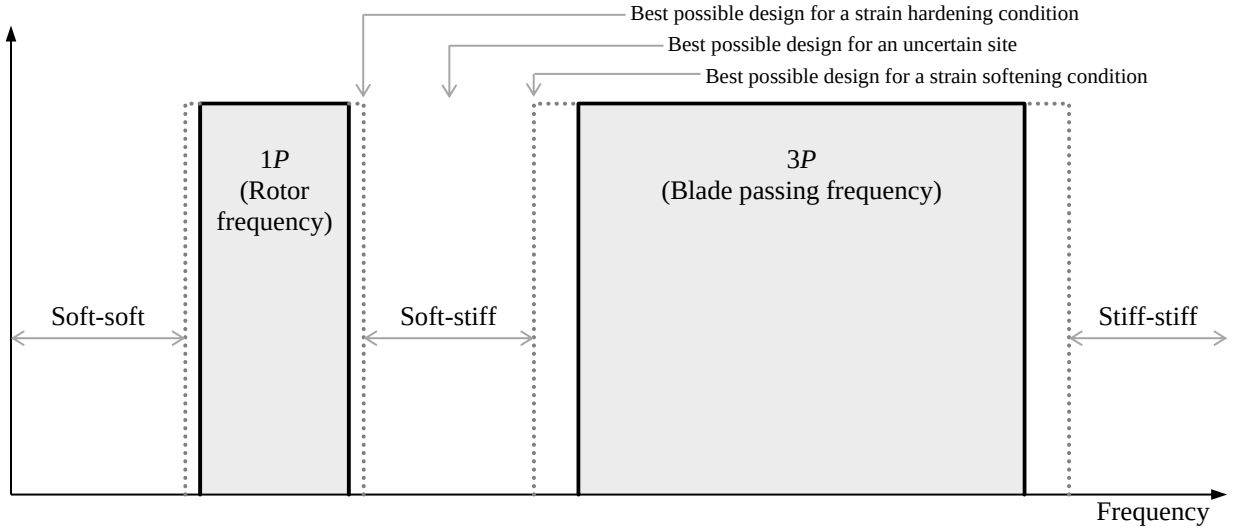

Figure 2.23: Frequency spectrum for wind turbine dynamic loads and design choices

To ensure that the natural frequency of the wind turbine system is acceptable, the technical guidelines provided by turbine manufacturers generally specify minimum rotational stiffnesses and associated lateral stiffnesses for the foundation that must be adhered to in the design. These values are specific to the turbine model used. For instance, the foundation stiffness requirements for a Vestas V112-3.0 MW wind turbine are shown in Table 2.3 and plotted in Figure 2.24. This table and figure indicate that the minimum rotational stiffness of the foundation should be limited to 68 GNm/rad, because any value lower than this would require very high lateral stiffness to fulfil the operational requirements of the turbine. Note that it is not possible for the foundation to be too stiff because the wind turbine is also evaluated with the assumption that the base of the tower is perfectly fixed for all rotations and translations (General Electric, 2013).

Table 2.3: Foundation stiffness requirements for a Vestas V112-3.0 MW wind turbine
Sourced from Vestas (2013)

Rotational stiffness, K_R (GNm/rad)	57	68	95	133	185	258	359	445	500
Lateral stiffness, K_H (MN/m)	5000	47.4	19.9	14.1	11.5	10.3	9.4	9.2	9.2

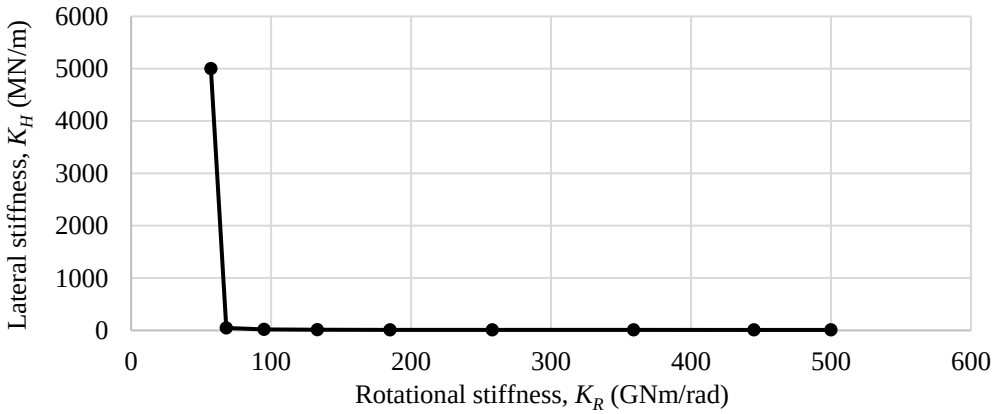

Figure 2.24: Plot of rotational stiffness versus lateral stiffness
Based on Table 2.3

The stiffness of the foundation can be calculated assuming the soil to be an elastic half-space, or a semi-infinite continuum of soil idealised as an elastic material. In doing so, the soil stiffness is represented by a set of springs that have been uncoupled into rotational and lateral components, as well as vertical and torsional components if necessary. The footing itself is then modelled as perfectly rigid and supported on the appropriate springs. For a circular foundation, the rotational and lateral spring stiffnesses can be calculated according to Equations 2.10 and 2.11 respectively. Note that these equations correspond to a homogeneous half-space only, and DNV/Risø (2002) provide alternative variants of them for additional scenarios, such as that of a soil stratum being located over bedrock, and/or the foundation being embedded.

Rotational: $$K_R = \frac{8G_{mass}R^3}{3(1-\nu)} \quad \text{Eqn. 2.10}$$

Lateral: $$K_H = \frac{8G_{mass}R}{2-\nu} \quad \text{Eqn. 2.11}$$

Where K_R = rotational stiffness (Nm/rad); K_H = lateral stiffness (N/m); G_{mass} = mass shear modulus (Pa); R = foundation radius (m); and ν = Poisson's ratio (unitless).

From these equations, it is evident that the foundation stiffness is highly dependent on the foundation radius and the shear modulus of the soil. Whilst the former parameter has an explicit value, there is a degree of uncertainty involved in estimating the latter. This is because, as

discussed later in §3.3.1, soil behaves in a highly nonlinear manner with its stiffness dependent on the magnitude of the induced strains. It is thus imperative that the shear modulus value that is used to calculate the spring coefficients is reflective of the level of shear strain that the soil will be exposed to under operating conditions. In this regard, DNV/Risø (2002) state that the induced vibrations on wind turbine foundations are of such a nature that the static stiffness will be representative of the dynamic stiffness that is required in a structural analysis. In other words, although wind turbines are dynamic structures, when considering the response of the ground due to cyclic loading over time, it would be more representative to use static stiffnesses for design as opposed to dynamic stiffnesses. Accordingly, the shear modulus of the soil selected for design is based on a reduction from the initial shear modulus at small strains, G_0 (which is representative of the dynamic stiffness), using a modulus reduction curve suitable for the soil type. In doing so, DNV/Risø (2002) suggest that the level of shear strains induced by wind loading is typically in the order of 10^{-3} and up to 10^{-2}, and this is used to quantify the reduction.

2.5.2.1 Minimum dimensions

Once representative G_{mass} and ν values are determined for each turbine location, the minimum design foundation diameter can be calculated. This can be done by rearranging Equation 2.10 to solve for the foundation radius, R, as shown in Equation 2.12 below. In doing so, K_R is equated to the minimum rotational stiffness, which is 68 GNm/rad in the case of the Vestas V112-3.0 MW as previously discussed. The resultant radius is then used to calculate the lateral stiffness using Equation 2.11, and subsequently crosschecked with the corresponding lower limit of the lateral stiffness specified by the manufacturer, which as shown in Table 2.3 is 47.4 MN/m for the same turbine. If this lower limit is not exceeded, then the foundation radius is increased. Conversely, if the lower limit of the lateral stiffness is satisfied, then the given foundation radius can be used as a starting point for the design, and it can subsequently be checked against the ultimate and serviceability limit states.

$$R = \sqrt[3]{\frac{3K_R(1-\nu)}{8G_{mass}}} \qquad \text{Eqn. 2.12}$$

It must be noted that using the manufacturer's stiffness requirements to estimate the minimum foundation size is just one of many options available. Any of the other design criteria can be used for this purpose, depending on which one is expected to control the size of the foundation. The controlling criteria will depend on the nature of the founding material. In general, for good quality founding material, the requirement for limiting gapping or overturning stability is likely to govern the design, whereas for poorer soils, bearing capacity or rotational stiffness will be more significant (Loubser & Jacobs, 2016). Furthermore, if available, initial dimensions can be estimated from previous designs in the area, or from the manufacturer's guidelines.

A more sophisticated approach for estimating the minimum foundation diameter was used by Wojtowitz and Vorster (2014), in which a three-dimensional finite element model of a representative soil profile for a wind farm site was created. A shallow foundation with combined

loading was modelled on this soil profile and several design criteria assessed simultaneously, including that of settlement being less than 3 mm/m, the factor of safety against bearing capacity failure being greater than 2.5, gapping being less than 1%, as well as the foundation stiffness being within the requirements for the specific turbine model used. The model was repeated by iteratively increasing the foundation diameter, until the minimum foundation size that satisfied all the criteria was established.

2.5.2.2 Assessment of degradation

A further consideration pertains to sites in areas where the stiffness and strength of the soil might degrade under cyclic loading. This phenomenon has been predominantly studied in the offshore sector where founding of turbines commonly occurs in clayey soils with monopiles or suction caissons. However, it is not well-defined in foundation design for onshore wind turbines, in which shallow gravity base foundations are more prevalent. Typically, in the onshore sector, if soils are identified that may be susceptible to degradation, limitations are put in place to prevent or highly restrict gapping of the foundation. This is to prevent multiple instances of zero pressure beneath the foundation, which in the presence of water, could lead to a breakdown of the in-situ soil structure. However, despite this rule of thumb, the long-term performance of gravity foundations has not been well incorporated in design guidelines for onshore wind turbines.

The primary implication of cyclic degradation, in the context of the foundation stiffness requirements, is that the mass shear modulus of the soil G_{mass} will decrease with an increasing number of load cycles. This will cause a reduction in K_R and K_H (Eqn. 2.10 and 2.11). Not only could this induce differential settlement, but it will also lower the natural frequency of the wind turbine system, and thus potentially cause it to coincide with the 1P and 3P frequencies. It follows that if the turbine is designed to fall within the soft-stiff frequency range, then for a strain softening site in which degradation occurs, the best possible scenario is to design it such that the natural frequency is initially at the upper limit of this range, as indicated in Figure 2.23. This is because there will be a decreased likelihood of resonance occurring if any further reduction in shear modulus, and thus natural frequency, is to take place.

The extent of stiffness reduction due to cyclic degradation is dependent on the type of soil present. Table 2.4 presents a summary of the degradation potential of different soil types as reported by Vucetic (1992). From this it is evident that the plasticity index (PI) and overconsolidation ratio (OCR) of the soil are highly influential in this regard, and this is discussed in further detail in §3.3.1.3. Soils with very high plasticity are the least susceptible to cyclic soil degradation, whereas non-plastic soils such as fully saturated sands are the most susceptible. However, because soils of the latter type are free-draining, it is only at very high loading rates, such as seismic loading, that these high-permeability soils are able to generate excess pore pressure and consequently degrade. The other two categories shown in Table 2.4, low and medium plasticity soils, fall between the two extremes. Considering that the frequency of cyclic wind loading imparted on wind turbine foundations is relatively low, it is unlikely that non-plastic soils will be susceptible to degradation due to their high permeabilities, and thus the soil type most susceptible to cyclic degradation would likely be that of low plasticity in combination with low permeability.

Table 2.4: Effect of soil type on degradation potential

Adapted from Vucetic (1992)

Type of soil	Non-plastic PI = 0% Sands and non-plastic silts	Low plasticity PI = low Silty clays, clayey silts, low plasticity clays	Medium plasticity PI = medium Medium plasticity clays	Highly plastic PI = high High plasticity clays
Degradation of stiffness and strength	Large, or complete during full liquefaction	Significant for normally consolidated or small OCR soils	Small, or insignificant for overconsolidated soils	Insignificant

To illustrate a potential avenue for incorporating cyclic degradation into wind turbine foundation design, reference is made to Wojtowitz and Vorster (2014) who identified the potential for cyclic degradation in the design of gravity base foundations for an onshore wind farm. In this design, clayey silts, silty clays and clays with a PI >15% were regarded as soils that may be susceptible to softening. Thus, in determining which turbine locations were at risk, soil descriptions in borehole and test pit logs, as well as Atterberg limit tests, were examined for occurrence of such soils.

For turbine locations where softening was considered to control the design, the value of G_{mass} of the design ground profile was assessed using two separate conditions. The first was an upper limit representing the unsoftened profile, and the second was a lower limit representing the softened case. The upper limit corresponded to the usual static soil stiffness, G, that DNV/Risø (2002) specifies should be used for foundation design, whereas the lower limit accounted for cyclic degradation by applying a further 50% reduction in G up to a depth of $0.5B$ (where B denotes the foundation width or diameter). The method proposed by Fraser and Wardle (1976) was used to quantify this stiffness reduction, so that it could be reflected in the values of G_{mass}. The foundation stiffnesses K_R and K_H were then calculated using both the upper and lower limits of G_{mass}, and this was used in the assessment of the foundation design, and ultimately controlled the dimensions of the footing. A further point of interest to note is that it can be inferred from Equation 2.12 that $R \propto G_{mass}{}^{-1/3}$, and thus any significant reduction in G_{mass} will vastly increase the required dimensions of the footing.

According to Wojtowitz and Vorster (2014), this design strategy was derived from discussions by Achmus *et al.* (2007). These authors developed a numerical model of an offshore monopile to investigate its behaviour under cyclic loading, and in turn make reference to the American Petroleum Institute regulations (API, 2000), which mention that cyclic loading can be accounted for by applying a reduction to the soil spring stiffness up to a certain depth below the seabed. It was based on this strategy that Wojtowitz and Vorster (2014) assumed a 50% reduction in stiffness up to a depth of $0.5B$. However, it must be emphasised that the effect of cyclic loading below gravity foundations is uncertain, and thus the designs produced under these assumptions could have potentially been too conservative, or not conservative enough. Therefore, further investigation is required to define the depth of stiffness degradation, as well as the amount of stiffness degradation, to be applied in wind turbine foundation design.

2.5.3 Ultimate limit state design checks

The ultimate limit states (ULS) are those concerning safety and thus correspond to the most critical factored load combinations and the maximum load-carrying resistance. For the geotechnical design of wind turbine foundations, the ULS includes checks for soil bearing capacity, stability against overturning and stability against sliding.

2.5.3.1 Bearing capacity

For shallow foundation design, it is essential to determine the ultimate and allowable bearing capacities of the foundation support materials within the depth of influence. This is to determine the load-carrying capacity of the underlying soil or rock, to verify its ability to bear and transmit the maximum loads from the structure. The ultimate bearing capacity, which is the maximum pressure that the foundation can withstand before the occurrence of shear failure, can be calculated for wind turbine foundations using the approach provided by DNV/Risø (2002). This corresponds to Equation 2.13 for drained conditions, and Equation 2.14 for undrained conditions. If a global factor of safety is being used rather than partial factors, then the allowable bearing capacity is obtained by dividing the ultimate bearing capacity by this factor of safety, which the ASCE/AWEA (2011) recommends should be at least 3.0 under service and fatigue loads, and 2.26 under unfactored extreme loads.

Drained: $$q_{ult} = c' N_c s_c i_c + q' N_q s_q i_q + 0.5\gamma' B' N_\gamma s_\gamma i_\gamma \quad \text{Eqn. 2.13}$$

Undrained: $$q_{ult} = c_u N_c^0 s_c^0 i_c^0 + q \quad \text{Eqn. 2.14}$$

Where q_{ult} = ultimate bearing capacity (Pa); c' = effective cohesion (Pa); c_u = undrained shear strength (Pa); q' = effective overburden pressure (Pa); γ' = effective unit weight (N/m^3); B' = effective foundation width (m); N_c, N_q, N_γ = bearing capacity factors (unitless); s_c, s_q, s_γ = shape factors (unitless); and i_c, i_q, i_γ = inclination factors (unitless).

Reference can be made to DNV/Risø (2002) for the various formulae used to calculate the factors in the above equations. Further, note that the above equations do not include depth factors and thus, in principle, apply to foundations that are not embedded. However, they may also be applied to embedded foundations, leading to a conservative result. Alternatively, DNV/Risø (2002) suggest that depth factors associated with embedded foundations can be calculated according to DNV (1992). However, if this approach is taken, it must be ensured that the foundation installation procedure and other critical aspects allow for the mobilisation of resisting shear stresses in the soil above the foundation level.

A further consideration is the bearing capacity associated with extremely eccentric loading conditions. In this regard, DNV/Risø (2002) specify that if the eccentricity (e) exceeds 0.3 times the foundation width (B), that is $e > 0.3B$, then an additional bearing capacity calculation must be conducted. This calculation is undertaken using Equation 2.15, and corresponds to the failure mode in which the soil beneath the unloaded area of the footing fails.

$$q_{ult} = c' N_c s_c i_c \left(1.05 + \tan^3 \phi'\right) + \gamma' B' N_\gamma s_\gamma i_\gamma \qquad \text{Eqn. 2.15}$$

Where ϕ' = angle of internal friction (degrees); and other parameters previously defined.

In order to assess the bearing capacity ULS, it is necessary to compare the allowable bearing capacity to the maximum bearing pressure below the foundation. The magnitude of the latter depends on several factors such as the methods and assumptions used to determine the pressure distribution, the radius of the foundation, the total vertical load, and the overturning moment. As the magnitude of the overturning moment under extreme wind loading is disproportionally higher than the vertical load from the self-weight of the tower, extreme eccentricities of the resultant load are produced. This causes a loss in contact area of the footing and thus an increase in bearing pressure, as illustrated in Figure 2.25.

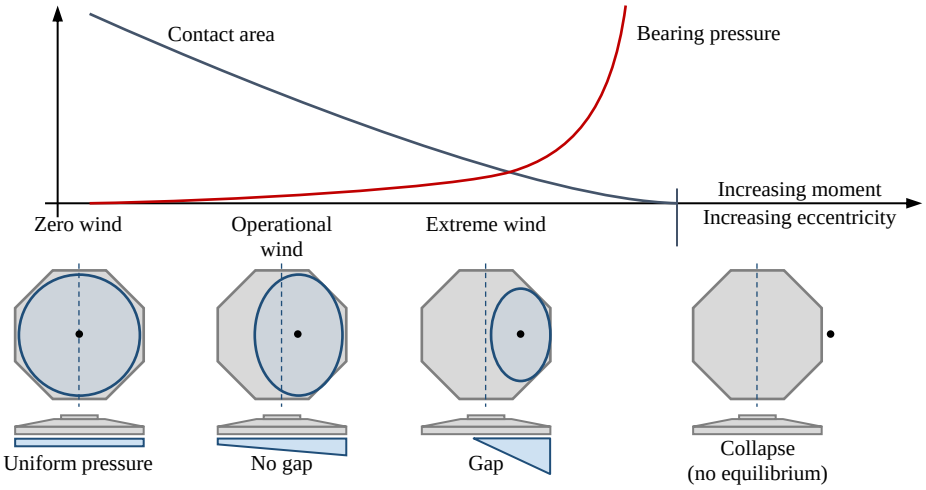

Figure 2.25: Eccentric loading effects on foundation bearing pressure
Adapted from Ntambakwa *et al.* (2016)

Procedures for incorporating load eccentricity effects into the calculations for bearing pressure are provided by DNV/Risø (2002). This involves using Meyerhof's method to determine the effective foundation area (A_{eff}) of the footing. This approach is relatively simple for a square or rectangular footing, as the effective area is simply reduced to a smaller rectangle with a new eccentric centre, however in the case of a circular foundation it involves additional calculations. This is because the effective area is first approximated into an ellipse, and then further simplified into a rectangle, as shown in Figure 2.26. The centre of the rectangle coincides with the centre of the ellipse, and is spaced from the geometric centre of the foundation by a distance equal to the eccentricity. Although this method produces conservative estimates of the bearing pressures, it is highly efficient and widely used in foundation design.

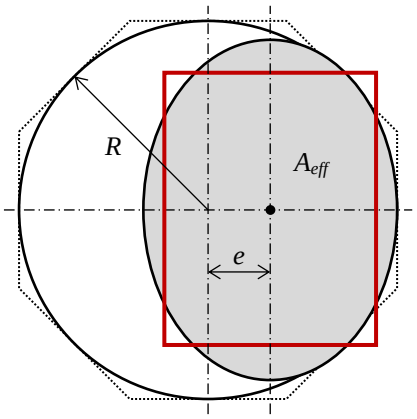

Figure 2.26: Effective area of circular foundation
Adapted from DNV/Risø (2002)

2.5.3.2 Overturning stability

For a shallow gravity base foundation, it is necessary to perform global stability analyses under design loading conditions, since the consequences of failure would be catastrophic. This is conducted by considering the subsoil and foundation to be rigid bodies, and assuming that rotation will occur about the toe of the foundation. The stabilising moments include that originating from the dead loads of the tower, foundation and backfill, as well as the buoyancy (applied with a negative value), each of which occurs at an eccentricity of $B/2$ or R (Vestas, 2011). The passive or shear resistances can also be considered to contribute to the stabilising moments, but only if they are justifiable in terms of the degree to which they can be mobilised before the onset of overturning. On the other hand, the destabilising moments are the sum of the shear force at the tower base acting at an eccentricity equal to the total foundation height, and the bending moment at the tower base. The factor of safety, which is the ratio between the stabilising moments and the unfactored destabilising moments, should be greater than 1.5 (ASCE/AWEA, 2011).

2.5.3.3 Sliding resistance

Foundations subjected to horizontal loading must be assessed for sufficient sliding resistance. However, although sliding resistance must be checked formally, in general there is a large bearing reserve present (Vestas, 2011). Nonetheless, according to DNV/Risø (2002), Equation 2.16 must be satisfied under drained conditions, whereas both Equation 2.17 and 2.18 are applicable to undrained conditions.

Drained:	$H < A_{eff} \cdot c' + V \cdot \tan\phi'$	Eqn. 2.16
Undrained:	$H < A_{eff} \cdot c_u$	Eqn. 2.17
	$H < 0.4V$	Eqn. 2.18

Where H = horizontal load (N); V = vertical load (N); and other parameters previously defined.

In calculating the vertical load *V*, only the dead weight of the structure, foundation and backfill soil should be considered. Further, according to ASCE/AWEA (2011), the factor of safety for sliding resistance, which is the ratio between the resisting forces and the unfactored driving forces, should not be less than 1.5.

2.5.4 Serviceability limit state design checks

The serviceability limit states (SLS) are those which restrict the functionality of a structure when subjected to normal operational loading, or which affect its durability. Some of the important SLS criteria associated with onshore wind turbine foundations include that of gapping, vertical and differential settlement, and local overstressing, each of which is subsequently described.

2.5.4.1 Gapping

Gapping is the temporary upliftment of the footing base at its windward side, in which there is a loss of contact between a part of the foundation area and the soil. If such a state occurs repeatedly due to cyclic loads, it is called *gapping cycles*. The allowance of gapping cycles in the design of wind turbine foundations can lead to a breakdown of the in-situ soil structure in certain soil conditions, particularly those that are not very stiff. Therefore, to limit the adverse effects of this in the long term, wind turbine manufacturers generally make recommendations to prevent or highly restrict gapping of the foundation. Typically, under normal operational loading, it is stipulated that no ground gap or zero pressures should occur. However, it is possible, but not required, to allow limited gapping under extreme load cases, as they are expected to occur infrequently. For instance, Vestas (2011) allows up to 25% gapping and General Electric (2013) up to 50% during extreme environmental conditions. A further consideration is that if gapping is allowed for, then the loss of contact area must be taken into account in the rotational foundation stiffness calculations.

2.5.4.2 Vertical and differential settlement

An analysis must be conducted to determine the vertical and differential settlement of the foundation, to ensure that it does not exceed the limits specified by the turbine manufacturer. This analysis must account for immediate elastic settlement, time-dependent primary and secondary consolidation settlements, as well as seismically induced settlement if applicable. For granular soils, total settlement is usually based on the application of extreme loads, while elastic and long-term consolidation settlements for cohesive soils are calculated under operational loading conditions (Ntambakwa *et al.*, 2016).

Uniform vertical settlement of the foundation from the combined mass of the turbine and foundation will not normally control the design, largely because of the low magnitude of the gravity loads in comparison to the operational overturning moments. Nonetheless, the geotechnical engineer must formally check that the vertical long-term settlement resulting from the combined gravity weight is less than the imposed limit. For turbines manufactured by General

Electric, this limit is 20 mm (General Electric, 2013), however it will differ across other manufacturers and turbine models.

Differential settlement and tilting of the foundation is usually one of the primary concerns for wind turbines due to the unconventionally large overturning moments that are experienced. Several factors need to be taken into account when analysing the differential settlement, including lateral variations in soil conditions within the foundation area, asymmetrical weight distributions and possible predominating directions of wind loads (DNV GL, 2016b). Typically, the maximum allowable differential settlement is in the order of 3 to 4.5 mm/m (0.17º to 0.26º) and is an important requirement specified by the turbine manufacturer. One of the reasons for this is that if the tower is out of vertical, the large mass at the top of the tower will produce an additional overturning moment. For instance, Vestas (2013) calculates that for the Vestas V112-3.0 MW turbine, if the tower is out of vertical by 8 mm/m, of which 5 mm/m is for manufacturing and installation tolerance and 3 mm/m for differential settlement, then the tower top mass of 193 808 kg will generate an additional moment of 2126 kNm at the base.

2.5.4.3 Local overstressing

An additional design check, related to cyclic degradation, was proposed by Wojtowitz and Vorster (2014) to assess the possibility of local failure occurring under serviceability load conditions. In doing so, the foundation design is assessed to determine the requirement for a contact layer below the foundation. With South African geological conditions in mind, this is conducted by evaluating available test pit and borehole data for the occurrence of hardpan calcrete, hardpan ferricrete, or dense granular materials within the contact depth below the foundation. If these materials are identified and perceived to be competent, then no contact layer is deemed necessary, pending site verification during construction.

On the other hand, if high plasticity materials are identified at founding level, then a further analysis should be undertaken to evaluate the need for a contact layer. The approach used by Wojtowitz and Vorster (2014) was to create a two-dimensional, axisymmetric finite element model of the foundation and soil profile. The maximum stress at the edge of the foundation under serviceability load conditions was calculated analytically according to the procedure provided by the manufacturer's technical guidelines, in this case by Vestas (2011), and the corresponding load applied across the foundation. The induced strains were then assessed to determine the requirement for a contact layer beneath the foundation. Specifically, the depth to which the shear strains exceeded 10^{-4} was deemed to be the minimum depth to which the fill layer should be assigned.

Chapter 3
CYCLIC LOADING OF SOIL

3.1 Introduction

The term *cyclic loading* is used generically to characterise variable loads that have repeated patterns, and a degree of regularity, in amplitude and frequency. This loading can be of environmental origin, such as wind, waves and earthquakes, or it can be anthropogenic, such as that emanating from rotating machinery, traffic and blasting operations. The characteristics of each of these cyclic load cases vary considerably, with each having different ranges of magnitude, frequency, and number of cycles. For instance, an earthquake consists of high frequency cycles applied over a duration of approximately one minute or less, whereas large sea waves acting on an offshore structure have a much lower frequency with an extreme design storm lasting for one to two days. Accordingly, critical cases for design range from a few extreme cycles to millions of low level fluctuations.

Although cyclic load histories usually consist of a succession of irregular amplitude waves distributed relatively randomly with time, tests conducted on soil to explore cyclic loading effects are usually restricted to limited timeframes and cyclic rates. Common practice is to conduct uniform cycling with a fixed frequency and constant stress amplitude (stress-controlled) or constant strain amplitude (strain-controlled). As illustrated in Figure 3.1(a), these tests can be defined by their period (T), average load (Q_a), cyclic load amplitude (Q_{cy}), and number of cycles, or by their displacement equivalents. A further consideration is the mode of cyclic loading that is applied, as this affects the response of the soil, whether it is in the laboratory or the field. Four generic modes of cyclic loading can be identified as shown in Figure 3.1(a) to (d). Two-way cycling implies that the zero stress level is crossed, and can be asymmetric or symmetric depending on whether Q_a is nonzero or not. On the other hand, one-way cycling occurs when the zero stress is not crossed, and can either be such that the minimum load (Q_{min}) returns to zero or is nonzero.

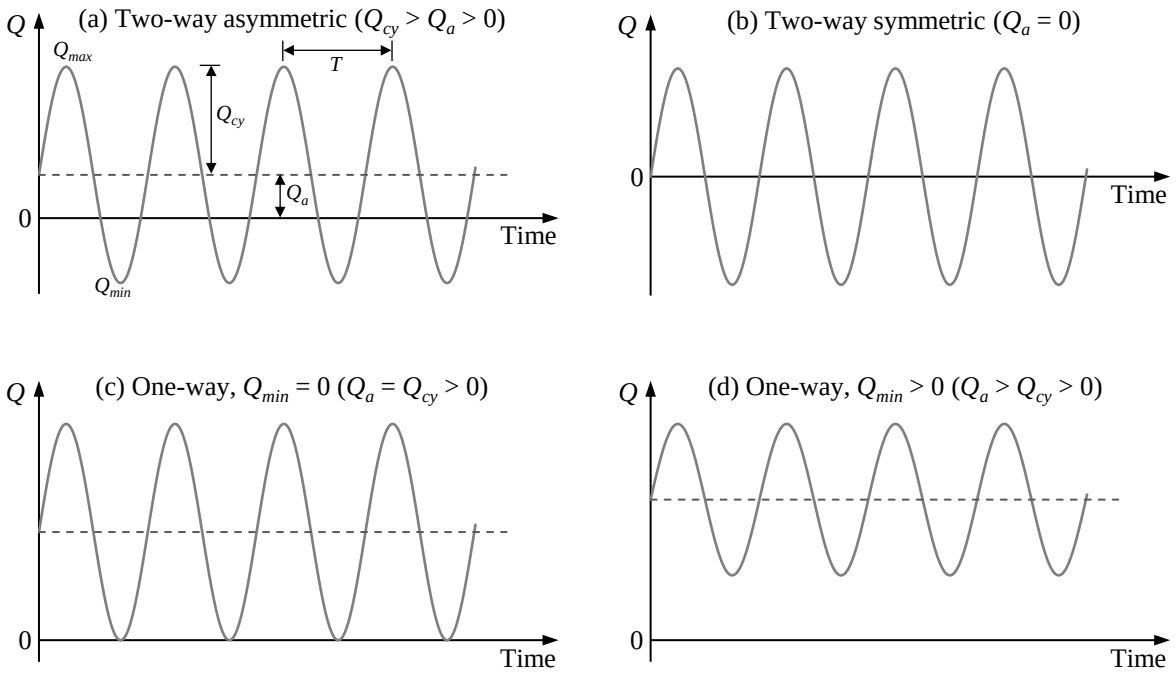

Figure 3.1: Modes of cyclic loading

3.2 Cyclic Loading Effects

Much of the research related to the effects of cyclic loading on foundation design has been conducted for offshore structures, traditionally for oil and gas production but more recently for offshore wind turbines, where the structures are subject to significant environmental cyclic loads originating from waves and wind. It is well recognized that there are several long-term implications associated with cyclic loading of such foundations, the primary of which are subsequently outlined as described by Andersen *et al*. (2013):

i) The stiffness of the underlying foundation soil will change over time, thus influencing the natural frequency of the entire structural system. If the effects are significant, this could cause the first natural frequency of the system to coincide with the excitation frequencies, leading to dynamic amplification and associated damaging resonant motions. In the case of strain-hardening soils such as loose to medium dense sand, the natural frequency is expected to increase, whereas for strain-softening soils such as normally consolidated clay, the natural frequency will decrease. The former occurs possibly due to densification of the soil, and the latter as a result of cyclic degradation.

ii) Cyclic loading will induce temporary elastic strain in the soil due to the elastic response of the soil-foundation system, as well as permanent plastic strain over the lifetime of the structure. The latter will give rise to accumulated vertical, horizontal and rotational displacements. This permanent strain can be separated into two components, the first being that which is developed during the cyclic loading, and the second being the strains developed due to the dissipation of cyclically induced pore pressure and creep. The

accumulated differential settlement of the foundation must be kept within tolerable limits, in compliance with the verticality criteria specified for the structure.

iii) The bearing capacity of the soil under cyclic loading may be lower than the capacity under monotonic loading. This is because cyclic loading tends to break down the soil structure, and create a tendency for volumetric reduction in the soil. In undrained conditions, volumetric changes will be prevented due to the low volumetric compressibility of water, and the normal stresses that were carried by the soil will be transferred to the pore water. This pore pressure build-up and the accompanying increase in cyclic and permanent shear strains may reduce the shear strength of the soil. However, the extent to which the capacity is reduced under cyclic loading depends on the number of cycles, the ratio between the cyclic and average loads, the composition of the cyclic amplitudes and the load period (Andersen *et al.*, 2013). The guideline for wind turbine support structures developed by DNV GL (2016b) suggests that the effects of cyclic loading can be included in this regard by applying partial load and material factors in the ultimate limit state design checks.

iv) Cyclic loading can alter the reaction stresses across the base and sides of a gravity base foundation, and cause a redistribution of these stresses. These changes must be accounted for, to ensure that the structural design is sufficiently robust to cope with the long-term soil pressure distributions and stiffness characteristics.

Not all the considerations mentioned above are relevant for all structures, although for onshore wind turbines the first two are of primary concern. With regards to stiffness, the wind turbine manufacturer usually specifies a minimum rotational stiffness and associated lateral stiffness that must be adhered to in the foundation design. Accordingly, the long-term change in the soil stiffness due to cyclic loading must be taken into consideration, as it could cause the natural frequency of the rotor-tower-foundation-soil system to shift and thus coincide with the 1*P* and 3*P* excitation frequencies. Keeping the accumulated differential settlement within acceptable limits is also a design requirement, and wind turbine manufacturers generally specify the maximum allowable differential settlement to be in the order of 3 to 4.5 mm/m (0.17º to 0.26º).

3.3 Strain Dependent Behaviour

A critical aspect concerning the cyclic loading of foundations is the behaviour of soil under varying levels of shear strain. In this regard, it is well recognised that the shear modulus and damping ratio of soil exhibits highly nonlinear behaviour, and that with an increase in shear strain amplitude, the former decreases whereas the latter increases. Each of these two facets of soil behaviour are subsequently discussed.

3.3.1 Stiffness

In the context of material mechanics, stiffness is a measure of the resistance of a body to deformation when subjected to an applied loading, and as such governs the relationship that is established between stress and strain over time. Stiffness is derived from (1) the shape of the body; (2) boundary conditions, such as fixities and load positions; and (3) the stiffness properties of the constituent materials (Clayton, 2011). In geotechnical engineering practice, the stiffness properties are normally defined within the framework of the mathematical theory of elasticity, although this is not strictly necessary. In doing so, soil stiffness is often expressed in terms of its elastic modulus (E) or shear modulus (G), both of which are interrelated through Poisson's ratio (ν) as shown in Equation 3.1.

$$E = 2G(1+\nu) \qquad \text{Eqn. 3.1}$$

Where E = elastic modulus (Pa); G = shear modulus (Pa); and ν = Poisson's ratio (unitless).

Experimental data shows that the shear modulus of soil decays in a nonlinear manner as the level of shear strain (γ) induced within it increases. For soil under cyclic loading, this translates to the cyclic shear strain (γ_c). This behaviour is evident in Figure 3.2, which represents the typical stress-strain relationship of soil under harmonic loading. Such a stress-strain curve can be considered as being composed of two curves, (1) the backbone curve which represents the path of first loading, and (2) the hysteretic loops, each of which is accrued for a single period of oscillation, and consist of unloading and reloading paths. The backbone curve is the locus of points corresponding to the tips of the hysteresis loops, with its slope representing the shear modulus. Therefore, it can be observed that at low strain amplitudes the shear modulus is at its maximum, but it decreases as the strain amplitude increases.

The shear modulus at very small strains is referred to as the *initial* or *maximum shear modulus*, denoted interchangeably as G_0 or G_{max}. This parameter is assumed to be constant and corresponds to strain amplitudes below the linear elastic threshold. At higher strain amplitudes, Figure 3.2 illustrates that the shear modulus can be defined according to the secant (G_{sec}) or the tangent (G_{tan}) of the backbone curve. The former provides an indication of the average stiffness over a range of strain, whereas the latter describes the actual stiffness at any given point. Tangent stiffness varies much more rapidly with strain than secant stiffness, and is more useful as it describes the way in which the soil will respond in generating change in stress as a result of a

small imposed deformation from the current state of the soil (Wood, 2004). However, Kramer (1996) states that most of the commonly used methods of ground response analysis are based on the secant shear modulus, and that it is important to realise that this is only an approximation of the actual nonlinear behaviour of the soil. Wood (2004) points out a further consideration in the case that the stress-strain response of the soil reveals strain softening after some peak – the tangent modulus will become negative, indicating negative incremental stiffness, which is a behavioural facet that would be concealed with the secant stiffness which remains resolutely positive.

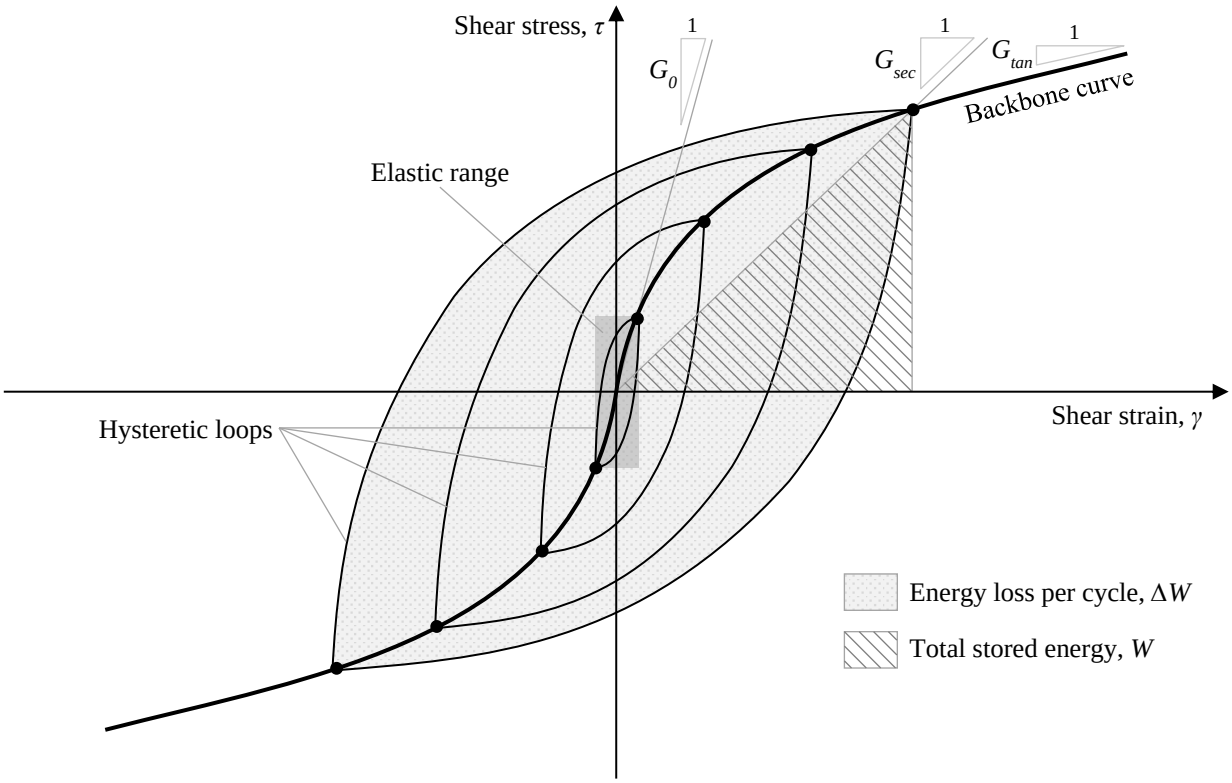

Figure 3.2: Stress-strain relationship for hysteretic soils and definition of parameters

The variation of soil stiffness with shear strain is better illustrated with a modulus reduction curve, such as that shown in Figure 3.3. This curve represents the derivative of the backbone curve, however the shear modulus is normalised (G/G_0) to show its deviation relative to G_0, and the cyclic shear strain is plotted on a logarithmic scale, as much of the initial variation with stiffness occurs at very small strains. Furthermore, note that the shear modulus (G) as shown in these curves (from the results of laboratory tests available in the literature) usually refers to the secant shear modulus (G_{sec}), and therefore the "sec" subscript has henceforth been dropped.

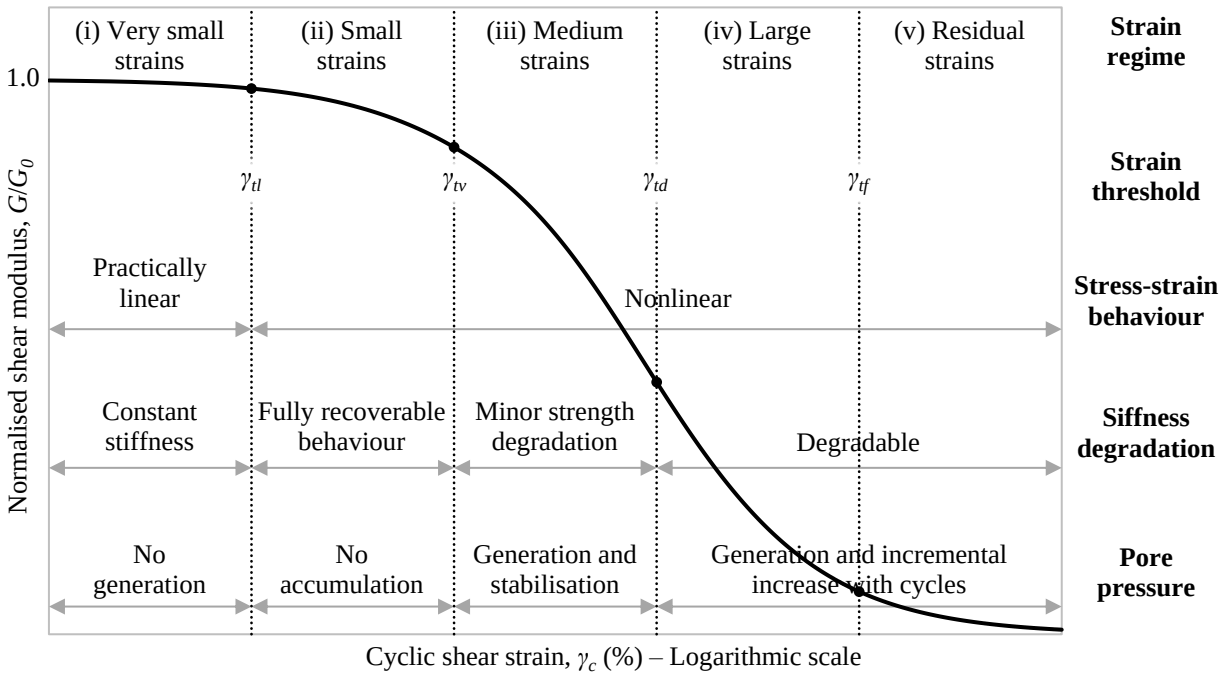

Figure 3.3: Conceptual shear modulus reduction curve with proposed strain thresholds for saturated clayey soils

Adapted from Diaz-Rodriguez and Lopez-Molina (2008)

Based on a synthesis of literature and published experimental data, Diaz-Rodriguez and Lopez-Molina (2008) proposed cyclic strain regime divisions, illustrated in Figure 3.3, which are applicable to saturated clayey soils. The criteria considered for the development of this approach included stress-strain behaviour, stiffness degradation, pore pressure generation, post-cyclic strength and microscale processes. The five strain regimes are separated by four shear strain thresholds, namely that related to linearity (γ_{tl}), volume change (γ_{tv}), degradation (γ_{td}) and flow (γ_{tf}). Each strain regime is subsequently outlined as described by Diaz-Rodriguez and Lopez-Molina (2008):

i) Very small strains ($\gamma_c < \gamma_{tl}$): This regime is characterised by linear elastic behaviour with approximately constant stiffness, and no generation of pore pressure. It is separated from the *small strain* regime by the linear shear strain threshold (γ_{tl}), which is arbitrarily defined as the shear strain corresponding to a normalised shear modulus of $G/G_0 = 0.99$. For most clayey soils, experimental results indicate that this threshold strain is in the order of 0.001% to 0.005%.

ii) Small strains ($\gamma_{tl} < \gamma_c < \gamma_{tv}$): The stress-strain relationship of soil in this regime is nonlinear, however the behaviour of the soil is fully recoverable because permanent changes to the microstructure still do not occur or are negligible (Vucetic, 1994). There is also no accumulation of pore pressure during undrained cyclic loading, nor is there permanent volume change for dry or partially saturated conditions. The volumetric shear strain threshold (γ_{tv}) provides the upper limit of this regime, and is likely to correlate to a normalised shear modulus of $G/G_0 = 0.6$ to 0.85 (Diaz-Rodriguez & Lopez-Molina, 2008).

iii) Medium strains ($\gamma_{tv} < \gamma_c < \gamma_{td}$): Once the volumetric shear strain threshold is exceeded, the stress-strain response of the soil becomes increasingly nonlinear, with minor strength degradation occurring if the degradation shear strain threshold (γ_{td}) is not surpassed. Therefore, repeated loading is not likely to lead to soil failure regardless of the number of cycles. Furthermore, the deformation and residual pore pressure have been found to stabilise after the first loading cycles in this strain regime, and remain practically constant with additional cycles (Lefebvre *et al.*, 1989).

iv) Large strains ($\gamma_{td} < \gamma_c < \gamma_{tf}$): In the *large strain* regime, permanent microstructural changes take place in the soil under cyclic loading, causing particle contacts and bonds to become irreversibly disturbed. Consequently, irreversible stiffness and strength degradation occurs. In undrained conditions, a permanent cyclic pore pressure develops, whereas in dry or partially saturated soils a permanent volume change accumulates, each of which accrues incrementally as the number of cycles increases.

v) Residual strains ($\gamma_c > \gamma_{tf}$): At cyclic shear strains exceeding the flow threshold (γ_{tf}), the soil reaches steady-state conditions where the residual strength is mobilised and it starts to behave as a viscoplastic material. Okur and Ansal (2007) suggest that this shear strain threshold corresponds to a G/G_0 ratio in the order of 0.1.

It can be concluded that in terms of loading parameters, the level of cyclic shear strain induced in the soil is the main factor characterising its dynamic response, and the number of cycles also becomes important if the degradation threshold is exceeded. At small cyclic strains, the stress-strain response is relatively linear and there is little or no degradation with the number of straining cycles, whereas significant nonlinearity, inelasticity and degradation occur at large strains.

A further consideration is the influence that other soil and loading parameters have on both the value of G_0 and the manner in which G/G_0 varies with cyclic shear strain. In this regard, Dobry and Vucetic (1987) reviewed experimental results from a broad range of laboratory and field tests, and provided the summary of influential parameters for normally consolidated and moderately overconsolidated clays shown in Table 3.1. From this, the authors concluded that the overconsolidation ratio (OCR) is the main soil parameter controlling the value of G_0, however it has practically no effect on the shape of the modulus reduction curve. The OCR value reflects the loading history of the soil deposit, and it was identified that overconsolidated clay has a higher G_0 and experiences less degradation during cyclic straining than normally consolidated soil. In terms of the shape of the modulus reduction curve, three parameters were identified as being most significant for further discussion, namely that of the plasticity index (PI), mean effective confining pressure (p') and number of loading cycles (N).

Table 3.1: Effect of various increasing parameters on G_0 and G/G_0 of normally consolidated and moderately overconsolidated clays

Adapted from Dobry and Vucetic (1987)

Increasing parameter	Initial shear modulus, G_0	Normalised shear modulus, G/G_0
Mean effective confining pressure, p'	Increases with p'	Stays constant or increases with p'
Void ratio, e	Decreases with e	Increases with e
Geologic age, t_g	Increases with t_g	May increase with t_g
Cementation, c	Increases with c	May increase with c
Overconsolidation ratio, OCR	Increases with OCR	Not affected
Plasticity index, PI	• Stays about constant if OCR = 1 • Increases with PI if OCR > 1	Increases with PI
Cyclic shear strain, γ_c	–	Decreases with γ_c
Strain rate, $\dot{\gamma}$	Increases with $\dot{\gamma}$	• G increases with $\dot{\gamma}$ • G/G_0 probably not affected if G and G_0 are measured at the same $\dot{\gamma}$
Number of loading cycles, N	Decreases after N cycles of large γ_c but recovers later with time	Decreases after N cycles of large γ_c (G_0 measured before N cycles)

3.3.1.1 Effect of plasticity

Vucetic and Dobry (1991) concluded that the PI of soil is the main factor controlling the position of the modulus reduction curve for a wide variety of saturated soils, ranging from clays to sands. Several studies and sets of published data were analysed in doing so, from which the curves illustrated in Figure 3.4 were produced. This chart shows that saturated cohesionless soils with a PI of 0%, such as gravels and sands, are the most nonlinear as they start to behave in a nonlinear manner at the smallest strain levels, and thus experience significant softening during continuous cyclic loading. As the PI increases, the curves essentially shift to the right, and accordingly the strain thresholds associated with linearity, volume change, degradation and flow also increase. Therefore, soils of high plasticity, as compared to soils of low plasticity, behave as more flexible and linearly elastic materials up to larger levels of cyclic shear strain. It must be noted that although Vucetic and Dobry (1991) recommended the chart in Figure 3.4 to be used for preliminary or even final evaluations of the cyclic response of saturated fine-grained soil deposits, they advised not using them for soils that have a sensitive structure, such as quick clays or cemented sands, as they may exhibit behaviour that is independent of their PI.

In a similar manner to the PI, trends relating the void ratio (e) of soil to its modulus reduction curve were identified by several authors including Vucetic and Dobry (1991). That is, as e increases, the modulus reduction curve shifts to the right. However, Vucetic and Dobry (1991) observed that this similarity in trends was due to the fact that PI and e are correlated, and that the

more consistent trends were obtained when PI was used rather than *e*. Other parameters and conditions being equal, higher plasticity soils generally have a more open structure and thus a larger *e*, hence giving rise to similar influences on the modulus reduction curve.

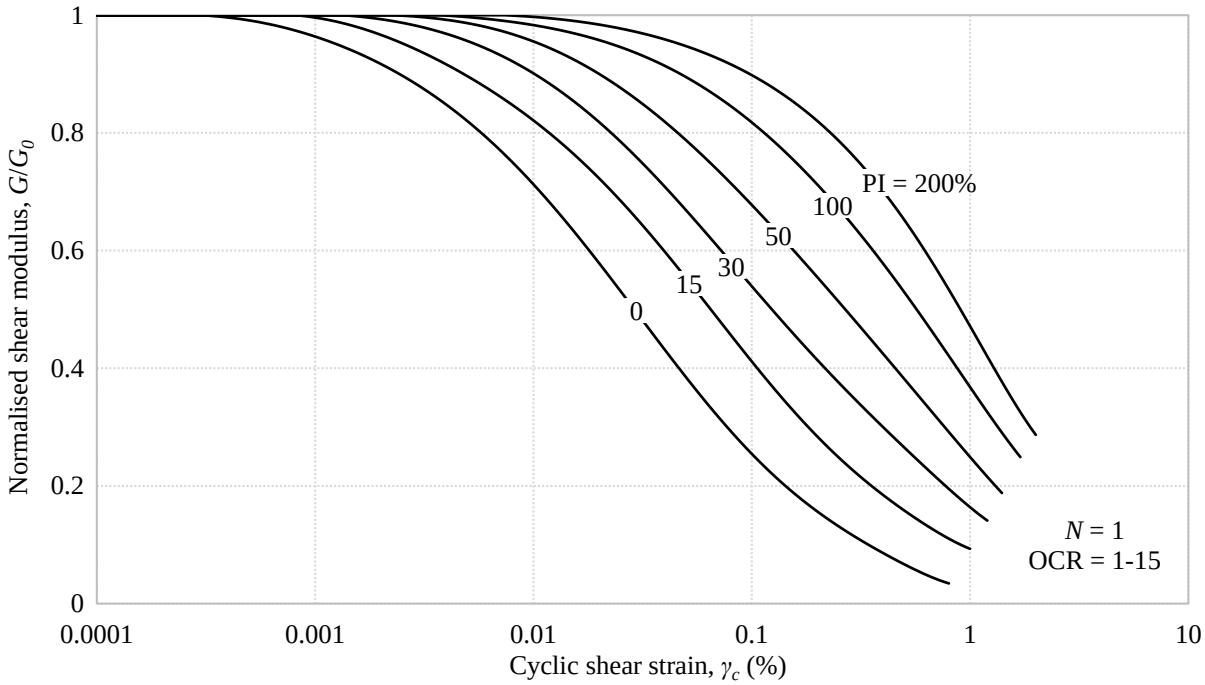

Figure 3.4: Effect of plasticity index on shear modulus reduction curve
Adapted from Vucetic and Dobry (1991)

3.3.1.2 Effect of confining pressure

Modulus reduction behaviour is also influenced by the mean effective confining pressure, *p'*. However, the effects of this parameter are only significant for soils of low plasticity. This is illustrated in Figure 3.5(a) and (b) where it is evident that there is a large disparity between the curves of different confining pressures for a PI of 0%, however this disparity diminishes when the PI is increased to 50%. Furthermore, it is observed that at high confining pressures, soils behave linearly up to greater shear strain levels than at low confining pressures. Note that Figure 3.5 is based on Equations 3.2 to 3.5 below, which were proposed by Ishibashi and Zhang (1993) to account for the combination of the effects of mean effective confining pressure and PI on modulus reduction behaviour.

$$\frac{G}{G_0} = K(\gamma_c, \mathrm{PI})(p')^{m(\gamma_c, \mathrm{PI}) - m_0} \qquad \text{Eqn. 3.2}$$

$$K(\gamma_c, \mathrm{PI}) = 0.5\left\{1 + \tanh\left[\ln\left(\frac{0.000102 + n(\mathrm{PI})}{\gamma_c / 100\%}\right)^{0.492}\right]\right\} \qquad \text{Eqn. 3.3}$$

$$m(\gamma_c, \mathrm{PI}) - m_0 = 0.272\left\{1 - \tanh\left[\ln\left(\frac{0.000556}{\gamma_c/100\%}\right)^{0.4}\right]\right\}\exp\left(-0.0145\mathrm{PI}^{1.3}\right) \quad \text{Eqn. 3.4}$$

$$n(\mathrm{PI}) = \begin{cases} 0.0 & \text{for PI} = 0\% \\ 3.37\times10^{-6}\,\mathrm{PI}^{1.404} & \text{for } 0\% < \mathrm{PI} \le 15\% \\ 7.0\times10^{-7}\,\mathrm{PI}^{1.976} & \text{for } 15\% < \mathrm{PI} \le 70\% \\ 2.7\times10^{-5}\,\mathrm{PI}^{1.115} & \text{for PI} > 70\% \end{cases} \quad \text{Eqn. 3.5}$$

Where $p' = (\sigma'_1 + \sigma'_2 + \sigma'_3)/3$ = mean effective confining pressure (kPa); $K(\gamma_c, \mathrm{PI})$ is a decreasing function of the cyclic shear strain amplitude; $m(\gamma_c, \mathrm{PI}) - m_0$ is an increasing function of the cyclic shear strain amplitude; $n(\mathrm{PI})$ is a modifying function to account for soil plasticity; and other parameters previously defined.

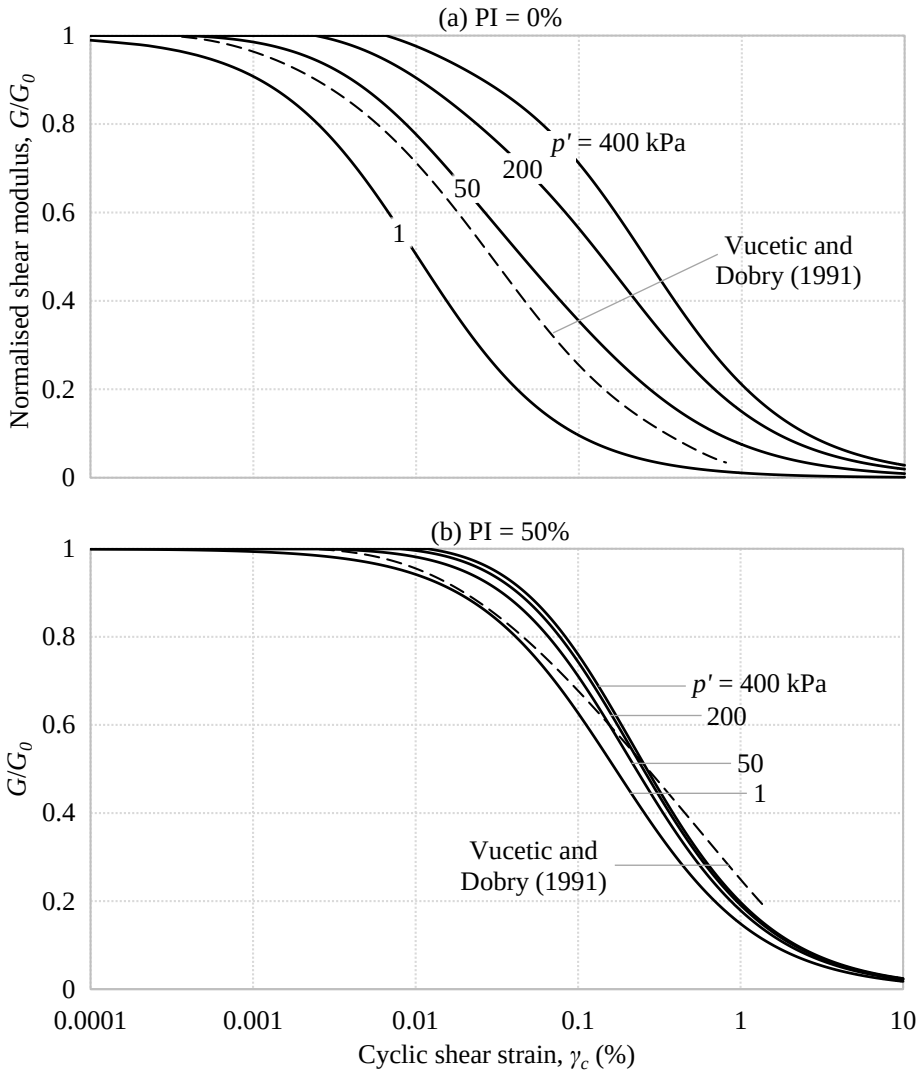

Figure 3.5: Effect of mean effective confining pressure on shear modulus reduction curve
Adapted from Ishibashi (1992)

3.3.1.3 Effect of degradation

The stiffness of fully saturated soil degrades when it is subjected to undrained cyclic loading at a shear strain amplitude that exceeds the degradation threshold γ_{td}. This is due to the accumulation of excess pore water pressure, as well as the deterioration of soil structure (Vucetic, 1994; Okur & Ansal, 2007; Towhata, 2008; Tabata & Vucetic, 2010). As illustrated in Figure 3.6, this can be interpreted as a progressive downward shift of the modulus reduction curve as the number of loading cycles (N) increases.

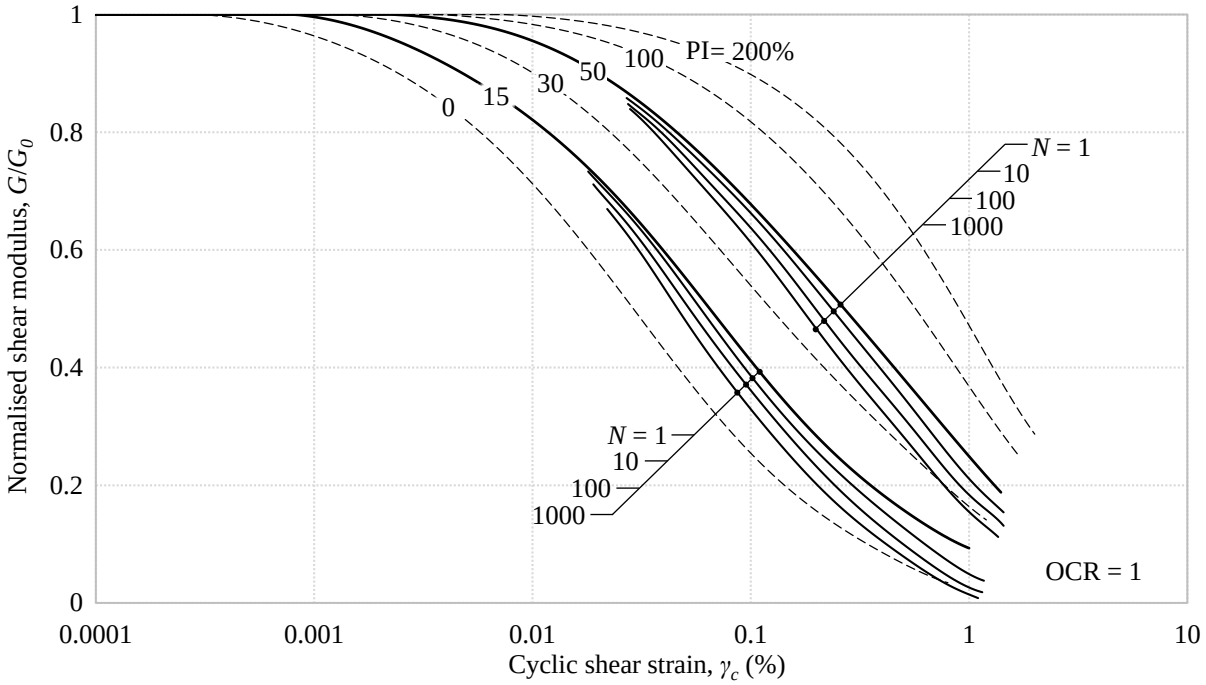

Figure 3.6: Effect of cyclic degradation on shear modulus reduction curve
Adapted from Vucetic and Dobry (1991)

One approach to quantifying cyclic degradation for a given cyclic shear strain amplitude is by using the concept of degradation index (δ), which was originally introduced by Idriss *et al.* (1978). This index describes the relative decrease of the secant shear modulus after N cycles (G_N) with respect to that in the first cycle (G_1), as shown in Equation 3.6.

$$\delta = \frac{G_N}{G_1} \qquad \text{Eqn. 3.6}$$

Where δ = degradation index (unitless); G_N = secant shear modulus after N cycles (Pa); and G_1 = secant shear modulus after the first cycle (Pa).

Prior to the commencement of cyclic loading, δ is equal to unity. However, as the cyclic loading progresses and the effect of degradation in the soil accumulates, δ decreases monotonically with N. Furthermore, if the cyclic straining conditions are uniform and δ is plotted versus N on a log-log scale, it has been shown that for many soils the data points plot along an approximately straight line. The gradient of this line is termed the *degradation parameter* (t), defined in Equation 3.7.

$$t = -\frac{\log \delta}{\log N} \text{ or } \delta = N^{-t} \qquad \text{Eqn. 3.7}$$

Where t = degradation parameter (unitless); and other parameters previously defined.

The degradation parameter t describes the rate of cyclic degradation with N. As shown in Figure 3.7(a) and (b), this parameter increases with increasing cyclic shear strain amplitude, and decreases with increasing OCR and PI. This implies that if a clay is overconsolidated versus normally consolidated, or if it has high plasticity versus low plasticity, the stiffness will degrade at a slower rate for the same applied cyclic strain.

Vucetic and Dobry (1988) place emphasis on the fact that a small variation in t can have a large effect on modulus degradation, and thus caution must be observed when curves such as that shown in Figure 3.7 are used. It is therefore suggested that it may be necessary to conduct cyclic tests on clay specimens from the site in question for a more accurate determination of t to be used in final design.

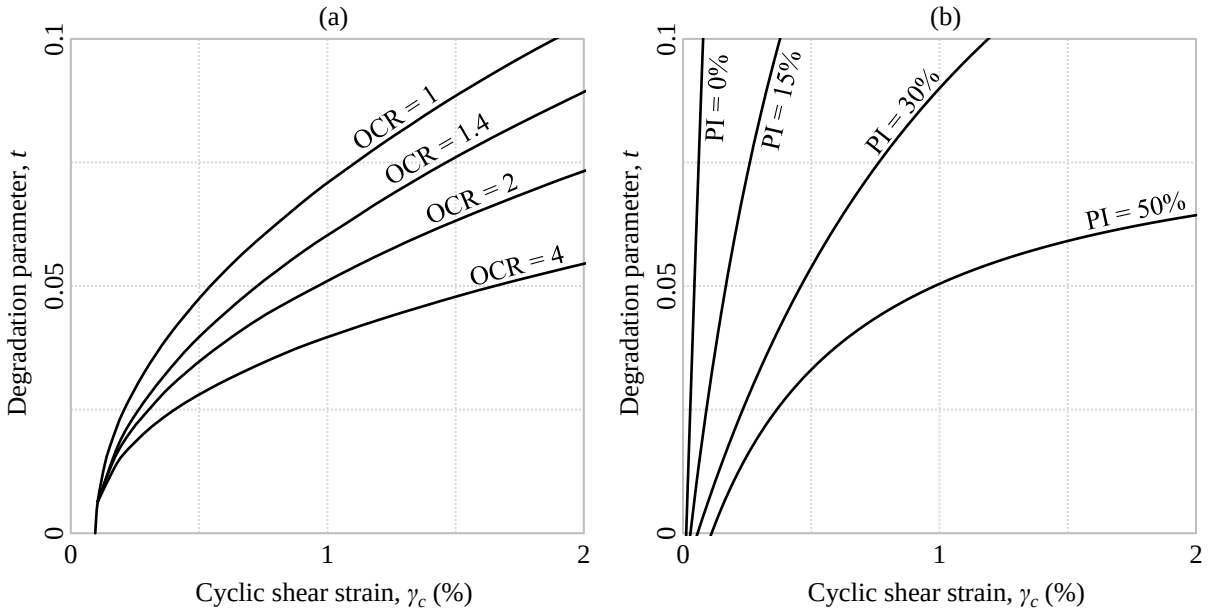

Figure 3.7: Relationship between degradation parameter t and γ_c for varying OCR and PI
(a) Effect of OCR (Adapted from Matasovic & Vucetic, 1995)
(b) Effect of PI for normally consolidated soils (Adapted from Vucetic, 1992)

Figure 3.8 further illustrates the concept of cyclic degradation and the definition of parameters. When $\gamma_c > \gamma_{td}$ as shown in Figure 3.8(a), t is nonzero and the shear modulus decreases with increasing N. Conversely, when $\gamma_c < \gamma_{td}$ as in Figure 3.8(b), t is equal to zero and the soil does not cyclically degrade.

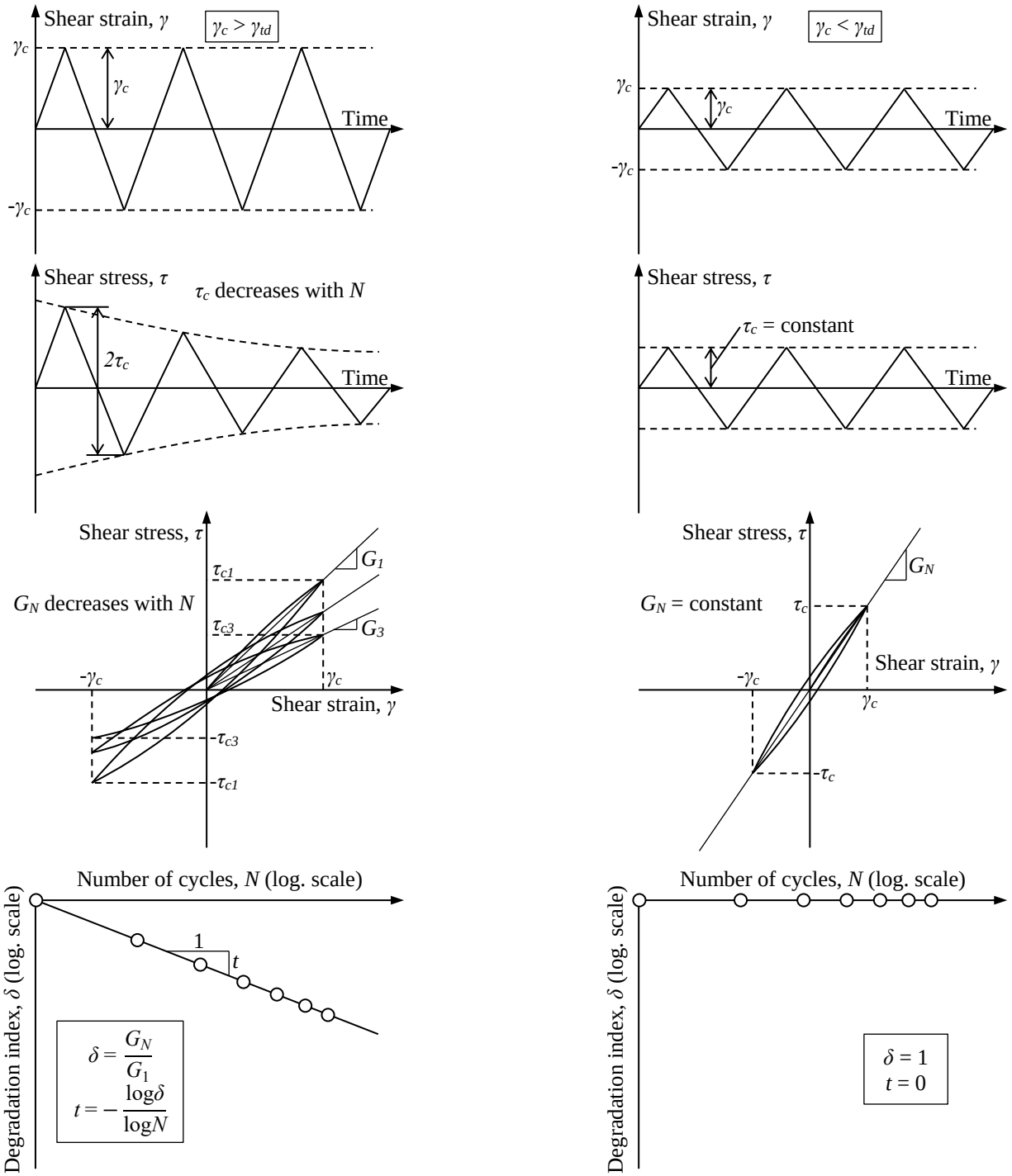

(a) Cyclic behaviour when $\gamma_c > \gamma_{td}$

(b) Cyclic behaviour when $\gamma_c < \gamma_{td}$

Figure 3.8: Phenomenon of cyclic degradation and definition of parameters

Adapted from Tabata and Vucetic (2010)

3.3.2 Damping

The phenomenon of damping refers to the dissipation of energy in a cyclically loaded or vibrating body of material or mechanical system, which causes a reduction in the amplitude of vibration. It follows that the term *damping* can be used to characterise the energy absorbing properties of a material. For instance, a material is said to have large damping if it dissipates a lot of energy during cyclic loading or vibrations. This is an important concept because the application of loading imparts energy to soil, resulting in the development of strain. If on removal of load the strain is lost, then the energy has been recovered and thus there is no damping. Conversely, if irrecoverable strains are produced on load removal, this indicates that the energy imparted during loading has been lost or dissipated and in a sense converted to the plastic deformation.

In soil dynamics, there are two types of damping that are important, namely radiation damping and soil damping. The former occurs due to the propagation of waves away from an energy source, whereas the latter occurs internally within the soil elements due to viscous and hysteretic effects. Consequently, the characterisation of soil damping is usually analysed in terms of its viscous damping, which is caused by the viscous nature of the soil, hysteretic damping, which is a result of the inherent nonlinear stress-strain behaviour, or a combination of both with relative contributions. An important distinction between these two concepts is that viscous damping is dependent on the frequency of loading, whereas hysteretic damping is not. It is for this reason that hysteretic damping is often considered to provide a more realistic representation of soil behaviour than viscous damping, as plastic deformations that occur in soils under cyclic loading are understood to be independent of the frequency of loading (Verruijt, 2010). However, an analysis involving viscous damping has the benefit of mathematical simplicity as it involves linear differential equations only, and thus it is often used in geotechnical engineering applications even if the damping is not truly viscous (Venkatramaiah, 2006). Thus, it is convenient to characterise the damping of soil by a so-called *equivalent viscous damping ratio* (ζ), otherwise simply referred to as the *damping ratio*, the expression of which is given in Equation 3.8.

$$\zeta = \frac{1}{4\pi}\frac{\Delta W}{W} \qquad \text{Eqn. 3.8}$$

Where ζ = damping ratio; ΔW = energy loss per cycle; and W = total stored energy.

Equation 3.8 shows that the damping ratio is proportional to the ratio between the energy loss per cycle (ΔW) and the total stored energy (W) during one cycle of loading. As illustrated in Figure 3.2, ΔW is represented by the area enclosed by the hysteresis loop, whereas W is equal to the area of the triangle bounded by a straight line defining the secant modulus.

The breadth of hysteresis loops of cyclically loaded soil increase with increasing shear strain amplitude, which indicates that the damping ratio also increases with increasing strain amplitude. This means that as the level of shear strain increases, more energy is dissipated during cyclic loading. Furthermore, in theory there is no energy dissipation at strain levels below the linear

shear strain threshold. However, evidence to the contrary has been observed from experimental data, whereby some energy dissipation is evident at very low strain levels. This implies that a minimum value of damping exists for soils, however this mechanism is not well understood (Kramer, 1996).

Studies into the factors affecting the damping ratio of soil are not as extensive as those for stiffness, however a summary of the effects of various material and loading parameters are provided in Table 3.2. Similarly to what was observed for modulus reduction behaviour, Vucetic and Dobry (1991) concluded that of these factors, the PI of the soil has the largest influence on the shape of the damping curve for a wide variety of saturated soils ranging from clays to sands. This is illustrated in Figure 3.9 where it is evident that the damping curves progressively lower as the PI of the soil increases. This implies that soil with a higher PI dissipates less energy during cyclic loading, and vice versa. This correlation, while strong at levels of large strain, becomes less clear at cyclic shear strain levels of approximately 0.01% and less (Vucetic & Dobry, 1991).

Table 3.2: Effect of various increasing parameters on the damping ratio of normally consolidated and moderately overconsolidated clays

Adapted from Dobry and Vucetic (1987)

Increasing parameter	Damping ratio, ζ
Mean effective confining pressure, p'	Stays constant or decreases with p'
Void ratio, e	Decreases with e
Geologic age, t_g	Decreases with t_g
Cementation, c	May decrease with c
Overconsolidation ratio, OCR	Not affected
Plasticity index, PI	Decreases with PI
Cyclic shear strain, γ_c	Increases with γ_c
Strain rate, $\dot{\gamma}$	Stays constant or may increase with $\dot{\gamma}$
Number of loading cycles, N	Not significant for moderate γ_c and N

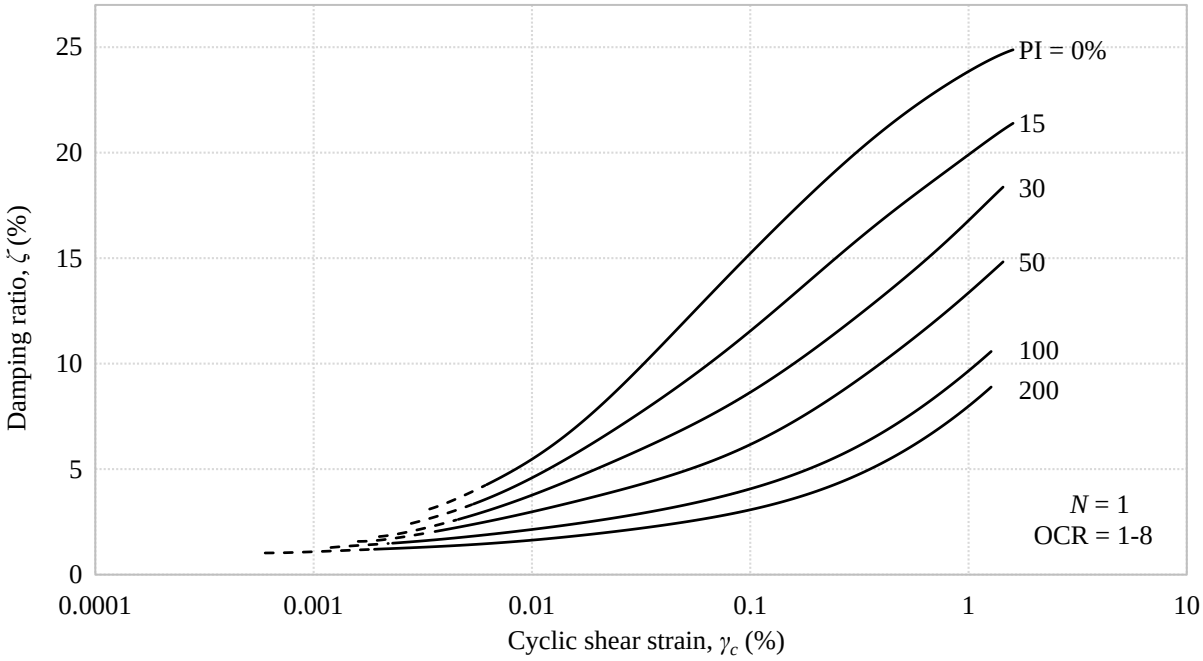

Figure 3.9: Effect of plasticity index on damping curve
Adapted from Vucetic and Dobry (1991)

In addition to the PI, damping behaviour of soil is largely influenced by effective confining pressure. This was demonstrated by Ishibashi and Zhang (1993) who developed an empirical expression for the damping ratio of plastic and nonplastic soils, expressed in Equation 3.9. Note that although the effective confining pressure *p'* is not an explicit parameter in this expression, it enters into the calculation of G/G_0 in Equation 3.2, which is applied in this equation.

$$\zeta = 0.333\frac{1+\exp\left(-0.0145\mathrm{PI}^{1.3}\right)}{2}\left[0.586\left(\frac{G}{G_0}\right)^2 - 1.547\left(\frac{G}{G_0}\right)+1\right] \qquad \text{Eqn. 3.9}$$

Where G/G_0 is calculated as per Equation 3.2; and other parameters previously defined.

3.4 Constitutive Modelling

A constitutive model is a mathematical representation of material behaviour, which for numerical analyses in geotechnical engineering is predominantly used to define the relationship between stresses and strains. Accordingly, constitutive equations are a necessary component of any finite element (FE) method model of a geotechnical problem, and their formulation requires careful consideration if reliable predictions of performance are to be achieved. However, soils are complex multiphase materials with a particulate nature, and consequently significant difficulties exist in developing models that can adequately reproduce their behaviour. Furthermore, although soil materials such as clay, silt and sand share some common characteristics, differences in the size, shape and mineralogy of their constituent particles result in significant differences in the way they respond to applied loads and deformations.

Currently, a single constitutive model with a reasonable number of input parameters that can describe all facets of real soil behaviour does not exist. However, an abundance of soil constitutive models has been proposed in recent decades and are available in the literature, each with their own advantages, disadvantages and circumstances of applicability. These models range in complexity and rigour, with some having been formulated on the basis of theoretical principles and others on experimental evidence. The most widely used models are generally available in packaged numerical software, however the majority of these models have limitations in various geotechnical engineering applications, particularly cyclic loading.

The development of reliable models for cyclic loading is a complex task in constitutive modelling. Such models are discussed in this section, however prior to doing so, it is useful to first consider the fundamental concepts of an elastoplastic framework. Although most conventional models based on elastoplasticity are only suitable for monotonic loading, several successful models for the behaviour of soils under cyclic loading have been proposed as developments of this framework.

3.4.1 Elastoplastic framework

Most practical constitutive models for soil subjected to monotonic loading are formulated based on an elastoplastic framework, which provides a convenient and efficient means of simulating the mechanical behaviour of soil. Models under this framework assume elastic behaviour prior to yield and therefore comprise of a combination of elasticity and plasticity theories. As illustrated in Figure 3.10, these theories consist of an elastic model, yield surface, plastic potential surface, plastic hardening/softening rule and a failure surface, each of which is subsequently characterised.

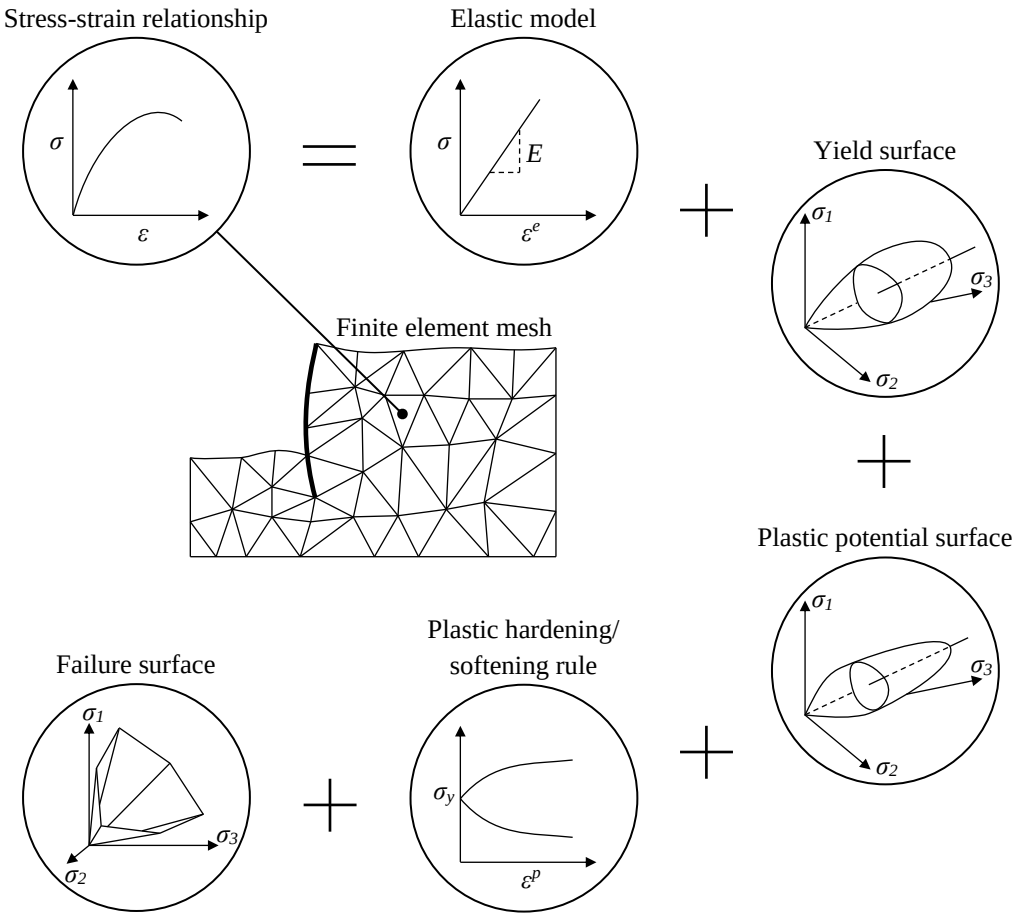

Figure 3.10: Constituents of an elastoplastic constitutive model
Adapted from Lade (2005)

3.4.1.1 Elastic model

Elasticity is the simplest form of the constitutive relationship in which the state of stress is a function of the current state of deformation only. That is, in the elastic domain (the domain of stress space interior to the yield surface) no permanent strains develop and the mechanical behaviour is completely reversible. There are several models used to describe this behaviour, the most notable of which, as outlined by several authors (e.g. Potts & Zdravkovic, 1999; Puzrin, 2012; Lees, 2016), are described below:

- Isotropic linear elasticity: This model, otherwise referred to as Hooke's law, is the simplest elastic model available as it assumes constant proportionality between general stress increments and strain increments. It requires only two input parameters, most commonly E and v, or G and bulk modulus K, which are assumed to be the same in all geometric directions. Since real soil behaviour is stress- and strain-dependent, it is important that the selected values for these parameters are appropriate for the anticipated stress and strain levels, as well as the stress path (such as primary loading or unload-reload path). Consequently, it may not be possible to select appropriate values for large ranges of stress and strain or for complex stress paths. The stress-dependency of stiffness can be partially

accounted for by specifying an increase in stiffness with depth, however any subsequent stiffness changes due to stress changes cannot be effected.

This model has been widely applied in conventional soil mechanics due to its simplicity, however it is generally too crude to capture essential features of real soil behaviour. Nonetheless, it is often used when an initial rough estimate of the solution is sought, as well as to represent the behaviour of structural elements or rock layers.

- Anisotropic linear elasticity: Soil deposits are formed in nature under gravity, which results in different soil properties in vertical and horizontal planes. This can be incorporated into the linear elastic model, which allows the different stiffness properties in the different geometric directions to be captured. However, the characterisation of an anisotropic elastic material requires the input of 21 independent elastic parameters, which is impractical for routine use. This can be simplified by assuming the soil material to be *transversely isotropic*, otherwise referred to as *cross-anisotropic*, in which the mechanical behaviour in all horizontal planes is identical, but still differs from that in the vertical planes. This reduces the number of input parameters to seven, of which only five need to be measured.

  Although this model serves as an improvement over the isotropic linear elastic model, it inherits the majority of the same limitations and is not able to simulate important facets of real soil behaviour. Furthermore, the more advanced nonlinear models described below usually adopt isotropic elasticity because of the high number of parameters that would be required to define nonlinear, anisotropic behaviour.

- Nonlinear elasticity and stress-path dependent stiffness: Nonlinear elastic models offer a substantial improvement over their linear counterparts. One of the most well-known and widely used models of this type is the *hyperbolic* model, which was originally developed by Kondner (1963) and implemented into a finite element code for the first time by Duncan and Chang (1970). This model combines two main ideas, first that the stress-strain curve under primary loading in drained triaxial tests can be approximated by a hyperbola, as illustrated in Figure 3.11, and second that the soil stiffness can be formulated as a stress-dependent parameter using a power law formulation (Brinkgreve, 2005). Another feature of this nonlinear elastic model is that it does not follow the same stress-strain path on unloading, but rather exhibits a stiffer, linear elastic response as shown in Figure 3.11.

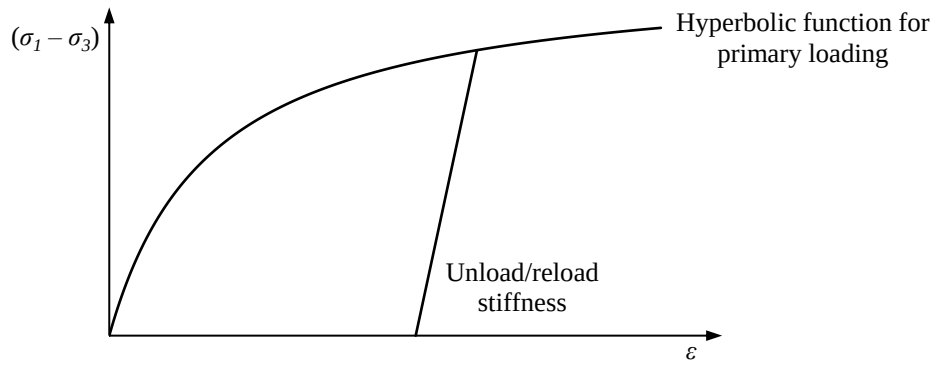

Figure 3.11: Hyperbolic stress-strain curve

Although the hyperbolic model provides good predictions of displacements under deviatoric monotonic loading and load reversals, it is nonetheless still regarded as an improved first order model and is incapable of representing many of the important characteristics of soil behaviour. The *hardening soil* model available in the finite element code *Plaxis* is also based on a hyperbolic stress-strain function, and it supersedes the original hyperbolic model through the implementation of several additional features.

- Stress-dependent stiffness: The isotropic and anisotropic linear elastic models assume the soil stiffness parameters to be constant, however in reality soil stiffness is dependent on confining stress. Although it is possible to specify increasing soil stiffness with depth when using these models, they do not take account of subsequent changes in stiffness caused by changes in stress. Therefore, full stress-dependency can be obtained if the constitutive model includes expressions relating stiffness moduli with confining stress. An example of this would be the power law that is implemented in the hyperbolic model. Stress-dependent stiffness is an important feature in a constitutive model if increased accuracy of deformation predictions is required, particularly in cases where stress changes are significant, such as heave under a deep excavation or settlement under a new embankment.
- Strain-dependent stiffness: As was discussed in §3.3.1, experimental evidence shows that soil stiffness is highly dependent on the amplitude of the induced strain. Specifically, Figure 3.3 demonstrates that maximum stiffness is attained at very small strains, after which it decreases nonlinearly as the amplitude of the strain increases. Incorporating this small-strain behaviour into a constitutive model considerably increases the overall reliability of the calculated deformations, as underestimations of soil stiffness at small strains can result in strains and displacements being overestimated. This is because in reality, only a limited volume of soil experiences large deformations and the strains in the remaining areas are very small, however since these small strains are integrated over a large area, their overall contribution can be substantial.

  Although the hyperbolic and hardening soil models discussed previously were developed to incorporate nonlinear behaviour, they have limitations with regards to simulating the very high stiffness at small strains. This shortcoming was addressed for the latter constitutive model by Benz (2007) through the addition of a small-strain overlay model, the result of which was the *hardening soil model with small-strain stiffness* that is available in *Plaxis*. This approach of combining two separate stress-strain models – one to describe the small-strain behaviour and another for the larger strains – is difficult to formulate mathematically and careful attention has to be paid to the way that the stiffness is modelled at the interface between the two models.

  An alternative approach is to use a curve-fitting function that better fits the full range of stress-strain behaviour. There are several functions available to do so, such as those that are hyperbolic, cubic, logarithmic, sigmoidal, and so forth. Each of these models can be used to fit a modulus reduction curve (or backbone curve) from the literature or from a programme of tests on the soil. One of the most well-known functions for this purpose is the *Ramberg-Osgood* model, which contains four parameters that can be adjusted to achieve a best fit of the data. However, despite the wide use of this model, Puzrin (2012)

points out that there are more accurate models available, such as that of a logarithmic function which is able to include a high level of nonlinearity at very small strains. A further consideration with regards to cyclic loading is the manner in which these models predict damping ratios, as some tend to provide underpredictions and others overpredictions in different strain ranges.

3.4.1.2 Yield surface

The yield surface is a surface in stress space that defines the boundary between purely elastic and elastoplastic material behaviour. Specifically, when the stresses in the material reach a combination that coincides with the yield surface, that material will undergo plastic straining. The stress state cannot go outside of the surface, but rather the stress increments are such that they stay on and run along it, even though the size and position of the surface may change. If unloading occurs, the stress state can move inside the yield surface and the material will behave elastically once again.

Yield surfaces are visualised on three axes of the principal effective (or total) stresses (σ'_1, σ'_2 and σ'_3). However, it is worth noting that to describe any point in that stress space, rather than use the three values of principal effective stresses, it is more useful to use alternative invariant quantities, which are combinations of the principal effective stresses. The reason for this is that an invariant has the same magnitude and direction no matter which directions are chosen for the coordinate axes. A convenient choice of these invariants, as used in soil mechanics, follows:

- Mean effective stress (p'): This is the average of the three principal effective stresses, which in physical terms represents the confinement of the soil. Changes in this stress cause volumetric strains.
- Deviatoric stress (q): This is the shear component of the stress remaining after subtracting p'. Changes in this stress cause deviatoric strains.
- Lode angle (θ): This is the angle between a chosen reference axis, and the line joining the space diagonal (the line corresponding to $\sigma'_1 = \sigma'_2 = \sigma'_3$) to the current stress state.

These three invariants create a separate polar coordinate system, the geometric significance of which can be interpreted from Figure 3.12. In defining a stress state, p' essentially represents a measure of the distance along the space diagonal, q represents a measure of the distance from the space diagonal to the current stress state along the deviatoric plane (the plane perpendicular to the space diagonal), and θ defines the direction of the current stress state.

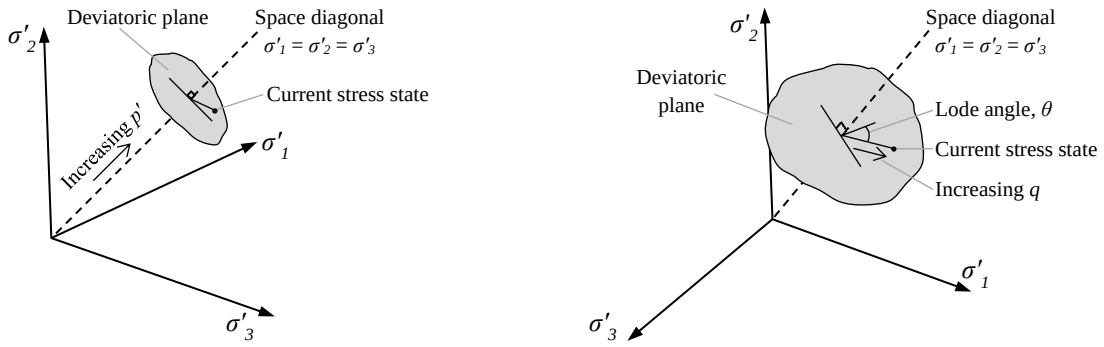

Figure 3.12: Principal effective stress space and the three stress invariants
Adapted from Lees (2016)

3.4.1.3 Plastic potential surface

At the onset of yielding, a flow rule is used to prescribe the mechanism of plastic straining of the material. In doing so, a plastic potential function (which can be plotted as a surface or series of surfaces in stress space) is introduced as a reference for defining the direction of plastic strain. In particular, an outward vector normal to the plastic potential surface, that passes through the current stress state, provides the relative (not absolute) magnitudes of the plastic strain increment components. Flow rules are important in constitutive modelling because they govern dilatancy effects, which in turn has a significant influence on volume changes and strength. Furthermore, in a multi-dimensional stress space, there are potentially six components of both stress and strain, and thus it is essential that a rule such as this exists to specify the ratio of each component at every stress state. With this, two types of flow rules apply:

- Associated flow: This is the case when the plastic potential surface is identical to the yield surface. The advantage of this is that it results in symmetric constitutive and global finite element stiffness matrices, which lowers the computational costs (Potts & Zdravkovic, 1999). However, Lade (2005) points out that frictional materials do not seem to fit well with the concept of an associated flow rule, as the prediction of volume dilation rates are much too high. This error is most pronounced for frictional materials with high effective friction angles, such as dense sand, while materials with less prominent frictional characteristics, such as clay, may be modelled with some approximation by associated flow rules.
- Non-associated flow: In this case the specified plastic potential surface is different from the yield surface. Although this adds complexity to the calculations, it is often a necessity for frictional materials such as soil and concrete to avoid the excessive dilation of associated flow rules. However, even though the dilation is less with a non-associated flow rule versus one that is associated, it is still able to continue indefinitely. Therefore, to keep it within realistic levels, it can be linked to plastic strain or a predefined cut-off can be specified.

3.4.1.4 Plastic hardening or softening rule

The hardening or softening rule specifies the change in size and position of the yield surface in stress space. If these rules are related to the magnitude of the accumulated plastic strains, the model is known as strain hardening/softening. Alternatively, but less commonly, if it is related to the magnitude of plastic work, the model is known as work hardening/softening. Furthermore, the mechanisms by which these rules can be specified are described below and illustrated in Figure 3.13:

- Perfectly plastic: The yield surface remains constant during yield (no hardening or softening).
- Isotropic hardening: The size of the yield surface increases but remains the same shape and centred about the same position.
- Kinematic hardening: The position of the yield surface is translated in stress space but does not change in size or shape. In general, both isotropic and kinematic hardening can be applied simultaneously.
- Isotropic softening: The size of the yield surface decreases during yield, for example due to dilation of a dense soil during shear.

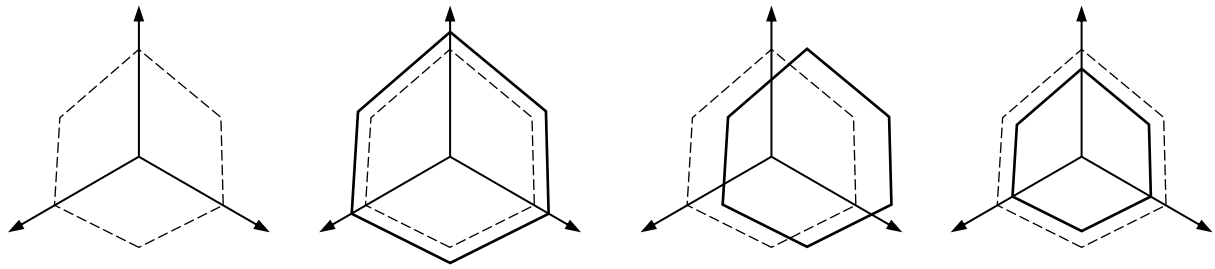

(a) Perfectly plastic (b) Isotropic hardening (c) Kinematic hardening (d) Isotropic softening

Figure 3.13: Hardening and softening mechanisms

3.4.1.5 Failure surface

The failure surface is a surface in stress space, which is generally fixed, that imposes some limit to the stresses that can be supported by the soil. That is, if the stress state coincides with this surface, the material is in a state of failure and the strains tend towards infinity. In the case of perfect plasticity, there is no hardening or softening and no change to the yield surface, and thus the failure surface is the same as the yield surface.

There are numerous failure surfaces that can be adopted in the constitutive modelling of geomaterials, the most prevalent of which are illustrated in Figure 3.14 and described below:

- Mohr-Coulomb: This is the most commonly used failure criterion in geotechnical engineering whereby the shear strength of soil is represented by the angle of internal friction (ϕ') and effective cohesion (c'). In principal stress space, the failure surface plots

as a hexagonal cone, with its six sides forming due to the six possible permutations of principal stresses. This failure criterion expresses the notion that the shear strength of soil increases with increasing normal effective stress applied on the potential shearing plane. This can be observed by the shape of the failure surface, whereby as p' increases and the stress state travels further up the space diagonal, the cross-sectional area of the surface increases, implying that a greater shear stress is required to reach a state of failure. A further consideration with regards to this failure surface is that it is not smooth, but rather possesses corners, which presents difficulties with its implementation into numerical modelling.

- Tresca: This failure surface has a hexagonal cross-section similar to that of the Mohr-Coulomb surface, however it plots as a prism in stress space rather than a cone. In fact, the Tresca failure criterion can be considered a particular case of the Mohr-Coulomb failure criterion, whereby if ϕ' is set to zero and c' to the undrained shear strength (c_u), the Mohr-Coulomb failure criterion becomes equivalent to that of Tresca. As such, the Tresca failure criterion is expressed in terms of total stresses and applies to undrained soil behaviour.
- Drucker-Prager: The Drucker-Prager criterion is an attempt to create a smooth approximation of the Mohr-Coulomb surface. It plots as a cylindrical cone in the space of principal stresses, with its axis coincident with the space diagonal. Although this provides the advantage of simplifying its mathematical formulation in numerical modelling, Davis and Selvadurai (2002) point out that it does not provide as accurate a representation of real soil response as the Mohr-Coulomb surface. Lees (2016) cautions that this is particularly the case for complex stress paths as it can lead to significant overestimations of shear strength, however it is capable of providing reasonably accurate failure predictions for simple stress paths.
- von Mises: The von Mises surface plots as a cylinder in stress space and provides a smooth approximation of the Tresca surface in the same manner that the Drucker-Prager surface does so for the Mohr-Coulomb surface. It thus also applies to undrained soil behaviour and is expressed in terms of total stresses. Like the Drucker-Prager surface, this simplified surface can significantly overestimate shear strength.

Although the hexagonal failure surface provides good predictions of failure for many stress paths, it does not perfectly match the results of experimental tests. To better fit observed data, other failure surfaces have been proposed whereby the similar shape of the hexagon is followed, but with rounded corners. Examples of these surfaces are that developed by Matsuoka and Nakai (1974) and Lade (1977), which are applicable for sands, and have been implemented into some constitutive models.

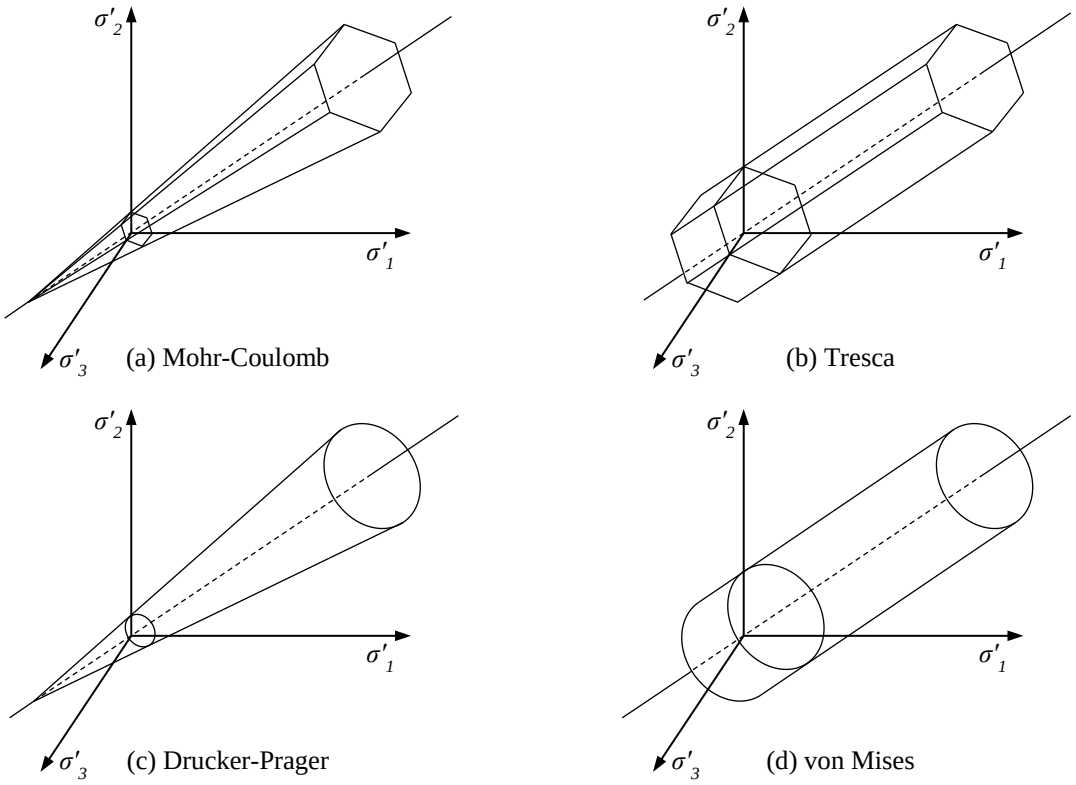

Figure 3.14: Common failure surfaces in principal stress space

3.4.2 Models for cyclic loading

Although simple elastoplastic models have proven to accurately and efficiently simulate the behaviour of soil under monotonic loading, the majority of these models are not able to describe the response of soil to cyclic loading. One of the underlying reasons for this is that these models do not include a mechanism of energy dissipation for stress cycles acting within the elastic regime. As mentioned previously, a conventional yield surface separates elastic behaviour from elastoplastic behaviour, and consequently only recoverable elastic straining occurs for stress paths remaining within the yield surface. Therefore, if the soil is unloaded and reloaded elastically for any number of cycles, in principle there will be no permanent strains developed. This is a deficiency of these models in the application of cyclic loading because it is known that real soil exhibits irreversible behaviour on unloading and reloading, and experimental research has demonstrated that this is the case even at very small strains.

The continued generation of plastic strain during stress-controlled cycling, and the accumulation of permanent pore water pressure in the case of undrained loading, are two of the principal features that distinguish cyclic behaviour from that exhibited during monotonic loading (O'Reilly & Brown, 1991). To account for the former in a finite element analysis, it is imperative that the response of the soil to stress reversals (unloading and reloading) is adequately modelled. An important aspect of this response is the variation in soil stiffness, an example of which is shown in Figure 3.15 for a sequence of stress reversals. From this figure, it is evident that the soil experiences a gradual reduction in stiffness during primary loading (0-A) as the magnitude

of shear strain progressively increases. This stiffness reduction is primarily due to slippage of intergranular contacts, which thereby removes their associated contributions from the elastic stiffness of the overall assembly. At the point of unloading (A-A') there is a dramatic increase in stiffness, followed by a subsequent decrease in stiffness as the soil is further unloaded (A'-B). The rate of change of stiffness in unloading is less than that of the primary loading curve because previously slipping contacts must first recoil elastically as they are unloaded (Vardanega & Bolton, 2013). Upon reloading (B-B'), the soil regains a stiffness in the order of its initial loading because previously slipping contacts re-engage (Vardanega & Bolton, 2013). If the reversed straining continues, elastic contacts will once again be lost, causing the stiffness to reduce as before, and so forth.

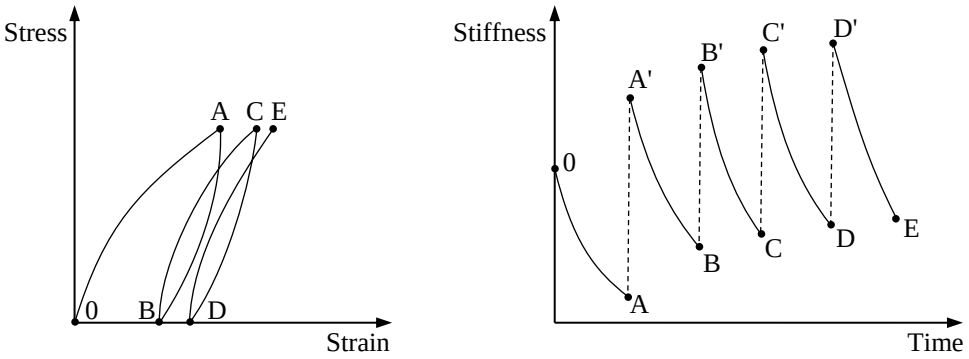

Figure 3.15: The effect of stress reversals on soil stiffness
Adapted from O'Reilly and Brown (1991)

There are several different plastic phenomena that can occur during cyclic loading, of which they can be based on either constant stress amplitude (stress-controlled) or constant strain amplitude (strain-controlled). Cambou and Hicher (2008) identified the various types of behaviour illustrated in Figure 3.16. Concerning constant stress amplitude loading, the so-called *adaption* phenomenon refers to a reduction in the energy dissipation of each cycle as the number of cycles increases, until eventual convergence to a non-dissipative elastic cycle is reached. *Accommodation* corresponds to cycles with energy dissipation and irreversible cumulative deformation, which progressively evolves towards a stabilised cycle with a hysteresis loop showing energy dissipation. Finally, *ratcheting* refers to cycles with irreversible strain accumulation, that keep the same shape. On the other hand, constant strain amplitude loading results in cyclic hardening or softening. The former occurs when there is an increase in the cyclic stress amplitude with increasing number of cycles, such as densification during testing of drained soil. On the contrary, the latter occurs when there is a reduction in cyclic stress amplitude as the number of cycles increases, such as due to the increase in pore pressure during the testing of undrained samples. Modelling these types of cyclic behaviour is not possible with a simple elastoplastic model, but requires one with added complexity that is capable of producing plastic deformations during the whole sequence of cycles.

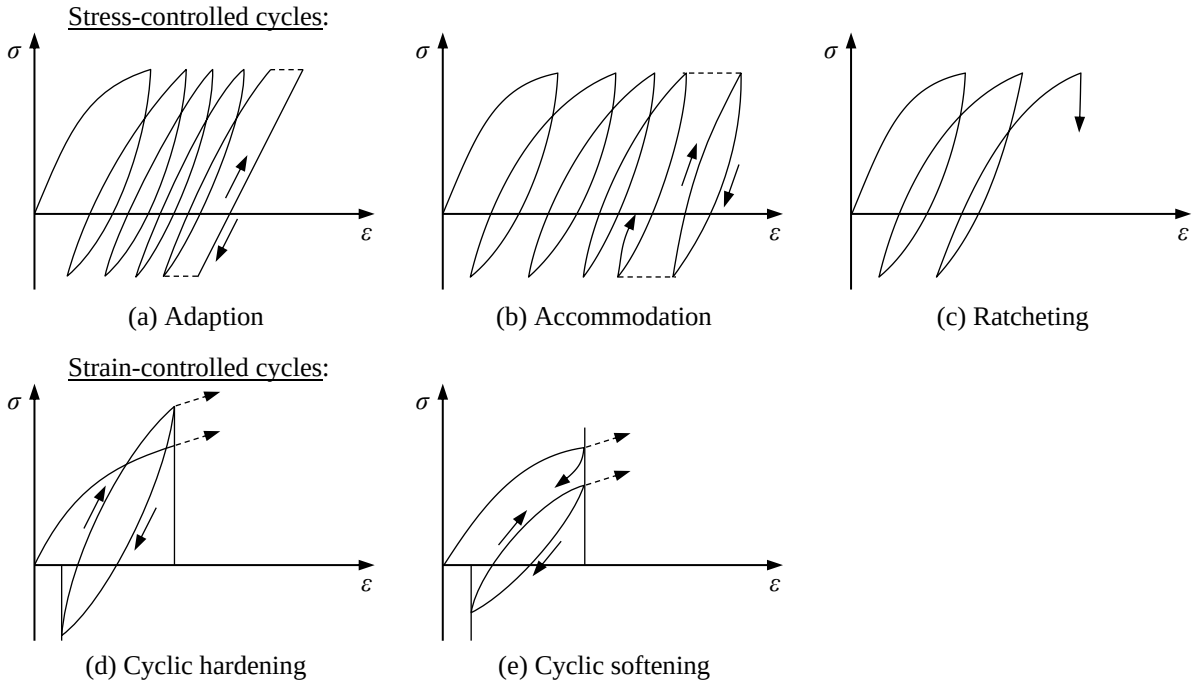

Figure 3.16: Types of cyclic behaviour
Adapted from Cambou and Hicher (2008)

With the previous discussion in mind, Kramer (1996) suggests that in general, soil models for cyclic loading can be categorised into three broad categories, namely (1) equivalent linear models; (2) cyclic nonlinear models; and (3) advanced constitutive models. Each of these types of models are subsequently discussed. However, it is worth noting that this discussion was limited to so-called *implicit* models, for which each cyclic loop is traced using small strain increments and the accumulation of strain results from the fact the loops are not perfectly closed. Such implicit numerical simulations are the conventional approach to modelling cyclic loading, however they are typically restricted to a limited number of cycles due to the accumulation of numerical errors and have a high computational cost. An alternative approach to modelling strain accumulation from cyclic loading is to use a model that applies an *explicit* formulation, otherwise referred to as a *high-cycle accumulation* model. These models, such as that proposed by Niemunis *et al.* (2005) for sand, predict the accumulation of strain due to a package of cycles at a time, without tracing the oscillating strain path during the individual cycles.

3.4.2.1 Equivalent linear models

Equivalent linear models can be used to provide an approximation of the actual nonlinear behaviour of soil. They do so by using an iterative procedure, whereby an initial estimate of the soil stiffness is made with a linear elastic model, from which the induced strains are calculated, and a new equivalent soil stiffness chosen for the next iteration, with the process repeated until finally strain-compatible soil properties are found. Although this approach is computationally efficient, the assumption of linearity embedded in its calculations has important implications when used to estimate ground response. In fact, it is only in the smallest amplitude cycles that

the unloading and reloading response of soil could plausibly be described as linear elastic. That is, if the induced shear strains are small enough such that they do not exceed the linear shear strain threshold shown in Figure 3.3, then the assumption of linear elasticity can suffice. This is because the modulus properties are expected to remain the same throughout the duration of cyclic stress application, and theoretically there is no dissipation of energy during each cycle.

3.4.2.2 Cyclic nonlinear models

The stress-strain response of soil becomes markedly nonlinear as the amplitude of shear strain increases, and therefore it becomes necessary to employ a cyclic nonlinear model that can follow the actual stress-strain path during cyclic loading. A variety of these types of models have been proposed, however they are all characterised by (1) a nonlinear backbone curve; and (2) a series of rules that govern behaviour in unloading and reloading, stiffness degradation, and so forth. The simplest of these models have relatively basic backbone curves and only a few straightforward rules, whereas more complex models may incorporate many additional rules to account for irregular loading, densification, pore pressure generation, and so on.

3.4.2.2.1 Backbone curve

As mentioned in §3.4.1.1, there are numerous functions that can be used to define the shape of a nonlinear backbone curve. Historically, two of the most commonly used functions for this purpose have been the hyperbolic and Ramberg-Osgood models. The former is expressed in its simplest form by Equation 3.10, and requires only two parameters to be defined, specifically G_0 and the reference shear strain (γ_r).

$$\frac{G}{G_0} = \frac{1}{1+\frac{\gamma}{\gamma_r}} \qquad \text{Eqn. 3.10}$$

The reference shear strain can be derived from a monotonic load test, as illustrated in Figure 3.17, and indicates a strain that would be attained at failure stress if the soil was to behave elastically. In terms of the modulus reduction curve, it corresponds to a normalised shear modulus value of 0.5. That is, if the induced shear strains were to equal the reference shear strain, the stiffness of the soil would reduce to half of its original value.

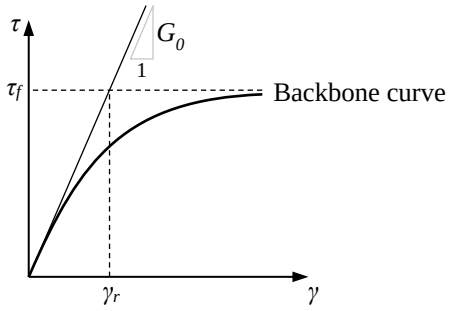

Figure 3.17: Definition of reference shear strain

In some cases, it is difficult to define the backbone curve and associated damping ratio by means of only two parameters. An alternative option is to use the Ramberg-Osgood model, which is characterised by four parameters. In addition to G_0 and γ_r, it includes two material parameters (α and r) which are adjusted to achieve a best fit of experimental data. This model is expressed in Equation 3.11 in its general form.

$$\frac{G}{G_0} = \frac{1}{1+\alpha\left[\frac{G}{G_0}\frac{\gamma}{\gamma_r}\right]^{r-1}} \qquad \text{Eqn. 3.11}$$

3.4.2.2.2 Unloading and reloading rules

To allow the aforementioned models to simulate cyclic loading, they are extended by defining a set of rules for unloading and reloading. The conventional approach to doing so is to apply the four so-called *extended Masing rules*, listed below. The first two are the original rules and are sufficient to describe regular cyclic loading with constant amplitude only, whereas the latter two rules were proposed as an extension (e.g. Pyke, 1979) in order for them to cover cyclic loading in general:

1. The shear tangent modulus at each loading reversal assumes a value equal to the initial tangent modulus of the backbone curve, G_0.
2. The shape of the unloading or reloading curve is the same as that of the backbone curve (with the origin shifted to the load reversal point), except that the scale is enlarged by a factor of two.
3. If an unloading or reloading curve exceeds the maximum past strain and crosses the backbone curve, further unloading or reloading continues along the backbone curve until the next stress reversal.
4. If an unloading or reloading curve intersects an unloading or reloading curve from a previous cycle, it will follow the curve of the previous cycle.

To illustrate how these rules are implemented, the example shown in Figure 3.18 is considered, as described by Kramer (1996). The cyclic loading begins at point A and the stress-strain curve during initial loading (A-B) follows the backbone curve. At point B, the loading is reversed and the initial unloading modulus is equal to G_0 as required by rule 1. The shape of the unloading portion of the curve, as it moves away from point B, follows along the path stipulated by rule 2. The unloading path intersects the backbone curve at point C, and according to rule 3, continues along the backbone curve until the next loading reversal at point D. The reloading curve then moves away from point D as required by rule 2, and the process is repeated for the remainder of the applied loading.

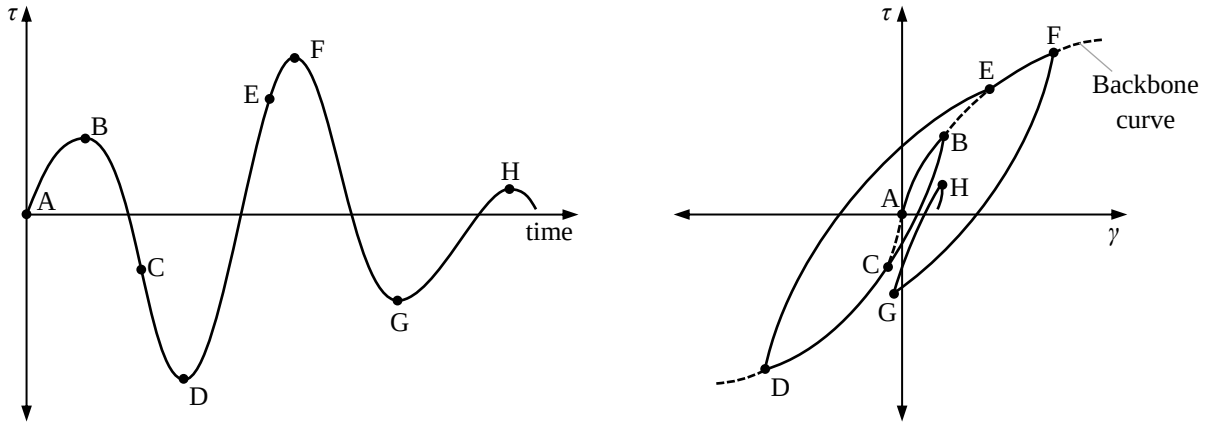

(a) Variation of shear stress with time (b) Resulting stress-strain behaviour

Figure 3.18: Application of extended Masing rules

Adapted from Kramer (1996)

These rules readily introduce hysteresis into the cyclic response of the soil, however they do not allow the ratcheting phenomenon to be modelled. This is because they result in hysteresis loops that remain constant with successive cycles of the same amplitude. One way to overcome this is to modify the second rule such that the scaling factors for unloading and reloading are different, and thus deviate from a value of two. The actual scaling factor to be used can be determined experimentally but usually varies between a value of one and two (Cambou & Hicher, 2008).

3.4.2.2.3 Stiffness degradation rule

Once the amplitude of the cyclic shear strain in an undrained soil body exceeds the degradation threshold, it will degrade with increasing cycles. To account for this cyclic degradation, Idriss *et al.* (1978) proposed that the degraded backbone curves for cohesive soils can be formed by multiplying the ordinates of the initial backbone curve by a scaling factor called the degradation index. This index, denoted δ, was previously introduced in §3.3.1.3 where it was shown that it decreases as the number of cycles increases. That is, in the first cycle $\delta = 1$, but during further cyclic loading $\delta < 1$.

To incorporate the effects of cyclic degradation into a constitutive model using this concept, Vucetic (1990) proposed modifications to the four Masing rules, and added a fifth rule. Of particular importance to cyclic loading involving a constant amplitude was the changes to the first two rules, specified below:

1. The shear tangent modulus at each loading reversal assumes a value equal to the initial tangent modulus of the backbone curve, but reduced by the corresponding degradation index, δ.
2. The shape of the unloading or reloading curve is the same as the backbone curve reduced by the corresponding degradation index, δ, (with the origin shifted to the load reversal point) except that the scale is enlarged by a factor of two.

In other words, the model for cyclic degradation proposed by Idriss *et al.* (1978) suggests that the first two Masing rules – which were originally developed for nondegrading materials – can be used when there is degradation, provided that a degraded backbone curve is used instead of the initial backbone curve. The degraded backbone curve is simply a scaled down version of the initial backbone curve as shown in Figure 4.3, from which the associated pairs of degraded reloading and unloading curves can be defined.

3.4.2.3 Advanced constitutive models

Advanced constitutive models allow considerable flexibility and generality in modelling the response of soils to cyclic loading, and are capable of reproducing a number of facets of real soil behaviour. However, with this there is an increase in the degree of difficulty and complexity involved in their theoretical formulation, and they are also usually too elaborate and sophisticated to be implemented in general engineering practice as they require specialist knowledge and expertise. Moreover, they typically require the calibration of numerous parameters, which entail extensive soil testing and thus add significant costs to the geotechnical investigation.

Various advanced constitutive models for cyclic loading have been developed in recent decades, such as those involving kinematic hardening, multiple yield surfaces, bounding surface theory, so-called *bubble* models, and so on. Although detailed descriptions of these advanced models are beyond the scope of this text, as a demonstration the concept of a bounding surface will be subsequently overviewed.

Bounding surface plasticity models are an extension of conventional elastoplastic models with the ability to generate a hysteretic response on cycles of unloading and reloading, as well as smooth out the changes in stiffness associated with an assumed yield point (Wood, 1991). In such models, no yield surface is assumed to exist, however a bounding surface is introduced which has similar characteristics. On one hand, the bounding surface represents full plastic flow in the same way as a conventional yield surface. This means that for stress states lying on the bounding surface, such as point C in Figure 3.19, plastic strains develop as per classical plasticity theory. If the soil is loaded further, the stress state remains on the bounding surface and the

plastic straining is controlled by a combination of the bounding surface acting as a conventional yield surface, the plastic potential, the hardening or softening rule and the elastic parameters.

However, on the other hand, a bounding surface differs from a conventional yield surface in that plastic straining can occur within it for certain stress trajectories. If the stress path corresponds to unloading, in which the stress state of the soil element moves from the bounding surface inwards, elastic behaviour occurs as per convention. However, if the stress state of the soil element lies within the bounding surface, due to a previous loading history followed by unloading, then the behaviour on subsequent loading departs from conventional plasticity theory. Specifically, rather than exhibiting elastic behaviour on reloading, in the bounding surface framework plastic deformations develop.

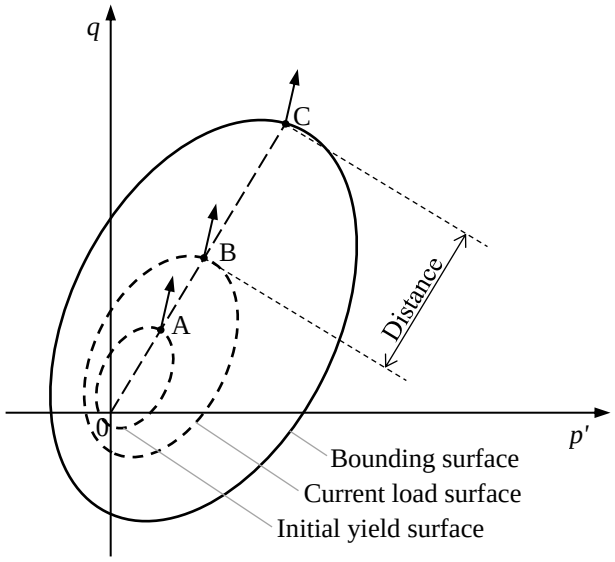

Figure 3.19: Bounding surface model

To illustrate this, consider the situation in which a soil sample has been subjected to loading and unloading such that the current stress state corresponds to point A in Figure 3.19. If the soil is subsequently reloaded, then the response will be plastic as per the discussion above. Point A can thus be defined as the most recent *initial yield point*. With this, an *initial yield surface* is implicitly established, which has the same shape as the bounding surface but scaled down to pass through the current stress state, as illustrated in Figure 3.19. Note that this surface is referred to as a yield surface because it defines the limit of the elastic domain, however strictly speaking it is not actually a yield surface because the stress point may first move elastically inwards and then cause plastic loading before it reaches the surface again. Nonetheless, the initial yield surface is used to distinguish between loading and unloading when the soil element is strained from point A. If loading occurs, such as from point A to point B in Figure 3.19, then a new surface called the *current load surface* is defined, which is also homothetic to the bounding surface, but passes through point B. To quantify the plastic strains that occur due to this loading, a so-called *mapping* rule is required, which is defined in the constitutive relations.

Several mapping rules have been proposed in the literature, however the simple *radial* rule is often employed as it has been shown to be appropriate in many cases (Potts & Zdravkovic, 1999). This rule involves determining the proximity of the current stress state to an image point on the bounding surface. With reference to Figure 3.19, a radial line is constructed that passes from the origin and through the current stress point (point B) until it intersects the bounding surface at the position defined as the image point (point C). The plastic component of strain occurring at the stress state is then related to the plastic component of strain that would occur at the image point in an elastoplastic model, but modified by an amount that depends on the distance between the stress state and the image stress. This ensures a predominantly elastic response when the current stress state is far away from the bounding surface, with plastic strains varying from zero at the origin to full plastic flow at the bounding surface.

Ultimately, the essence of the bounding surface concept is that plastic deformations can occur for stress states lying within it, and this occurs at a progressive rate that depends on the proximity of the stress state to the bounding surface. Thus, unlike classic elastoplastic models, plastic states are not restricted to only those lying on a yield surface. Additionally, the sudden change in behaviour associated with the yield surface is diminished. This provides an improvement in capturing the behaviour of real soil subjected to cyclic loading, however its inability to reproduce plastic strains during unloading is a shortcoming in this regard. This has been addressed with several other concepts, such as bubble models where a small kinematic yield surface, called the bubble, is introduced into the bounding surface. This inner bubble defines the stress states corresponding to true elastic behaviour, whereas stress states outside of this zone behave elastoplastically.

Chapter 4
NUMERICAL MODEL DEVELOPMENT

4.1 Introduction

This chapter details the development of the numerical model used to investigate the objectives of this research, which involved evaluating the effect of cyclic soil degradation on the design of onshore wind turbine gravity foundations. For the purposes of this investigation, a case study of a wind farm in the Western Cape, South Africa, was considered. Three separate ground profiles from this wind farm were modelled, each of which was recognised as being susceptible to cyclic soil degradation, based on the PI of the soils and the G_0 stiffness profile from the CSW tests. The effect of the degradation was quantified by evaluating its depth of influence below the foundation, and applying a reduction factor to the ground modulus within this depth in the foundation design, so as to account for the potential decrease in soil stiffness in the future. Accordingly, the main aim of the numerical model was to predict the depth below the foundation to which the stiffness degradation was significant. Acknowledging this aim prior to developing the numerical model was important, as every decision made during the design of the model required consideration of its effect on the key outputs. Finally, a parametric study was conducted to evaluate the dependency of cyclic degradation on various input parameters.

The numerical modelling was undertaken through the development of three-dimensional (3D) finite element (FE) models. The software package selected for doing so was *RS*^{3} (version 2.010), which is a general-purpose finite element analysis program developed by software company *Rocscience Inc*. As this program was intended specifically for civil and geotechnical engineering applications involving both soil and rock, and offered considerable flexibility in numerous modelling aspects, it was suitable for this study.

This chapter begins with an overview of the modelling approach, after which the constitutive model used to describe the material behaviour in the model is defined. The wind farm site adopted for the case study is then characterised, followed by details of the wind turbine model used in the analysis and its design loads. Several general model characteristics are subsequently discussed, after which details of the parametric study are provided.

4.2 Modelling Approach

The approach to modelling the cyclic degradation was of fundamental importance to this study. However, prior to establishing the methodology for doing so, it was imperative to first consider what type of analysis needed to be undertaken. This included assessing whether a quasi-static or dynamic FE analysis was required, as well as whether long-term drained or short-term undrained conditions were applicable.

4.2.1 Quasi-static versus dynamic analysis

In FE modelling of cyclic loading, a distinction can be made between quasi-static and dynamic analyses. Although cyclic loading is time-dependent, the former does not take this time-dependency into account, and essentially comprises a repetition of the static load because the frequency of the loading is sufficiently low such that inertia effects do not need to be considered. Conversely, the latter does consider the time-dependence of the load, including the inertia of the subsoil and damping. With this, it was identified in §2.4.2 that the three main sources of cyclic loading for an onshore wind turbine are the wind and its turbulence, the rotation of the rotor system (1*P*), and blade shadowing effects (3*P*), indicated in Figure 4.1(a). It was further discussed that cyclic wind loads can be considered quasi-static due to their low frequencies, whereas the 1*P* and 3*P* loads with considerably higher frequencies are likely to act dynamically. Under these assumptions, Nikitas *et al.* (2016) state that the soil-structure interaction associated with cyclic loading of wind turbine foundations can be simplified into two superimposed cases:

i) Soil behaviour due to non-dynamic cyclic loading. This is the fatigue type of problem illustrated in Figure 4.1(b), and is mainly attributed to large amplitude, low frequency wind loading.

ii) Soil behaviour due to dynamic loading, which causes dynamic amplification of the foundation response. This is the resonance type of problem shown in Figure 4.1(c), and is primarily a consequence of the 1*P* and 3*P* loading.

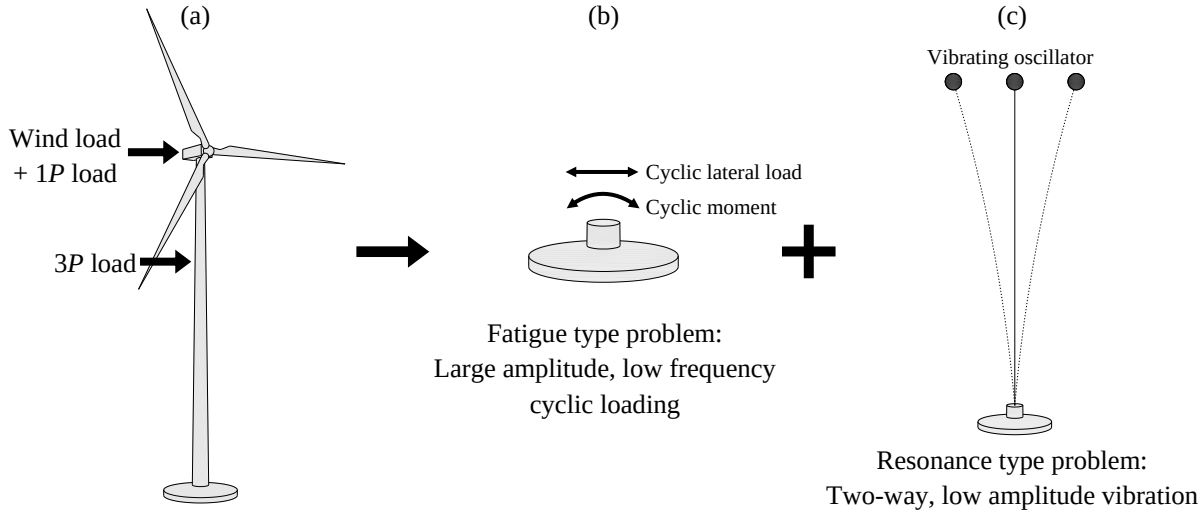

Figure 4.1: Two of the soil-structure interaction problems for onshore wind turbines
Adapted from Nikitas *et al.* (2016)

To model the soil-structure interaction, Nikitas *et al.* (2016) suggest that either the fatigue type problem can be modelled independently, or a combination of the fatigue type and resonance type problems can be modelled concurrently. As this research focussed on the change in stiffness of the foundation soil over time, the extent of which is highly dependent on the magnitude of the induced shear strains, only the fatigue type problem was investigated in this study. This is because, even though the 1*P* and 3*P* loads have the highest dynamic amplifications, their load amplitudes are orders of magnitude lower than that from the wind, such that the shear strains induced from them are likely to remain closer to the linear elastic range of the soil.

Furthermore, cyclic overturning moments from wind have a typical frequency in the order of 0.01 Hz (Lopez-Querol *et al.*, 2017). Priest (2012) suggests that the transition from quasi-static to dynamic loading occurs when the load is applied at frequencies greater than around 1 Hz, whereas Wichtmann and Triantafyllidis (2012) propose that this transitional frequency is in the order of 5 Hz. In either case, the frequency of the large amplitude wind loading was deemed to be sufficiently below these transitional frequencies such that the inertia effects in the soil domain would be negligible. Consequently, a dynamic analysis was not undertaken in this study, but rather a quasi-static numerical model was developed.

4.2.2 Long-term versus short-term conditions

An important aspect of the FE model was the modelling of groundwater and drainage conditions of the soil. In this regard, it must be acknowledged that because one of the mechanisms for cyclic degradation is the accumulation of excess pore water pressure with increasing number of loading cycles, it is primarily associated with fully saturated soil conditions. It must further be recognised that in terms of soil behaviour, cyclic loading can be categorised into short-term or long-term loading. During long-term cyclic loading, the pore pressure generated by cyclic loading dissipates and drained soil behaviour may be assumed. Conversely, short-term cyclic loading leads to undissipated pore pressures which decrease the effective stresses in the soil and thus result in stiffness degradation. It therefore follows that all fine-grained soils in this study were modelled with undrained behaviour, a situation which may arise for onshore wind turbines during storm conditions. Although it is inevitable that drainage will occur, and the excess pore pressures eventually reduce, there can nonetheless be long-term implications, such that the changes to the microstructure and stiffness of the soil are irreversible. However, the occurrence of this is dependent on whether the shear strain thresholds shown in Figure 3.3 are exceeded, as previously discussed in §3.3.1.

4.2.3 Modelling methodology

Cyclic degradation occurs when fully saturated soil is subjected in undrained conditions to cyclic loading at a shear strain amplitude that exceeds the degradation threshold (Tabata & Vucetic, 2010). Therefore, in order to study the changes in soil stiffness due to cyclic strains, the developing strain in the soil around the shear zone needed to be taken into consideration. With this understanding, the methodology for modelling the cyclic degradation is outlined below, with

corresponding illustrations of each step shown in Figure 4.2. The constitutive model applied in this approach incorporated nonlinear elasticity in conjunction with the cyclic degradation model originally proposed by Idriss *et al.* (1978), however further details of this are discussed in §4.3.

i) A 3D model of the soil profile was created based on site investigation data, and the circular wind turbine foundation generated using appropriate dimensions.

ii) For each soil type, the nonlinear constitutive model described in §4.3 was implemented, and appropriate material parameters selected. Bedrock was modelled as linear elastic.

iii) A load case representative of an SLS design storm was applied to the foundation. The model was subsequently computed and the distribution of shear strains in the soil examined in the model output.

iv) An *isosurface*, which is a surface in 3D space representing points of equal value (analogous to a contour line on a map), was plotted in the output of RS^3 based on the value of the degradation shear strain threshold γ_{td}. In this way, it could be readily observed where the soil had exceeded this threshold, that is, where the degradation was deemed to occur. The primary purpose of this was to identify the maximum depth below founding level that γ_{td} had reached.

v) The first stiffness iteration of the FE model was undertaken, in which the stiffness of the soil was degraded up to a depth equal to a third of the maximum depth of the γ_{td} isosurface determined from Step iv). The reasons for selecting this depth, rather than the full depth of the isosurface for instance, were twofold. The first was that, due to the foundation loading being dominated by the overturning moment, the shear strains were primarily concentrated on one side of the foundation soil, and thus were not spread evenly below the foundation. Consequently, applying the stiffness reduction to a third of the maximum depth was deemed to be representative of the average depth to which the degradation would occur. The second reason was that cyclic degradation occurs incrementally, with the soil closer to the foundation-soil interface degrading at a faster rate than that below, due to the magnitude of the induced strains being larger. Accordingly, superior accuracy of the final solution was achieved by applying smaller increments of depth for the stiffness iteration.

   The actual stiffness reduction was effected by defining a new horizontal soil layer directly below founding level, with a thickness according to the above discussion. The soil within this new layer was defined as a new material, and the stiffness of it degraded relative to the original material. This was implemented by reducing the initial shear modulus, G_0, to the shear modulus after N cycles, G_N, using the equation $G_N = G_0\delta = G_0N^{-t}$, which is based on the concept proposed by Idriss *et al.* (1978). Regarding this equation, it was pointed out by Dobry and Vucetic (1987) that the extent of stiffness reduction does not depend on the exact combination of the number of loading cycles N and degradation parameter t, but only on the final value of the degradation index δ achieved. Therefore, considering that δ begins at unity in the first loading cycle and decreases progressively, it was not calculated using N and t (particularly because of the uncertainties in these parameters), but it was rather assumed to decrease in increments of 5% ($\Delta\delta = 0.05$). That is, in this first stiffness iteration, the degradation index corresponded to $\delta = 1 - 0.05 = 0.95$ for the degraded soil.

vi) The model was computed again and the new shear strains examined. As before, the value of γ_{td} was plotted as an isosurface and the new maximum depth of this surface determined.

vii) Another stiffness iteration was undertaken, in which the soil stiffness was further degraded. This was carried out by creating another soil layer directly below the layer previously created. The thickness of this new layer was equal to half of the distance between the bottom of the layer above and the maximum depth of the new γ_{td} isosurface. The stiffness within both layers was then degraded using the same principles as before, with the exception that for the first layer from Step v), δ was decreased again by $\Delta\delta = 0.05$ (from 0.95 to 0.9), and within the second (most recent) layer, δ was 0.95.

viii) Steps vi) and vii) were repeated, each time decreasing the value of δ by $\Delta\delta = 0.05$ within the layers and examining the new γ_{td} isosurface. For instance, after the third iteration, the uppermost layer had $\delta = 0.85$, the second $\delta = 0.9$, and the third (most recent) $\delta = 0.95$.

ix) Step viii) was continued until the value of δ in the uppermost layer reached 0.6, as this was deemed to be representative of the amount of degradation that would likely occur below the foundation, for reasons discussed in §5.2.2. The maximum depth of the γ_{td} isosurface in this final iteration was defined as the depth of influence of the cyclic degradation.

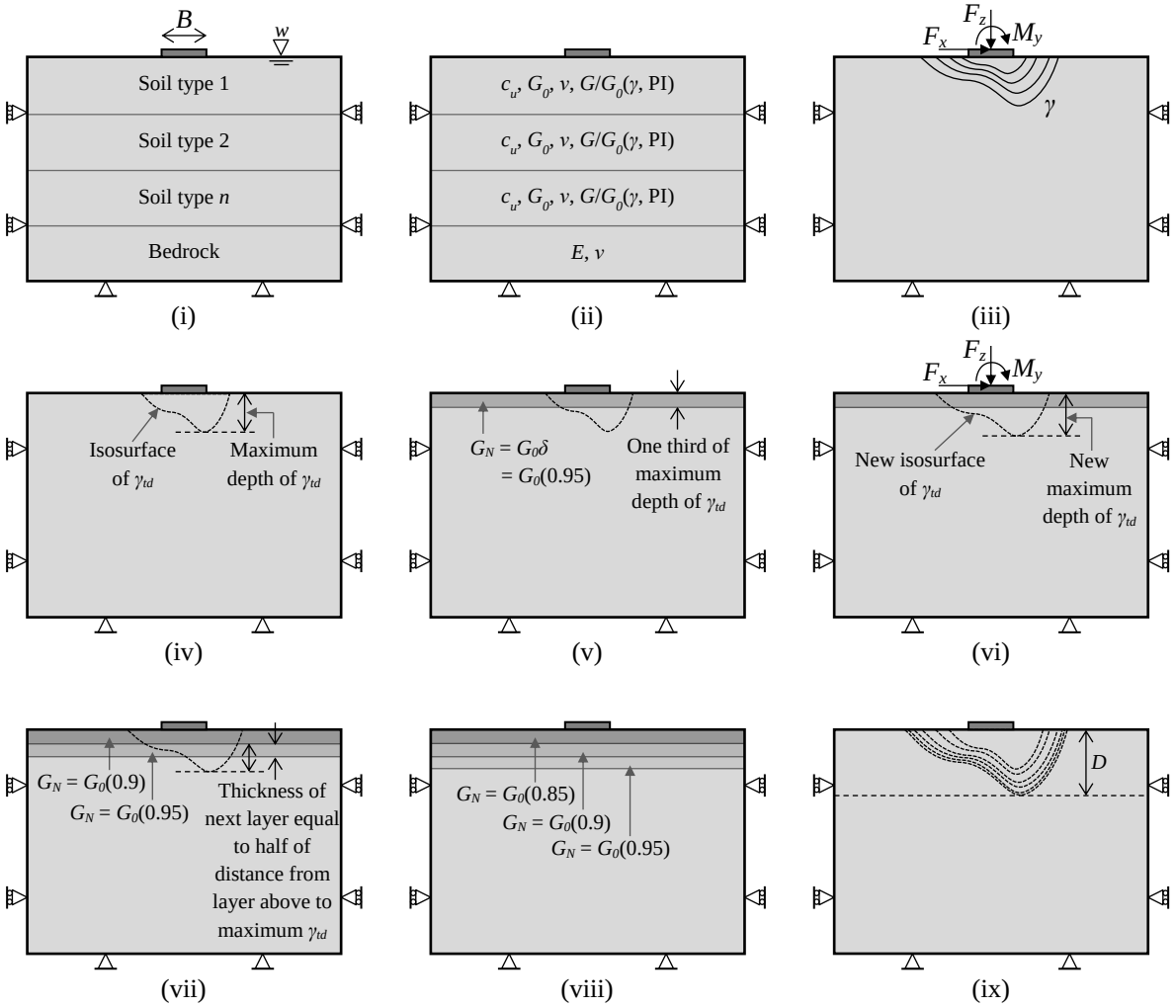

Figure 4.2: Modelling methodology

Several aspects of this modelling methodology required further explanation and justification:

- Although the actual loading of the wind turbine foundation was cyclical in nature, the loading was applied statically in the numerical model. In this regard, it must be acknowledged that each time the static loading was applied and shear strains induced in the soil, it was assumed that repeated applications of that same loading (with the load returning to zero after each) would induce the same shear strains repeatedly for a certain number of loading cycles. In this way, each application of the static loading was representative of numerous loading cycles, despite it only being applied once. This was also the reason behind G_0 being degraded by relatively small increments at a time.
- The methodology was based on the assumption that the soil below the foundation would degrade uniformly within the horizontal plane. This was due to the implemented approach of only degrading the soil stiffness within the full extent of the new horizontal layers of soil that were added below the foundation-soil interface. It thus did not account for the possibility of the soil only degrading, or degrading at a faster rate, on the leeward side of the foundation. However, the assumption was justified for this study on the basis that the wind turbine can receive wind from any direction, and consequently the degradation would conceivably even out beneath the entire foundation area over time.
- The modelling approach only partially accounted for the fact that degradation occurs at different rates for different volumes of soil depending on the magnitude of the shear strains. Theoretically, the degradation parameter t (which defines the rate of cyclic degradation) is dependent on the level of shear strain, as shown in Figure 3.7, and the value of γ_{td} corresponds to the point at which t becomes zero. Thus, the soil will not degrade uniformly within the full extent of the γ_{td} isosurface, but will degrade at a higher rate where the strains are the largest, which is closer to the foundation-soil interface. This was partially accounted for by only degrading the soil stiffness up to a fraction of the maximum depth of the γ_{td} isosurface at a time, and degrading the upper layers by greater amounts than those below.
- The FE model did not explicitly evaluate the continuous generation of excess pore pressure that occurs concurrently with cyclic degradation as the number of loading cycles increase. According to Matasovic and Vucetic (1995), this is an adequate approach when the cyclic pore water pressures are not considered an important design component, as a reasonably good response of the soil behaviour can be predicted by focussing solely on the level of cyclic degradation while ignoring the cyclic pore water pressure generation. This can also be inferred from Figure 3.3, where it is shown that the cyclic shear strain can be related to degradation without necessarily focussing on pore water generation. Accordingly, the pore pressure generation was only implicitly accounted for through the modelling strategy of decreasing the soil stiffness in geometric volumes that exceeded γ_{td}, as this threshold is also associated with the generation of permanent pore pressure, as indicated in Figure 3.3. Furthermore, the effect of OCR on pore pressure generation was not considered. This aspect makes modelling the generation of cyclic pore pressure in clay somewhat difficult, because although the pore pressure generated in normally consolidated clays is always positive, it may be negative for overconsolidated clays (Matasovic & Vucetic, 1992).

4.3 Constitutive Model

The accuracy of an FE analysis is heavily dependent on the constitutive model adopted for each material. However, it is important to recognise that all constitutive models are an approximation of real material behaviour, and no model exists that can recreate all aspects of this behaviour. It is therefore imperative that the constitutive model is tailored to the particular problem of interest and the required accuracy of solution. In this way, it should aim to reproduce the vital aspects of the response of the soil while ignoring other features which are deemed to be less important. The choice of aspects which are deemed to be vital depends on the required outputs of the model, and consequently the same soil can be modelled in different ways depending on the application.

As this study was concerned with the degradation of soil stiffness due to cyclic loading, the extent of which is largely controlled by the magnitude of the shear strains induced in the soil, accurately capturing the nonlinearity of the stress-strain response was identified to be critical for the analysis. This was to ensure that the full range of stresses from low, near-surface stresses to high stresses under the loaded foundation could be accounted for adequately. Considering the importance of the nonlinearity, the stiffness of the soil was modelled using a modified hyperbolic function in *RS*^{3}, which had the form shown in Equation 4.1. This function was used to fit a modulus reduction curve from the literature for each soil, based on its classification.

$$\frac{G}{G_0} = \left(1 + a\frac{\gamma}{\gamma_r}\right)^b \qquad \text{Eqn. 4.1}$$

Where G = shear modulus (Pa); G_0 = initial shear modulus (Pa); γ = shear strain (unitless); γ_r = reference shear strain (unitless); and a, b = modified hyperbola material parameters.

Note that the modulus reduction curves adopted in this analysis did not account for the influence of confining pressure. This aspect of soil stress-strain behaviour was previously discussed in §3.3.1.2, where it was demonstrated that the mean effective confining pressure has a marked effect on the shape of the modulus reduction curves, specifically for soil with low plasticity. Furthermore, the constitutive model did not include an expression relating the magnitude of G_0 to confining stress.

The strength of the soil also required characterisation in the constitutive model. However, it must be emphasised that the present study was predominantly concerned with the stiffness of the soil, and although there may have been plastic deformations occurring, it was not anticipated that there would be significant regions of failure. Nonetheless, the stiffness function described above was coupled with the Mohr-Coulomb failure criterion, which under undrained conditions became equivalent to the Tresca failure criterion. Further, it was important to exclude a hardening mechanism upon yielding, as this behaviour was not applicable to the fine-grained soils that formed the basis of this study. Finally, no dilation angle was specified for the fine-grained materials, which was representative of a non-associated flow rule.

The final aspect of the constitutive model was the definition of the stiffness degradation rule. The addition of this rule made the constitutive model analogous to the cyclic nonlinear models described in §3.4.2.2, however the rule was not explicitly defined in the underlying mathematical framework, but rather applied through 'manual' iterations as evident from the modelling methodology. As mentioned previously, the degradation model proposed by Idriss *et al.* (1978) was adopted. This degradation model was implemented in conjunction with the modified Masing rules described in §3.4.2.2.3, albeit implicitly, which include (1) reducing the shear tangent modulus on each loading reversal by the degradation index δ, and (2) keeping the same shape of the backbone curve for the unloading or reloading curves but reducing it by the degradation index, δ. Through multiplying G_0 by δ as described in the modelling strategy, both rules were satisfied. Accordingly, the degradation of soil stiffness was reflected in the change in shape of the backbone curve, as indicated in Figure 4.3.

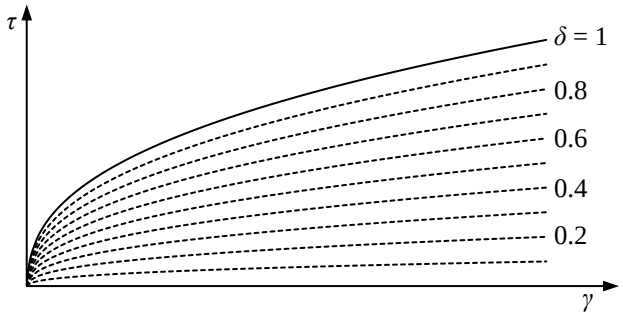

Figure 4.3: Degraded backbone curves

Considerations were also required for modelling the rock and concrete. In this regard, it was recognised that these materials are very stiff compared to soil, and thus it was deemed sufficient to model their stiffness with linear elasticity. Further, plastic behaviour was not included for either of these materials, as it was not considered necessary for the present analysis.

4.4 Site Characterisation

The wind farm used as the case study in this investigation was located near Vredenburg in the Western Cape, South Africa. It covered an area of approximately 2000 ha, and consisted of undulating topography with shallow to moderately steep side slopes and crests. Due to the large site footprint and variable topographical conditions, an extensive geotechnical investigation was undertaken by the project consultants, comprising in-situ soil exploration methods and laboratory testing. The relevant information from this geotechnical investigation, such as the borehole logs, CSW test results, laboratory test results and so forth, was obtained from the project consultants and not measured during the course of this study. The site's ground conditions are subsequently described, including the geology, groundwater conditions, the three soil profiles selected for modelling, and the respective material properties. However, prior to doing so, the wind climate for the site was analysed as this provided insight into the wind turbine loading regimes.

4.4.1 Wind climate

Wind data for the site was obtained from the WASA project. Phase one of this project involved erecting ten wind masts around the Western, Northern and Eastern Cape, from which wind speeds were recorded in 10-minute intervals using cup anemometers at heights of 10, 20, 40, 60 and 62 m above ground level (AGL). One of these masts was located in Vredenburg in close proximity to the wind farm, from which approximately three years of data (June 2010 to May 2013) was logged, and made freely available in the public domain. Figure 4.4 provides a summary of some of the pertinent wind data from this period for an extrapolated height of 100 m AGL. The wind rose in Figure 4.4(a) shows the relative frequencies of wind direction, and indicates that the region is dominated by wind originating from the south. Figure 4.4(b) and (c) are Weibull distributions showing the variation of wind speed at 100 m AGL for the three-year period, with the former corresponding to all directions, and the latter only to the dominant wind direction in the wind rose. As indicated in these diagrams, the observed mean wind speed at the mast location was 7.50 m/s in all directions, and 9.09 m/s in the dominant direction.

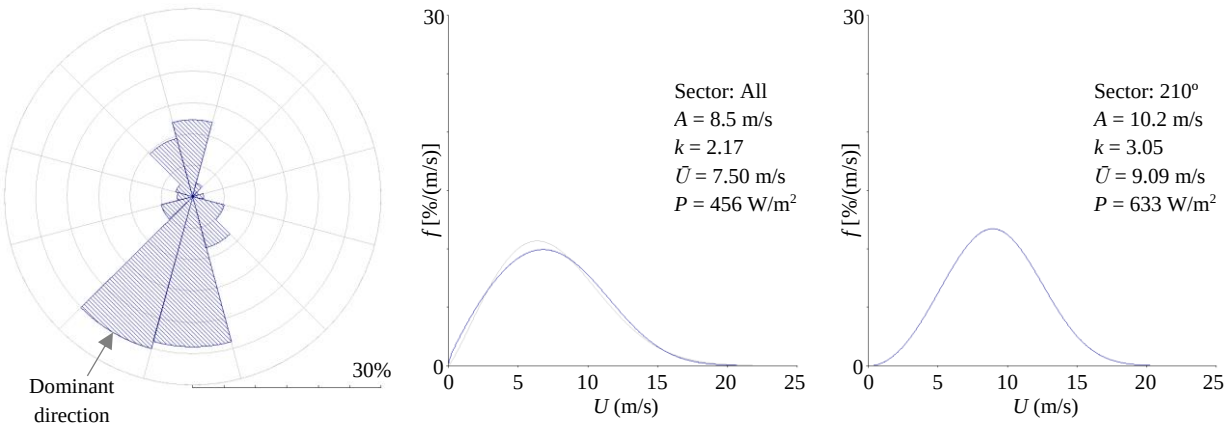

(a) Wind rose (b) Wind speed, all directions (c) Wind speed, dominant direction

Figure 4.4: Wind rose and wind speed distribution for Vredenburg mast at 100 m AGL
Data sourced from WASA (2013) for 3-year period from June 2010 to May 2013 (R-class 1)

Although the wind data recorded at the Vredenburg mast was deemed to be reasonably representative of the wind climate at the wind farm due to its close proximity, numerical analyses undertaken as part of the WASA project were able to provide more accurate data at the exact location of the site. Specifically, a verified numerical wind atlas of the WASA domain was developed, from which datasets for tens of thousands of model grid points within the domain were made available. These grid points are spaced 3 km apart and essentially represent virtual wind masts, two of which fell within the boundary of the wind farm. The wind data shown in Figure 4.5 was extracted from these two grid point locations based on the guide provided by Mabille (2014). From the wind roses in this figure, it was evident that the site was dominated by southerly wind. Moreover, the mean wind speeds in this dominant direction were determined from the Weibull distributions to be 11.39 and 11.63 m/s at each respective location.

Note that the software package WAsP (version 11.06.0012) was used to extract the data provided by the WASA project. Furthermore, in doing so, the roughness length of the terrain was assumed to be 0.03 m (R-class 1), which corresponds to the landscape category of *farmland with very few buildings and trees* (Mabille, 2014).

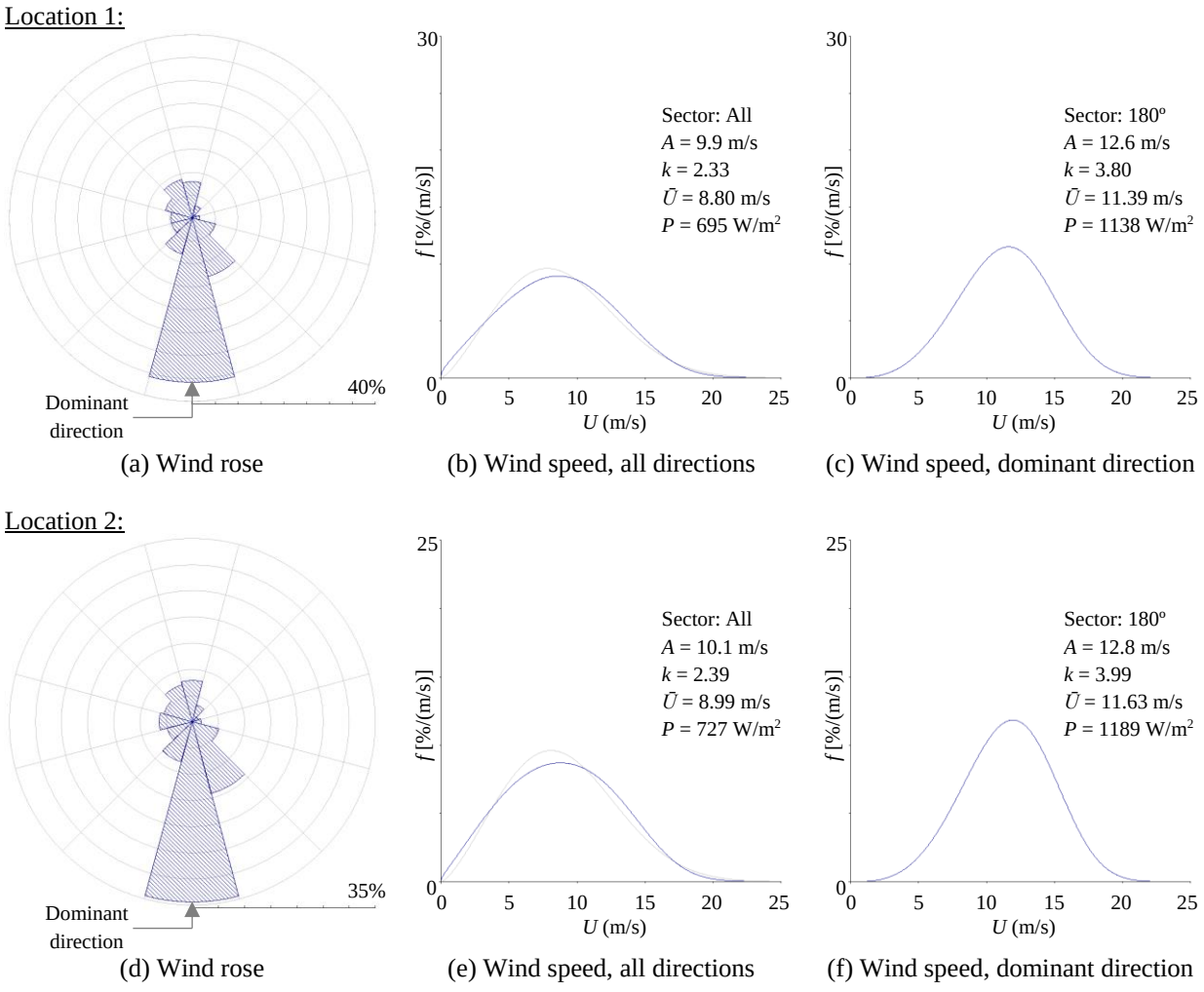

(a) Wind rose (b) Wind speed, all directions (c) Wind speed, dominant direction

(d) Wind rose (e) Wind speed, all directions (f) Wind speed, dominant direction

Figure 4.5: Wind rose and wind speed distribution within wind farm at 100 m AGL

Data sourced from WASA (2014) (R-class 1)

4.4.2 Site geology

The site is underlain by granite bedrock of the Saldanha-Langebaan Pluton, which forms part of the Cape Granite Suite. As observed by the project consultants, the upper surface of this bedrock is highly irregular, varying in depth from 0.5 m to greater than 31.5 m below ground level from the boreholes drilled on site. Overlying the bedrock are residual granite soils generally comprising a combination of silt, gravel, sand and clay, which in turn are overlain by pedogenically altered silty, sandy soils with intermittent layers of hardpan calcrete, soilcrete or ferricrete. Finally, hillwash consisting of gravelly silty sand masks the site.

4.4.3 Groundwater

During the geotechnical investigation undertaken by the project consultants, piezometers were installed in selected boreholes to measure groundwater levels. From this, the consultants observed that water levels varied between 0 to 20.6 m below the ground surface. As shown in Figure 4.6, these water levels correlated well (R^2 = 0.977) with the surface elevation, with no significant outliers observed for the wider project area. Therefore, it was identified that the water levels measured within the boreholes were a true reflection of the regional groundwater table, and further that the groundwater table mimicked the surface topography within the project area.

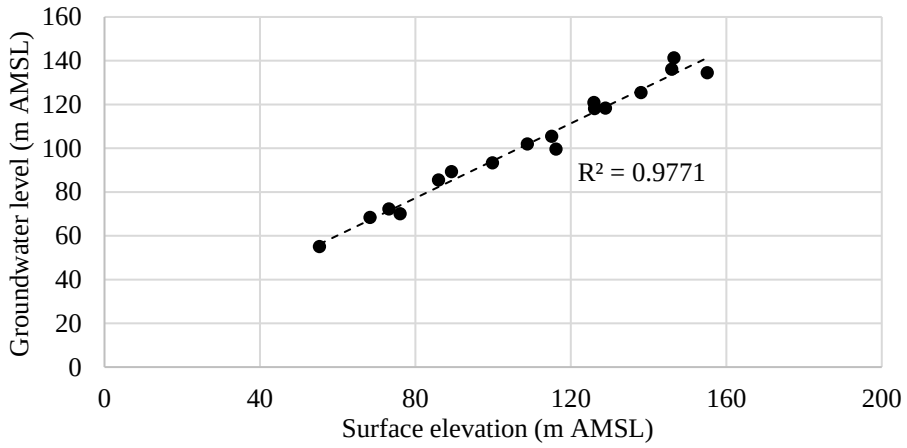

Figure 4.6: Correlation between surface elevation and groundwater level

4.4.4 Ground profiles

Within the wind farm site, the project consultants specified at least one borehole to be drilled at the location of each wind turbine, of which there were over forty. From this available data, three representative soil profiles were selected for analysis, each of which is discussed below and illustrated in Figure 4.7, Figure 4.8, and Figure 4.9 respectively. These profiles were specifically chosen for three primary reasons, (1) they contained soil strata that were deemed to be susceptible to cyclic degradation, which as discussed in §2.5.2.2, was likely to be soil comprising low plasticity in combination with low permeability, (2) they represented the softest profiles at the site with respect to their G_0 profiles with depth, as determined from the CSW tests, and (3)

they illustrated different scenarios in ground conditions, with Profile A being representative of a deep clayey profile (Figure 4.7), Profile B containing similar soils but with bedrock located at a depth equal to half of the foundation diameter (Figure 4.8), and Profile C also containing clayey soils but with a stratum of very dense sand overlying them at founding level (Figure 4.9).

Note that a founding level of 3 m below ground surface was used in the FE models of the three soil profiles, as this was the founding level used in the wind farm project. Therefore, apart from the contribution to overburden stress, the top 3 m of the soil profiles described below were not included in the analyses. Further, for all soil profiles, the groundwater table was assumed to be located at founding level, as this is the condition under which cyclic degradation would occur and be most significant. With this, a saturated unit weight of γ_{sat} = 19 kN/m^3 was assumed for all soil layers. This was based on suggested values for the soil type provided by British Standard 8004:2015 (BSI, 2015), which in turn makes reference to Bond (2013). Finally, the PI of all fine-grained soils within the three ground profiles was assumed to be 15%. This was derived from the results of numerous foundation indicator tests conducted on soil samples taken from the boreholes, the vast majority of which indicated low plasticity soils with a PI in the order of 15%.

- **Ground Profile A: Deep clayey profile.** This profile consisted of gravel hillwash within 1.5 m of ground level, underlain by a thin layer of hardpan ferricrete, which in turn was underlain by residual granite soils. Considering that the founding level was 3 m below ground level, the hillwash and ferricrete were excluded from the analysis. The residual granite material primarily consisted of slightly sandy silty gravelly clay, ranging from firm to stiff with depth. The stiffness profile from the CSW test indicated an approximately constant G_0 of 60 MPa up to a depth of 17.7 m below founding level, at which there was a sharp increase to 230 MPa. Finally, bedrock was not encountered in this borehole.
- **Ground Profile B: Clayey profile with bedrock at depth equal to half of foundation diameter.** This profile was selected to assess the effect that bedrock, located in relatively close proximity to the ground surface, would have on the degradation of the soil above it. That is, whether its presence would influence the distribution of shear strain, and possibly suppress it from advancing further downward than Ground Profile A. In a similar manner to Ground Profile A, this profile contained sand hillwash and pedogenic material near the ground surface, however it was again excluded from the analysis as it was situated above founding level. Underlying this material was reworked residual granite comprising firm to stiff, fine gravelly silty clay, with G_0 of 60 MPa as for the soil in Ground Profile A. Bedrock was located at 9 m below founding level, equal to half of the foundation diameter.
- **Ground Profile C: Clayey profile with stratum of dense sand located at founding level.** This profile was chosen to evaluate the extent to which a layer of dense sand, located at founding level, would act as a contact layer below the foundation. Specifically, to assess the effectiveness of this layer in containing the shear strains induced in the soil, and thus preventing cyclic degradation of the more susceptible soils below. At the foundation-soil interface, the dense sand had a thickness of 1.5 m and G_0 of 390 MPa. Below this was residual granite material comprising fine gravelly silty clay, similar to that of the previous two ground profiles, with G_0 of 60 MPa up to a depth of 12.2 m, and 190 MPa below.

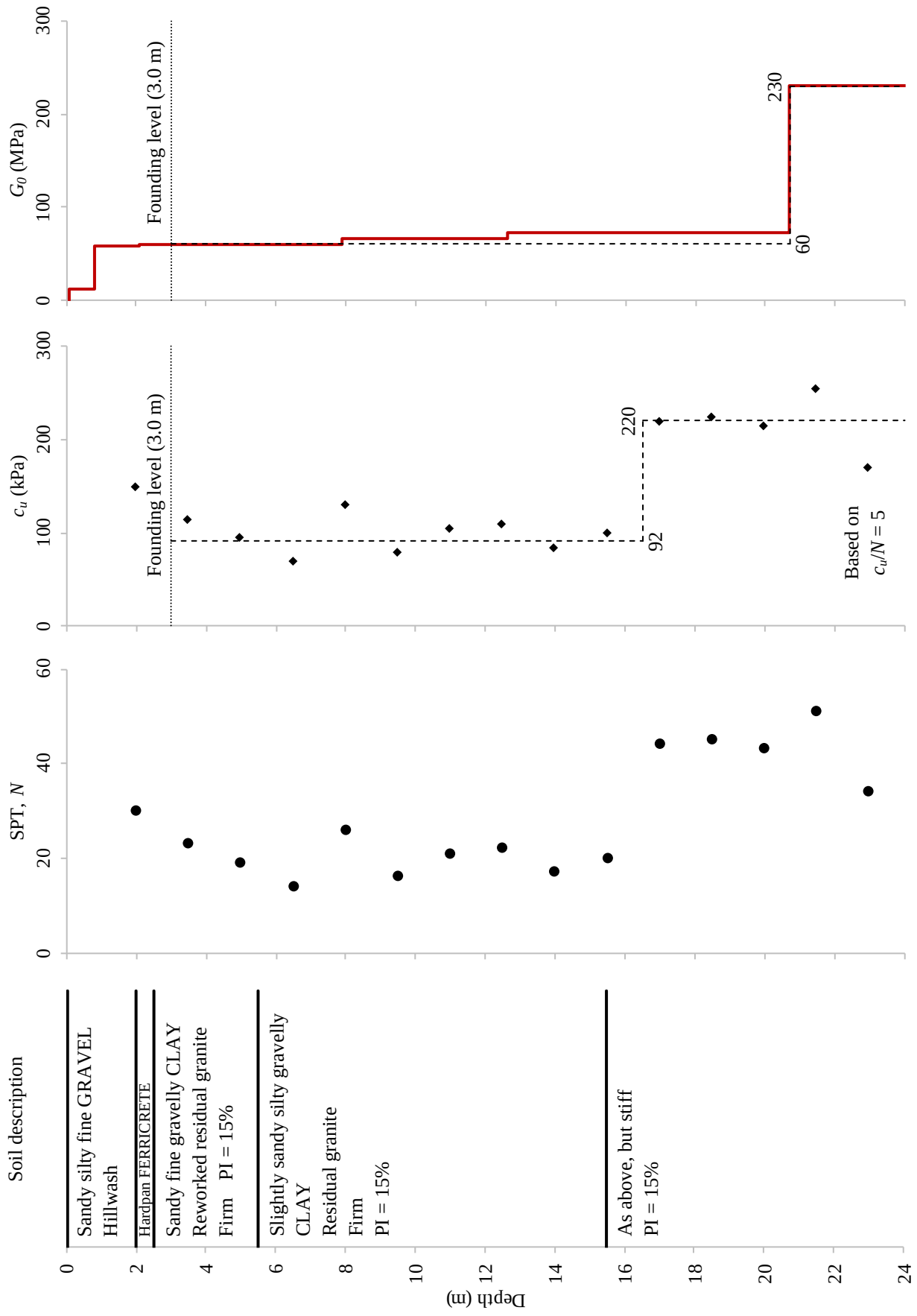

Figure 4.7: Ground Profile A

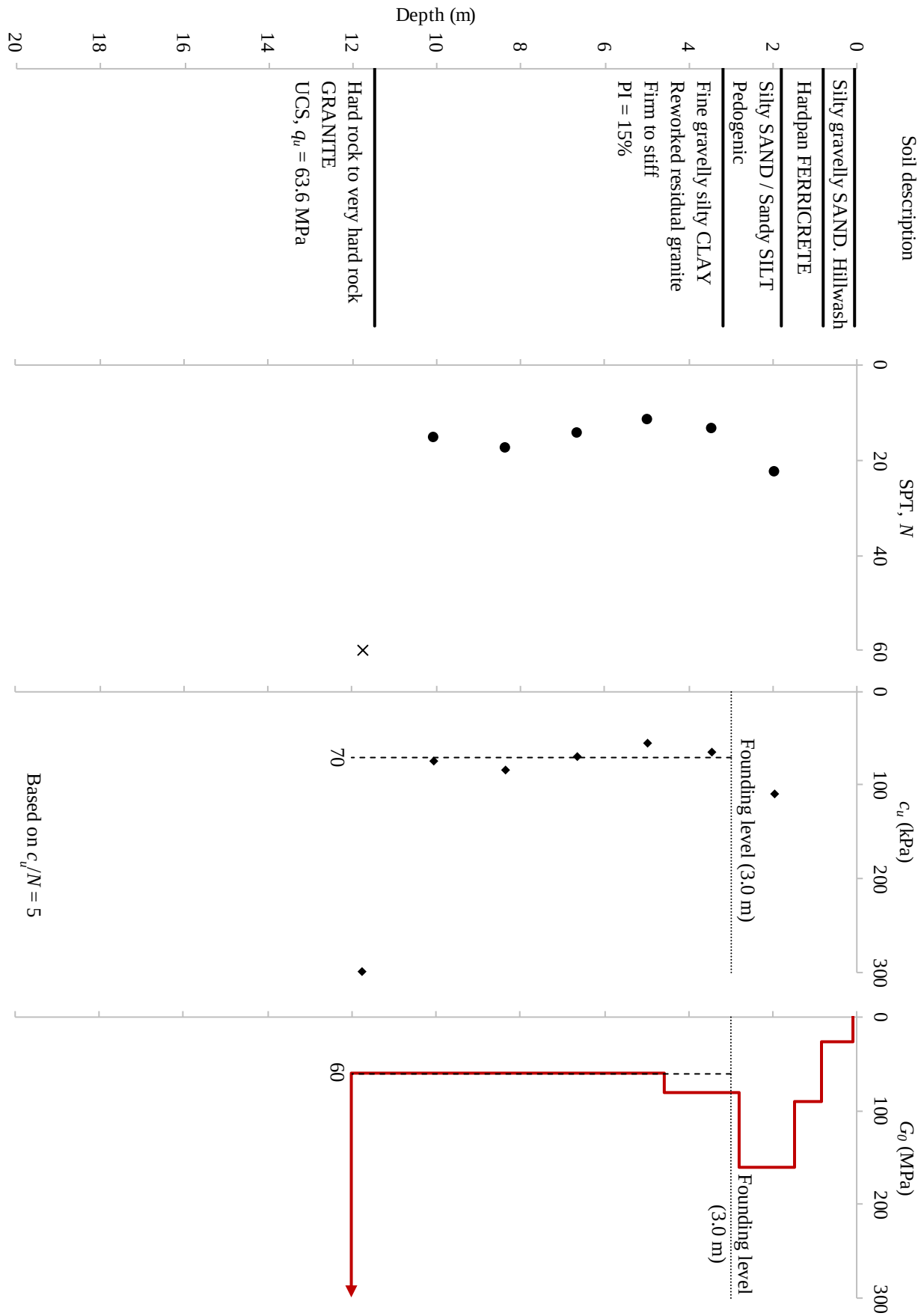

Figure 4.8: Ground Profile B

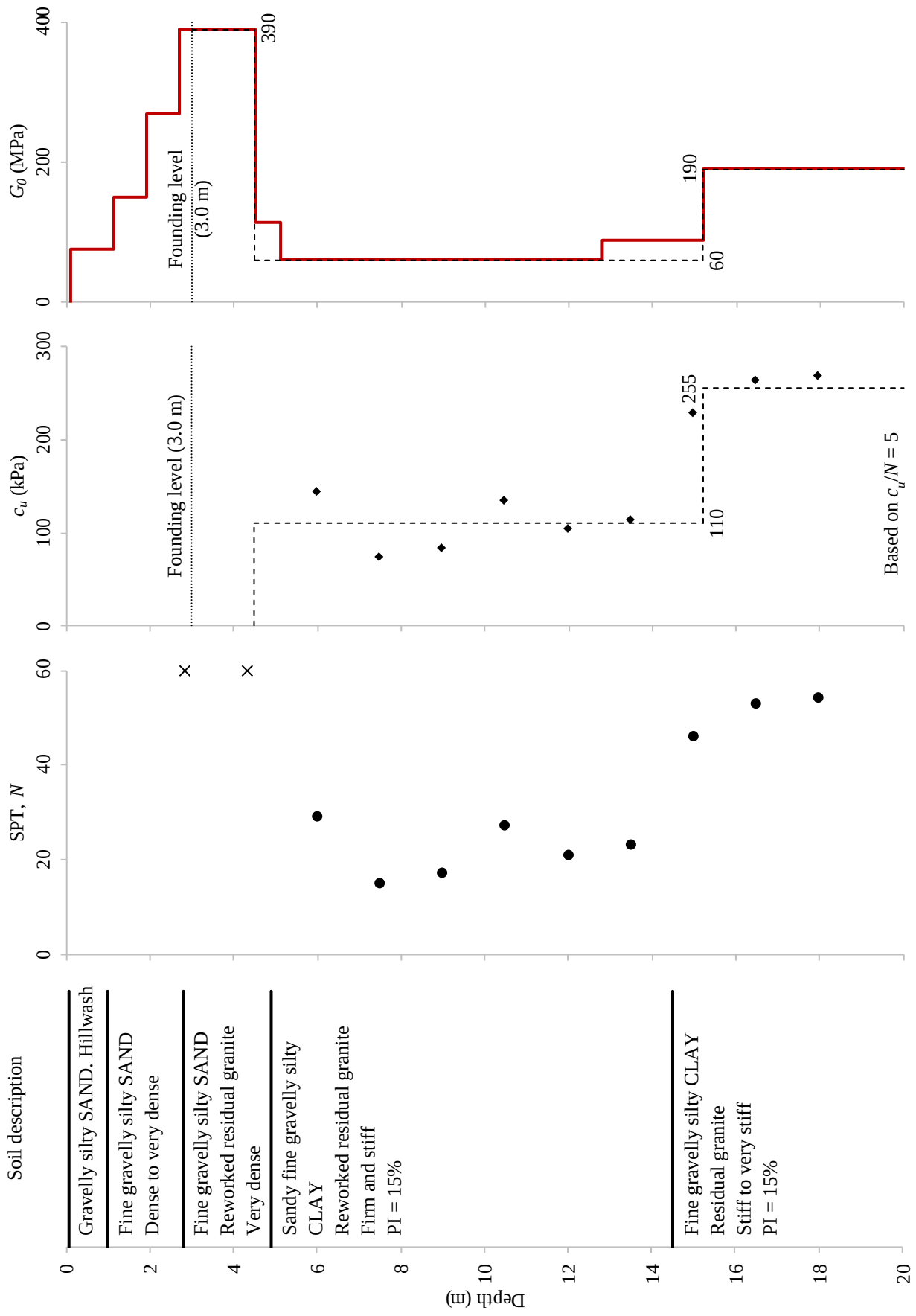

Figure 4.9: Ground Profile C

4.4.5 Material properties

Material properties characterising the stiffness, degradation, and strength of the various strata in the ground profiles required assessment. Several of these properties were illustrated in Figure 4.7, Figure 4.8, and Figure 4.9 respectively, however their derivations are subsequently described.

4.4.5.1 Soil stiffness

Three components were necessary to define the soil stiffness, namely the Poisson's ratio ν, initial shear modulus G_0, and the shape of the modulus reduction curve G/G_0. Regarding the former, clays in an undrained state have a Poisson's ratio of 0.5, however to avoid numerical instabilities in the FE models, a value of 0.499 was adopted. For the dense sand material in Ground Profile C, which was modelled as drained, the Poisson's ratio was assumed to be 0.3, as suggested by Kulhawy and Mayne (1990) for this soil type.

CSW testing was conducted at each wind turbine location, from which profiles of G_0 with depth were established. As the soil stiffness was deemed to be the most important facet of material behaviour in the various analyses, these stiffness profiles were used to define the positions of the upper and lower boundaries of each stratum in the FE models, with additional layers defined based on shear strength properties where applicable. In doing so, significant variations in G_0 were interpreted as layer boundaries. However, where the variations in G_0 were negligible, the soil was kept in the same layer with the lower bound value of G_0 assigned to the layer.

Finally, the shape of the modulus reduction curve was required for each soil stratum. For this, the PI of the soil was used to define the modulus reduction curves based on the chart provided by Vucetic and Dobry (1991), shown previously in Figure 3.4. As mentioned before, the PI was taken to be 15% for all fine-grained soils in the three ground models, which was based on the Atterberg limit test results from the foundation indicator tests. The values of the specific parameters used to fit the modulus reduction curve (Eqn. 4.1) are derived in §4.7.1 and shown in Table 4.7. For the granular soil in Ground Profile C, the modulus reduction curve corresponding to a PI of 0% was adopted, also from the chart provided by Vucetic and Dobry (1991).

4.4.5.2 Degradation shear strain threshold

In line with the modelling methodology, the degradation shear strain threshold γ_{td} of the soil was required for this analysis. However, this parameter was not measured in the laboratory testing programme for the wind farm project, as it requires specialist testing procedures such as cyclic triaxial tests or cyclic direct simple shear tests. Consequently, γ_{td} was estimated from the literature for this investigation.

For cohesive soils, experimental evidence shows that γ_{td} generally increases with the PI of the soil (Tabata & Vucetic, 2010). This trend is shown in Figure 4.10, which provides a correlation between these two parameters. As this chart is recommended by Tabata and Vucetic (2010) for

practical applications, it was used to estimate γ_{td} in this study. In doing so, γ_{td} was approximated to be 0.00023 for a PI of 15%, which for later reference coincided with a G/G_0 ratio of 0.7 from the corresponding shear modulus reduction curve proposed by Vucetic and Dobry (1991).

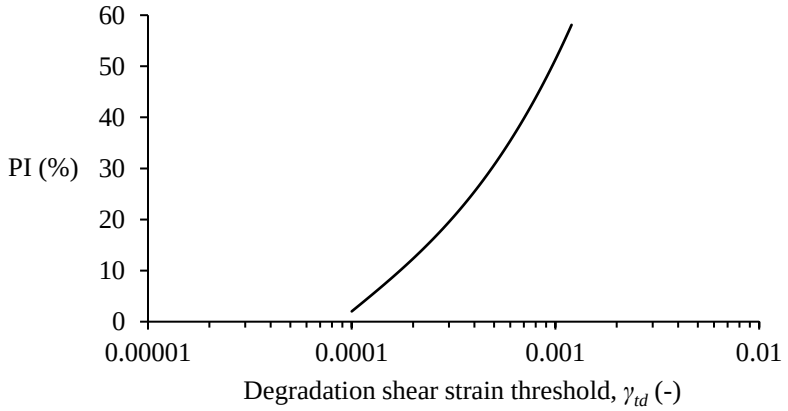

Figure 4.10: Trend of degradation shear strain threshold versus plasticity index
Adapted from Tabata and Vucetic (2010)

A further aspect requiring consideration was the definition of shear strain, and with this the compatibility between the shear strains presented in the output of *RS*^{3} and the value of γ_{td} selected from the literature. This was important because the value of γ_{td} was used to plot the isosurfaces in *RS*^{3} based on its output of shear strain, however the two definitions of shear strain differed. Specifically, the shear strains provided by *RS*^{3}, referred to as the *maximum shear strain* in the program, were equivalent to the deviatoric strain (ε_q), which is an invariant of strain tensor (Rocscience, n.d.(a)). The FE software calculated this maximum shear strain using Equation 4.2. However, another measure of the deviatoric strain is γ, calculated using Equation 4.3, which was the shear strain used in the constitutive model (Eqn. 4.1), and also the shear strain which corresponded to γ_{td}. Therefore, in order to accurately plot the isosurfaces in *RS*^{3}, the value of γ_{td} had to be converted to an equivalent value of ε_q, and this was done by multiplying it by the square root of two divided by three, as shown in Equation 4.2.

$$\varepsilon_q = \sqrt{\frac{2}{3} e_{ij} e_{ij}} = \sqrt{\frac{2}{3}} \gamma \qquad \text{Eqn. 4.2}$$

$$\gamma = \sqrt{e_{ij} e_{ij}} \qquad \text{Eqn. 4.3}$$

Where ε_q = deviatoric strain (unitless); e_{ij} = strain deviator (unitless); and γ = deviatoric strain (unitless).

4.4.5.3 Undrained shear strength

The undrained shear strength c_u of each fine-grained soil stratum was also necessary as input for the FE models. However, laboratory tests were not conducted to directly measure this parameter, and thus c_u was estimated based on SPT *N*-values from the respective boreholes. This was done using principles by Clayton (1995), who in turn suggests the use of correlations provided by Stroud (1974). These correlations are applicable to insensitive clays and are illustrated in Figure 4.11, from which it is shown that the ratio c_u/N ranges from approximately 4 to 7 kPa depending on the plasticity index of the clay. Therefore, for simplicity and to err on the side of conservatism, a c_u/N value in the lower end of the range of 5 kPa was adopted throughout this analysis. Although this provided a very approximate value of the undrained shear strength, according to Byrne *et al.* (2008), the correlations by Stroud (1974) are applicable to a wide range of residual and transported clay soils in Southern Africa. The average c_u value over the depth of each soil layer was then computed, with non-conservative outliers ignored, and this was used as input into the model. The c_u values were also cross-checked with tables provided by Brink and Bruin (2002), to verify if they approximately correlated with the indicated soil consistency.

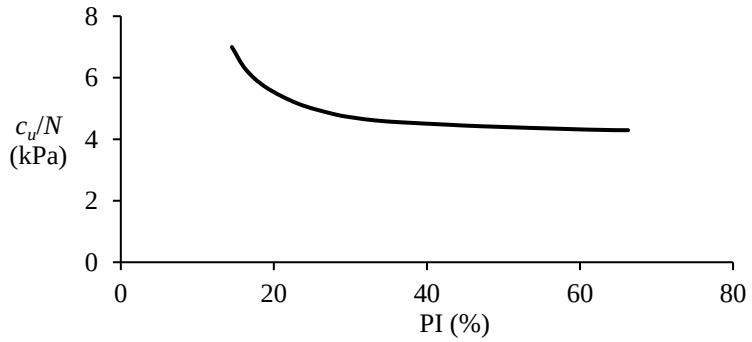

Figure 4.11: Correlation between SPT *N*-value and c_u for insensitive clays
Adapted from Stroud (1974)

4.4.5.4 Drained shear strength

The drained shear strength, specifically the angle of internal friction ϕ', was required for the granular soil in Ground Profile C. This was estimated to be 40º based on its description as *very dense* in the borehole log (SPT refusal), in accordance with correlations provided by Byrne *et al.* (2008), as well as Bond (2013). The effective cohesion c' was taken to be 0 kPa.

4.4.5.5 Rock properties

The bedrock in Ground Profile B was modelled as linear elastic, and thus the Poisson's ratio v and elastic modulus E were the necessary input parameters to characterise it stiffness. Regarding the former, Look (2014) suggests that the typical range for granite rock is 0.15 to 0.25, hence v was assumed to be 0.2. In estimating the latter, Byrne *et al.* (2008) provides correlations with the results of unconfined compressive strength (UCS) tests. For the borehole corresponding to

Ground Profile B, a UCS test was conducted on a rock sample taken from a depth of 13.9 m, from which the unconfined compressive strength (q_u) was measured to be 63.6 MPa. With this result, Byrne *et al.* (2008) suggests that the ratio E/q_u has a wide scatter of 100 to 1000, but proposes that a ratio of 300 can be used for design when no direct correlation for the rock type is obtained. This assumption was adopted for the present analysis, from which E was estimated to be 63.6×300 ≈ 19000 MPa. Additionally, the unit weight of the rock was determined during the UCS testing process to be 25.7 kN/m^3.

Note that the rock material was only modelled with elastic behaviour and thus did not include a plastic mechanism. This was deemed appropriate based on the assumption that the stresses in this material would be sufficiently low such that the linear elastic range was not exceeded. Furthermore, the purpose of modelling the rock was to determine how a very stiff stratum located at depth would affect the distribution of strain above it (and thus the degradation), and consequently only the stiffness characteristics were considered necessary.

4.4.6 Summary of ground models

The various strata and material properties for the three ground models are summarised in Table 4.1 below. This data was used as input into the FE models.

Table 4.1: Summary of ground models

Ground profile	Stratum	Depth below foundation (m)	Stiffness							Degradation	Strength	
					Equation 4.1							
			G_0 (MPa)	ν (-)	PI (%)	γ_r (-)	a (-)	b (-)	E (GPa)	γ_{td} (-)	c_u (kPa)	ϕ' (deg)
A	1	0 to 13.5	60	0.499	15	6.5× 10^{-4}	2.35	-0.6	–	2.3× 10^{-4}	92	–
	2	13.5 to 17.7	60	0.499	15	6.5× 10^{-4}	2.35	-0.6	–	2.3× 10^{-4}	220	–
	3	17.7 to depth	230	0.499	15	6.5× 10^{-4}	2.35	-0.6	–	2.3× 10^{-4}	220	–
B	1	0 to 9.0	60	0.499	15	6.5× 10^{-4}	2.35	-0.6	–	2.3× 10^{-4}	70	–
	2	9.0 to depth	–	0.2	–	–	–	–	19	–	–	–
C	1	0 to 1.5	390	0.3	0	2.9× 10^{-4}	1.8	-0.7	–	–	–	40
	2	1.5 to 12.2	60	0.499	15	6.5× 10^{-4}	2.35	-0.6	–	2.3× 10^{-4}	110	–
	3	12.2 to depth	190	0.499	15	6.5× 10^{-4}	2.35	-0.6	–	2.3× 10^{-4}	255	–

4.5 Turbine Model and Loads

The wind turbine model selected for this analysis was the Vestas V112-3.0 MW, which is a pitch regulated upwind turbine with an active yaw system and a three-bladed rotor. Further general specifications are summarised in Table 4.2. The primary reasons for this choice were twofold. The first was that in South Africa, a large number of existing wind farms have been contracted to Vestas, and thus they are one of the main turbine suppliers in the country. The second reason was that, with a generating capacity of approximately 3 MW, hub height of 119 m, and rotor diameter of 112 m, it is a relatively large turbine that was deemed to be representative of the scale of modern wind turbine structures. Therefore, the foundation loading conditions associated with this turbine model were considered to be indicative of foundation design for South African wind farms in the near future.

Table 4.2: General specifications of the Vestas V112-3.0 MW wind turbine
Sourced from Vestas (2010)

Operating data	Rated power	3.075 kW
	Cut-in wind speed	3 m/s
	Rated wind speed	13 m/s
	Cut-out wind speed	25 m/s
Rotor	Rotor diameter	112 m
	Swept area	9852 m^2
	Operational interval	6.2-17.7 rpm
Tower	Type	Tubular steel
	Hub height	119 m (IEC IIIA)
	Maximum diameter	4.2 m

The foundation loads required estimation based on the turbine model selected. This included the resultant vertical load, as well as the cyclical lateral load and simultaneous overturning moment. For this, reference was made to the manufacturer's load document (Vestas, 2013), which provided the load cases shown in Table 4.3.

Table 4.3: Foundation load cases for Vestas V112-3.0 MW wind turbine
Sourced from Vestas (2013)

	M_{res} (kNm)	M_z (kNm)	F_{res} (kN)	F_z (kN)
Characteristic extreme load during normal operation (SLS)	49100	731.0	554.0	-4620
Characteristic extreme load for normal load cases (ULS)	66700	-353.0	695.0	-4590
Characteristic extreme load for abnormal load cases (ULS)	85100	1551	1031	-4500

Of the load cases shown in Table 4.3, that corresponding to the *characteristic extreme load during normal operation* was adopted in this analysis, which is applicable to SLS design. However, regarding SLS design loads for wind turbine foundations, it must be acknowledged that they can either be representative of quasi-permanent SLS or rare SLS (CFMS, 2011). As the name of the load case mentioned above implies, it was representative of the latter. This was deemed suitable for the present analysis given that the soil was analysed in terms of short-term undrained conditions, which may occur during a design storm. Nonetheless, two additional load cases were analysed in the parametric study, each of which was more representative of the quasi-permanent SLS loading.

To summarise, the load case used in the numerical modelling is presented in Table 4.4. Note that the notation was changed from F_{res} to F_x, and from M_{res} to M_y, with the subscripts indicating the directions in which the loads were applied in the FE models. Further note that the torsional moment M_z was neglected in this analysis.

Table 4.4: Extreme loads during normal operation for Vestas V112-3.0 MW foundation
Sourced from Vestas (2013)

Load	Value
F_z (kN)	-4620
F_x (kN)	554.0
M_y (kNm)	49100

It must be reiterated that the loading in this numerical model was applied quasi-statically, and a dynamic analysis was not performed. This was due to the assumption that the wind thrust was slowly-varying, and thus had a sufficiently low frequency such that the inertia effects in the soil domain were negligible. However, as an illustration, Figure 4.12 depicts what the equivalent waveform of the cyclical overturning moment would resemble if it was applied in a dynamic analysis. Further note that the cyclical loads were applied as one-way cyclic loading in the numerical model, and were not multidirectional.

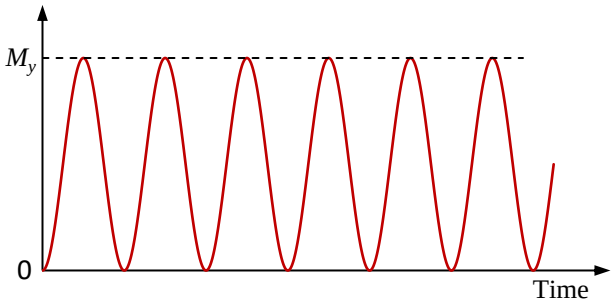

Figure 4.12: Waveform of cyclical overturning moment

4.6 General Model Characteristics

Several general model characteristics required consideration throughout the development of the FE models. These characteristics are subsequently described, including the staging of the models, the boundary locations and types of restraints, the approach to modelling the foundation element, the modelling of the groundwater, and finally the generation of the mesh.

4.6.1 Analysis stages

The ability to stage an FE model to simulate a construction process is one of many advantages that the finite element method has over conventional analytical solutions. However, in this case the construction process was relatively straightforward, and thus an elaborate staging sequence was not necessary. Only three stages were required for each iteration of the modelling strategy, that is, for each time that the soil stiffness was altered. As depicted in Figure 4.13, this included (1) generating the initial stresses; (2) installing the foundation; and (3) applying the loads. Details of each of these stages are described in the following sections.

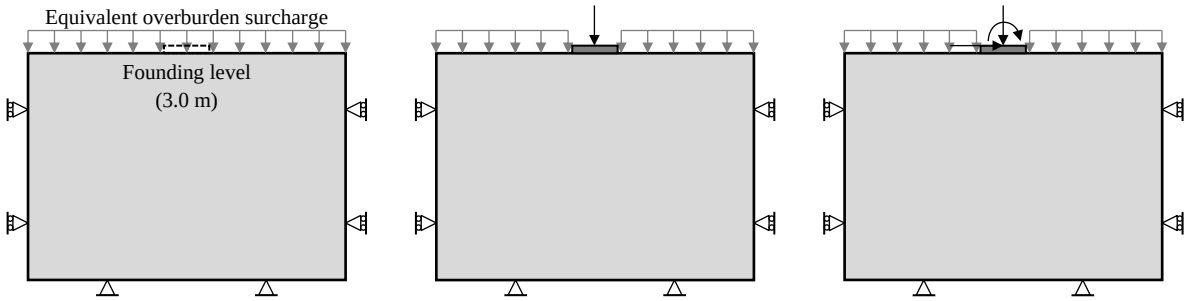

Figure 4.13: Analysis stages of finite element model

4.6.1.1 Stage 1: Initial stresses

The first stage of any geotechnical FE analysis is the generation of initial stresses. In this context, initial stresses refer to stresses that exist in the ground in greenfield conditions, that is, prior to any significant man-made stress changes. This is an important aspect of an FE model given that soil and, to a certain extent, rock are frictional materials with their strength and stiffness heavily dependent on internal stresses.

In calculating the initial stresses, vertical stresses are assumed to vary linearly with depth and are relatively straightforward to calculate given that the unit weight of the overlying material is known. Horizontal stresses are then calculated by multiplying the vertical stresses by the coefficient of lateral earth pressure at rest (K_0). This K_0 method was appropriate for the given analysis, considering that the geometry of the ground surface, soil strata, and groundwater levels in all models were horizonal. It is of interest to note that if the geometry were not horizontal, then the K_0 method would lead to the existence of unbalanced initial forces within the soil body,

and in that case a gravity loading procedure would be more suitable to establish the initial stresses.

In generating the initial stresses, a uniform unit weight of 19 kN/m^3 was assumed for the ground, barring Ground Profile B which contained rock with a unit weight of 25.7 kN/m^3. Further, in the FE model, the upper ground surface was set to founding level (3.0 m) rather than the original ground surface. Consequently, in order to include the weight of the ground excluded from the mesh in the calculation of the stresses, a uniform surcharge load equivalent to the overburden weight was applied to the upper surface, as indicated in Figure 4.13. This surcharge was equal to 19×3 = 57 kN/m^2. Although this configuration omitted the strength and stiffness of the ground above founding level, it was a conservative assumption. Moreover, given that this analysis involved undrained soil conditions, a theoretical K_0 value of one was adopted. Accordingly, this coefficient was expressed in terms of total rather than effective stresses.

4.6.1.2 Stage 2: Foundation installation

The foundation element was activated in this stage. In doing so, the surcharge representing the soil overburden was removed from the foundation area only, and the weight of the foundation included in its material properties. Additionally, the vertical load F_z was applied in this stage, as it represented the self-weight of the wind turbine structure and thus contributed to the static portion of the resultant loads. Further details of modelling the foundation element are provided in §4.6.3.

4.6.1.3 Stage 3: Load application

In this stage, the quasi-static loads were added to the model. This included applying the horizontal thrust force F_x and the resultant overturning moment M_y to the foundation element concurrently. After the model was computed, the shear strains corresponding to the outputs of the stage were obtained and an isosurface of γ_{td} plotted, which was used to define the stiffness degradation in the subsequent iterations.

4.6.1.4 Stiffness iterations

For the subsequent stiffness iterations, the methodology described in §4.2.3 was followed. For each of these iterations, the model computations were repeated from the first to the third stage.

Although another method of conducting the stiffness iterations would have been to add an additional stage to the model for each, and make the appropriate stiffness reductions within these stages, this approach was inherently problematic. This was because, as described by Rocscience (n.d.(b)), the finite element method requires there to be a change in load state, thus putting the model out of equilibrium, in order for the computation of stresses or strains to be undertaken. Simply making an alteration to the modulus between stages is insufficient for the calculations to be conducted, and hence does not yield any results.

4.6.2 Boundaries and restraints

The boundaries of the FE model were placed sufficiently far away from the area of interest such that the restraints imposed at these boundaries would not cause any significant boundary effects. As illustrated in Figure 4.14, vertical boundaries were defined at a distance of 3*B* from the edges of the foundation, giving a total width of 7*B*, whereas the base of the model was placed at 5*B* from the upper ground surface. With a foundation diameter of 20 m, which was the largest used in the parametric study, this resulted in an overall block dimension of 140×140×100 m, which was used throughout all the analyses. It was assumed that extending this model size would have negligible effects on the outputs of the model, particularly because the cyclic loading applied was quasi-static in nature. If on the other hand, dynamic loading was applied to the foundation, then additional considerations would have been required for the boundaries due to the propagation of shear and pressure waves through the soil. In such a case, one option would be to set the boundaries to absorb these waves, such that they do not cause spurious reflections and thereby contaminate the wave field below the foundation. Although these considerations were not required for this study, future studies involving dynamic loading would need to take them into account.

Standard restraints were imposed for the boundaries of the FE model geometry. This included allowing the boundary on the uppermost surface to deform in all directions, fixing the vertical boundaries in the lateral directions, and fixing the boundary at the base in both the lateral and vertical directions. Imposition of these standard restraints allowed deformation of the soil to occur at the points of interest, whilst hindering it at points further away, so as to obtain realistic stress distributions throughout the soil body.

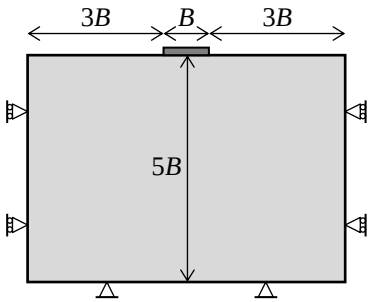

Figure 4.14: Model boundaries and restraints

4.6.3 Foundation element

The first consideration regarding modelling the foundation element was its geometry. Due to the variability in ground conditions across the wind farm in question, each wind turbine foundation was designed individually and consequently the foundation diameters ranged from 16.5 to 20.0 m. As the exact foundation diameter at each of the three chosen soil profiles was unknown, a median value of 18.0 m was assumed across all analyses. Further assumed dimensions of the actual foundation geometry are illustrated in Figure 4.15(a), with a 3D model shown in Figure

4.15(b). This geometry resulted in an overall foundation volume of 458.7 m^3. In order to simplify the foundation geometry for input into the model, it was converted to a disc with a volume equivalent to the actual foundation. This resulted in a disc thickness of 1.8 m as shown in Figure 4.15(c) and (d). This simplification was deemed acceptable due to the decision to model the foundation as a rigid element, which is discussed further on in this section.

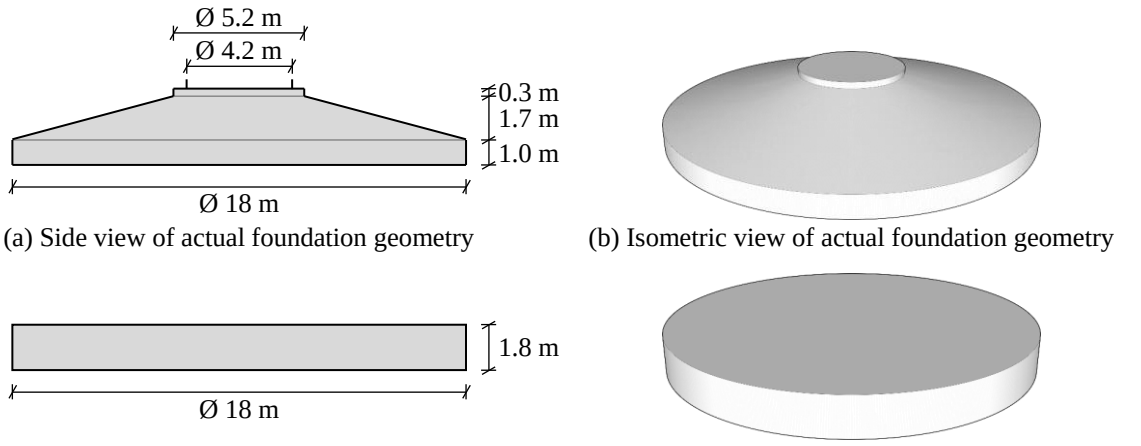

(a) Side view of actual foundation geometry

(b) Isometric view of actual foundation geometry

(c) Side view of simplified foundation geometry

(d) Isometric view of simplified foundation geometry

Figure 4.15: Actual and simplified geometry of foundation element

The second aspect that required consideration was that in FE analyses, structural elements such as foundations can be represented by continuum or non-continuum elements. Continuum elements refer to volume or solid elements normally used to represent soil or rock, whereas non-continuum elements, such as plates and shells, are planar like membrane elements that have rotational as well as displacement degrees of freedom at their nodes so that they possess bending stiffness (Lees, 2016). There are advantages and disadvantages to each approach, however for the purposes of this analysis, the foundation was modelled as a continuum element rather than a non-continuum plate element. The main reason for using a continuum element was that it was not possible to apply a moment to a liner element in the version of *RS*^{3} used in this study. However, regardless of this, it was further recognised that there are several assumptions associated with plate elements that should be valid whenever they are used. One of these assumptions is that the thickness of the element is small relative to its overall geometry, and thus they are intended for thin-walled structures (Lees, 2016). Since the foundation under consideration had a significant volume and was relatively thick, having been simplified to a disc with thickness-to-diameter ratio of 1/10, this was deemed to be more than the limit of what could normally be modelled reasonably accurately with a non-continuum plate element. A further reason for not using a plate element was that some of the main benefits of doing so were not required in this analysis. One of the benefits of using a plate element is that the analysis can provide a direct output of the structural forces in the element, including axial and shear forces, as well as moments. However, this information was not a necessary output of this model. A further benefit is that, relative to a continuum element, the flexural rigidity of a plate element

can be modelled with superior precision, and can thus provide more accurate deformation predictions. For instance, the properties of the steel reinforcement in a reinforced concrete plate element can be included as input into a model. However, since the foundation element was modelled with rigid behaviour, this added precision was not required.

The material behaviour of the wind turbine foundation was modelled with linear elasticity. Brinkgreve *et al.* (2016) state that in situations where internal forces and deformations of structural elements are not regarded as relevant output data, such elements can simply be modelled as 'rigid' by specifying an arbitrary stiffness that is sufficiently large compared to the stiffness of the soil. As this was the case for the present analysis, the linear elasticity approach to modelling the foundation element was adopted. Thus, as shown in Table 4.5, an arbitrarily large elastic modulus of 500 GPa was specified, such that the foundation generated a rigid response. The other material properties, unit weight and Poisson's ratio, were representative of typical concrete properties. Additionally, the foundation element was specified to only behave elastically with no plastic mechanism, and cracking of the concrete was also neglected in this analysis.

Table 4.5: Material properties of foundation element

Property	Value
Unit weight (kN/m^3)	24
Elastic modulus, E (GPa)	500
Poisson's ratio, v (-)	0.15

In assuming the foundation element to behave as a rigid body, an important factor that required consideration was the impact that this assumption had on the contact stresses below the foundation. In this regard, it is well recognised that the relative stiffness between a structural element and soil mass plays a significant role in controlling the distribution of contact stresses. As illustrated in Figure 4.16(a) and (b), flexible foundations subjected to uniformly distributed loads generally experience uniform stress distributions because they can bend as necessary to maintain this, and accordingly they undergo nonuniform settlement. Conversely, the settlement of a rigid foundation is uniform because the whole footing settles as a rigid element, but the contact stresses are nonuniform to maintain this, as shown in Figure 4.16(c) and (d). Therefore, in this case, considering that the soil was cohesive and the foundation was modelled as rigid, the foundation was expected to have highly concentrated edge stresses and lower stresses in its centre. This mechanism of high edge stresses was observed in the outputs of the analyses, but was deemed to be acceptable for the purposes of the current investigation as it was likely to result in the stresses being distributed deeper into the soil profile on the leeward side of the foundation, particularly because the loading was highly eccentric, and thus was regarded as being more conservative. Moreover, the assumption of rigidity was further justified from the foundation's

considerable thickness, as well as the fact that wind turbine foundations are generally constructed of high strength concrete and with large proportions of reinforcing steel.

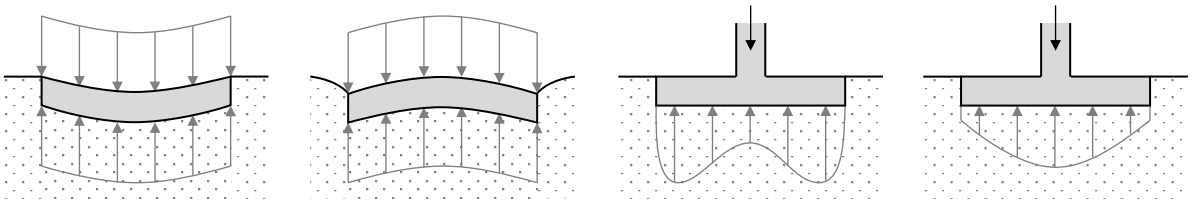

(a) Flexible footing on clay (b) Flexible footing on sand (c) Rigid footing on clay (d) Rigid footing on sand

Figure 4.16: Pressure distribution beneath a footing subjected to concentric vertical load
Adapted from Coduto (2001)

The final aspect of modelling the foundation element that needed to be characterised was the manner in which the loads were applied. As illustrated in Figure 4.17, the vertical force F_z and lateral force F_x were applied as circular line loads distributed over the circumference of the anchor bolt cage, which as shown in Figure 4.15(a), had an assumed diameter of 4.2 m within the centre of the foundation. Note that this diameter was chosen to be equal to the tower base diameter, as indicated in Table 4.2. On the other hand, *RS*^{3} did not offer an explicit means of adding an overturning moment to a foundation element. Therefore, the overturning moment M_y was applied to the foundation as a coupled force, which included placing one vertical force in the positive *z*-direction, and another in the negative *z*-direction, at either side of the anchor bolt cage as shown in Figure 4.17. The magnitude of these coupled forces was calculated to be the overturning moment M_y divided by the anchor bolt cage diameter of 4.2 m. Note that the requirement to apply a coupled force to the foundation was an additional reason as to why it had to be modelled as a rigid element. This was because, if the foundation had been assigned an elastic modulus representative of its actual stiffness, the forces in the force couple would have resulted in large stresses and strains at their points of application on the foundation element itself, without transferring these loads correctly to the soil.

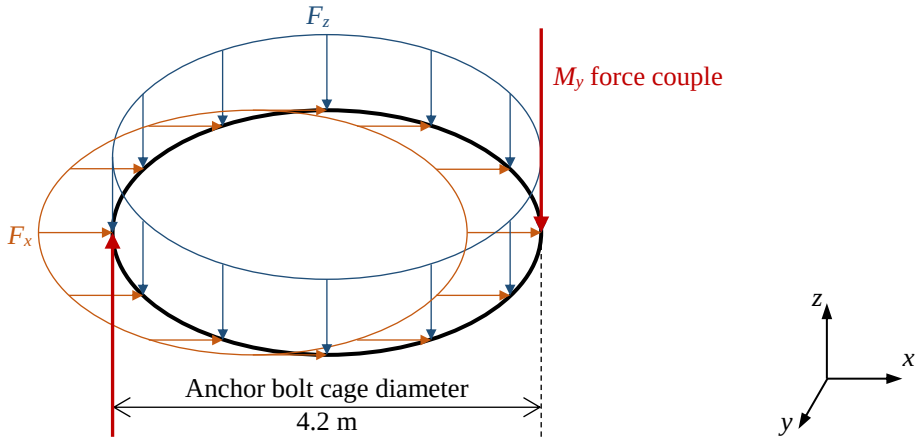

Figure 4.17: Application of loads on the foundation element

4.6.4 Groundwater and drainage conditions

All fine-grained soils in this investigation were modelled with undrained behaviour, as discussed in §4.2.2. It must be reiterated that this is usually the case with regards to cyclic loading (Andresen, 2015), and although there might be drainage in the long-term, the soil response in each individual cycle is undrained as the excess pore pressures cannot dissipate due to the quick succession of the load cycles (Dobry & Vucetic, 1987). That is, the time increments over which the loads are applied are very small in comparison to the typical fluid drainage times within the clay microstructure. As fluid cannot move into or out of the model, volumetric changes are prevented because the compressibility of the water is low compared to the compressibility of the soil skeleton. Furthermore, whether the generated excess pore pressure becomes permanent or not, as well as whether the microstructure and stiffness of the soil is altered irreversibly, depends on whether the shear strain thresholds defined in Figure 3.3 are exceeded, as previously discussed in §3.3.1.

It must be emphasised that, although the accumulation of excess pore pressure with increasing number of loading cycles is one of the principal features that distinguishes cyclic behaviour from that exhibited during monotonic loading, modelling of this facet of behaviour was not possible in the current FE model. Rather, the effects of this pore pressure generation were implicitly accounted for through the modelling strategy of decreasing the soil stiffness in geometric volumes that exceeded the degradation shear strain threshold.

Groundwater was represented in the model by constant hydraulic boundary conditions in the form of a phreatic surface placed horizontally at founding level. The high bulk modulus (K) of the undrained soil mass was set indirectly by specifying a Poisson's ratio of 0.499. Additionally, the analysis type undertaken was *uncoupled*, which meant that changes in pore pressure did not affect deformation, and vice versa, as is the case for a total stress analysis. Moreover, where the ground models contained some layers that required a drained analysis and some that required an undrained analysis, the model was run with the appropriate assumption for each layer concurrently. This was the case for Ground Profile C, for which the granular soil below founding level was modelled as drained.

One further detail required clarification, as explained by Dobry and Vucetic (1987). During cyclic loading, the soil is subjected to both undrained compression and shear. Similarly to the static case, compressive stresses produce mainly reversible increases in pore pressure due to the large difference in compressibility between pore water and the soil skeleton. Therefore, there is little immediate change in effective stresses and the stiffness of the clay in compression, represented by the bulk modulus K, is controlled exclusively by the compressibility of the pore fluid. Consequently, the stress-strain behaviour in compression is linear and there is little stiffness degradation during cyclic loading. On the other hand, because water has no shear resistance, the undrained cyclic shear stresses are taken completely by the soil skeleton. This results in nonlinear and often irreversible behaviour, with stiffness degradation occurring during cyclic loading. This is the reason for much of this research having been focussed on the behaviour of soil in shear.

4.6.5 Mesh generation and sensitivity analysis

The model geometry was discretised into a finite element mesh in *RS*^{3} using 10-noded tetrahedral elements. In doing so, a graded mesh was used throughout, which differs from a uniform mesh in the sense that the mesh density is increased in areas of interest, or in complex geometry, and decreased in areas further away where the stresses and strains are more uniform. With this understanding, it was important to adopt an appropriate mesh density in the areas of interest. This was because analyses carried out by the finite element method inevitably contain discretisation errors, and although it is possible to reduce this error by using a very fine mesh, the consequence of this is increased computational cost. Therefore, generating a mesh that achieved an optimum balance between computational effort and the accuracy of the solution produced was beneficial, particularly considering the large number of analyses and iterations undertaken.

It is not possible to quantify discretisation error from the result of one analysis with only one mesh configuration. Therefore, to quantify the discretisation error for the numerical model in question, a mesh sensitivity analysis was performed with progressively finer meshes until no significant change in the required output was observed. In this case, the required output was the maximum depth to which the degradation shear strain threshold γ_{td} was reached. Ground Profile A was used for conducting this analysis, however as a simplification, only the upper soil layer in this ground profile was modelled throughout (c_u = 92 kPa; G_0 = 60 MPa; $G/G_0(\gamma$, PI=15%); ν = 0.499). Further, only one loading cycle was applied, without accounting for the effects of degradation.

Initially, the default graded mesh generated by the program was analysed. Based on the outputs of this, the mesh was subsequently refined in a 20×20×20 m block centred below the foundation-soil interface, where the stress concentration was highest. The element size within this refined area, which represents the approximate side length of each element, was varied as shown in Table 4.6. The effect of this element size on the maximum depth of γ_{td} below the foundation is plotted in Figure 4.18, with an illustration of each mesh presented in Figure 4.19.

Table 4.6: Mesh dependency of shear strain depth

Mesh number	Element size within refined area (m)	Total number of elements	Depth of γ_{td} below founding level (m)
1	10	4612	8.43
2	5	9874	7.31
3	3	27247	6.82
4	2.5	41966	6.06
5	2	72911	5.74
6	1.5	157852	5.72

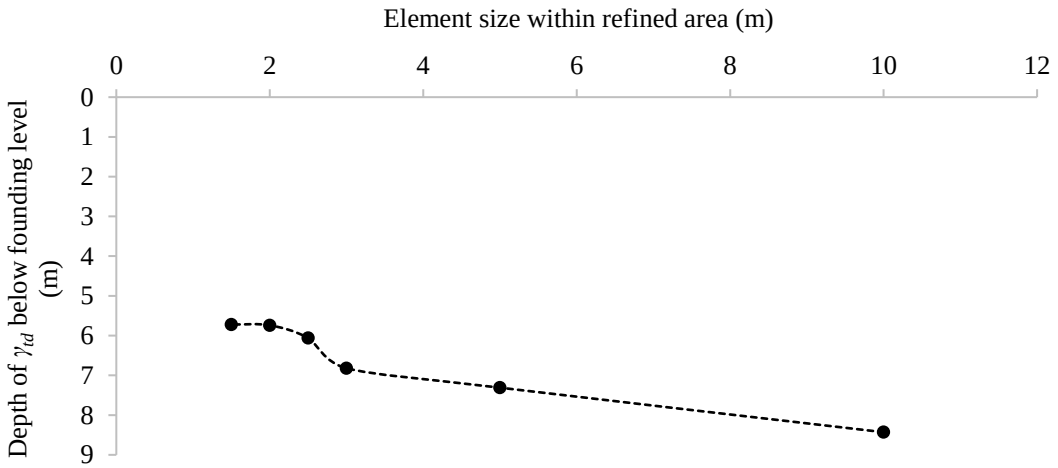

Figure 4.18: Refined element size versus strain depth

From Figure 4.18, it is evident that as the element size within the refined area was reduced, and thus the total number of elements increased, the calculated maximum depth of γ_{td} below founding level decreased. Therefore, the output became less conservative with a finer mesh. Furthermore, there was an insignificant change in the depth of γ_{td} with element sizes of 2 m and less, with it having converged to approximately 5.7 m. Thus, it was deemed reasonable to adopt a refined element size of 2 m for the subsequent analyses, as an increase in density beyond this had negligible effects on the outputs, and any inaccuracy regarding mesh density would have also erred on the side of conservatism. The computational time was also reasonable for this mesh density, with exponentially higher computational times observed for finer meshes.

Finally, it was also important to inspect the mesh quality throughout the various analyses, particularly with respect to the shape of the elements as long thin elements tend to be unsatisfactory in FE analyses. This was done in *RS*^{3} by examining the percentage of total elements with unfavourable aspect ratios. However, the mesh quality was not a significant concern considering the relatively simple nature of the geometry.

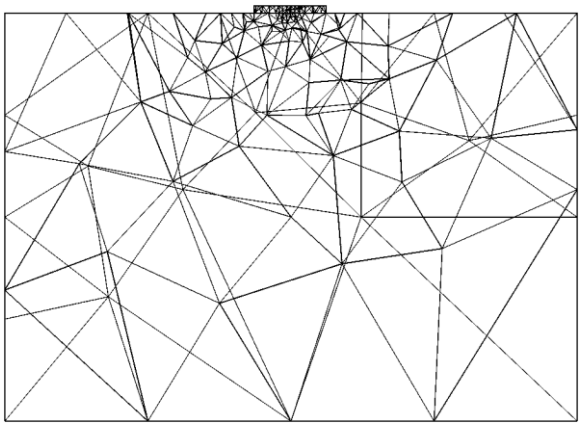

(a) Refined element size 10 m

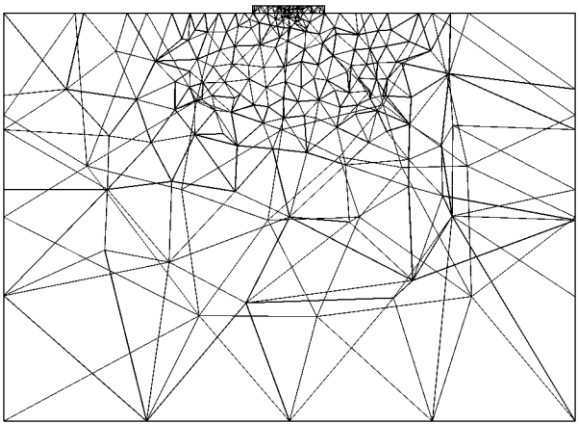

(b) Refined element size 5 m

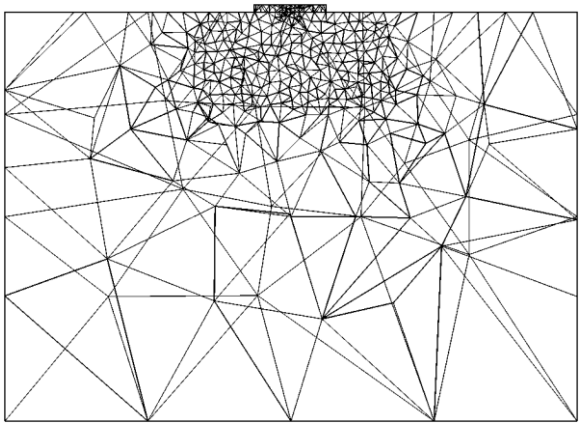

(c) Refined element size 3 m

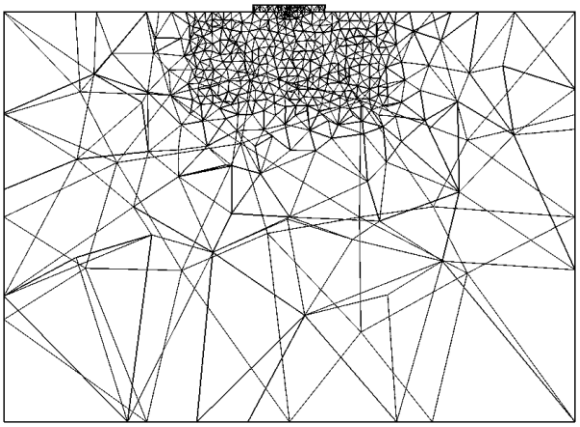

(d) Refined element size 2.5 m

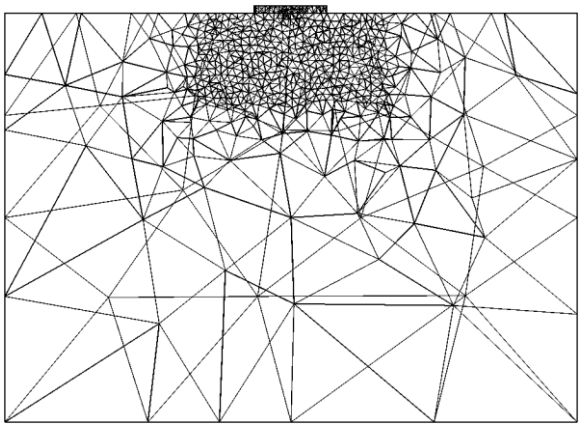

(e) Refined element size 2 m

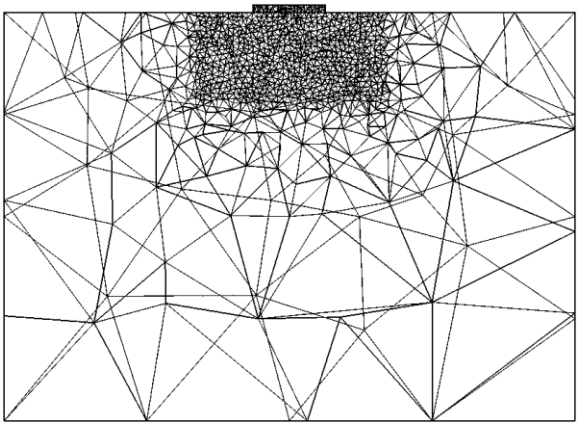

(f) Refined element size 1.5 m

Figure 4.19: Cross-section of meshes used in mesh sensitivity analysis

4.7 Parametric Study

Inevitably, some input parameters have a dominant influence on the outcome of numerical analyses whereas other parameters may have little influence. To evaluate which parameters had a high influence in this analysis, a parametric study was performed. This involved varying several input parameters between certain ranges to determine their impact on the model outputs. Although the results of the numerical model require further validation, the intention of this parametric study was to at least identify important parameters affecting the results, which was a suggestion similarly proposed by Achmus *et al.* (2007) in the development of their numerical model. This allowed the critical parameters to be identified that potentially require the most attention in wind turbine foundation design involving cyclic soil degradation.

Ground Profile A was used for this parametric study. However, as for the mesh sensitivity analysis, this profile was simplified such that only the top soil layer was modelled throughout. The reason for this was to allow the parameters to be uniformly varied throughout the soil body. The characteristic properties of this soil layer were c_u = 92 kPa; G_0 = 60 MPa; $G/G_0(\gamma$, PI=15%); ν = 0.499; and γ_{td} = 0.00023. Furthermore, for this parametric study, only the first loading cycle was analysed for each variation in the input parameters, without implementing the iterative procedure described in the modelling methodology. This was because this provided sufficient data from which comparisons could be drawn between the various parameters. With this, the parameters described in the subsequent sections were included in the parametric study.

4.7.1 Plasticity index, initial shear modulus, and degradation threshold

In the numerical model, the stiffness of the soil was characterised based on its PI and initial shear modulus G_0, whereas the degradation was quantified according to the degradation shear strain threshold γ_{td}. Consequently, these parameters were considered to be important in the analyses, and thus they were varied in this parametric study. However, rather than only doing so for one of these parameters at a time, permutations involving all three were analysed. Specifically, for each modulus reduction curve that was modelled based on the PI, a range of G_0 values was analysed, and for each G_0 value, γ_{td} was varied between an upper and lower bound value. This provided a broader overview of the influence of these parameters.

4.7.1.1 Plasticity index

It is evident from the chart proposed by Vucetic and Dobry (1991), shown in Figure 4.20, that there is a strong correlation between the PI of soil and its stress-strain behaviour. Considering this, the PI of the soil was varied in this parametric study from values of 0, 15, 30, 50, 100, and 200%. Note that a PI of 0% was included, despite this mainly being associated with free-draining granular soils, which would only cyclically degrade at very high loading rates, such as seismic loading. However, it was added for purposes of comparison and to illustrate the worst-case scenario.

In varying the PI, the modulus reduction chart provided by Vucetic and Dobry (1991) was employed. However, a shortcoming of this chart was that no mathematical formulations were given by the authors for the degradation curves that they indicate. Therefore, in order to implement these curves into the numerical model, they were fitted to the modified hyperbolic function used in *RS*^{3} (Eqn. 4.1). The procedure for doing so began by selecting a reference shear strain γ_r that corresponded to a G/G_0 ratio of 0.5. Subsequently, the material parameters *a* and *b* were adjusted until a reasonable fit was achieved. The resultant parameters for each PI are shown in Table 4.7, with the respective curves illustrated in Figure 4.20.

Table 4.7: Modified hyperbola parameters for varying plasticity index

	Plasticity index (%)					
	0	15	30	50	100	200
Reference shear strain, γ_r (–)	0.00029	0.00065	0.0012	0.0027	0.0057	0.0090
Material parameter, *a* (–)	1.8	2.35	2.7	2.6	1.65	1
Material parameter, *b* (–)	-0.7	-0.6	-0.53	-0.57	-0.75	-1

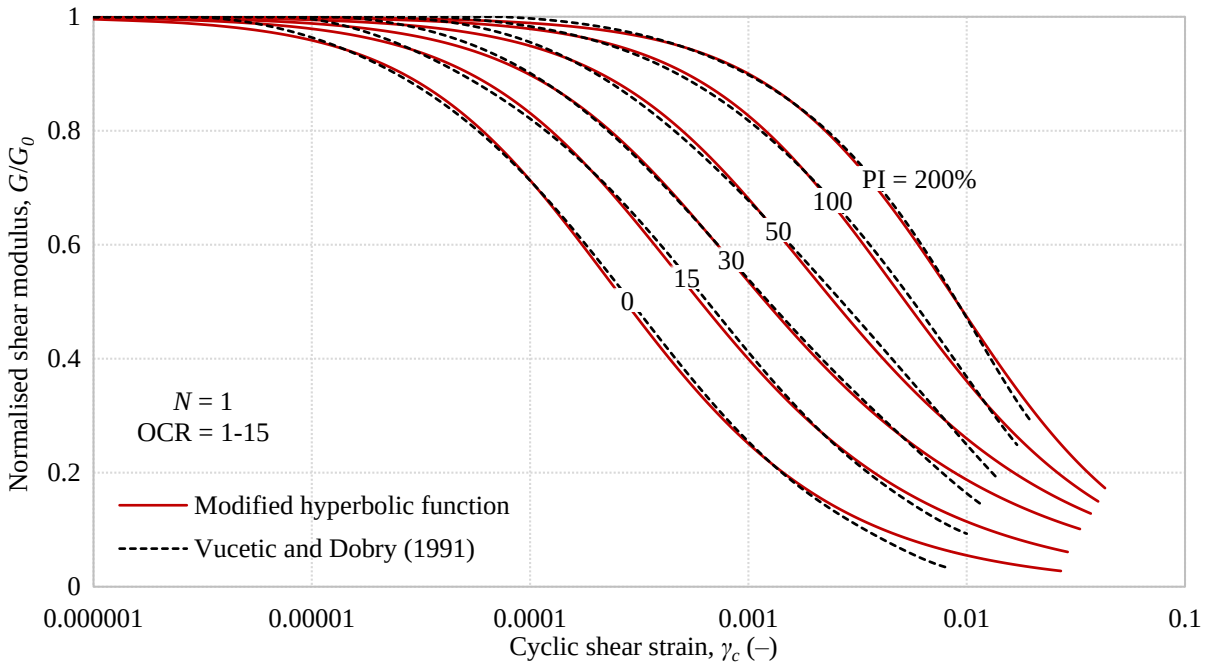

Figure 4.20: Modified hyperbola modulus reduction curves for varying plasticity index
Adapted from Vucetic and Dobry (1991)

4.7.1.2 Initial shear modulus

For each modulus reduction curve described previously, the initial shear modulus G_0 was varied between a range of values. The lower end of this range was selected to be 20 MPa, as values less than this generally resulted in the model not reaching a state of equilibrium. The upper end of the range was taken to be 150 MPa, as the results of values larger than this were found to have diminishing significance. Within this range, increments of 5 MPa were analysed.

4.7.1.3 Degradation shear strain threshold

The degradation shear strain threshold γ_{td} is correlated to the PI of the soil, as discussed previously in §4.4.5.2. Consequently, as the plasticity of the soil changed by virtue of the change in modulus reduction curves, γ_{td} was adjusted accordingly.

For the soil with PI of 15%, the characteristic value of γ_{td} selected for the analyses of the three ground profiles in the case study was 0.00023, as per the chart developed by Tabata and Vucetic (2010) shown in Figure 4.10. Using this same chart, characteristic values of γ_{td} were derived for the soil PI's shown in Table 4.8. Note that Figure 4.10 only included the range of PI from 0 to 60%, and thus characteristic values could not be obtained for the PI's of 100 or 200%. Rather, these PI's were only analysed between the range of upper and lower bound values of γ_{td} subsequently described.

Table 4.8: Assumed characteristic values of degradation threshold for varying PI

Based on Figure 4.10

Plasticity index (%)	Degradation shear strain threshold, γ_{td} (-)	Corresponding G/G_0 ratio from chart by Vucetic and Dobry (1991)
0	0.0001	0.71
15	0.00023	0.70
30	0.00049	0.67
50	0.00096	0.68

The G/G_0 ratio corresponding to each assumed characteristic value of γ_{td} is also shown in Table 4.8, as extracted from the modulus reduction curves by Vucetic and Dobry (1991). From this, it was recognised that the values of γ_{td} approximately coincided with a G/G_0 ratio of 0.7 across all PI's. However, Lombardi *et al.* (2013) propose that two values of G/G_0 can represent upper and lower bound values of γ_{tv}, specifically 0.6 and 0.85. Although the definition of γ_{tv} differs slightly from that of γ_{td}, Tabata and Vucetic (2010) suggest that these parameters are essentially the same or very similar, as they are based on the same fundamental mechanisms. Considering the similarity between these parameters, γ_{td} was varied between the range of shear strain values corresponding to the G/G_0 range of 0.6 to 0.85, in increments of 0.05. Accordingly, the values of γ_{td} used in the analysis of each soil PI are presented in Table 4.9, having been derived from the chart by Vucetic and Dobry (1991).

Table 4.9: Degradation shear strain threshold for various PI and $\gamma_{td} \triangleq G/G_0$ combinations

	Plasticity index (%)					
$\gamma_{td} \triangleq G/G_0$	0	15	30	50	100	200
0.6	0.000180	0.000396	0.000724	0.00156	0.00360	0.00620
0.65	0.000140	0.000304	0.000553	0.00117	0.00280	0.00504
0.7	0.000107	0.000230	0.000419	0.000875	0.00214	0.00401
0.75	0.0000800	0.000168	0.000312	0.000642	0.00159	0.00311
0.8	0.0000580	0.000118	0.000227	0.000459	0.00114	0.00230
0.85	0.0000390	0.0000780	0.000158	0.000314	0.000771	0.00159

4.7.2 Foundation size

The size of the foundation influences the magnitude of the stresses transferred to the soil, and accordingly it also influences the distribution of strains. Consequently, it is likely to have an impact on the extent of the cyclic degradation of the bearing materials. Specifically, as the foundations size increases, the strain level in the soil decreases, and thus the degradation will also decrease.

As mentioned previously, the foundation diameter used in the analyses of the three soil profiles was 18 m. Therefore, in order to gauge the impact that foundation size has on cyclic degradation, additional diameters of 15, 16, 17, 19, and 20 m were analysed. In doing so, the same range of G_0 values described in §4.7.1.2 were evaluated for each diameter.

4.7.3 Load magnitude

The load case used in the analysis of the three soil profiles was representative of extreme conditions during normal operation, which as mentioned in §4.5, is the load case used for SLS design in *rare* conditions. However, the wind turbine will not always be subjected to these conditions, and thus it is also relevant to analyse load cases that are more representative of long-term fatigue behaviour. Accordingly, two additional load cases were analysed in the parametric study, the first being the fatigue load case provided by the wind turbine manufacturer, and the second being the load case which was calculated based on the site-specific wind climate. Again, G_0 was varied within the same range of values described in §4.7.1.2 for each load case.

4.7.3.1 Fatigue load case

In addition to providing extreme load cases for design, the foundation load document provided by the manufacturer (Vestas, 2013) also includes a fatigue load case, shown in Table 4.10. These loads are provided for the intended purpose of undertaking fatigue analyses of the structural materials in the foundation, namely steel and concrete. They are essentially equivalent loads corresponding to 10^7 load cycles, that when applied to these materials would produce the same

impact as that of a more complex fatigue calculation involving so-called *Markov* matrices. Accordingly, these fatigue loads are specific to the structural materials and are not necessarily intended for modelling the fatigue behaviour of the soil. Regardless, this load case was analysed as it was somewhat representative of the long-term loading conditions of the turbine.

Table 4.10: Equivalent and mean fatigue loads for Vestas V112-3.0 MW foundation
Sourced from Vestas (2013)

	Mean load	Range, m = 4 (Steel)	Range, m = 7 (Concrete)
F_x (kN)	222.0	440.0	382.0
M_y (kNm)	20470	21320	22670

The maximum and minimum loads are calculated from Table 4.10 by taking the mean, plus and minus half the range. The maximum horizontal thrust force from this data correlated to the first range in this table, and was calculated in Equation 4.4. Similarly, the maximum overturning moment corresponded to the second range in the table, and was calculated using Equation 4.5.

$$\begin{aligned} F_{x(\max)} &= F_{x(mean)} \pm \frac{F_{x(range)}}{2} \\ &= 222.0 + \frac{440.0}{2} \\ &= 442.0\ \text{kN} \end{aligned} \qquad \text{Eqn. 4.4}$$

$$\begin{aligned} M_{y(\max)} &= M_{y(mean)} \pm \frac{M_{y(range)}}{2} \\ &= 20470 + \frac{22670}{2} \\ &= 31805\ \text{kNm} \end{aligned} \qquad \text{Eqn. 4.5}$$

Regarding the vertical load F_z, it is evident from Table 4.3 that it remains approximately constant, regardless of the load case for the wind turbine, as it is predominantly based off the self-weight of the turbine components. Therefore, F_z was assumed to be the largest of the three load cases shown in Table 4.3, which corresponded to a value of -4620 kN. Note that this load magnitude excluded the weight of the foundation itself, as this component of the overall vertical load was accounted for through the unit weight of the concrete material in the numerical model. To summarise, the loads corresponding to the fatigue load case are shown in Table 4.11.

Table 4.11: Summary of fatigue load case for Vestas V112-3.0 MW foundation
Sourced from Vestas (2013)

Load	Value
F_z (kN)	-4620
F_x (kN)	442.0
M_y (kNm)	-31805

4.7.3.2 Site-specific load case

The foundation loads were also calculated based on site-specific wind data for the wind farm in question. For the calculation, the simplified equation suggested by Arany *et al.* (2017) was used, shown in Equation 4.6 below, with its purpose being to estimate the thrust force acting on a wind turbine rotor due to wind loading. The overturning moment at foundation level was subsequently calculated by multiplying this thrust force by the corresponding eccentricity from the foundation.

$$F_x = \tfrac{1}{2} C_t \rho_a A U^2 \qquad \text{Eqn. 4.6}$$

Where F_x = rotor thrust in x-direction (N); C_t = thrust coefficient (unitless); ρ_a = air density (kg/m^3); A = rotor swept area (m^2); and U = wind speed (m/s).

With reference to Equation 4.6, to calculate the thrust on the rotor, it is necessary to know the thrust coefficient C_t. This coefficient is a function of wind speed and is wind turbine specific, being dependent on the blade geometry, rotational speed of the rotor, the applied control strategy of the wind turbine, and so forth. Arany *et al.* (2017) provide simplified formulae for estimating this coefficient, however this approach should only be adopted in the absence of specific data for the wind turbine in question, as it produces conservative approximations. In the present case, thrust coefficients were available for the Vestas V112-3.0 MW wind turbine, the variation of which with wind speed is plotted in Figure 4.21. Superimposed onto this figure is the rotor thrust calculated using Equation 4.6, in which the rotor swept area was taken from Table 4.2 as 9852 m^2 and the air density was assumed to be 1.225 kg/m^3. It is of interest to note that the maximum thrust occurs just before the rated wind speed of 13 m/s, which correlates to the activation of the pitch control mechanism.

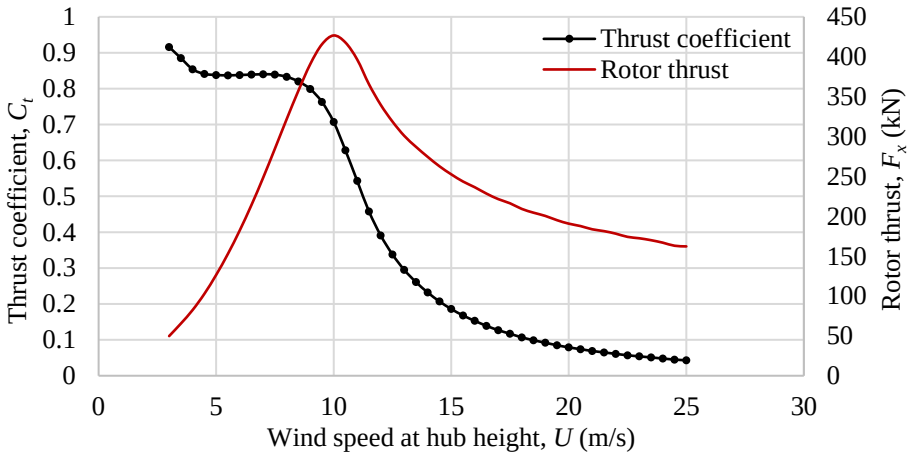

Figure 4.21: Thrust coefficient and calculated rotor thrust for Vestas V112-3.0 MW
Data sourced from Vestas (2009)

With the rotor thrust estimated for the range of operational wind speeds, the wind data for the site was used to evaluate the representative magnitude of this force, as well as the corresponding overturning moment at foundation level. In doing so, it was acknowledged that there is a significant degree of variability and randomness associated with environmental loading, and thus it is a difficult parameter to quantify. However, it was deemed reasonable to assume that the average rotor thrust in the long-term would be correlated to the mean wind speed at the site. As discussed in §4.4.1 and shown in Figure 4.5, the numerical wind atlas developed by the WASA project estimated the mean wind speed in the dominant wind direction at the wind farm site to be 11.39-11.63 m/s at a height of 100 m AGL, of which the average was ~11.5 m/s. This wind speed corresponded to a thrust coefficient of C_t = 0.458 for the Vestas V112-3.0 MW wind turbine (Vestas, 2009). Therefore, the wind thrust F_x was calculated in Equation 4.7 below to be 365.5 kN. This rotor thrust was then multiplied by the hub height of 119 m, as shown in Equation 4.8, from which the overturning moment M_y was estimated to be 43495 kNm at the base. Finally, a summary of the site-specific load case is presented in Table 4.12.

$$\begin{aligned} F_y &= \tfrac{1}{2} C_t \rho_a A U^2 \\ &= \tfrac{1}{2}(0.458)(1.225)(9852)(11.5)^2 \\ &= 365.5 \text{ kN} \end{aligned} \qquad \text{Eqn. 4.7}$$

$$\begin{aligned} M_x &= F_y \times H \\ &= 365.5 \times 119 \\ &\approx 43495 \text{ kNm} \end{aligned} \qquad \text{Eqn. 4.8}$$

Table 4.12: Summary of site-specific load case for Vestas V112-3.0 MW foundation

Load	Value
F_z (kN)	-4620
F_x (kN)	365.5
M_y (kNm)	43495

Chapter 5
RESULTS AND DISCUSSIONS

5.1 Introduction

In this chapter, the results of the finite element analyses of the wind turbine foundations are presented and discussed. These include the three ground profiles selected from the case study, as well as the parametric study.

5.2 Ground Profile A

This profile represented a deep clayey profile at the wind farm site, the 3D model of which is illustrated in Figure 5.1 as generated in *RS*^{3}. The results of this model are subsequently discussed with respect to the depth of influence of cyclic degradation, as well as the effect that accounting for cyclic degradation had on the required foundation diameter.

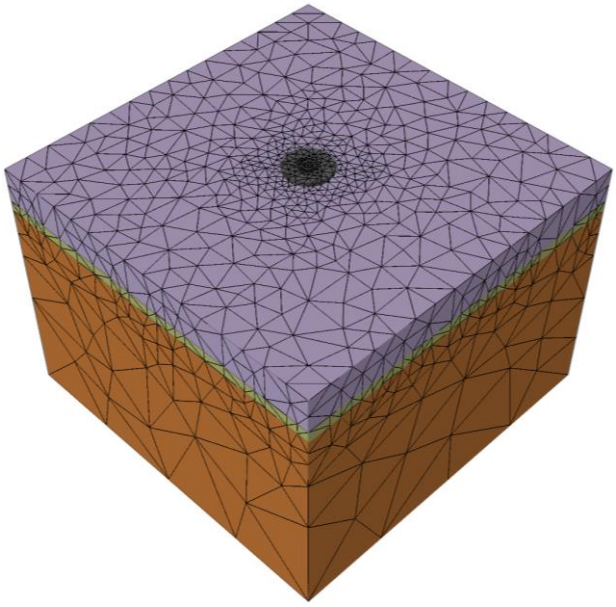

Figure 5.1: Model of Ground Profile A

5.2.1 Depth of influence of degradation

The depth of influence of cyclic degradation was primarily controlled by the distribution of shear strain below the foundation-soil interface. Accordingly, the cross-sectional plot of maximum (deviatoric) shear strain, taken through the centre of the foundation, is presented in Figure 5.2 for the first loading cycle. Stage 2 corresponded to the installation of the foundation and application of the vertical load, whereas Stage 3 involved the application of the horizontal and moment loads. Due to the foundation being modelled with rigid behaviour, the strains were primarily concentrated around the edges of the foundation. Furthermore, for Stage 3, the maximum shear strain was in the order of ε_q = 0.0008, which was converted to an equivalent value of γ using Equation 4.2 as γ = 0.00098. The reason for this conversion was previously explained in §4.4.5.2. This shear strain was in very close agreement with DNV/Risø (2002), which states that the magnitude of cyclic shear strains induced from wind loading is typically γ_c = 0.001.

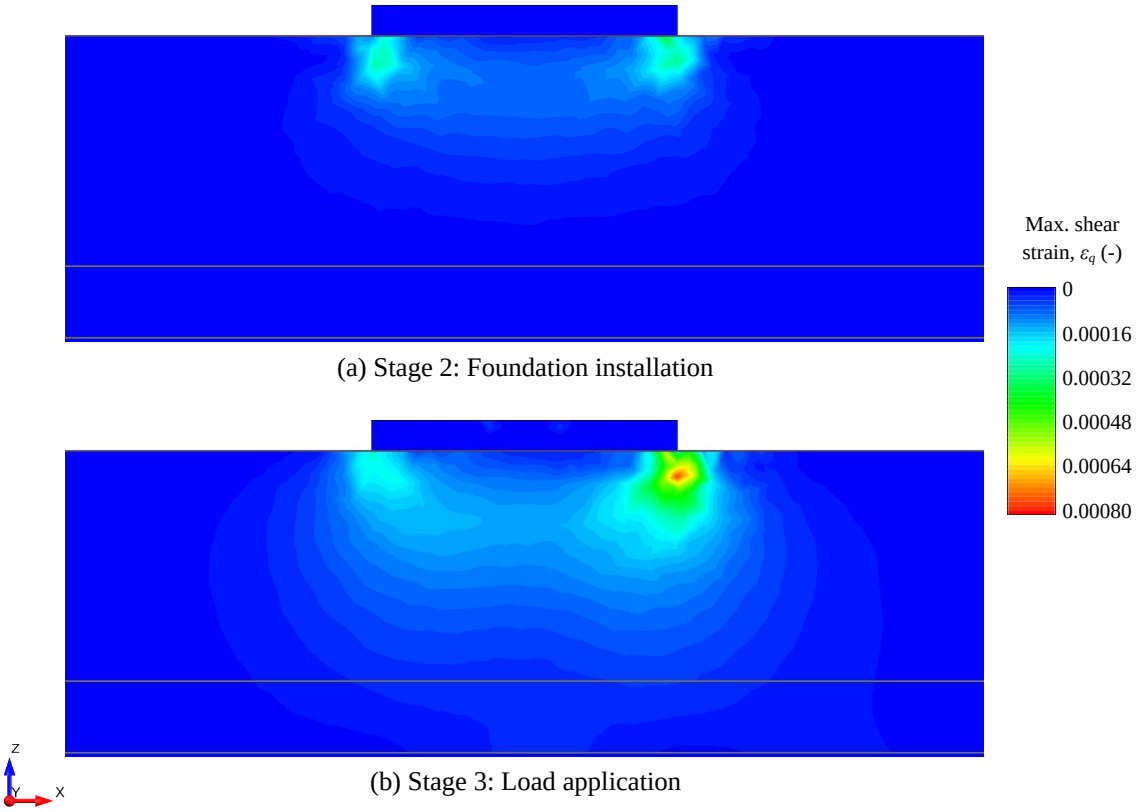

(a) Stage 2: Foundation installation

(b) Stage 3: Load application

Figure 5.2: Shear strains after first loading cycle for Ground Profile A

Based on the output of shear strains illustrated above, an isosurface of the degradation shear strain threshold γ_{tv} was plotted. In doing so, the assumed characteristic value of γ_{tv} = 0.00023 was converted to an equivalent value of ε_q using Equation 4.2, which yielded ε_q = 0.0001878. This conversion was to ensure compatibility between the value of γ_{tv} and the outputs of RS^3. With this, the isosurface of γ_{tv} is illustrated in Figure 5.3 for the first loading cycle. As indicated in the cross-section in Figure 5.3(a), this isosurface reached a maximum depth of 5.97 m, which was

normalised relative to the foundation width (diameter) B = 18 m as approximately 0.33B. From the 3D view of the γ_{tv} isosurface shown in Figure 5.3(b), it was evident that it was concentrated around the edges of the foundation, with it reaching greater depths on the leeward side due to the application of the large overturning moment.

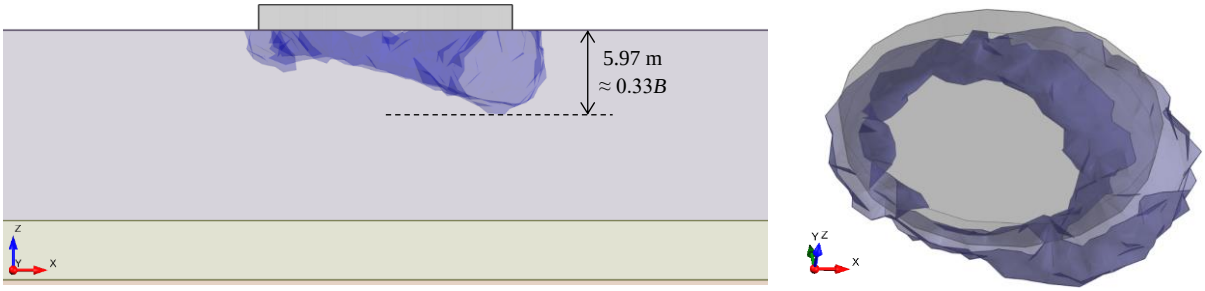

(a) Cross-section (b) 3D view

Figure 5.3: Isosurface of γ_{td} after first loading cycle for Ground Profile A

In line with the modelling methodology, the first stiffness iteration was undertaken by reducing the stiffness of the soil by a factor of δ = 0.95 up to a depth of a third of the maximum depth of the γ_{tv} isosurface. As mentioned previously, this depth was selected as it was deemed to be representative of the average depth of the γ_{tv} isosurface, which varied unevenly below the foundation. Accordingly, a new soil layer was added below the foundation-soil interface with a thickness of 5.97/3 = 1.99 m, and the stiffness of this layer adjusted to $\delta \times G_0$ = 0.95 × 60 = 57 MPa. Using this softened profile, the model was computed again and a new isosurface of γ_{tv} plotted, as shown in Figure 5.4(a). From the outcome, it was evident that the resultant isosurface did not actually increase in depth relative to before, but rather decreased from 5.97 to 5.71 m. Although this was initially interpreted as counter-intuitive, the reason for it was believed to be that, as the soil directly below the foundation-soil interface decreased in stiffness, the strains spread further in the lateral direction rather than in the vertical direction, as it offered the path of lesser resistance. The occurrence of this increased lateral spread of strain stemmed from the assumption in the modelling methodology that the soil stiffness would degrade uniformly in the horizontal plane below the foundation, rather than just on the leeward side where the strains were the highest. However, this assumption was justified for this study on the basis that the wind turbine can receive wind from any direction, and consequently the degradation would conceivably even out beneath the entire foundation area over time.

The second stiffness iteration was subsequently conducted by again adding a new soil layer to the model, on this occasion directly below the soil layer from the previous iteration. The thickness of this soil layer was equal to half of the vertical distance between the maximum depth of the previous γ_{tv} isosurface, and the bottom of the previous layer. This thickness was thus calculated to be (5.71–1.99)/2 = 1.86 m. The value of G_0 within this new layer was then reduced by a factor of δ = 0.95, whereas the factor for the soil layer from the first iteration was decreased to δ = 0.9. The model was then computed and the new γ_{tv} isosurface plotted. For this stiffness iteration, the isosurface increased in depth to 6.21 m, as indicated in Figure 5.4(b).

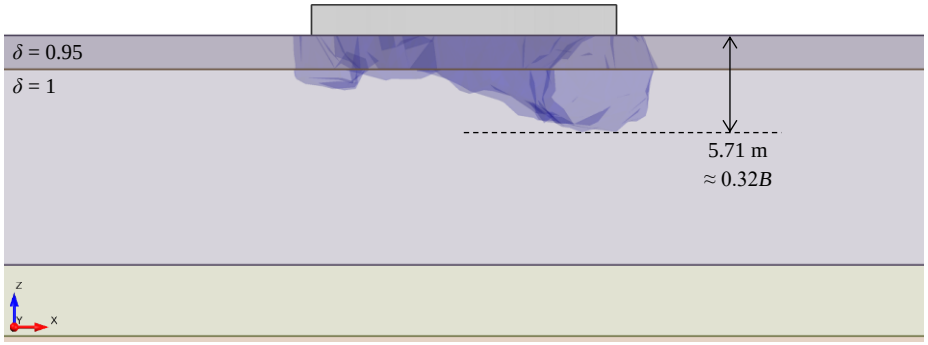

(a) Iteration 1

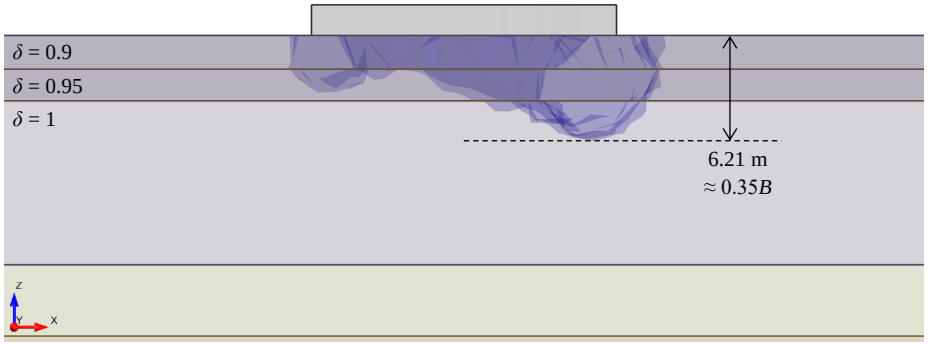

(b) Iteration 2

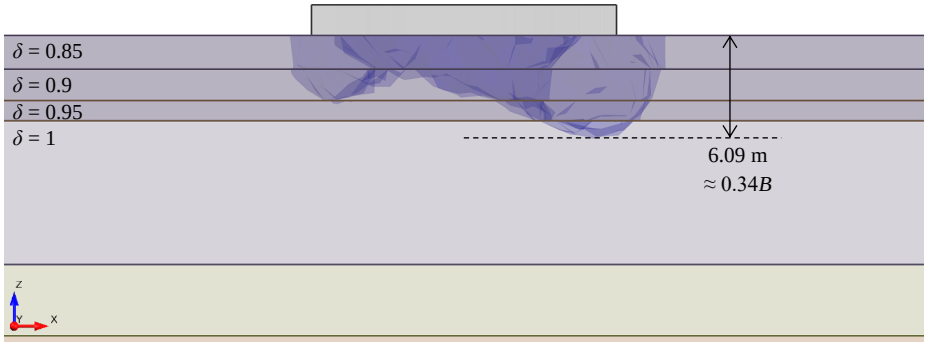

(c) Iteration 3

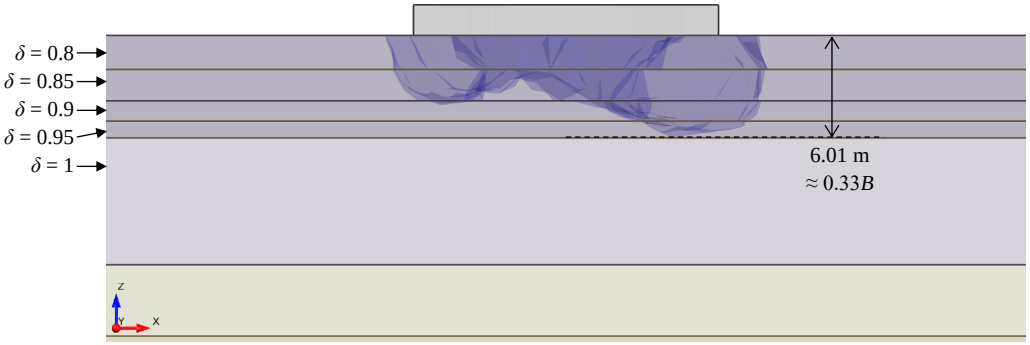

(d) Iteration 4

Figure 5.4: Progression of γ_{td} isosurfaces for stiffness iterations 1-4 for Ground Profile A

The same procedure described above was repeated for stiffness iteration 3, shown in Figure 5.4(c). As for the first stiffness iteration, the maximum depth of the γ_{tv} isosurface in this iteration decreased relative to the previous one, this time from 6.21 to 6.09 m. This was again attributed to the notion that the strains spread further laterally, rather than vertically, as the lateral direction offered the path of lesser resistance. For stiffness iteration 4, the maximum depth of the γ_{tv} isosurface further decreased to 6.01 m, illustrated in Figure 5.4(d). Note that the bottom of the new soil layer added for this iteration was conservatively taken to the maximum depth of the isosurface from iteration 3. This was because, if the thickness of this layer had rather been taken as half of the distance between the previous layer and the maximum depth of the isosurface, as specified in the modelling methodology, it would have been relatively thin. Thus, its discretisation would have resulted in an excessive number of elements due to the software attempting to keep their aspect ratios acceptable, and consequently the computational time of the model would have increased exponentially.

The results for stiffness iteration 5 are illustrated in Figure 5.5(a). On this occasion, because the isosurface from iteration 4 did not exceed the depth of the most recent soil layer that was added, as evident from Figure 5.4(d), the thickness of the new soil layer for iteration 5 was taken to be equal to 1 m, directly below the previous soil layer. Despite this conservative assumption, this iteration resulted in a negligible change in the maximum depth of the γ_{tv} isosurface.

For stiffness iterations 6, 7, and 8, shown in Figure 5.5(b), (c) and (d) respectively, no new soil layers were added to the model as the isosurfaces did not exceed the maximum depth of the layer added in iteration 5. Rather, only the stiffness of the soil was degraded in these iterations, with the values of δ indicated in the respective figures. It is shown that despite the progressive softening of the soil moduli, the isosurfaces only marginally increased in depth. The iterative procedure was ended at iteration 8, where the maximum normalised depth of the isosurface was approximately 0.37B. This was selected to be the last iteration because the δ value of 0.6 was deemed to be a reasonable lower bound value, as discussed in the subsequent section. Nonetheless, the depth of influence of the cyclic degradation was rounded up to be approximately 0.4B for Ground Profile A.

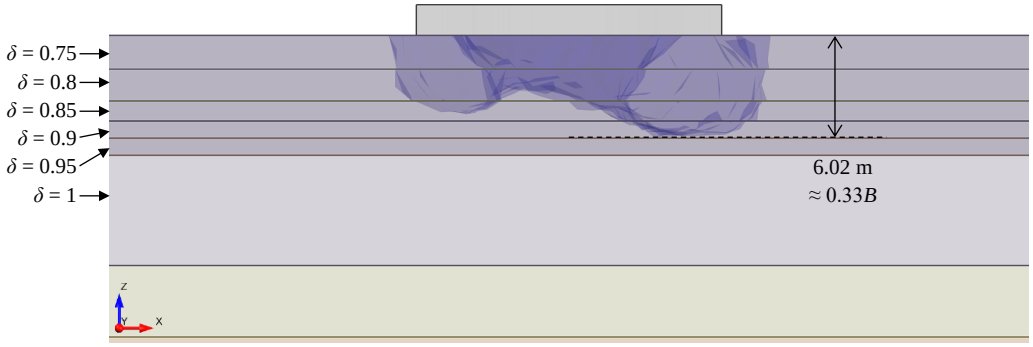

(a) Iteration 5

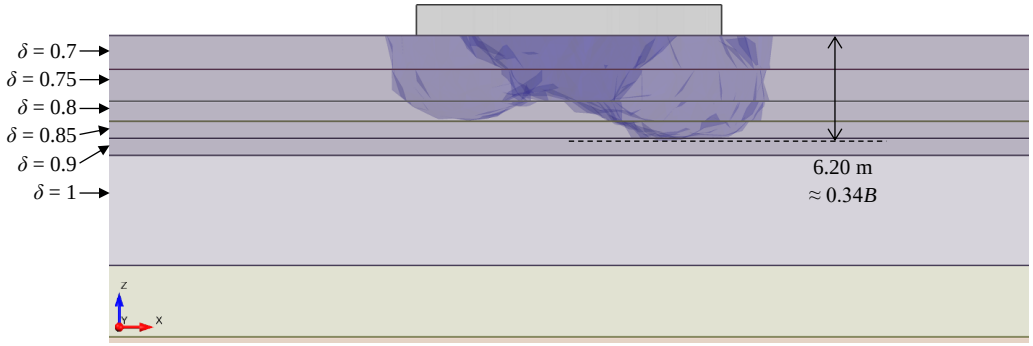

(b) Iteration 6

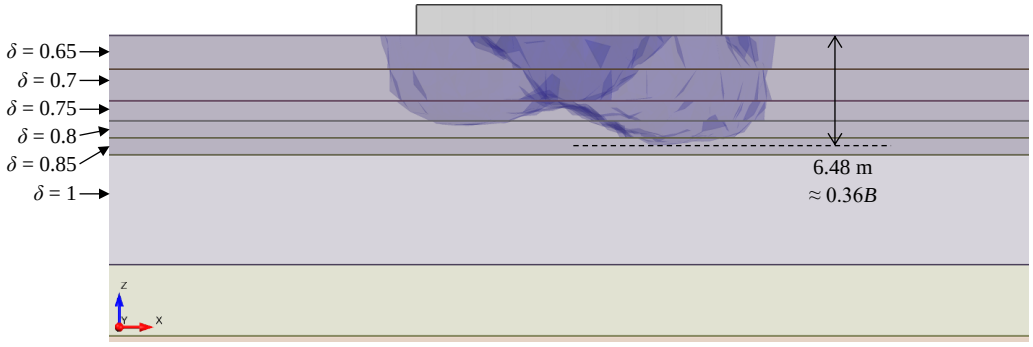

(c) Iteration 7

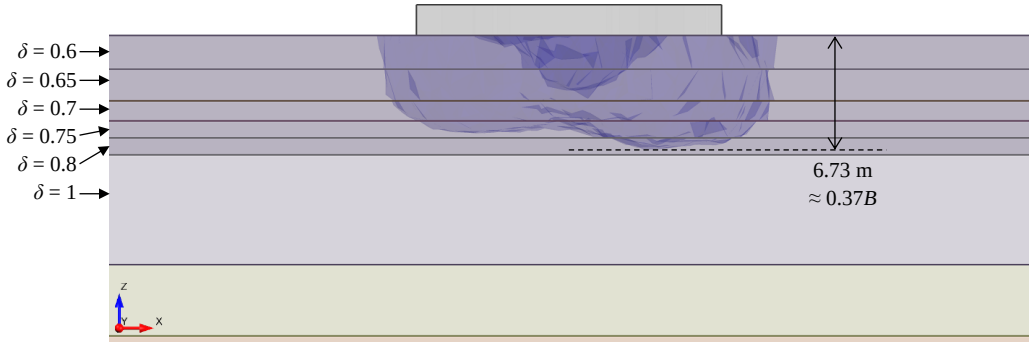

(d) Iteration 8

Figure 5.5: Progression of γ_{td} isosurfaces for stiffness iterations 5-8 for Ground Profile A

5.2.2 Impact on foundation design

Having estimated the depth of influence of cyclic degradation for Ground Profile A to be approximately 0.4*B*, the impact that this had on the required size of the foundation was assessed. This was undertaken by considering two separate cases of the ground stiffness profile. The first corresponded to an upper limit, which was representative of the initial in-situ stiffness as determined from the CSW test, and the second was a lower limit, which accounted for degradation by applying a reduction factor to the ground modulus up to the depth of 0.4*B*.

Although the numerical modelling was conducted to assess the depth of influence of cyclic degradation, it was unable to estimate the amount of degradation that would eventually occur. That is, the magnitude of the reduction factor to be applied to the ground modulus in the lower bound stiffness profile could not be evaluated from the numerical modelling. This was because, following the same degradation model proposed by Idriss *et al.* (1978) as before, in which $\delta = N^{-t}$, the reduction factor (equivalent to the degradation index δ) is in principle dependent on the number of loading cycles N, as well as the degradation parameter t. The value of the former parameter is, to an extent, arbitrary and at the discretion of the designer. The latter parameter is dependent on the amplitude of the cyclic shear strain induced in the soil, and is difficult to characterise considering that the distribution of shear strain is nonuniform and varies to a great extent below the foundation.

Considering the above, the value of δ that was applied to the lower bound stiffness profile was determined analytically. For this, reference was made to Figure 3.7(b), which is a chart correlating γ_c and t for varying PI, as proposed by Vucetic (1992). This chart is reproduced in Figure 5.6 below. Using the curve corresponding to a PI of 15%, and the suggested value of γ_c = 0.001 from DNV/Risø (2002), which correlated well with the strains shown in Figure 5.2, t was estimated to be ~0.03 as shown below.

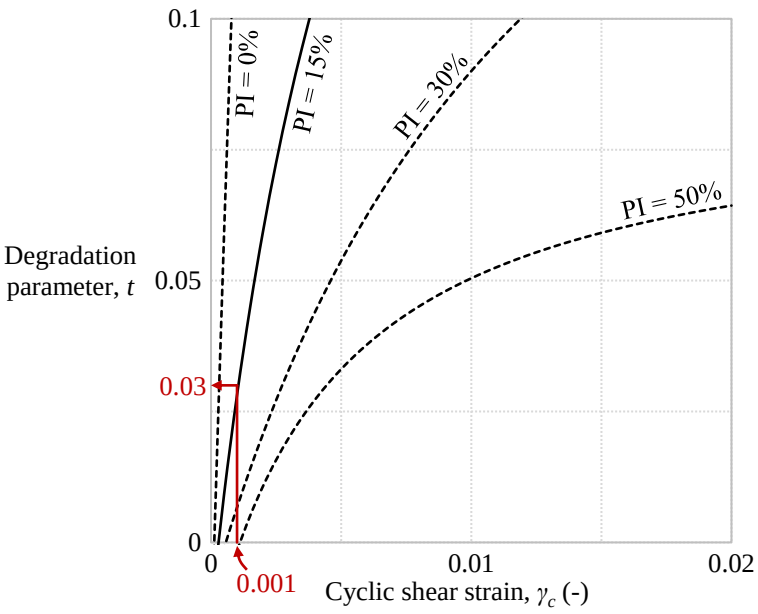

Figure 5.6: Relationship between degradation parameter *t* and γ_c for varying PI
Adapted from Vucetic (1992)

To assess the influence that the assumed value of t had on δ, a plot of the latter parameter's variation with N is presented in Figure 5.7, which is again based on the equation $\delta = N^{-t}$. This plot is shown for 10^7 loading cycles, as this is the number of loading cycles that Vestas (2013) associated with the fatigue load case in the loading document for the Vestas V112-3.0 MW turbine. For this number of loading cycles, δ reduces to 0.62 for t = 0.03. Similarly, considering more conservative values of t of 0.04 and 0.05, δ reduces to 0.52 and 0.45 respectively. All of these values of δ are in agreement with Yu *et al*. (2016), who on the basis of a review of literature by various authors, state that a degradation level of between 40 to 60% (δ = 0.6 to 0.4) is typical for wind turbine foundations, albeit for piles specifically.

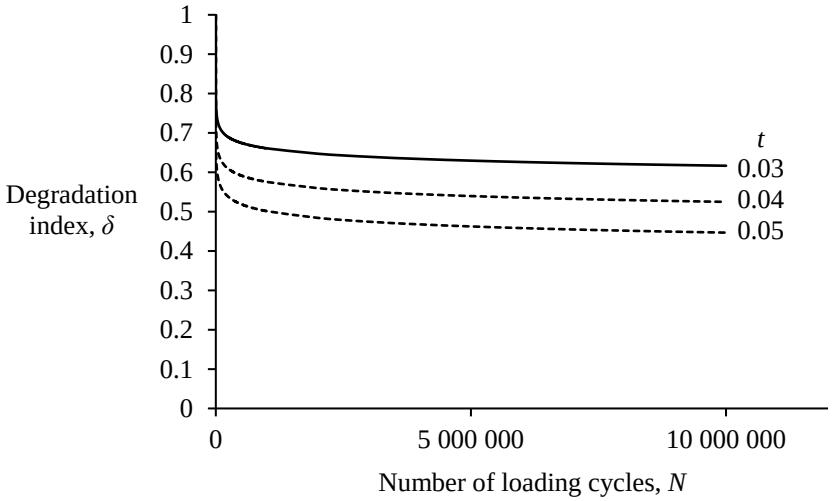

Figure 5.7: Degradation index versus number of loading cycles

Considering the information presented above, it was deemed reasonable to apply a δ value of 0.6 to the depth of influence of cyclic degradation in the lower bound stiffness profile. Although this was at the upper end of the range suggested by Yu *et al*. (2016), and only correlated well with the assumed value of t = 0.03, it was regarded as appropriate for this foundation design due to two primary reasons. The first was that, over the course of 10^7 loading cycles, or less, there would inevitably be some pore pressure dissipation that would lead to a recovery of δ closer to a value of unity. The second reason was that the value of δ was applied within the full depth of influence of cyclic degradation determined from the numerical modelling. This was a conservative simplification because, in reality, the soil closer to the foundation-soil interface would degrade at a faster rate than the soil further below, as it experiences a higher amplitude of cyclic shear strain, and thus has a larger t. Hence, the overall approach of applying the reduction factor was considered conservative, and thus warranted a marginally less conservative value of δ.

The undegraded and degraded stiffness profiles for Ground Profile A are shown in Figure 5.8(a) and (b). For each of these profiles, the mass shear modulus G_{mass} was calculated using the procedure proposed by Fraser and Wardle (1976). These calculations, including all associated assumptions, are presented in §B.1 of Appendix B. The result of this was G_{mass} = 24.9 MPa for the upper bound stiffness profile, and G_{mass} = 18.6 MPa for the lower bound stiffness profile.

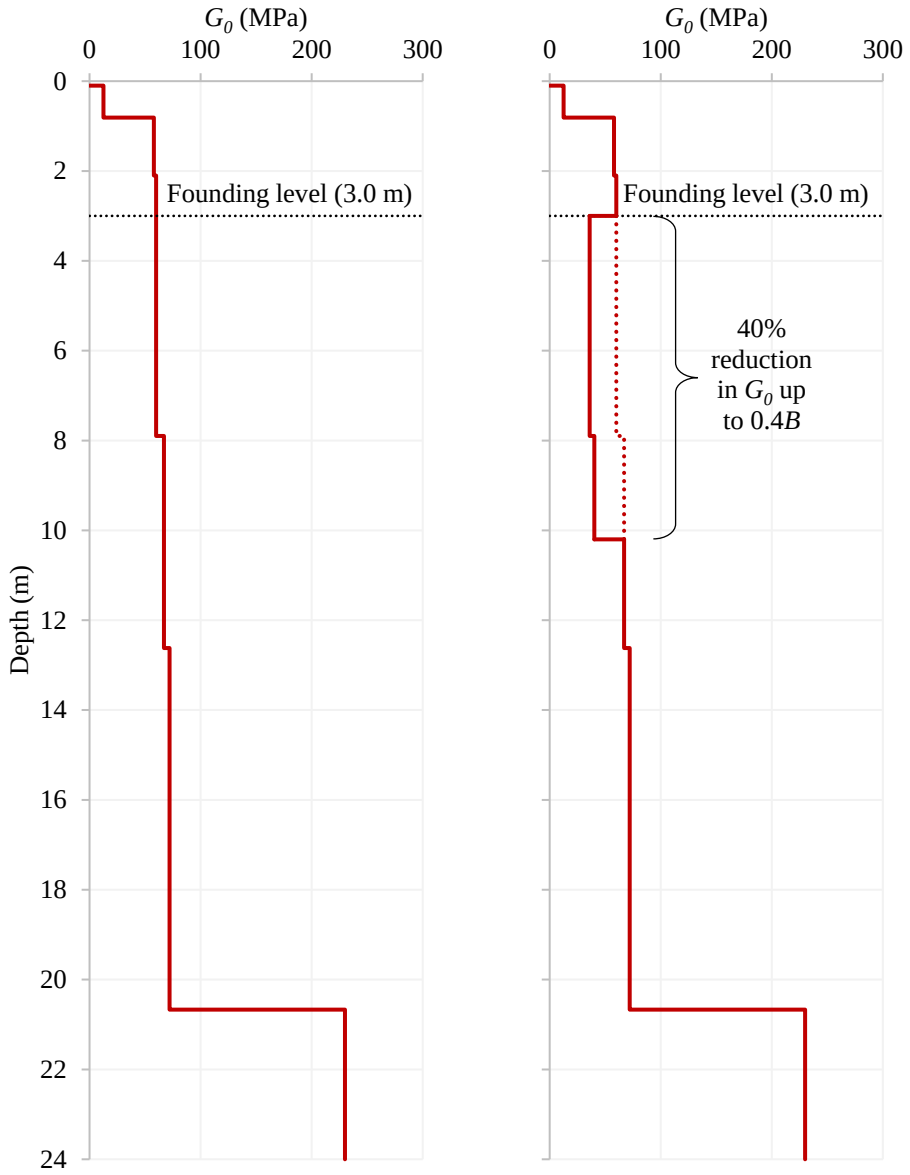

(a) Case 1: Upper bound stiffness profile (b) Case 2: Lower bound stiffness profile

Figure 5.8: Upper and lower bound stiffness profiles for Ground Profile A

Subsequently, the G_{mass} value of each stiffness profile was used to calculate the minimum required foundation diameter, based solely on the stiffness requirements stipulated by the wind turbine manufacturer. Details of these calculations are also provided in §B.1 of Appendix B. From this, the minimum required foundation diameter for the upper bound stiffness profile was calculated to be 16.0 m, whereas the diameter increased to 17.6 m for the lower bound stiffness profile. Therefore, by accounting for cyclic degradation in the foundation design, the required diameter of the foundation increased by 10%. Considering that the diameter of a wind turbine foundation typically ranges from 15 to 20 m (Ntambakwa *et al.*, 2016), the increase in diameter could have potentially caused the stiffness requirements to become the design driver for this foundation. However, the occurrence of this is dependent on whether the minimum required diameters from the ULS and SLS design checks exceed 17.6 m.

5.3 Ground Profile B

Ground Profile B was representative of a clayey profile with bedrock located at a depth equal to half of the foundation diameter. The primary purpose of modelling this profile was to assess the effect that bedrock, located in relatively close proximity to the ground surface, would have on the degradation of the soil above it. Specifically, to determine whether its presence would influence the distribution of shear strain, and possibly suppress it from advancing deeper into the soil profile.

The 3D model of Ground Profile B is shown in Figure 5.9, as developed in *RS*^{3}. The results of the numerical analyses of this model are subsequently discussed with respect to the depth of influence of cyclic degradation. This is followed by an assessment of the effect that the cyclic degradation had on the minimum required diameter of the foundation.

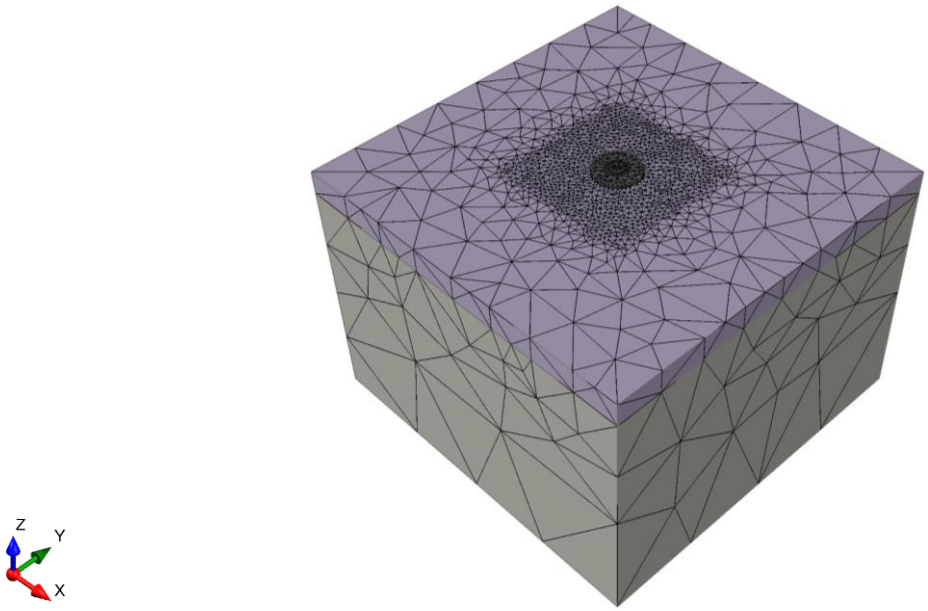

Figure 5.9: Model of Ground Profile B

5.3.1 Depth of influence of degradation

The cross-sectional plot of maximum shear strain, taken through the centre of the foundation, is illustrated in Figure 5.10 for the first loading cycle of Ground Profile B. For Stage 3 of the FE model, which involved the application of the horizontal and moment loads in addition to the vertical load from Stage 2, the shear strain peaked at ε_q = 0.00063. This corresponded to γ = 0.00077 using Equation 4.2. This maximum shear strain was approximately 21% less than that of Ground Profile A for the first loading cycle, despite the stiffness of the soil being identical in the upper layers of the two models. Nonetheless, this shear strain was still less than that suggested by DNV/Risø (2002) of γ_c = 0.001, and thus was deemed to be a reasonable output of the model. Furthermore, again due to the foundation being modelled with rigid behaviour, the strains were primarily concentrated around the edges of the foundation.

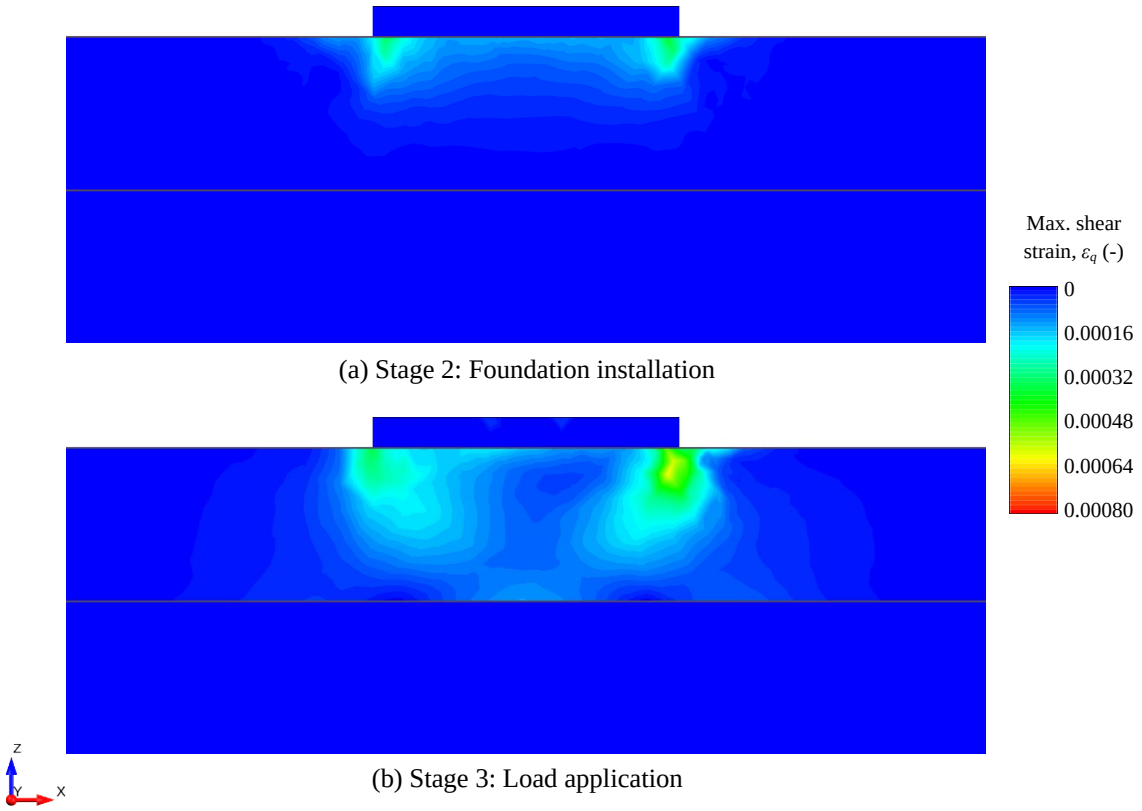

(a) Stage 2: Foundation installation

(b) Stage 3: Load application

Figure 5.10: Shear strains after first loading cycle for Ground Profile B

An isosurface of the degradation shear strain threshold γ_{tv} was plotted based on the distribution of shear strains illustrated above, as shown in Figure 5.11. This isosurface reached a maximum depth of 5.54 m, which was normalised relative to the foundation diameter as approximately 0.31*B*. This depth was slightly less than the depth of the γ_{tv} isosurface for the first loading cycle of Ground Profile A, which was 5.97 m, or 0.33*B*. Therefore, the presence of the stiff bedrock stratum had a marginal effect on the depth of the shear strains in the first loading cycle.

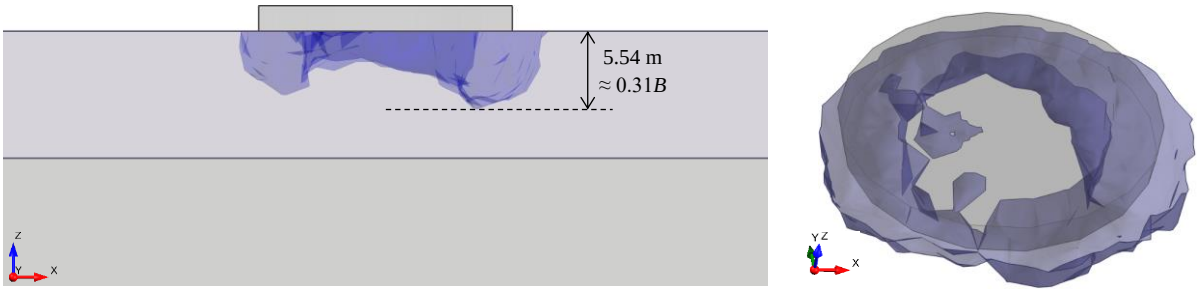

(a) Cross-section

(b) 3D view

Figure 5.11: Isosurface of γ_{td} after first loading cycle for Ground Profile B

The modelling strategy was subsequently implemented to estimate the depth of influence of cyclic degradation. The first four stiffness iterations are illustrated in Figure 5.12. As for several of the stiffness iterations for Ground Profile A, the maximum depths of the γ_{tv} isosurfaces in these four stiffness iterations marginally decreased as the profile became softer. This was likely a result of the strains spreading further laterally, due to the stiffness reductions having been implemented within the entire horizontal plane.

For the latter four stiffness iterations, shown in Figure 5.13, the maximum depths of the γ_{tv} isosurfaces continued to increase gradually. At the end of the final stiffness iteration, the maximum normalised depth of the γ_{tv} isosurface was 0.36*B*. This result was almost identical to that of Ground Profile A, which had a corresponding depth of approximately 0.37*B* in the final iteration. Therefore, the presence of the bedrock layer, which was in close proximity to the founding level, did not have a significant impact in limiting the advancement of the γ_{tv} isosurfaces deeper into the soil profile. Accordingly, as for Ground Profile A, the depth of influence of cyclic degradation was rounded up to approximately 0.4*B* for Ground Profile B.

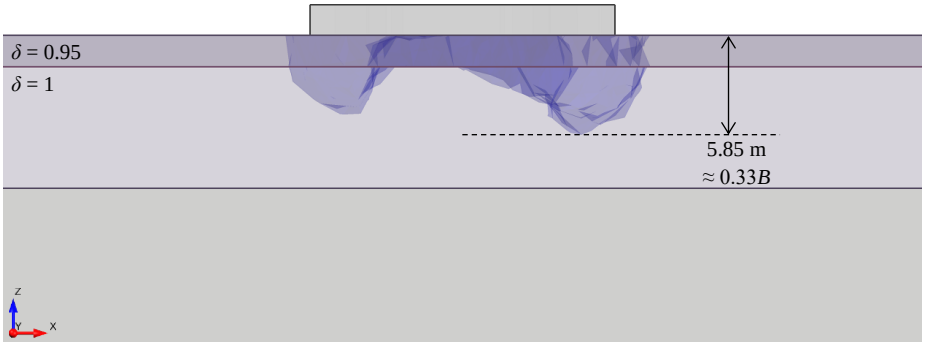

(a) Iteration 1

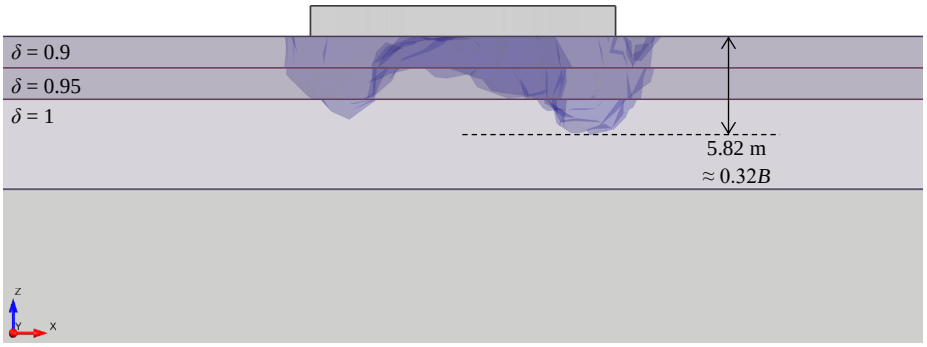

(b) Iteration 2

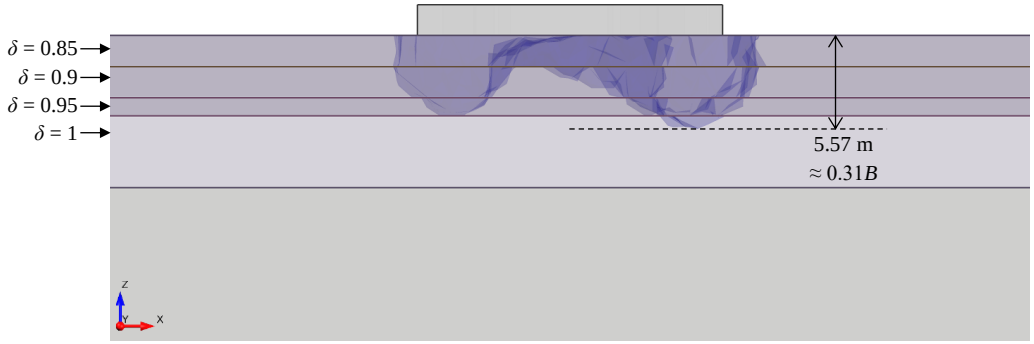

(c) Iteration 3

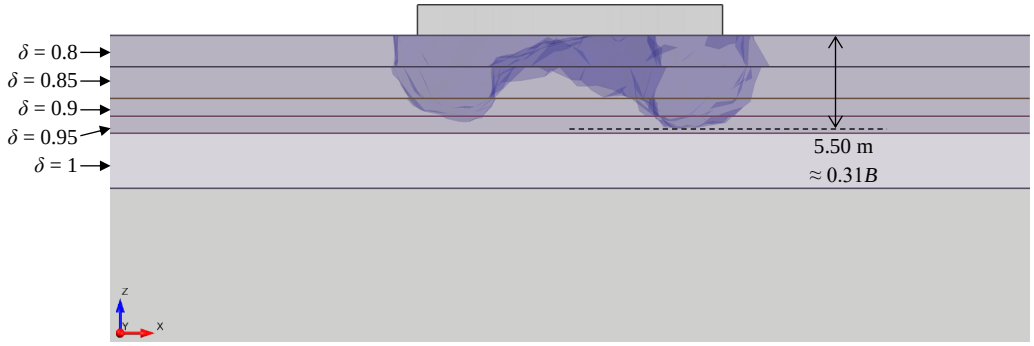

(d) Iteration 4

Figure 5.12: Progression of γ_{td} isosurfaces for stiffness iterations 1-4 for Ground Profile B

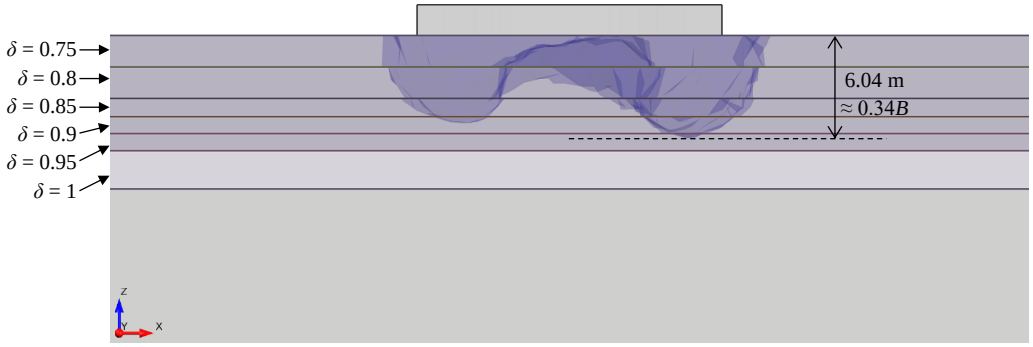

(a) Iteration 5

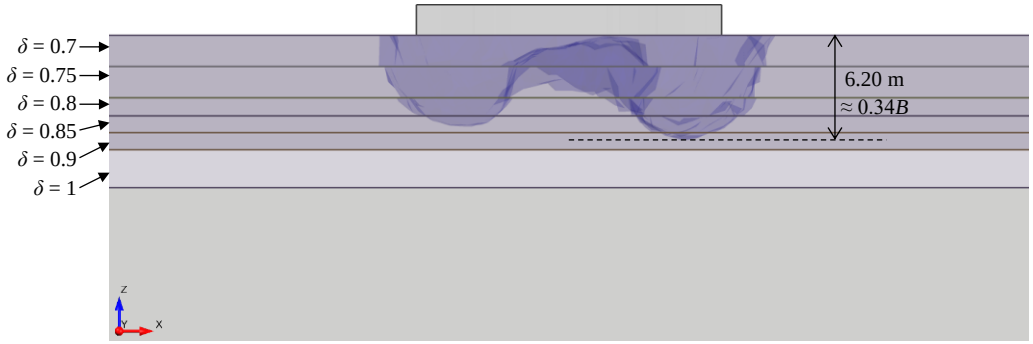

(b) Iteration 6

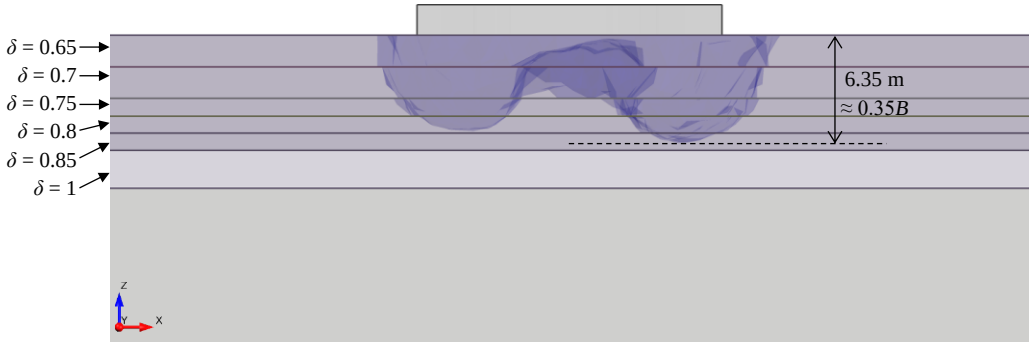

(c) Iteration 7

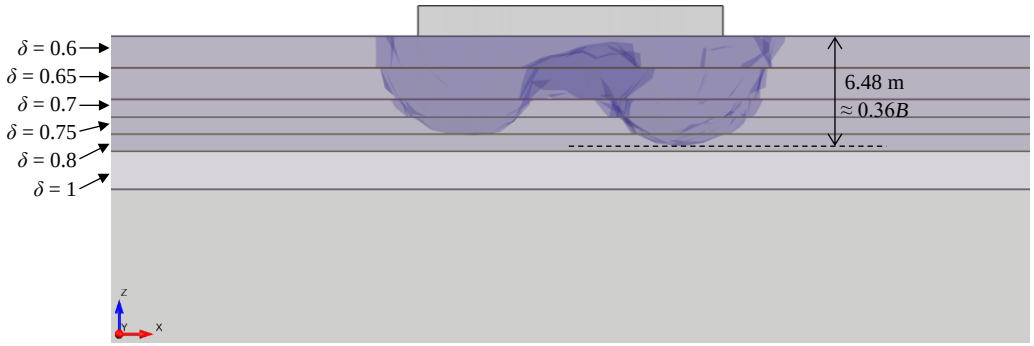

(d) Iteration 8

Figure 5.13: Progression of γ_{td} isosurfaces for stiffness iterations 5-8 for Ground Profile B

5.3.2 Impact on foundation design

The impact that the cyclic degradation had on the foundation design was assessed by calculating the minimum required foundation diameter for the upper and lower bound stiffness profiles. These stiffness profiles are illustrated in Figure 5.14 for Ground Profile B. Note that the cyclic degradation was accounted for in the lower bound stiffness profile by applying the same factor of $\delta = 0.6$ as was used for Ground Profile A, within the estimated depth of influence of $0.4B$.

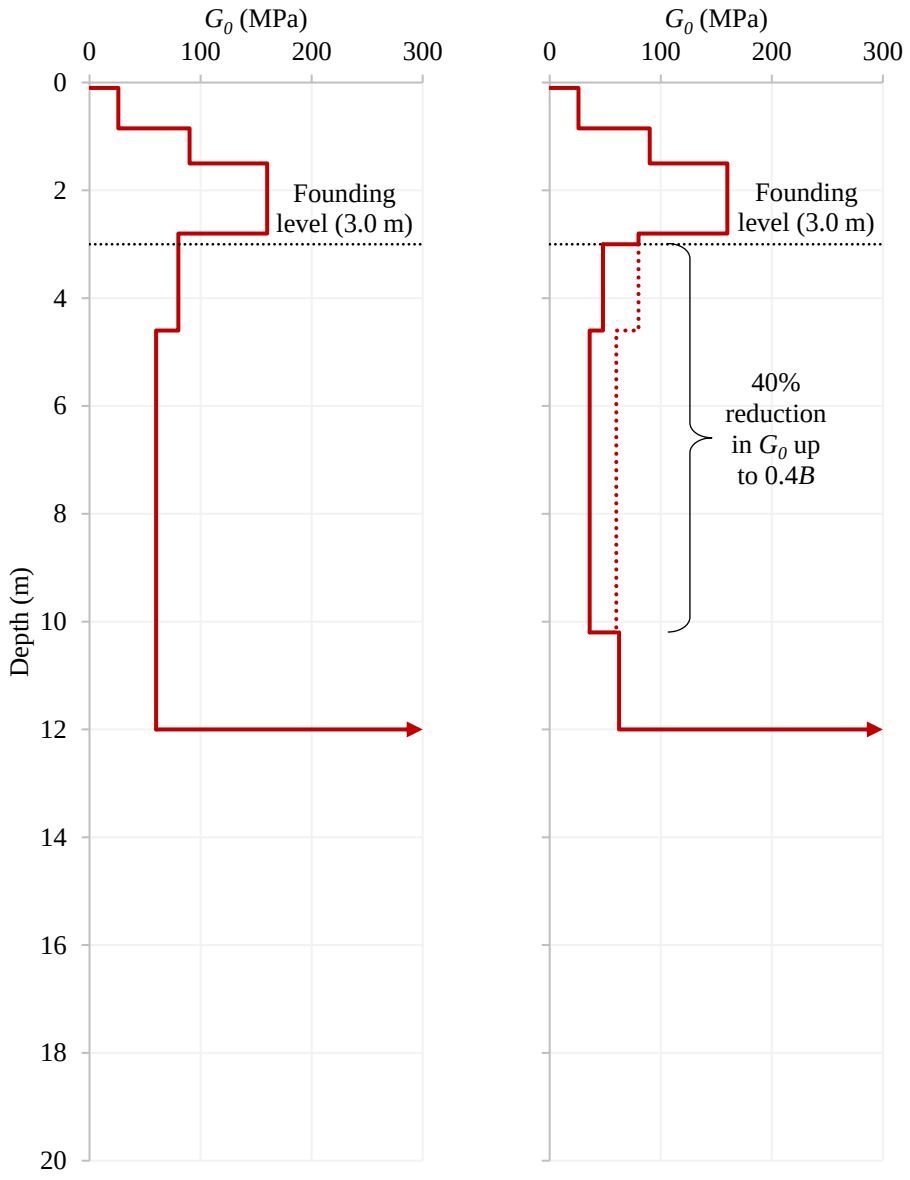

(a) Case 1: Upper bound stiffness profile (b) Case 2: Lower bound stiffness profile

Figure 5.14: Upper and lower bound stiffness profiles for Ground Profile B

Using the method developed by Fraser and Wardle (1976), the mass shear modulus G_{mass} was calculated for both the undegraded and degraded stiffness profiles. This was undertaken up to the level of the bedrock only, as the procedure for calculating the foundation diameter differed

in this case due to the presence of the bedrock. Nonetheless, G_{mass} was estimated to be 22.0 MPa for the upper bound stiffness profile, and 14.3 MPa for the lower bound stiffness profile. Details of these calculations are presented in §B.2 of Appendix B.

The values of G_{mass} were subsequently used to calculate the minimum required foundation diameter based on the wind turbine manufacturer's stiffness requirements. These calculations are also provided in §B.2 of Appendix B. For the upper bound stiffness profile, this minimum diameter was 12.2 m, whereas for the lower bound stiffness profile, this increased to 14.5 m. Although this represented a substantial increase of 19% in the foundation diameter, it was likely to be inconsequential considering that the diameter of a wind turbine foundation typically lies within the range of 15 to 20 m. Therefore, despite the cyclic degradation causing a considerable increase in the required foundation diameter, the stiffness requirements of the foundation were unlikely to govern the design. This was largely due to the presence of the bedrock, which had the effect of increasing the overall ground stiffness, despite the soil above it being relatively soft.

5.4 Ground Profile C

Ground Profile C consisted of a clayey profile with a stratum of very dense sand located at founding level. The 3D model of this is shown in Figure 5.15. The main reason behind modelling this profile was to assess the extent to which a layer of dense sand would act as a contact layer directly below the foundation. That is, to evaluate the effectiveness of this layer in containing the shear strains induced in the soil, and thus preventing cyclic degradation of the more susceptible soils below. As for the previous two ground profiles, the depth of influence of cyclic degradation was first assessed based on the numerical modelling. This was followed by calculating the minimum required foundation diameter for the upper and lower bound stiffness profiles, to determine the impact that accounting for degradation would have on the design.

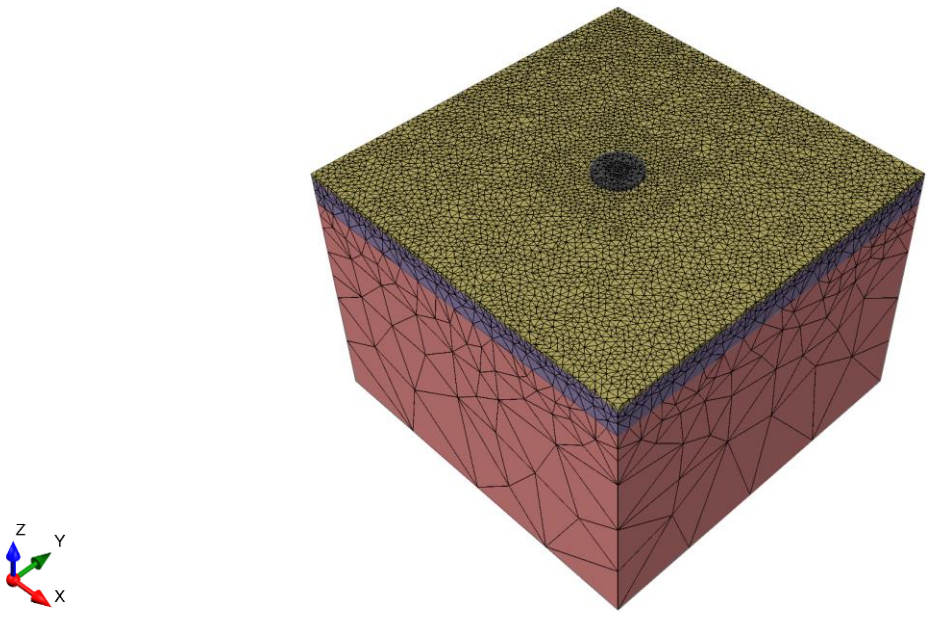

Figure 5.15: Model of Ground Profile C

5.4.1 Depth of influence of degradation

The distribution of maximum shear strain for the first loading cycle of Ground Profile C is presented in Figure 5.16. For Stage 3 of the FE model, this shear strain peaked at ε_q = 0.00053, which corresponded to γ = 0.00065 using Equation 4.2. This shear strain was significantly less than that of Ground Profiles A and B, which peaked at γ = 0.00098 and γ = 0.00077 respectively. This was the case due to the presence of the very dense sand layer, which had a relatively high initial stiffness of G_0 = 390 MPa. Regardless, the peak shear strain was less than that suggested by DNV/Risø (2002) as being typical of cyclic wind loading (γ_c = 0.001), and thus was considered to be an acceptable model output. Moreover, the strains were predominantly concentrated around the edges of the foundation, which was again attributed to the fact that the foundation was modelled as a rigid element.

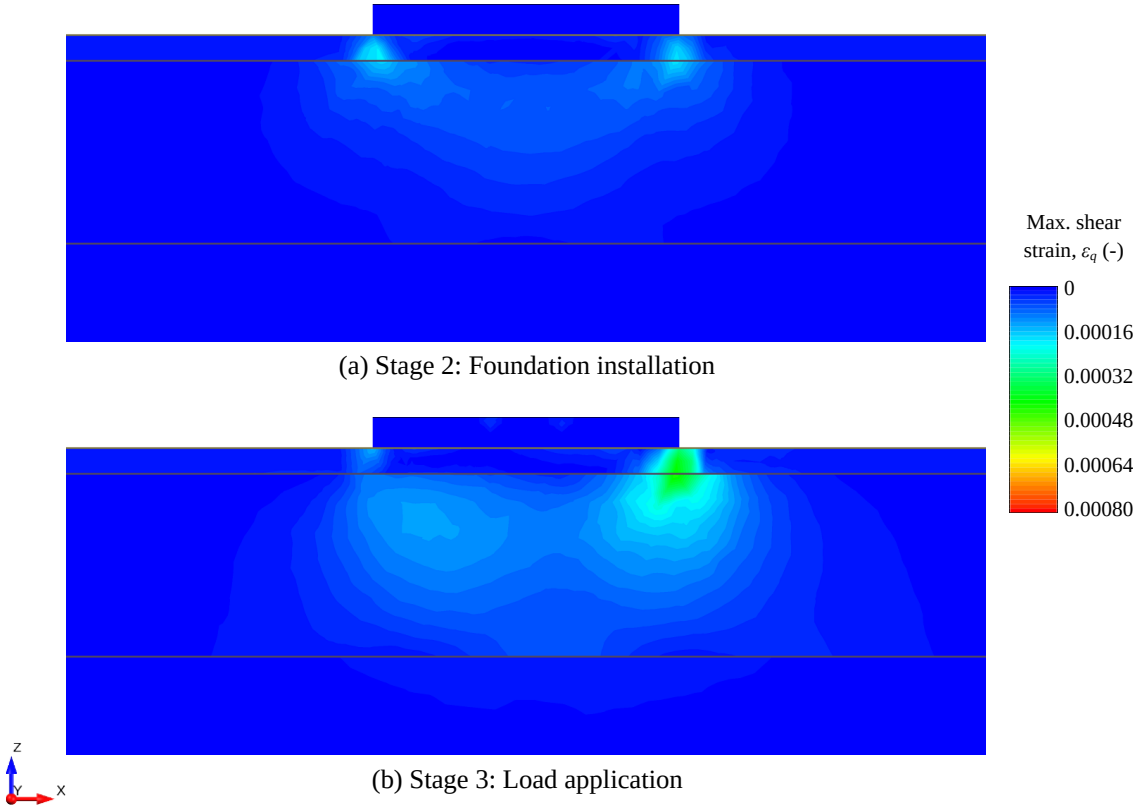

(a) Stage 2: Foundation installation

(b) Stage 3: Load application

Figure 5.16: Shear strains after first loading cycle for Ground Profile C

The isosurface of γ_{tv}, corresponding to the distribution of shear strains illustrated above, is illustrated in Figure 5.17. Relative to the previous two ground profiles, the maximum depth of this isosurface (for the first loading cycle) was moderately less. Specifically, it reached a maximum normalised depth of 0.26*B*, whereas Ground Profiles A and B reached depths of 0.33*B* and 0.31*B*. This was attributed to the presence of the dense sand layer, which had the effect of partially constraining the shear strains induced in the soil. Furthermore, as evident from Figure 5.17, the γ_{tv} isosurface for this ground profile was primarily situated on the leeward side of the

foundation, whereas for Ground Profile B particularly, it was more uniform beneath the foundation as shown in Figure 5.11. This suggested that the cyclic degradation for this ground profile would potentially be predominantly situated on one side of the foundation, which could increase differential settlement.

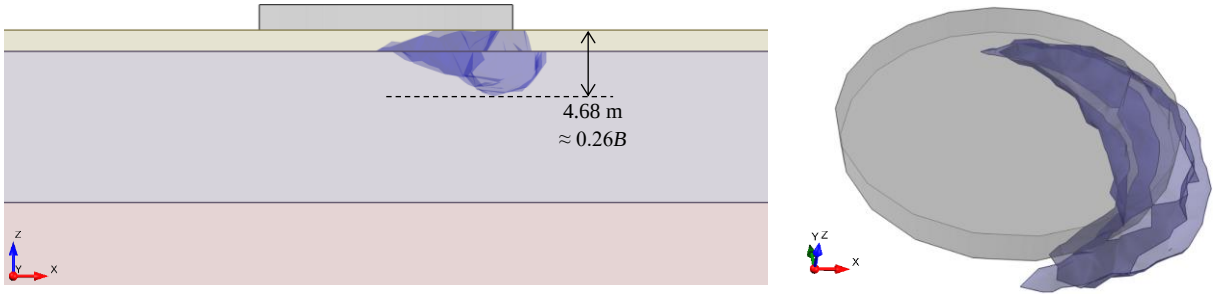

(a) Cross-section (b) 3D view

Figure 5.17: Isosurface of γ_{td} after first loading cycle for Ground Profile A

The depth of influence of cyclic degradation was subsequently estimated by implementing the modelling methodology. Note that for this ground profile, the modulus of the dense sand layer was not degraded for any of the stiffness iterations. This was due to the inherently high permeability of this soil layer, which would cause it to behave as a drained material, consequently preventing the generation of excess pore pressure, which is one of the mechanisms for cyclic degradation.

For the first four stiffness iterations, illustrated in Figure 5.18, the variation in the maximum depth of the γ_{tv} isosurfaces was negligible despite the decrease in stiffness of the profile. Specifically, the maximum depths remained at a normalised depth of approximately 0.26*B*. As for the previous two ground profiles, this was likely due to the strains spreading in the lateral direction, rather than in the vertical direction.

The results for the latter four stiffness iterations are shown in Figure 5.19. For these iterations, the maximum depths of the γ_{tv} isosurfaces continued to increase gradually. As indicated in Figure 5.19(d), the normalised depth of the γ_{tv} isosurface reached 0.30*B* at the end of the last stiffness iteration. This was somewhat less than that of Ground Profiles A and B, both of which were rounded up to 0.4*B*. This indicated that the presence of the dense sand layer did have an impact in limiting the advancement of the γ_{tv} isosurface deeper into the soil profile. Accordingly, for the purpose of the foundation design in the subsequent section, the depth of influence of cyclic degradation was taken to be 0.3*B* for Ground Profile C.

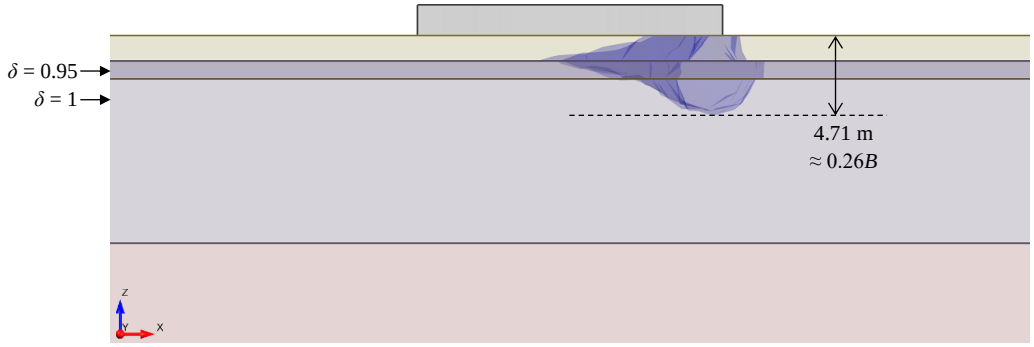

(a) Iteration 1

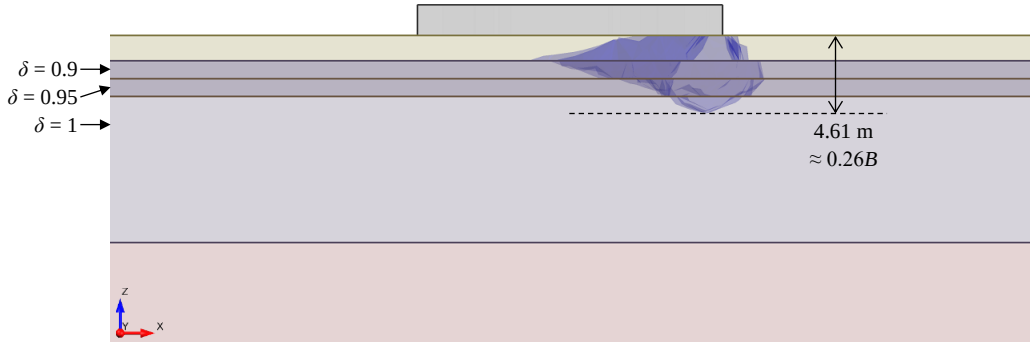

(b) Iteration 2

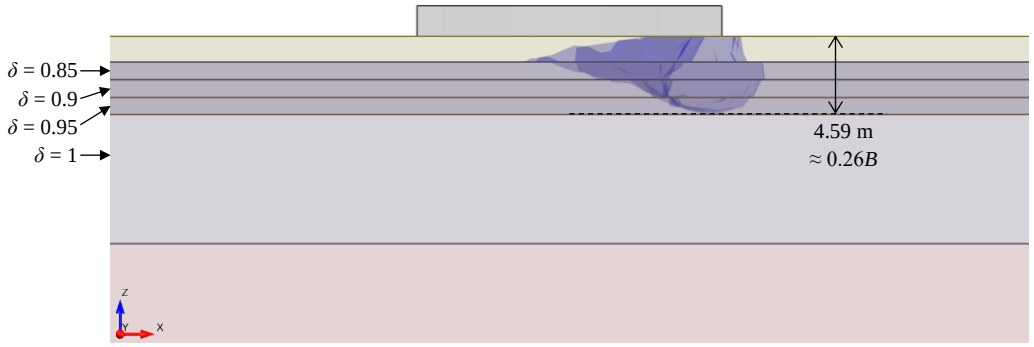

(c) Iteration 3

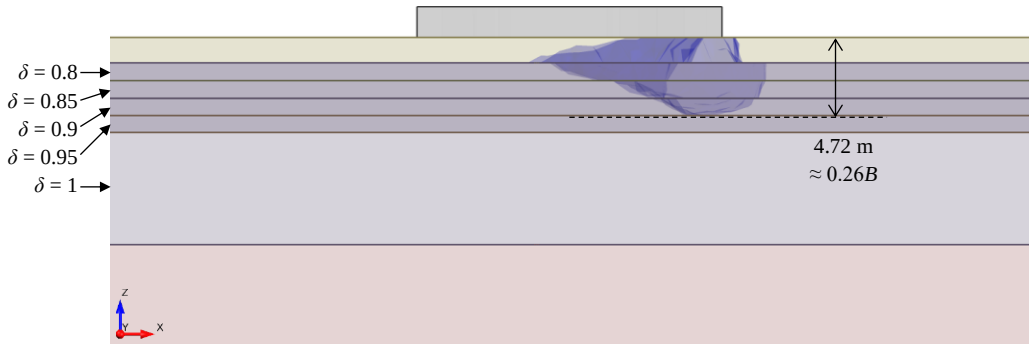

(d) Iteration 4

Figure 5.18: Progression of γ_{td} isosurfaces for stiffness iterations 1-4 for Ground Profile C

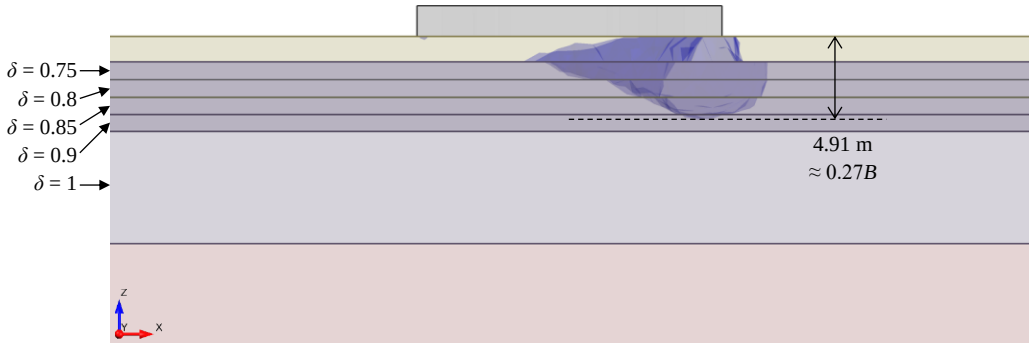

(a) Iteration 5

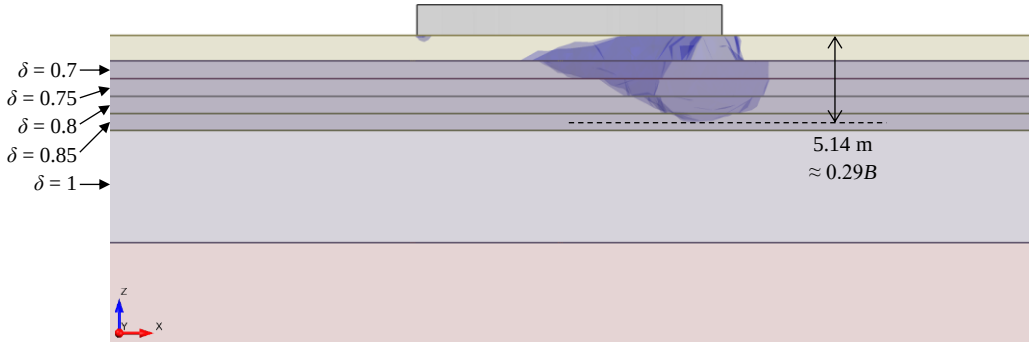

(b) Iteration 6

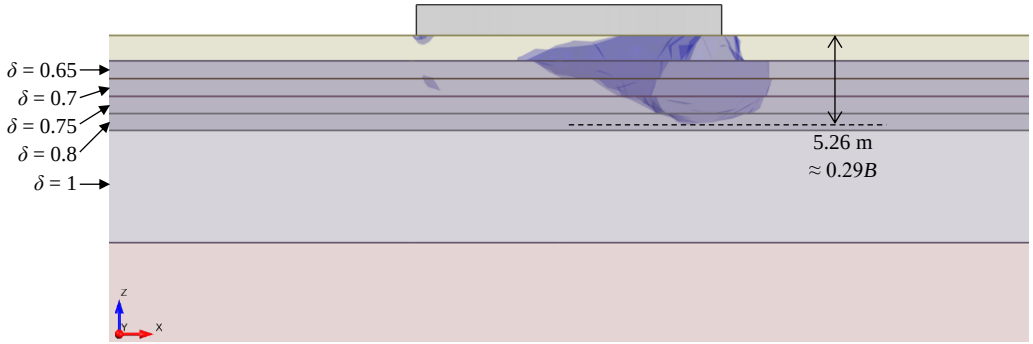

(c) Iteration 7

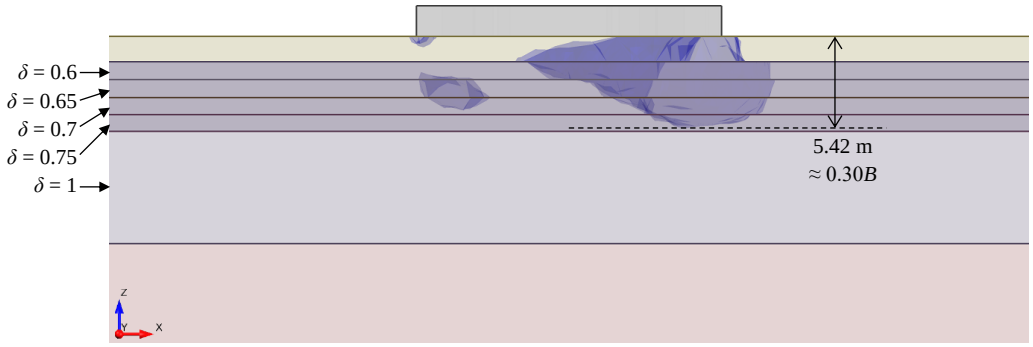

(d) Iteration 8

Figure 5.19: Progression of γ_{td} isosurfaces for stiffness iterations 5-8 for Ground Profile C

5.4.2 Impact on foundation design

The minimum required foundation diameter was calculated for the upper and lower bound stiffness profiles, to assess the impact that accounting for cyclic degradation had on the foundation design. As for the previous two ground profiles, only the stiffness requirements stipulated by the wind turbine manufacturer were considered in this assessment. The upper and lower bound stiffness profiles are illustrated in Figure 5.20 for Ground Profile C. The cyclic degradation was taken into account in the latter profile by applying the same factor as before (δ = 0.6) to the ground modulus within the depth of influence of cyclic degradation, which on this occasion was 0.3*B*. However, note that because cyclic degradation of the dense sand layer was not considered, this factor was not applied to the ground modulus within 1.5 m of founding level, where this coarse-grained material was situated.

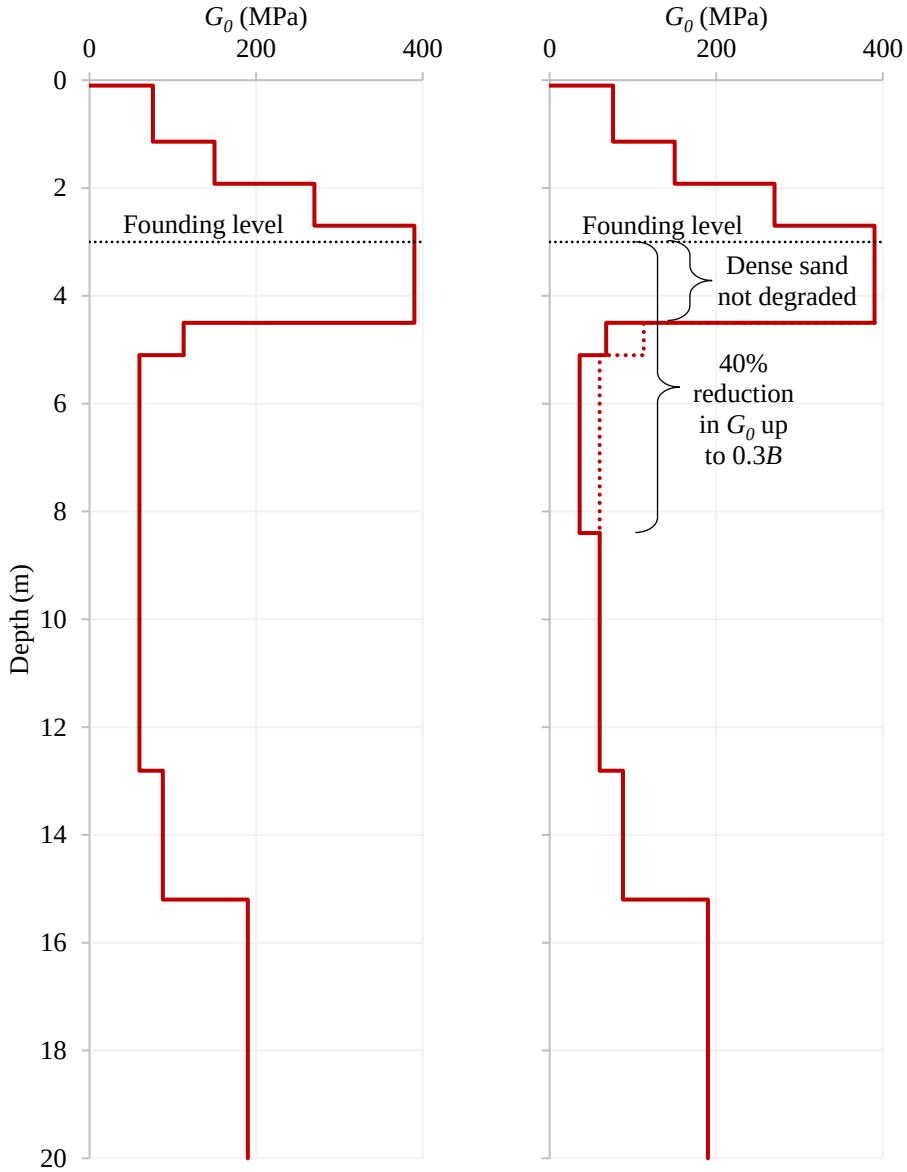

(a) Case 1: Upper bound stiffness profile (b) Case 2: Lower bound stiffness profile

Figure 5.20: Upper and lower bound stiffness profiles for Ground Profile C

The mass shear modulus G_{mass} was calculated for both stiffness profiles illustrated above using the method by Fraser and Wardle (1976). These calculations are shown in §B.3 of Appendix B. The result of this was a G_{mass} of 30.9 MPa for the upper bound stiffness profile, and 24.8 MPa for the lower bound stiffness profile. These values were subsequently used to calculate the minimum required foundation diameter based on the stiffness requirements, with details of this also shown in §B.3 of Appendix B. The upper bound stiffness profile required a minimum diameter of 15.1 m, whereas this increased to 16.2 m for the lower bound stiffness profile. Consequently, accounting for cyclic degradation in this foundation design resulted in an approximate increase of 7% in the foundation diameter.

Considering that the diameter of wind turbine foundations typically range from 15 to 20 m, accounting for degradation in this design could have caused the stiffness requirements to be the design driver, depending on the results of the ULS and SLS design checks. Despite this, it must be acknowledged that the presence of the dense sand layer substantially decreased the required foundation diameter relative to the situation in which it was absent. This was observed by comparing Ground Profiles A and C, which had very similar stiffness characteristics, barring the dense sand layer. The former required a foundation diameter of 17.6 m for the lower bound stiffness profile, whereas the corresponding requirement for Ground Profile C was 16.2 m. Therefore, the dense sand layer substantially reduced the required size of the foundation, despite it only reducing the amount of degradation that would occur by a limited margin.

The above discussion illustrates the potential for ground improvement techniques to provide more economical foundation solutions, particularly when soils that are susceptible to cyclic degradation are present. For instance, soil replacement, geosynthetic reinforcement, or stone columns can be implemented to perform a similar role as the dense sand layer did in this design, potentially resulting in more cost-effective foundations.

5.5 Parametric Study

The study was conducted with the simplified model shown in Figure 5.21. This consisted of only one soil type so that the parameters could be varied uniformly throughout the soil body. As before, the output of interest in these analyses was the maximum depth to which the degradation shear strain threshold γ_{td} was reached. Furthermore, only the first loading cycle was modelled for each variation of the input parameters, as this provided sufficient data to draw comparisons between them.

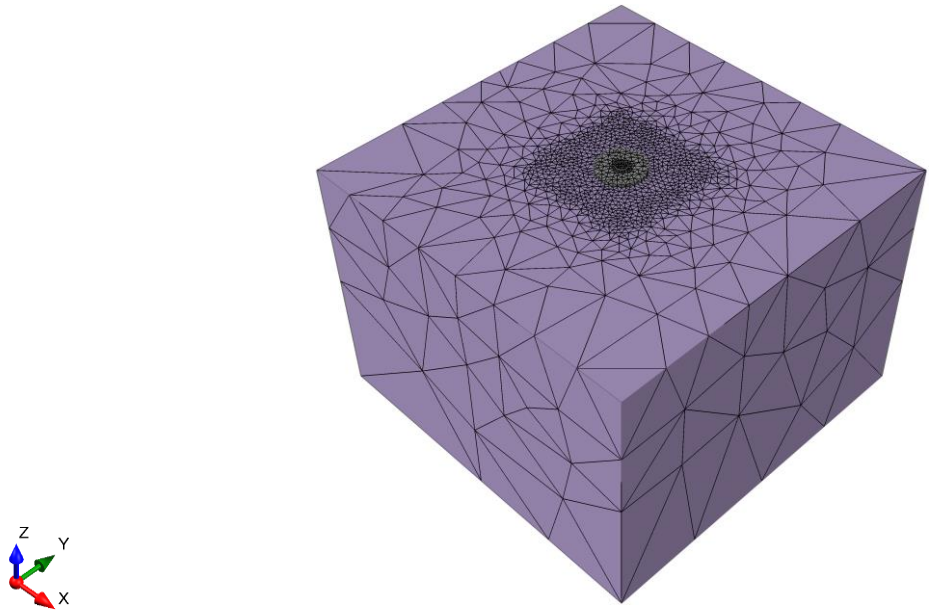

Figure 5.21: Model used for parametric study

5.5.1 Plasticity index, initial shear modulus, and degradation threshold

The soil PI, initial shear modulus G_0, and degradation shear strain threshold γ_{td} were varied simultaneously, with permutations involving all three of these parameters being analysed within a range of values for each. This was undertaken systematically by first selecting a modulus reduction curve corresponding to a particular soil PI, which was taken from the chart produced by Vucetic and Dobry (1991) shown in Figure 4.20. Using each modulus reduction curve, the model was computed for multiple values of G_0, which was varied between 20 and 150 MPa in increments of 5 MPa. Further, for each G_0 value, the maximum depth of γ_{td} was assessed based on its assumed characteristic value, as well as within a range of upper and lower bound values coinciding with G/G_0 ratios of 0.6 and 0.85 respectively.

The results of the computations for the PI of 15% are presented in Figure 5.22. This figure illustrates the relationship between the maximum depth of γ_{td} and G_0 for the range of values analysed, with each curve corresponding to a different value of γ_{td}. On the left-hand axis, the maximum depth of γ_{td} has been normalised relative to the foundation width (diameter) B, whereas the right-hand axis represents the actual depth calculated.

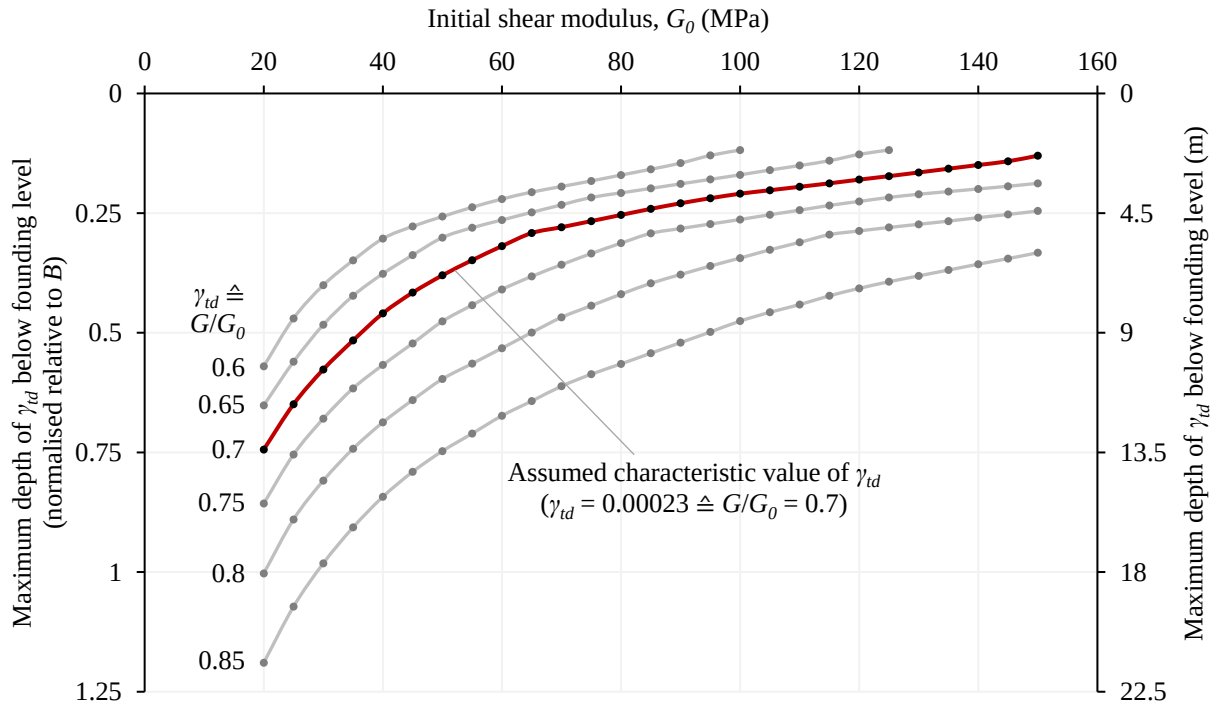

Figure 5.22: Variation in maximum depth of γ_{td} for PI = 15%

From Figure 5.22, the first aspect to note was that the magnitude of G_0 had a marked effect on the depth of γ_{td}. This effect became exponential for small values of G_0, approximately less than 60 MPa in this case, where the curves continued to increase in gradient as G_0 decreased. The reason for this was likely to be that the curves became asymptotic to the y-axis as G_0 approached 0 MPa, whereby the shear strains theoretically approach infinity. The effect of G_0 on the shear strains is also illustrated in Figure 5.23, which shows the variation in isosurfaces of γ_{td} for the range of G_0 values analysed, but for the assumed characteristic value of γ_{td} = 0.00023 only. It is evident from this figure that when G_0 was small, the isosurfaces were large and thus the influence of cyclic degradation was likely to be significant. As G_0 increased, the isosurfaces diminished in size and thus the effects of cyclic degradation were likely to be less consequential. This implies that G_0 is one of the critical parameters characterising cyclic degradation.

The second inference from Figure 5.22 was that the upper and lower bound values of γ_{td} produced a wide range of maximum depths thereof. For instance, considering a fixed G_0 of 60 MPa, the normalised maximum depths of γ_{td} ranged from 0.22B to 0.67B between the upper and lower limit of γ_{td}, with the difference being 0.45B. This is also shown in Figure 5.24, where the disparity between the sizes of the isosurfaces is evident. This disparity indicates that in addition to G_0, γ_{td} is a critical parameter influencing cyclic degradation. However, an important aspect to note is that much less uncertainty exists in estimating the former than the latter. This is because CSW testing is commonly conducted for geotechnical investigations of wind farms in South Africa, which produces a reasonably reliable profile of the in-situ G_0 with depth. On the other hand, evaluating γ_{td} requires specialist laboratory testing such as cyclic triaxial tests or cyclic direct simple shear tests, and consequently it is less likely to be included in the testing programme. Thus, γ_{td} is generally estimated from correlations in the literature, of which limited data exists.

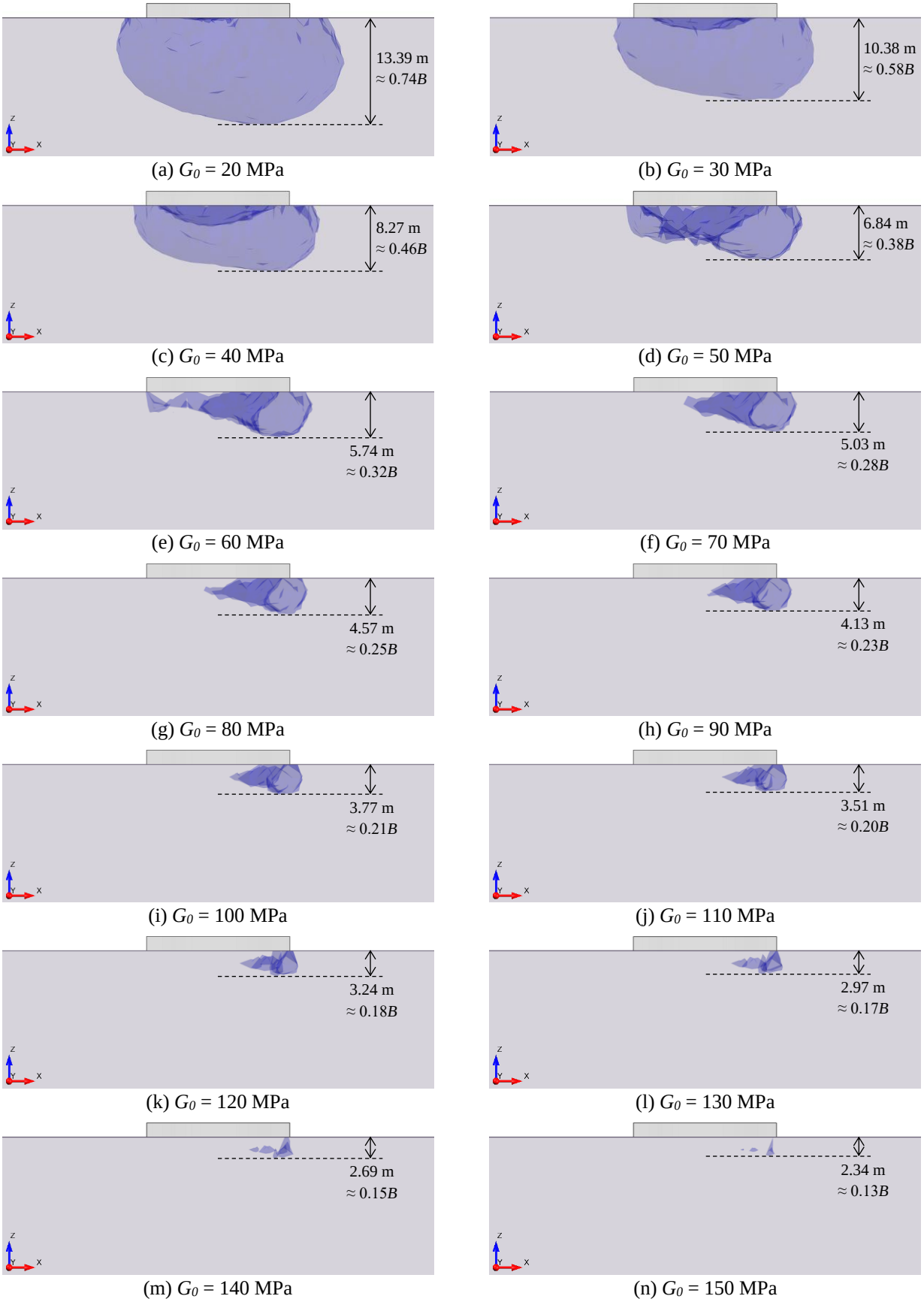

(a) G_0 = 20 MPa (b) G_0 = 30 MPa

(c) G_0 = 40 MPa (d) G_0 = 50 MPa

(e) G_0 = 60 MPa (f) G_0 = 70 MPa

(g) G_0 = 80 MPa (h) G_0 = 90 MPa

(i) G_0 = 100 MPa (j) G_0 = 110 MPa

(k) G_0 = 120 MPa (l) G_0 = 130 MPa

(m) G_0 = 140 MPa (n) G_0 = 150 MPa

Figure 5.23: Shear strain isosurfaces corresponding to $\gamma_{td} \triangleq G/G_0 = 0.7$ for PI = 15% and various values of G_0

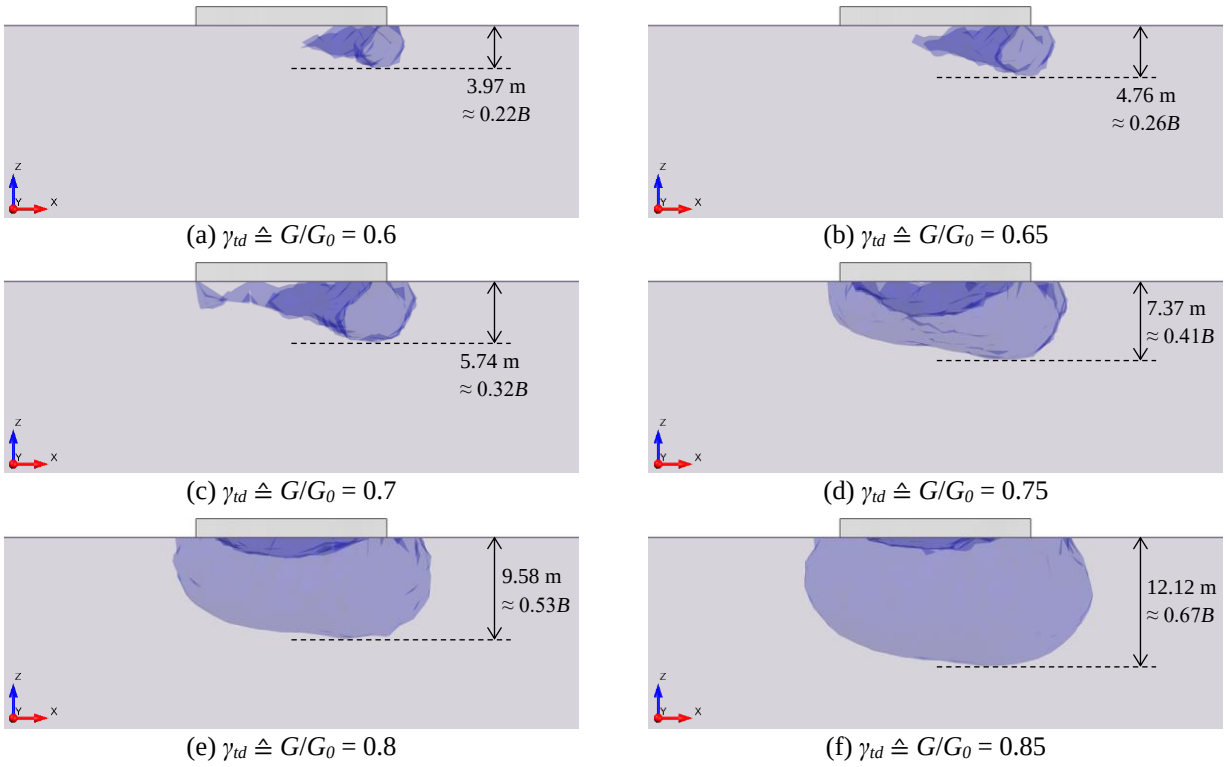

(a) $\gamma_{td} \triangleq G/G_0 = 0.6$ (b) $\gamma_{td} \triangleq G/G_0 = 0.65$

(c) $\gamma_{td} \triangleq G/G_0 = 0.7$ (d) $\gamma_{td} \triangleq G/G_0 = 0.75$

(e) $\gamma_{td} \triangleq G/G_0 = 0.8$ (f) $\gamma_{td} \triangleq G/G_0 = 0.85$

Figure 5.24: Shear strain isosurfaces corresponding to various values of γ_{td} for G_0 = 60 MPa and PI = 15%

The results for the modulus reduction curve corresponding to the PI of 0% are plotted in Figure 5.25. Note that in this case, the lowest value of G_0 analysed was 45 MPa, as values less than this caused the FE model to not reach a state of equilibrium. Nonetheless, amongst all the PI's evaluated, these results represented the worst-case scenario regarding the depths of the γ_{td} isosurfaces. This was expected given that the modulus reduction curve for this soil PI was the most nonlinear, and started to behave nonlinearly at the smallest strain levels. Moreover, as for the previous results, G_0 was significant in governing the depths of the γ_{td} isosurfaces, as evident from the increase in steepness of the curves in Figure 5.25 as G_0 decreased. There was also a large disparity between the depths of γ_{td} for its upper and lower bound values, which was in the order of 0.5B in this case. This again indicated that γ_{td} is an important parameter controlling cyclic degradation.

It must be reiterated that the PI of 0% was only included in this parametric study for purposes of comparison, and it is not anticipated that soil of this type would be susceptible to cyclic degradation under the action of slowly-varying wind loading on the wind turbine. This stems from the fact that soils with no plasticity are associated with free-draining, granular materials. As one of the mechanisms for cyclic degradation is the continuous generation of pore water pressure with increasing number of load cycles, it is only at very high loading rates, such as seismic loading, that such generation would occur in this type of material. Furthermore, although the other types of cyclic loading imparted on wind turbine foundations have higher loading rates, specifically the 1P and 3P loads, the amplitude of cyclic shear strain from this loading is

significantly lower than that of the wind loading. Consequently, the soil's response under the 1*P* and 3*P* loading is likely to remain closer to the linear elastic range of the stress-strain curves, resulting in the degradation being less pronounced.

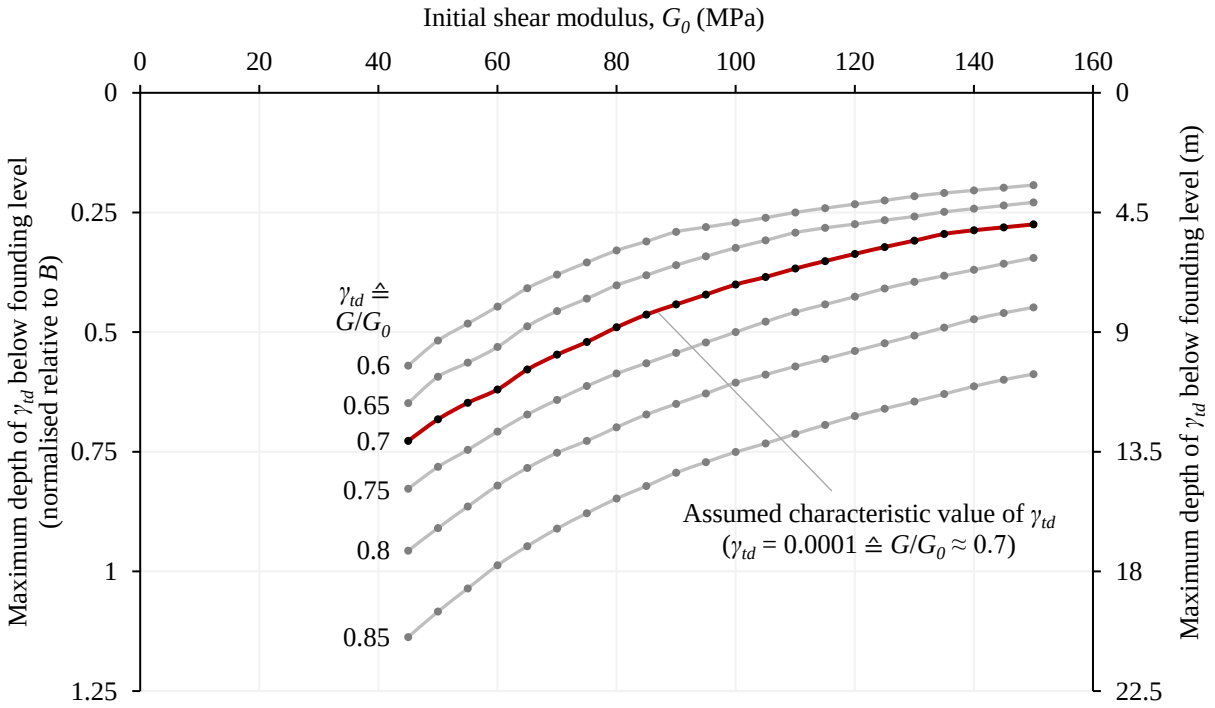

Figure 5.25: Variation in maximum depth of γ_{td} for PI = 0%

Further results for the PI of 30, 50 and 100% are illustrated in Figure 5.26, Figure 5.27, and Figure 5.28 respectively. These figures show that as the PI increased, the maximum depths of γ_{td} decreased substantially. For the PI of 30% shown in Figure 5.26, it can be inferred that degradation may still be significant for soft profiles with low values of G_0. However, as before, this is largely dependent on the value of γ_{td} adopted, as it again produced a wide range of results between the upper and lower limit.

As the PI increased to 50%, illustrated in Figure 5.27, the depth of the γ_{td} isosurfaces became practically negligible for the assumed characteristic value of γ_{td}. However, the lower bound value of γ_{td} still produced relatively deep isosurfaces thereof, but only at the very low end of the G_0 spectrum. With the PI of 100%, Figure 5.28 shows that γ_{td} was not exceeded for G_0 values in excess of approximately 40 MPa. Thus, cyclic degradation will likely be inconsequential for this type of material. Finally, for the modulus reduction curve corresponding to the PI of 200%, γ_{td} was not exceeded for any G_0 value, and thus no results were plotted.

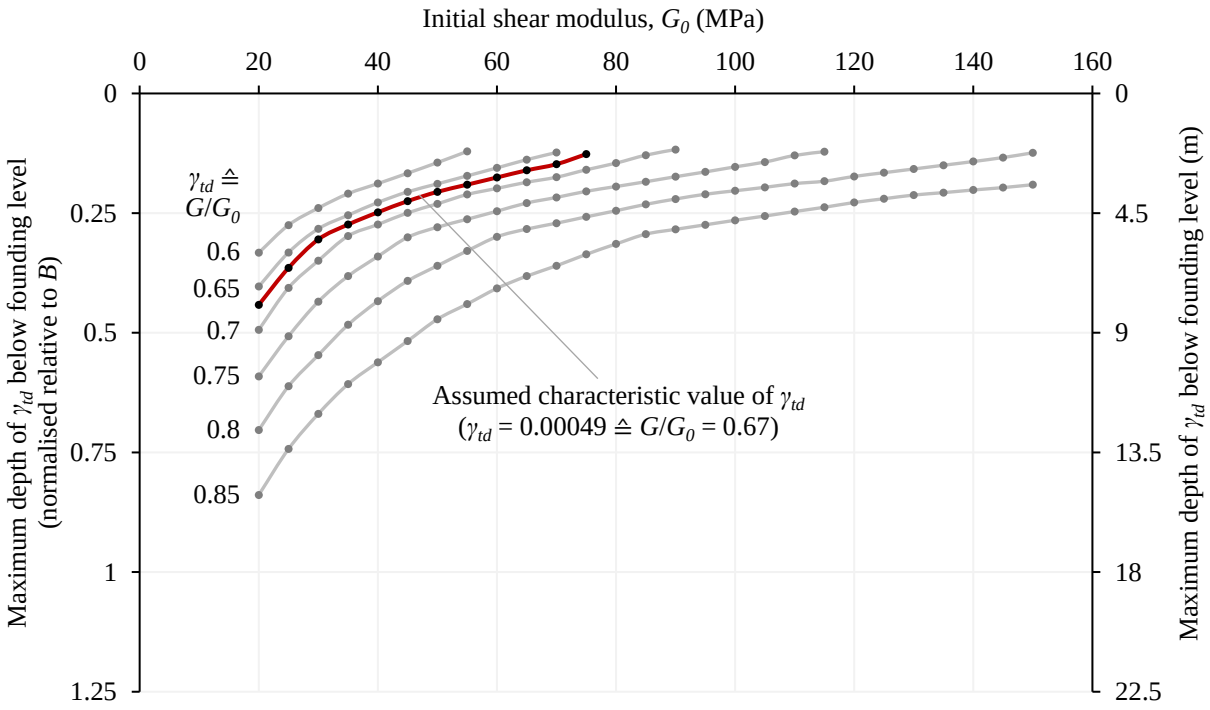

Figure 5.26: Variation in maximum depth of γ_{td} for PI = 30%

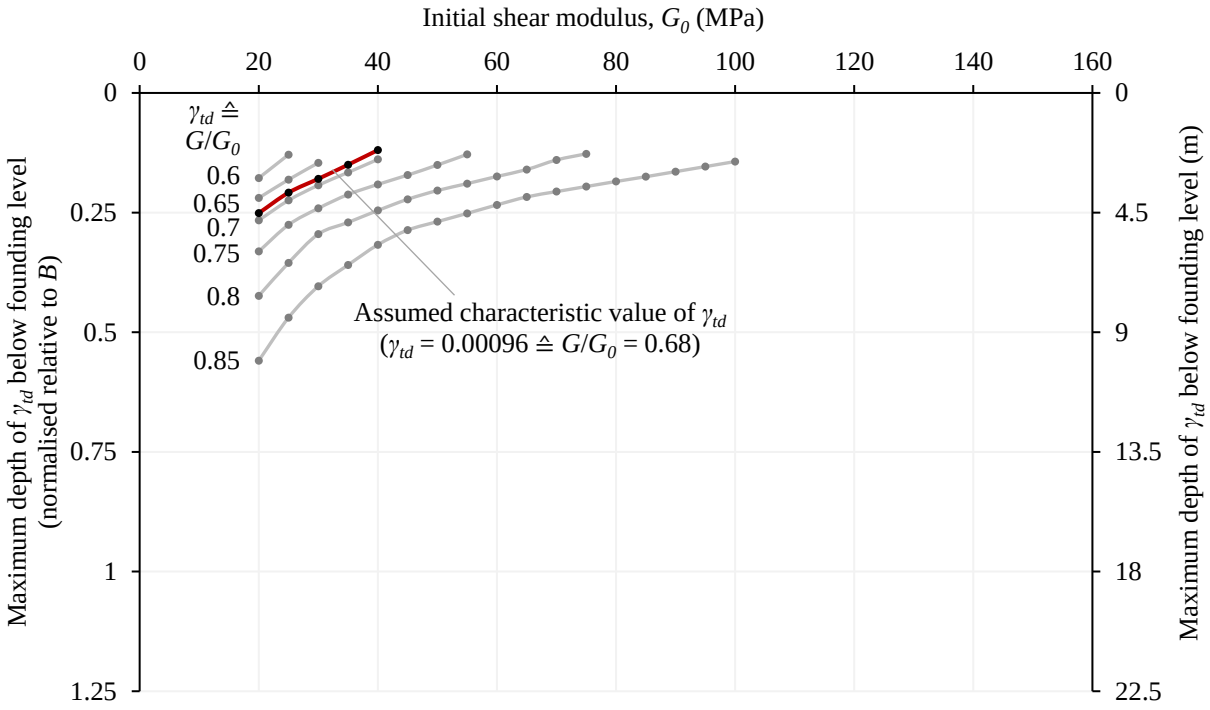

Figure 5.27: Variation in maximum depth of γ_{td} for PI = 50%

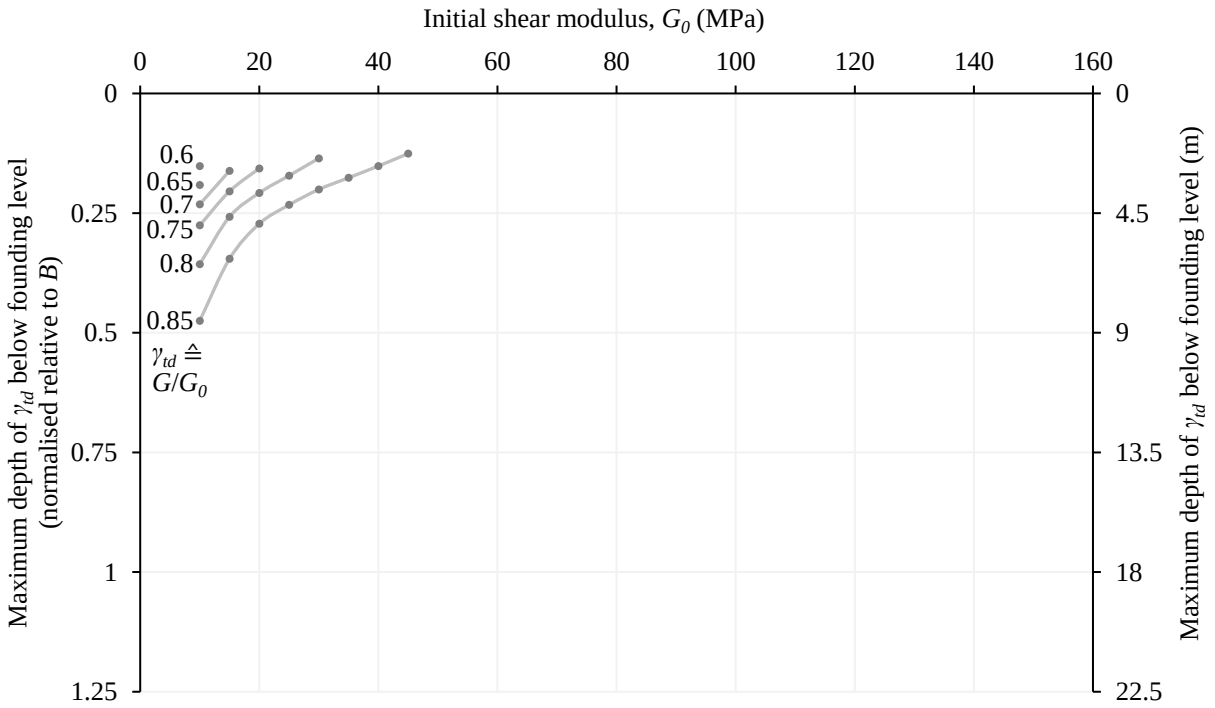

Figure 5.28: Variation in maximum depth of γ_{td} for PI = 100%

By examining the assumed characteristic values of γ_{td} only, the influence of the soil PI on the maximum depth of the γ_{td} isosurfaces is summarised in Figure 5.29. This figure indicates that the PI of the soil has a significant effect on its susceptibility to cyclic degradation, with lower PI's being the most susceptible. This is a result of the differences in the shapes of the modulus reduction curves, as well as the corresponding variation in the values of γ_{td} for each PI. Specifically, as the PI decreases, the modulus reduction curves become more nonlinear, and with this there is also a decrease in γ_{td}. Therefore, soils of low plasticity, in contrast to soils of high plasticity, require smaller cyclic shear strains to cyclically degrade.

Considering the significance of the soil PI in influencing cyclic degradation, it is also important to recognise the uncertainties involved in estimating the PI during a geotechnical investigation. As with most soil parameters, the first consideration is that natural soil deposits exhibit a high degree of non-homogeneity, and their physical properties can vary to a great extent within even a few metres. Accordingly, as the soil PI is measured on soil samples taken from discrete locations within the soil profiles, they may not necessarily be representative of the wider soil material. The second consideration is that the Atterberg limit tests, used to measure the soil PI in the laboratory, are in themselves sensitive to operator error. This is because they are largely based on the subjectivity of the tester, and thus the quality of the result produced is dependent on the competence of the personnel performing the test. The combination of these uncertainties could have consequences in the design stage of wind turbine foundations involving cyclic degradation, given the large disparity in results shown in Figure 5.29 for the different PI's. Therefore, caution should be observed when relying on the PI for correlations of design parameters from the literature, such as in this study where it was used to define both the modulus reduction curves and characteristic values of γ_{td}.

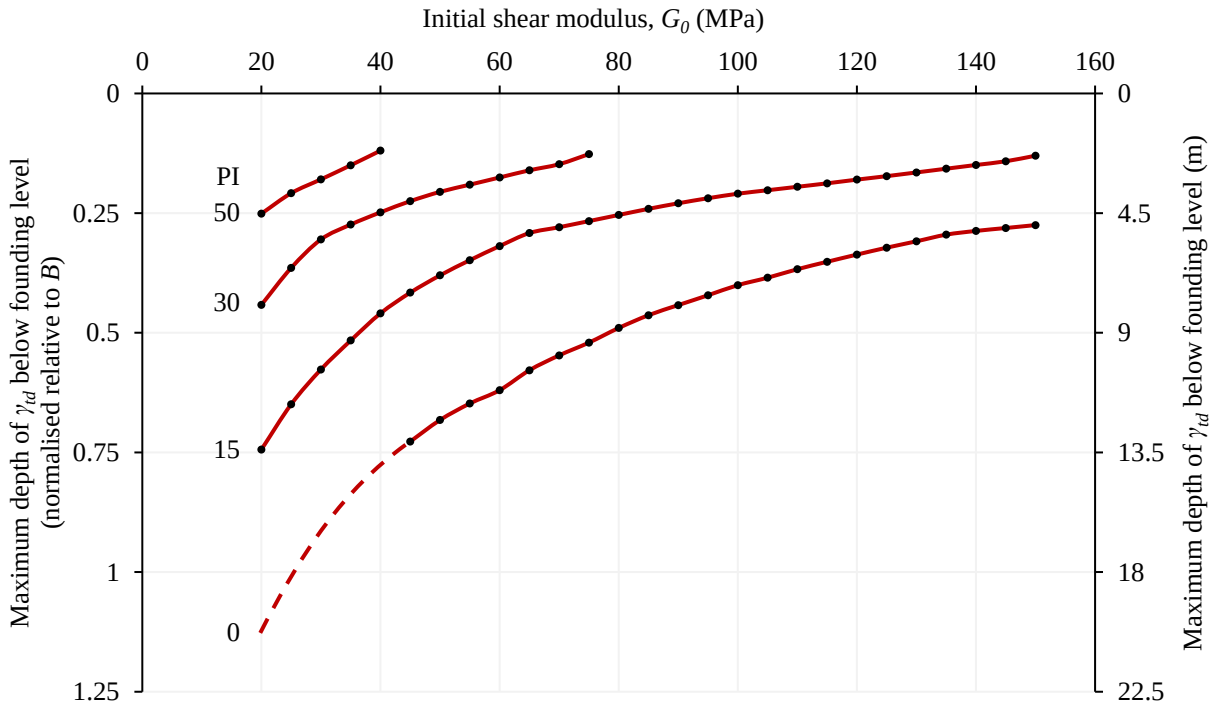

Figure 5.29: Variation in maximum depth of assumed characteristic value of γ_{td} for varying PI and G_0

5.5.2 Foundation size

The diameter of the foundation in the FE model was varied between 15 and 20 m in increments of 1 m. This was undertaken using the same range of G_0 values as before, from 20 to 150 MPa. In doing so, the modulus reduction curve corresponding to a PI of 15% was used throughout, as well as the assumed characteristic value of γ_{td} = 0.00023 for this PI.

The results of the various foundation sizes are illustrated in Figure 5.30. From this figure, it is evident that the largest foundation diameter of 20 m yielded the shallowest isosurfaces of γ_{td} within the full range of G_0 values analysed, whereas the smallest diameter of 15 m produced the deepest. This is also shown in Figure 5.31 for a G_0 of 60 MPa only. This behaviour was expected given that larger foundations spread the loads over a greater bearing area, and thus induce smaller stresses and strains into the soil.

It can also be observed from Figure 5.30 that the difference in maximum depths of γ_{td} between the 15 and 20 m foundation diameters was largest at the lower end of the G_0 range, and reduced in extent as G_0 increased. This is shown by the curves somewhat converging as G_0 approached 150 MPa. This suggests that although the foundation diameter is an important parameter that can be used to control cyclic degradation, its impact in this regard is likely to be more significant for softer profiles than those that are stiff.

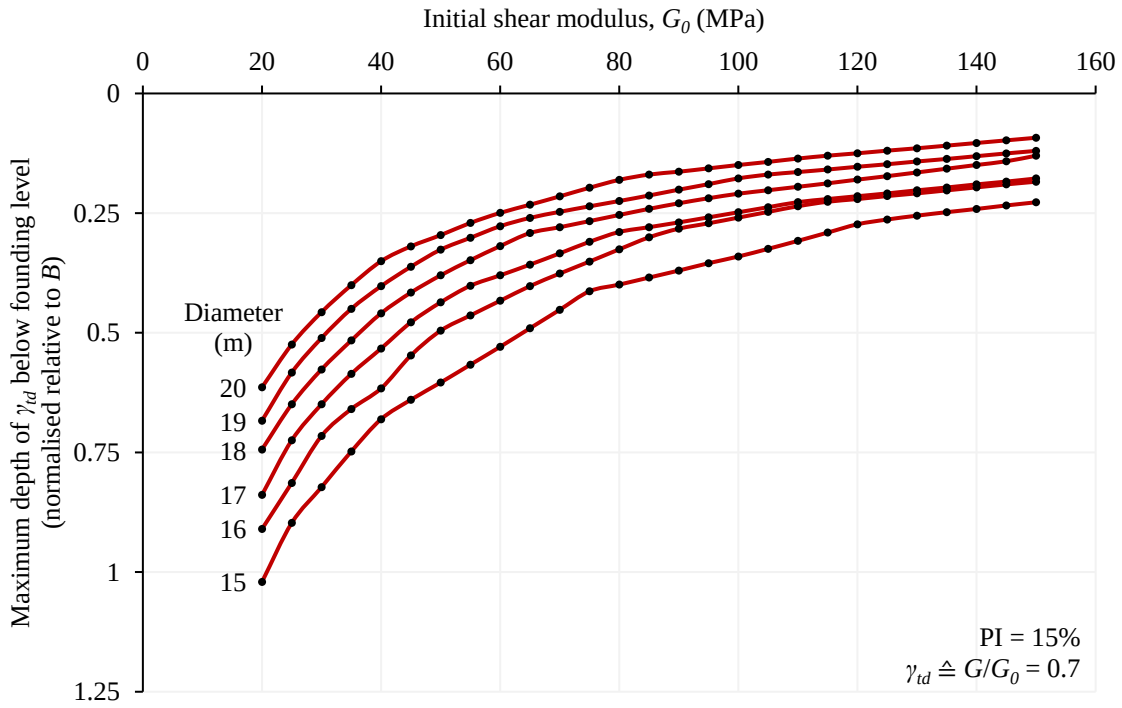

Figure 5.30: Variation in maximum depth of γ_{td} for different foundation diameters

The practical implication of the above discussion is that the foundation designer can iteratively solve for the most economical foundation size. This is particularly the case for soft stiffness profiles and where foundation stiffness requirements control the design. With reference to Equation 2.10, quoted again below, a change in foundation size has an effect on two parameters when calculating the foundation's rotational stiffness K_R. On one hand, there is a direct change in the foundation radius R, which has a cubic relationship with K_R. However, on the other hand, adjusting the foundation size also alters the depth of influence of cyclic degradation, as evidenced from Figure 5.30, and thus leads to a change in G_{mass}. For instance, decreasing the foundation diameter increases the extent of cyclic degradation, resulting in a further decrease in G_{mass}. Therefore, the design can theoretically be optimised by finding a value of R that balances its own magnitude and G_{mass} to produce the minimum required K_R specified by the turbine manufacturer.

$$K_R = \frac{8G_{mass}R^3}{3(1-\nu)} \qquad \text{Eqn. 2.10}$$

Where K_R = rotational stiffness (Nm/rad); G_{mass} = mass shear modulus (Pa); R = foundation radius (m); and ν = Poisson's ratio (unitless).

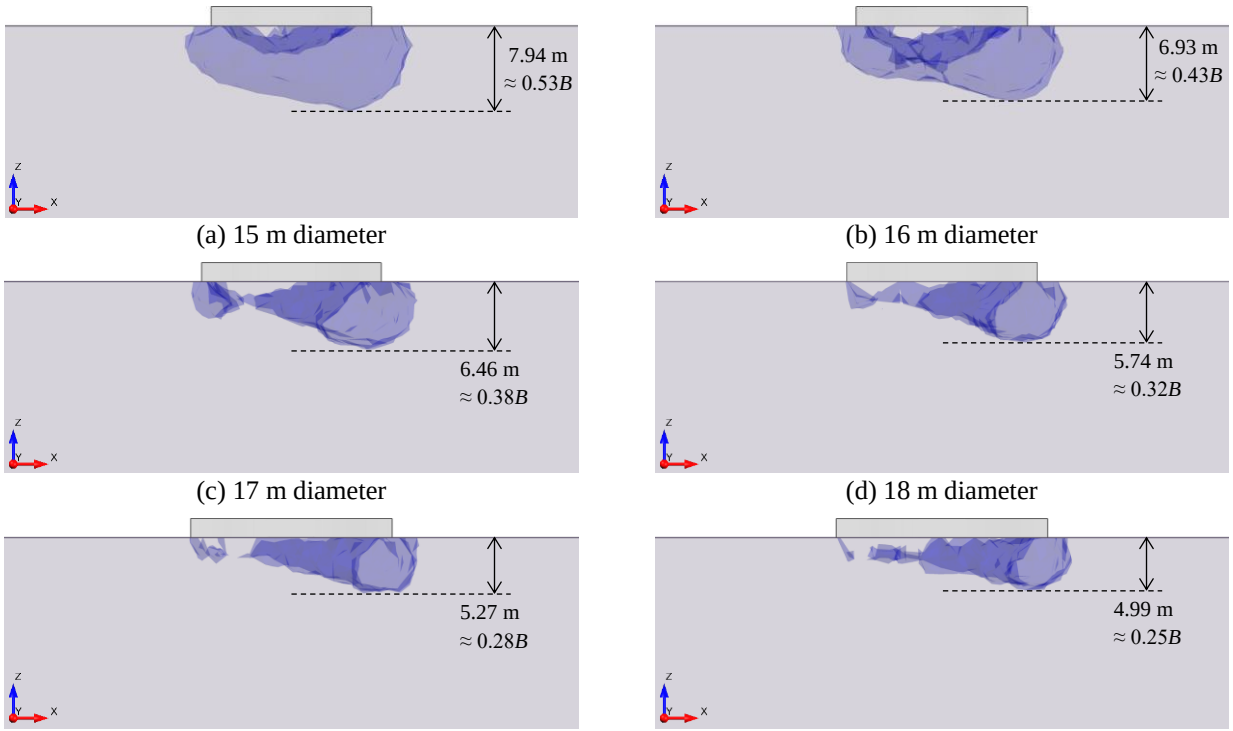

(a) 15 m diameter (b) 16 m diameter

(c) 17 m diameter (d) 18 m diameter

(e) 19 m diameter (f) 20 m diameter

Figure 5.31: Shear strain isosurfaces corresponding to different foundation sizes for $\gamma_{td} \triangleq G/G_0 = 0.7$, $G_0 = 60$ MPa and PI = 15%

5.5.3 Load magnitude

Three different load cases were analysed as part of the parametric study. As before, this was done using the modulus reduction curve corresponding to a PI of 15%, the assumed characteristic value of $\gamma_{td} = 0.00023$, and by varying G_0 between 20 and 150 MPa.

The first load case was the fatigue load case provided by the turbine manufacturer, which had an overturning moment in the order of 31.8 MNm. The second was the site-specific load case which was calculated based on the wind climate of the specific wind farm in question, with an overturning moment of 43.5 MNm. The final load case was that which was used in the previous analyses, and corresponded to the SLS design in *rare* conditions, with an overturning moment of 49.1 MNm.

Despite the considerable differences in overturning moments between the three load cases, the maximum depth of γ_{td} did not vary significantly between them for the range of G_0 values analysed. This is shown in Figure 5.32, where it is evident that there is little variation in the plotted curves, particularly for G_0 in excess of 60 MPa. This is further illustrated in Figure 5.33, where the sizes and shapes of the γ_{td} isosurfaces are shown to have not differed substantially.

This finding suggests that cyclic degradation may not only be significant for rare SLS conditions, such as a design storm, but may also accumulate in normal operating conditions during the lifetime of the structure. However, the occurrence of this is particularly dependent on the

presence of groundwater, as also suggested by Bonnett (2005). Nonetheless, this highlights the importance of accounting for cyclic degradation in the design stage of wind turbine foundations.

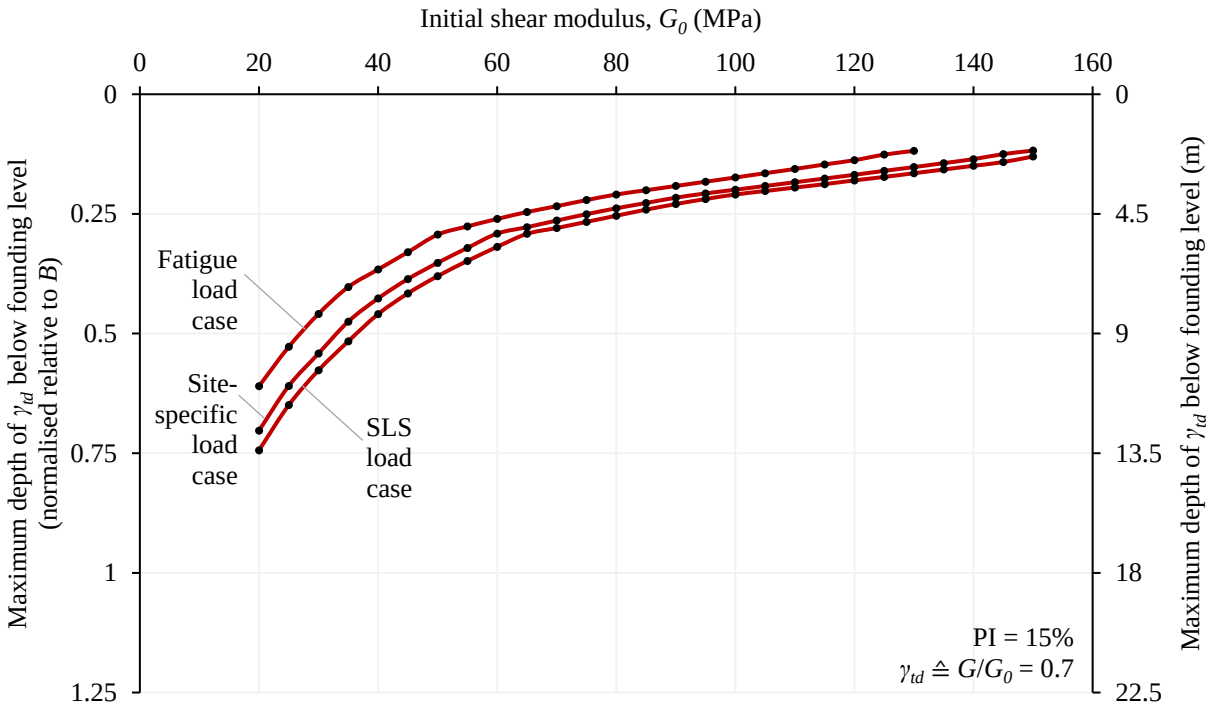

Figure 5.32: Variation in maximum depth of γ_{td} for different load cases

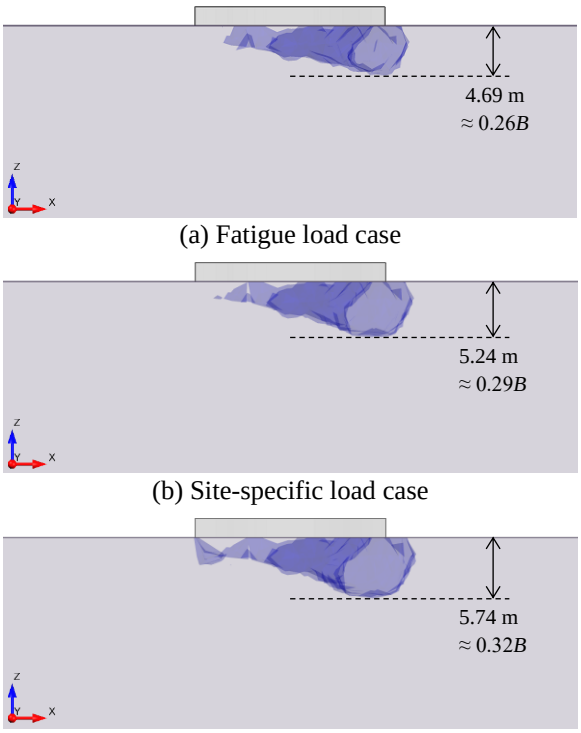

Figure 5.33: Shear strain isosurfaces corresponding to different load cases for $\gamma_{td} \triangleq G/G_0 = 0.7$, $G_0 = 60$ MPa and PI = 15%

Chapter 6
CONCLUSIONS AND RECOMMENDATIONS

6.1 Introduction

The objective of this study was to investigate the effect of cyclic soil degradation on the design of onshore wind turbine gravity foundations. In doing so, a case study of a wind farm in the Western Cape, South Africa was considered. Three separate ground profiles from the wind farm were analysed, having been selected based on the presence of fine-grained soil with low plasticity, soft G_0 stiffness profiles, and to illustrate different scenarios in ground conditions. A 3D FE model was developed of each ground profile, and an iterative procedure conducted to determine the depth of influence of cyclic degradation, which was assessed by virtue of the maximum depth below founding level to which the degradation shear strain threshold γ_{td} of the soil was reached. The minimum required foundation diameter was then assessed based on the stiffness requirements stipulated by the wind turbine manufacturer. This was undertaken for an upper bound stiffness profile, that was representative of the in-situ, undegraded stiffness determined from the CSW testing, and a lower bound stiffness profile, that accounted for cyclic degradation by applying a reduction factor to the soil modulus up to the depth of influence determined from the numerical modelling.

In addition, a parametric study was conducted to evaluate the dependency of cyclic degradation on various input parameters. From the parametric study, the critical parameters that potentially require the most attention in wind turbine foundation design involving cyclic degradation were identified.

Finally, recommendations for further research were made. These were separated into those that could improve the numerical model adopted in this study, and those that could investigate alternative scenarios involving cyclic soil degradation.

6.2 Case Study

The effect of cyclic degradation on the design of wind turbine gravity foundations is summarised in Table 6.1 for the three ground models. In all three cases, accounting for degradation of the soil profile resulted in considerable increases in the minimum required foundation diameter:

- **Ground Profile A: Deep clayey profile.** Based on the numerical modelling results, the depth of influence of cyclic degradation was approximately equal to 0.4*B*. By applying the estimated reduction factor of $\delta = 0.6$ to the ground modulus within this depth, the minimum required foundation diameter increased by 10%, from 16.0 to 17.6 m. Considering that the diameter of a typical wind turbine foundation ranges from 15 to 20 m, this increase in diameter could potentially have caused the stiffness requirements to drive the design.
- **Ground Profile B: Clayey profile with bedrock at 0.5*B*.** The presence of the bedrock had a negligible effect on the depth of influence of cyclic degradation relative to Ground Profile A, in this case also rounded up to 0.4*B*. Accounting for cyclic degradation caused the required diameter to increase by 19%, from 12.2 to 14.5 m. Despite this substantial increase, the stiffness requirements were unlikely to govern the design, which was largely attributed to the proximity of the bedrock increasing the overall stiffness of the profile.
- **Ground Profile C: Clayey profile with stratum of dense sand at founding level.** The dense sand marginally contained the depth of influence of cyclic degradation relative to the previous profiles, in this scenario being 0.3*B*. This containment, in conjunction with the high stiffness of the dense sand increasing G_{mass}, meant that the required diameter was less than Ground Profile A, being 16.2 m for the lower bound stiffness profile. Therefore, the presence of the dense sand resulted in the foundation stiffness requirements being less likely to drive the design. This highlighted the potential for ground improvement techniques to perform a similar role, thus providing more economical foundation solutions.

Table 6.1: Summary of the effect of cyclic degradation on the wind turbine foundation design for the three ground profiles analysed in the case study

		Ground Profile A	Ground Profile B	Ground Profile C
Depth of influence of cyclic degradation		0.4*B*	0.4*B*	0.3*B*
Mass shear modulus, G_{mass} (MPa)	Upper bound	24.9	22.0	30.9
	Lower bound	18.6	14.3	24.8
Minimum required foundation diameter based on stiffness requirements (m)	Upper bound	16.0	12.2	15.1
	Lower bound	17.6	14.5	16.2
Percentage change in minimum required foundation diameter (%)		+10	+19	+7

6.3 Parametric Study

The first component of the parametric study consisted of varying the soil PI, initial shear modulus G_0, and degradation shear strain threshold γ_{td} simultaneously. Based on the outputs of these analyses, all three soil parameters were shown to be significant in controlling cyclic degradation:

- **Soil PI:** As the PI decreased, the maximum depths of the γ_{td} isosurfaces increased considerably, thus indicating a corresponding increase in the susceptibility of the soil to cyclic degradation. This increase in susceptibility was due to the shape of the modulus reduction curves proposed by Vucetic and Dobry (1991), which became more nonlinear as the PI decreased, with corresponding decreases in γ_{td}. Therefore, soils of low plasticity, in contrast to soils of high plasticity, required smaller cyclic shear strains to degrade.
- **Initial shear modulus, G_0:** The maximum depths of the γ_{td} isosurfaces increased substantially as G_0 decreased. As G_0 became very small, the γ_{td} depths increased exponentially. Therefore, G_0 was significant in governing the extent of cyclic degradation.
- **Degradation shear strain threshold, γ_{td}:** This parameter was varied between a range of upper and lower bound values. The depths of γ_{td} varied considerably within this range, with the disparity being in the order of $0.5B$ for low plasticity soils. Thus, accurately quantifying cyclic degradation was recognised as being heavily dependent on the value of γ_{td} adopted.

Accordingly, the soil PI, G_0 and γ_{td} were identified as being key parameters that require careful consideration in wind turbine foundation design involving cyclic degradation. However, it was also important to recognise that there are different degrees of uncertainty involved in estimating these parameters. The lowest uncertainty exists for G_0, because the CSW testing used to measure this parameter is reasonably reliable. The soil PI presents a moderate degree of uncertainty, largely due to soil variability and possibly operator error during Atterberg limit testing. Finally, γ_{td} exhibits the most uncertainty, as evaluating its magnitude requires specialist laboratory testing which is less likely to be included in the testing programme for the geotechnical investigation.

The influence of foundation size was also evaluated in the parametric study. The model outputs indicated that, as expected, the depths of the γ_{td} isosurfaces decreased as the foundation diameter increased. However, the disparity between the results of the largest and smallest diameters was most significant for lower values of G_0. This correlation suggested that, although the influence of the foundation diameter should be considered when quantifying cyclic degradation, the impact of the diameter in this regard is likely to be more critical for soft profiles than those that are stiff.

Finally, three different load cases were analysed in the parametric study: (1) a fatigue load case, with an overturning moment of M = 31.8 MNm; (2) a site-specific load case, with M = 43.5 MNm; and (3) a load case for SLS design in *rare* conditions, with M = 49.1 MNm. Despite the considerable differences in M between these load cases, the maximum depths of γ_{td} did not vary significantly between them. The lack of variation in results suggested that cyclic degradation may not only be significant in rare SLS conditions, such as a design storm, but may also accumulate in normal operating conditions during the lifetime of the structure. This emphasised the importance of accounting for cyclic degradation in wind turbine foundation design.

6.4 Recommendations for Further Research

The recommendations for further research were separated into those that could improve the numerical model and modelling methodology adopted in this study, and those that could investigate alternative scenarios involving cyclic degradation. Regarding the former, the following recommendations were made:

- The modelling methodology adopted in this study did not account for the possibility of the soil degrading at an increased rate on the leeward side of the foundation (relative to the windward side), as it was based on the assumption that the soil below the foundation would degrade uniformly within the horizontal plane. Therefore, a further study could investigate the situation wherein cyclic degradation is predominantly concentrated on the foundation's leeward side, which might be the case for a wind farm dominated by wind from a single direction. This could be implemented by only degrading the soil stiffness within the extent of the γ_{td} isosurfaces, rather than within horizontal soil layers that are added to the model. However, it must be noted that this approach would lead to an exponential increase in the computational times of the models, as the geometry of the isosurfaces are complex and thus they are automatically discretised into a very large number of elements by the FE software.
- The approach to implementing the cyclic degradation of the soil in the numerical model was to 'manually' degrade its stiffness in horizontal layers based on the induced shear strains. In this way, the cyclic degradation model proposed by Idriss *et al.* (1978) was applied implicitly in the FE model. However, to improve the accuracy of this process, this degradation model could rather be explicitly incorporated into the constitutive model, thus having the degradation occur automatically depending on the precise distribution of the shear strains. This would improve the accuracy of the model outputs in the sense that the degradation parameter *t*, which describes the rate of cyclic degradation, would be defined more accurately within the extent of the soil body.
- The modelling approach did not account for the effect of the cyclic stress ratio, and thus a future investigation could aim to incorporate this into the FE model. The cyclic stress ratio is the ratio between the mean or average component of the shear stress, and the cyclic component of the shear stress. Analogous definitions of these components are shown in Figure 3.1(a). Researchers working on the subject of cyclic loading, particularly in the offshore sector such as Andresen *et al.* (2011), suggest that this ratio is important in characterising the development of pore pressure and shear strain.
- The modulus reduction curves adopted in this study neglected the influence of confining pressure. This aspect of soil stress-strain behaviour was discussed in §3.3.1.2, where it was demonstrated that the mean effective confining pressure has an effect on the shape of the modulus reduction curves, particularly for soil with low plasticity. Furthermore, the constitutive model did not include an expression relating the magnitude of G_0 to confining stress. Both of these aspects of stress-strain behaviour can be incorporated into the FE model in a future study.

- The foundation was modelled as a rigid element in the numerical model. This assumption influenced the distribution of stress and strain below the foundation-soil interface, causing it to be primarily concentrated around the edges of the foundation. To assess the extent to which this assumption affected the strain distribution, and thus the amount of cyclic degradation that was deemed to occur, a new model can be developed in which the foundation element is assigned its actual stiffness. This stiffness would be based on the elastic properties of the concrete and the detailing of the steel reinforcement.
- An advanced constitutive model, such as bounding surface plasticity, can be used to describe the behaviour of the soil in the FE model, and rules for cyclic degradation incorporated into it. An example of such a constitutive model is that proposed by Hu *et al.* (2012).

The recommendations for further research involving alternative scenarios include the following:

- The effect of cyclic degradation on other onshore wind turbine foundation types can be investigated. Of particular interest would be pile foundations, as this foundation type is a common solution for onshore wind turbines in the scenario that the ground conditions are not suitable for gravity foundations.
- The potential for geosynthetics to mitigate cyclic degradation can be explored. This can be undertaken by adding geosynthetic reinforcement to the FE model and assessing how it affects the distribution of strain below the foundation-soil interface. Additionally, several other ground improvement techniques can be investigated, such as stone columns, soil mixing, wick drains (which provide drainage paths for dissipating the excess pore pressure generated by cyclic loading), and so forth.
- The 1*P* and 3*P* dynamic loads can be modelled to assess their influence on cyclic degradation. These dynamic loads were excluded from the FE analyses in this study as the shear strain amplitudes induced from them were deemed to likely be orders of magnitude lower than those of the cyclic wind loading. However, this can be validated by conducting a dynamic FE analysis in which the 1*P* and 3*P* loads are applied to the foundation. Note that this would require an analysis that is dynamic in nature as the 1*P* and 3*P* loads have higher loading rates than that of the wind, with frequencies closer to the natural frequency of the wind turbine structure. Consequently, the time-dependence of the load would need to be taken into consideration, including the inertia of the subsoil, damping, wave propagation, and so forth.
- The effect of cyclic loading on pedocretes can be investigated. These materials are formed by cementation and/or replacement of pre-existing soils by various minerals (most commonly calcium, iron, or silica) precipitated from soil water or groundwater, and can either be indurated, forming hard layers or nodules, or non-indurated, with soft or powdery forms (Day, 2013). Pedocretes are encountered on the west coast, southern coast, and northern interior of South Africa (Warren-Codrington, 2013), and consequently many wind farm developments have taken place in areas underlain by these materials. Although

pedocretes may not necessarily be susceptible to cyclic degradation, they are highly variable materials and may be prone to other problems that have a similar effect on their stiffness. For instance, during the design of gravity foundations for a wind farm located in the Eastern Cape, Parrock (2013) found that the application of dynamic compaction to calcretised formations decreased their G_0 stiffness values. Although this was initially an unexpected result, Parrock (2013) hypothesised that this sudden stiffness reduction occurred due to the calcrete being representative of potentially collapsible material. Specifically, in its initial state, the calcrete exhibited high stiffness due to the rigidity of the cemented structure, however the subsequent application of the compaction broke the bonds and resulted in a less stiff structure (Parrock, 2013). Considering that this reduction in stiffness could have a similar impact on the dynamics of wind turbine systems as cyclic degradation, it could be the subject of a future study.

- An experimental study can be undertaken in which the foundation of a utility-scale wind turbine is monitored in-situ for cyclic degradation. One approach to doing so would be to install strain gauges and tiltmeters in the base of the tower, as indicated in Figure 6.1. The selection of this instrumentation stems from the fact that the rotational stiffness K_R, although typically calculated using Equation 2.10 in wind turbine foundation design, is also defined as the ratio between the overturning moment M and the angle of rotation of the foundation θ in radians ($K_R = M/\theta$). Therefore, K_R is a measure of the overturning moment that is required to tilt the foundation by one radian. It follows that if the parameters M and θ of the foundation can be measured, they can be used to calculate K_R, which in turn can be used to assess the amount of cyclic degradation that occurs in the soil over time.

  Direct measurements of θ can be taken with the tiltmeters installed in the base of the tower. On the other hand, the magnitude of M transferred to the foundation can be monitored with the strain gauges, also installed in the base of the tower, in conjunction with theoretical calculations. Specifically, the strain gauges measure the strain ε in the walls of the tower base, which is used to calculate the corresponding stress σ with Hooke's law in Equation 6.1. Temperature sensors installed alongside the strain gauges can be used to calibrate the strain readings. The section modulus S of the tower base, which represents its resistance to bending, can be calculated with Equation 6.2 based on its cross-sectional dimensions. Finally, using the quantities of σ and S, M can be computed with Equation 6.3.

$$\sigma = E \cdot \varepsilon \qquad \text{Eqn. 6.1}$$

$$S = \frac{\pi(d_2^{\,4} - d_1^{\,4})}{32 d_2} \qquad \text{Eqn. 6.2}$$

$$M = \sigma \cdot S \qquad \text{Eqn. 6.3}$$

Where σ = stress (Pa); E = elastic modulus of steel used in tower (Pa); ε = strain (unitless); S = section modulus of tower (m^3); d_2 = outer diameter of tower; d_1 = inner diameter of tower; and M = overturning moment (Nm).

Data from the various instruments can be recorded via a data logger. Processing of this data can subsequently be undertaken to calculate the variation of K_R with time, by applying the above principles. These outputs can be used to qualitatively assess patterns of cyclic degradation that occur. Similarly, the measured values of K_R can be used to back-calculate G_{mass} using Equation 2.10, to directly quantify the amount of cyclic degradation that has occurred. However, it must be noted that some inaccuracies may be present in this back-calculation given that Equation 2.10 is based on several assumptions, such as that of the foundation being perfectly rigid.

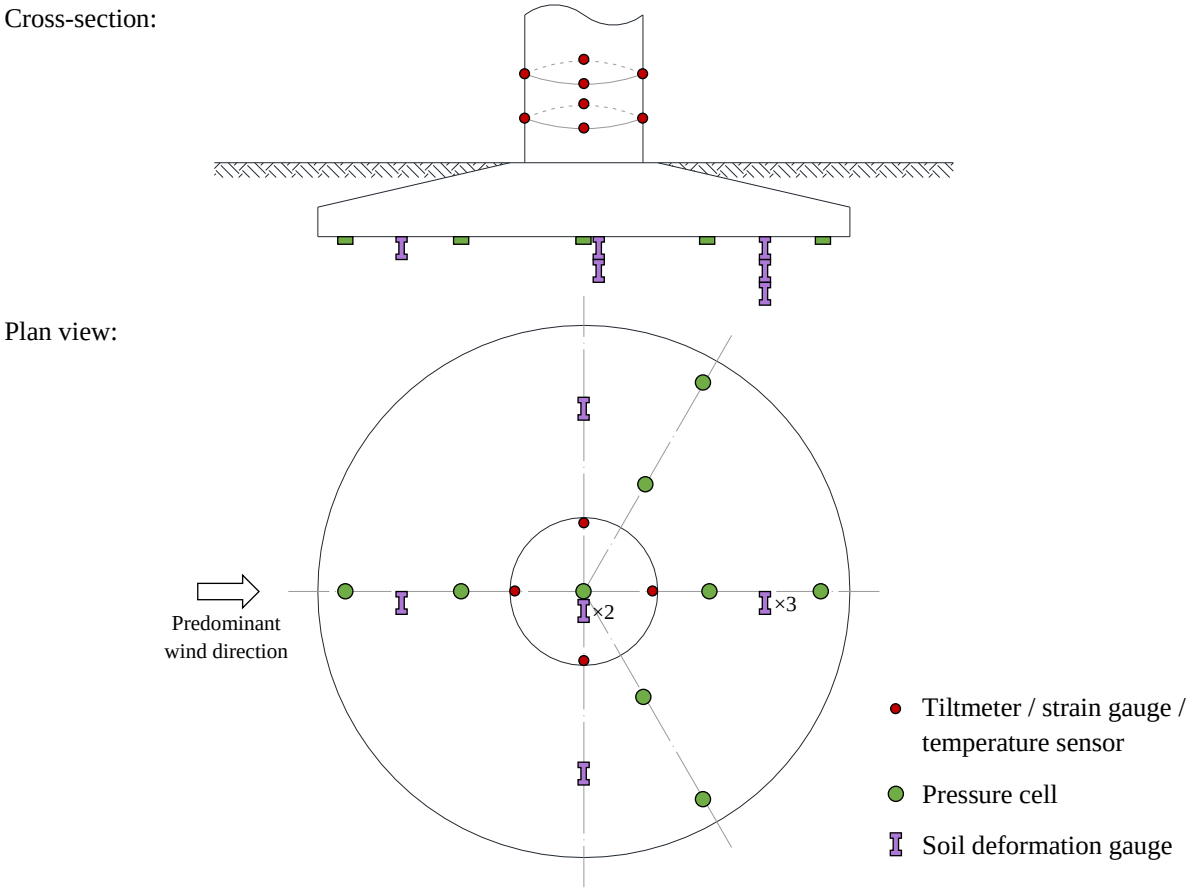

Figure 6.1: Proposed layout of instrumentation for experimental study

To expand on the experimental study, pressure cells and soil deformation gauges can be installed in the soil underlying the foundation, as shown in Figure 6.1. These can be aligned with the predominant wind direction to maximise their effectiveness. The purpose of the pressure cells would be to monitor the contact pressure distribution at the foundation-soil interface. This can be useful in verifying various aspects of wind turbine foundation design, such as the uniformity of the pressure distribution and whether high edge pressures occur, the magnitudes of maximum bearing pressures, the occurrence of gapping, and so forth. Additionally, the soil deformation gauges can measure the strain levels in the soil, identifying its distribution with depth, as well as monitoring differential settlement.

REFERENCES

Achmus, M., Abdel-Rahman, K. & Kuo, Y. 2007. Behavior of large diameter monopiles under cyclic horizontal loading. In *12th International Colloquium on Structural and Geotechnical Engineering*. 10-12 December 2007. Cairo, Egypt.

Adhikari, S. & Bhattacharya, S. 2012. Dynamic analysis of wind turbine towers on flexible foundations. *Shock and Vibration*. 19(1):37–56.

Andersen, K.H., Puech, A.A. & Jardine, R.J. 2013. Cyclic resistant geotechnical design and parameter selection for offshore engineering and other applications. In *Proceedings of the 18th International Conference on Soil Mechanics and Geotechnical Engineering (18th ICSMGE), TC 209 Workshop - Design for cyclic loading: piles and other foundations*. A.A. Puech, Ed. 2-6 September 2013. Paris, France: ISSMGE. 9–44.

Andresen, L. 2015. *Finite element analyses in design of foundations and anchors for offshore structures*. [COGAN Webinar Recording]. Norwegian Geotechnical Institute. 2 September.

Andresen, L., Jostad, H.P. & Andersen, K.H. 2011. Finite element analyses applied in design of foundations and anchors for offshore structures. *International Journal of Geomechanics*. 11(6):417–430.

API. 2000. *Recommended practice for planning, designing and constructing fixed offshore platforms - working stress design*. 21st ed. (API Recommended Practice 2A-WSD). Washington, DC: American Petroleum Institute.

Arany, L., Bhattacharya, S., Macdonald, J.H.G. & Hogan, S.J. 2014. Simplified critical mudline bending moment spectra of offshore wind turbine support structures. *Wind Energy*. 18(12):2171–2197.

Arany, L., Bhattacharya, S., Macdonald, J.H.G. & Hogan, S.J. 2017. Design of monopiles for offshore wind turbines in 10 steps. *Soil Dynamics and Earthquake Engineering*. 92(2017):126–152.

ASCE/AWEA. 2011. *Recommended practice for compliance of large land-based wind turbine support structures*. (ASCE/AWEA RP2011). Washington, DC: American Wind Energy Association.

Benz, T. 2007. Small-strain stiffness of soils and its numerical consequences. Ph.D. Thesis. University of Stuttgart.

Beurskens, J. 2014. The history of wind energy. In *Understanding wind power technology: theory, deployment and optimisation*. A.P. Schaffarczyk, Ed. Chichester, United Kingdom: John Wiley & Sons. 1–44.

Bhattacharya, S., Nikitas, N., Garnsey, J., Alexander, N.A., Cox, J., Lombardi, D., Wood, D.M. & Nash, D.F.T. 2013. Observed dynamic soil-structure interaction in scale testing of offshore wind turbine foundations. *Soil Dynamics and Earthquake Engineering*. 54(2013):47–60.

Bond, A.J. 2013. *Geocentrix ReWaRD 2.7 reference manual*. Surrey, United Kingdom: Geocentrix Ltd.

Bonnett, D. 2005. Wind turbine foundations - loading, dynamics and design. *The Structural Engineer*. 83(3):41–45.

Brink, A.B.A. & Bruin, R.M.H. Eds. 2002. *Guidelines for soil and rock logging in South Africa*. 2nd Impression: Association of Engineering Geologists; South African Institution of Civil Engineering; and South African Institute for Engineering and Environmental Geologists.

Brinkgreve, R.B.J., Kumarswamy, S. & Swolfs, W.M. Eds. 2016. *PLAXIS 3D reference manual*. (Build 8327). Delft, Netherlands: Plaxis bv.

Brinkgreve, R.B.J. 2005. Selection of soil models and parameters for geotechnical engineering application. In *Proceedings of Geo-Frontiers 2005 – Soil Constitutive Models: Evaluation, Selection, and Calibration (GSP 128)*. J.A. Yamamuro & V.N. Kaliakin, Eds. 24-26 January 2005. Austin, Texas: American Society of Civil Engineers. 69–98.

BSI. 2015. *Code of practice for foundations*. (Document number: BS 8004:2015). London: The British Standards Institution.

Burton, T., Jenkins, N., Sharpe, D. & Bossanyi, E. 2011. *Wind energy handbook*. 2nd ed. Chichester, United Kingdom: John Wiley & Sons.

Byrne, G., Berry, A.D., Wetter, C., Mackintosh, N., Friedlaender, E.A., Schwartz, K., Everett, J.P. & Braatvedt, I.H. 2008. *A guide to practical geotechnical engineering in Southern Africa*. 4th ed. Franki Africa.

Cambou, B. & Hicher, P. 2008. Elastoplastic modeling of soils: cyclic loading. In *Constitutive modeling of soils and rocks*. P. Hicher & J. Shao, Eds. Hoboken, New Jersey: John Wiley & Sons. 143–186.

CFMS. 2011. *Recommendations for the design, calculation, installation and inspection of wind turbine foundations*. (Final version 1.1). France: Comite Francais de Mecanique des Sols et de Geotechnique.

Clayton, C.R.I. 1995. *The standard penetration test (STP): methods and use*. (CIRIA Report 143). London: Construction Industry Research and Information Association.

Clayton, C.R.I. 2011. Stiffness at small strain: research and practice. *Geotechnique*. 61(1):5–37.

Clayton, C.R.I. & Heymann, G. 2001. Stiffness of geomaterials at very small strains. *Geotechnique*. 51(3):245–255.

Coduto, D.P. 2001. *Foundation design: principles and practices*. 2nd ed. Upper Saddle River, New Jersey: Prentice Hall.

CSSA. 2016. Gouda Wind Farm precast concrete towers. *Concrete Beton*. (144):8–10.

Davis, R.O. & Selvadurai, A.P.S. 2002. *Plasticity and geomechanics*. Cambridge, United Kingdom: Cambridge University Press.

Day, P.W. 2013. A contribution to the advancement of geotechnical engineering in South Africa. Ph.D. Thesis. Stellenbosch University.

Diaz-Rodriguez, J.A. & Lopez-Molina, J.A. 2008. Strain thresholds in soil dynamics. In *Proceedings of the 14th World Conference on Earthquake Engineering*. 12-17 October 2008. Beijing, China.

Divone, L. V. 2009. Evolution of modern wind turbines Part A: 1940 to 1994. In *Wind turbine technology: fundamental concepts of wind turbine engineering*. 2nd ed. D.A. Spera, Ed. New York: ASME Press. 105–170.

DNV/Risø. 2002. *Guidelines for design of wind turbines*. 2nd ed. Copenhagen, Denmark: Det Norske Veritas & Risø National Laboratory.

DNV. 1992. *Foundations, classification notes no. 30.4*. Hovik, Norway: Det Norske Veritas.

DNV GL. 2016a. *Lifetime extension of wind turbines*. (DNVGL-ST-0262 - Edition March 2016). Oslo, Norway: Det Norske Veritas and Germanischer Lloyd.

DNV GL. 2016b. *Support structures for wind turbines*. (DNVGL-ST-0126 - Edition April 2016). Oslo, Norway: Det Norske Veritas and Germanischer Lloyd.

Dobry, R. & Vucetic, M. 1987. State-of-the-art report: dynamic properties and response of soft clay deposits. In *Proceedings of the International Symposium on Geotechnical Engineering of Soft Soils, Vol. 2*. M.J. Mendoza & L. Montanez, Eds. 13-14 August 1987. Mexico City, Mexico: Mexican Society of Soil Mechanics. 51–87.

DoE. 2011. *Integrated Resource Plan for electricity 2010-2030*. Revision 2. Department of Energy.

DoE. 2015. *State of renewable energy in South Africa*. Pretoria, South Africa: Department of Energy.

DoE. 2016. *Integrated Resource Plan update: assumptions, base case results and observations*. Revision 1 (Draft for consultation). Department of Energy.

Duncan, J.M. & Chang, C. 1970. Nonlinear analysis of stress and strain in soils. *Journal of the Soil Mechanics and Foundations Division*. 96(5):1629–1653.

Earth Systems Global. 2009. *P&H foundations for wind turbine support*. California: Earth Systems Global, Inc.

Eberhard, A., Kolker, J. & Leigland, J. 2014. *South Africa's Renewable Energy IPP Procurement Program: success factors and lessons*. Washington, DC: Public-Private Infrastructure Advisory Facility.

Fraser, R.A. & Wardle, L.J. 1976. Numerical analysis of rectangular rafts on layered foundations. *Geotechnique*. 26(4):613–630.

General Electric. 2013. *Technical specification, wind turbine generator systems, all types: information on the design, detailing and execution of the foundation for the wind turbine generator system*. (Document number: 109W4732). General Electric Power and Water.

Guo, Z., Yu, L., Wang, L., Bhattacharya, S., Nikitas, G. & Xing, Y. 2015. Model tests on the long-term dynamic performance of offshore wind turbines founded on monopiles in sand. *Journal of Offshore Mechanics and Arctic Engineering*. 137(4).

GWEC. 2016. *Global Wind Report 2015 - Annual Market Update*. Global Wind Energy Council.

GWEC. 2017. *Global Wind Report 2016 - Annual Market Update*. Global Wind Energy Council.

Hansen, M.O.L. 2015. *Aerodynamics of wind turbines*. 3rd ed. Abingdon, United Kingdom: Routledge.

Hau, E. 2013. *Wind turbines: fundamentals, technologies, application, economics*. 3rd ed. Heidelberg, Germany: Springer.

Hemami, A. 2012. *Wind turbine technology*. New York: Cengage Learning.

Heymann, G. 2007. Ground stiffness measurement by the continuous surface wave test. *Journal of the South African Institution of Civil Engineering*. 49(1):25–31.

Hu, C., Liu, H. & Huang, W. 2012. Anisotropic bounding-surface plasticity model for the cyclic shakedown and degradation of saturated clay. *Computers and Geotechnics*. 44(2012):34–47.

Idriss, I.M., Dobry, R. & Singh, R.D. 1978. Nonlinear behavior of soft clays during cyclic loading. *Journal of the Geotechnical Engineering Division*. 104(12):1427–1447.

IEC. 2005. *Wind turbines - Part 1: Design requirements*. 3rd ed. (Document number: IEC 61400-1:2005). Geneva, Switzerland: International Electrotechnical Commission.

Ishibashi, I. 1992. Discussion of "effect of soil plasticity on cyclic response" by Vucetic, M. and Dobry, R. *Journal of Geotechnical Engineering*. 118(5):830–832.

Ishibashi, I. & Zhang, X. 1993. Unified dynamic shear moduli and damping ratios of sand and clay. *Soils and Foundations*. 33(1):182–191.

Knorr, K., Zimmermann, B., Bofinger, S., Gerlach, A.-K., Bischof-Niemz, T. & Mushwana, C. 2016. *Wind and solar PV resource aggregation study for South Africa*. (RFP number: 542-23-02-2015). CSIR, SANEDI, Eskom and Fraunhofer IWES.

Kondner, R.L. 1963. Hyperbolic stress-strain response: cohesive soils. *Journal of the Soil Mechanics and Foundations Division*. 89(1):115–144.

Kramer, S.L. 1996. *Geotechnical earthquake engineering*. Upper Saddle River, New Jersey: Prentice Hall.

Kulhawy, F.H. & Mayne, P.W. 1990. *Manual on estimating soil properties for foundation design.* (EPRI EL-6800 Research Project 1493-6). New York: Cornell University Geotechnical Engineering Group.

Lade, P. V. 1977. Elasto-plastic stress-strain theory for cohesionless soil with curved yield surfaces. *International Journal of Solids and Structures*. 13(11):1019–1035.

Lade, P. V. 2005. Overview of constitutive models for soils. In *Proceedings of Geo-Frontiers 2005 – Soil Constitutive Models: Evaluation, Selection, and Calibration (GSP 128)*. J.A. Yamamuro & V.N. Kaliakin, Eds. 24-26 January 2005. Austin, Texas: American Society of Civil Engineers. 1–34.

Lantz, E., Wiser, R. & Hand, M. 2012. *IEA Wind Task 26: The past and future cost of wind energy*. (Technical Report NREL/TP-6A20-53510). Colorado: National Renewable Energy Laboratory.

Lees, A. 2016. *Geotechnical finite element analysis: a practical guide*. London: ICE Publishing.

Lefebvre, G., LeBoeuf, D. & Demers, B. 1989. Stability threshold for cyclic loading of saturated clay. *Canadian Geotechnical Journal*. 26(1):122–131.

Lombardi, D., Bhattacharya, S. & Wood, D.M. 2013. Dynamic soil-structure interaction of monopile supported wind turbines in cohesive soil. *Soil Dynamics and Earthquake Engineering*. 49(2013):165–180.

Look, B.G. 2014. *Handbook of geotechnical investigation and design tables*. 2nd ed. London: CRC Press.

Lopez-Querol, S., Cui, L. & Bhattacharya, S. 2017. Numerical methods for SSI analysis of offshore wind turbine foundations. In *Wind energy engineering: a handbook for onshore and offshore wind turbines*. T.M. Letcher, Ed. London: Academic Press. 275–298.

Loubser, P.B. & Jacobs, A.R. 2016. Optimised design of wind turbine gravity foundations. In *Insights and Innovations in Structural Engineering, Mechanics and Computation: Proceedings of the 6th International Conference on Structural Engineering, Mechanics and Computation*. A. Zingoni, Ed. 5-7 September 2016. Cape Town, South Africa: CRC Press. 953–958.

Lynn, P.A. 2012. *Onshore and offshore wind energy: an introduction*. Chichester, United Kingdom: John Wiley & Sons.

Mabille, E. 2014. *South African Wind Atlas (WASA) guide*. Council for Scientific and Industrial Research.

Manwell, J.F., McGowan, J.G. & Rogers, A.L. 2009. *Wind energy explained: theory, design and application*. 2nd ed. Chichester, United Kingdom: John Wiley & Sons.

Matasovic, N. & Vucetic, M. 1992. A pore pressure model for cyclic straining of clay. *Soils and Foundations*. 32(3):156–173.

Matasovic, N. & Vucetic, M. 1995. Generalized cyclic-degradation-pore-pressure generation model for clays. *Journal of Geotechnical Engineering*. 121(1):33–42.

Matsuoka, H. & Nakai, T. 1974. Stress-deformation and strength characteristics of soil under three different principal stresses. *Japan Society of Civil Engineers*. 232:59–70.

Mawer, B.W. 2015. An introduction to geotechnical design of South African wind turbine gravity foundations. M.Sc. Dissertation. University of Cape Town.

Mawer, B.W., Kalumba, D. & Warren-Codrington, C.J. 2017. Loading and dynamic response considerations for the design of wind turbine foundations on South African soils. *Geotechnical Engineering Journal of the SEAGS & AGSSEA*. 48(3).

McGovern, M. 2017. Will president's pledge unlock PPA jam? *Windpower Monthly*. 33(4):22–24.

Niemunis, A., Wichtmann, T. & Triantafyllidis, T. 2005. A high-cycle accumulation model for sand. *Computers and Geotechnics*. 32(4):245–263.

Nikitas, G., Vimalan, N.J. & Bhattacharya, S. 2016. An innovative cyclic loading device to study long term performance of offshore wind turbines. *Soil Dynamics and Earthquake Engineering*. 82(2016):154–160.

Ntambakwa, E., Yu, H., Guzman, C. & Rogers, M. 2016. Geotechnical design considerations for onshore wind turbine shallow foundations. In *Proceedings of*

the Geotechnical and Structural Engineering Congress 2016. 14-17 February 2016. Phoenix, Arizona: American Society of Civil Engineers. 1153–1165.

O'Reilly, M.P. & Brown, S.F. 1991. Cyclic loading in geotechnical engineering. In *Cyclic loading of soils: from theory to design*. M.P. O'Reilly & S.F. Brown, Eds. Glasgow: Blackie and Son. 1–18.

Okur, D.V. & Ansal, A. 2007. Stiffness degradation of natural fine grained soils during cyclic loading. *Soil Dynamics and Earthquake Engineering*. 27(9):843–854.

Oyague, F. 2009. *Gearbox modeling and load simulation of a baseline 750-kW wind turbine using state-of-the-art simulation codes*. (NREL/TP-500-41160). Colorado: National Renewable Energy Laboratory.

Parrock, A. 2013. Geotechnical aspects of an Eastern Cape wind farm. *SAICE Civil Engineering Magazine*. 21(3):20–25.

Potts, D.M. & Zdravkovic, L. 1999. *Finite element analysis in geotechnical engineering: theory*. London: Thomas Telford.

Price, T.J. 2005. James Blyth - Britain's first modern wind power pioneer. *Wind Engineering*. 29(3):191–200.

Priest, J. 2012. Dynamic and seismic loading of soils. In *ICE manual of geotechnical engineering: Vol. I - geotechnical engineering principles, problematic soils and site investigation*. J. Burland, T. Chapman, H. Skinner, & M. Brown, Eds. London: ICE Publishing. 259–269.

Puzrin, A.M. 2012. *Constitutive modelling in geomechanics: introduction*. Heidelberg, Germany: Springer.

Pyke, R.M. 1979. Nonlinear soil models for irregular cyclic loadings. *Journal of the Geotechnical Engineering Division*. 105(6):715–726.

Rocscience. n.d.(a). *Preliminaries on constitutive models*. Available: https://www.rocscience.com/help/RS3/webhelp2/RS3.htm [2017a, September 16].

Rocscience. n.d.(b). *Phase2 FAQs: theory*. Available: https://www.rocscience.com/help/phase2/webhelp/FAQs/Phase2_FAQs__Theory.htm [2017b, October 19].

SANEDI. 2015. *Wind Atlas for South Africa Phase 1*. Sandton: South African National Energy Development Institute.

SANRAL. 2002. *Code of procedure for the planning and design of highway and road structures in South Africa*. Pretoria: The South African National Roads Agency Limited.

Schaffarczyk, A.P. 2014. *Introduction to wind turbine aerodynamics*. Heidelberg, Germany: Springer.

Siegfriedsen, S. 2014. The drive train. In *Understanding wind power technology: theory, deployment and optimisation*. A.P. Schaffarczyk, Ed. Chichester, United Kingdom: John Wiley & Sons. 202–252.

Smith, E. & Myers, A.T. 2015. Innovative manufacturing of conical steel tubular towers supporting wind turbines [Recording]. In *2015 NASCC: The Steel Conference*. 25-27 March 2015. Nashville, Tennessee: American Institute of Steel Construction.

Spera, D.A. 2009. Introduction to modern wind turbines. In *Wind turbine technology: fundamental concepts of*

wind turbine engineering. 2nd ed. D.A. Spera, Ed. New York: ASME Press. 47–104.

van der Spuy, P. 2014. Wind turbine foundation design: case studies from the South African REIPPPP [Presentation]. In *The 14th Annual African Utility Week Conference and Exhibition*. 13-14 May 2014. Cape Town, South Africa.

Stroud, M.A. 1974. The standard penetration test in insensitive clays and soft rocks. In *Proceedings of the European Symposium on Penetration Testing (ESOPT), Vol. 2:2 Papers*. 5-7 June 1974. Stockholm, Sweden: National Swedish Building Research. 367–375.

Tabata, K. & Vucetic, M. 2010. Threshold shear strain for cyclic degradation of three clays. In *Proceedings of the 5th International Conference on Recent Advances in Geotechnical Earthquake Engineering and Soil Dynamics*. 24-29 May 2010. San Diego, California: Missouri University of Science and Technology. 12.

The Energy Blog. 2017. *Energy project database*. Available: http://www.energy.org.za/data-and-tools/project-database [2017, October 11].

Tong, W. 2010. Fundamentals of wind energy. In *Wind power generation and wind turbine design*. W. Tong, Ed. Southampton, United Kingdom: WIT Press. 3–48.

Towhata, I. 2008. *Geotechnical earthquake engineering*. Berlin, Germany: Springer.

Vardanega, P.J. & Bolton, M.D. 2013. Stiffness of clays and silts: normalizing shear modulus and shear strain. *Journal of Geotechnical and Geoenvironmental Engineering*. 139(9):1575–1589.

Venkatramaiah, C. 2006. *Geotechnical engineering*. 3rd ed. New Delhi, India: New Age International.

Verruijt, A. 2010. *An introduction to soil dynamics*. Dordrecht, Netherlands: Springer.

Vestas. 2009. *General specification, V112-3.0 MW IEC IIA*. (Document number: 0004-7993 V02). Randers SV, Denmark: Vestas Wind Systems A/S.

Vestas. 2010. *General specification, V112-3.0 MW 50/60 Hz*. (Document number: 0011-9181 V03). Randers SV, Denmark: Vestas Wind Systems A/S.

Vestas. 2011. *Foundation design guidelines, V80/V90/V100/V112, foundation with anchors*. (Document number: 0020-3286 V00). Randers SV, Denmark: Vestas Wind Systems A/S.

Vestas. 2013. *Foundation loads, V112 3MW 1540rpm HH 94 IEC2A*. (Document number: 0024-5696 V03). Randers SV, Denmark: Vestas Wind Systems A/S.

Viterna, L.A. & Ancona, D.F. 2009. Commercial wind turbine systems and applications. In *Wind turbine technology: fundamental concepts of wind turbine engineering*. 2nd ed. D.A. Spera, Ed. New York: ASME Press. 203–280.

de Vries, E. 2010. Tower advances lift hub height restrictions. *Wind Power Special Report: Husum Wind Energy Trade Fair Special*. (September):26–28.

Vucetic, M. 1990. Normalized behavior of clay under irregular cyclic loading. *Canadian Geotechnical Journal*. 27(1):29–46.

Vucetic, M. 1992. Soil properties and seismic response. In *Proceedings of the 10th World Conference on Earthquake Engineering, Vol. III*. 19-24 July 1992. Madrid, Spain: Balkema, Rotterdam. 1199–1204.

Vucetic, M. 1994. Cyclic threshold shear strains in soils. *Journal of Geotechnical Engineering*. 120(12):2208–2228.

Vucetic, M. & Dobry, R. 1988. Degradation of marine clays under cyclic loading. *Journal of Geotechnical Engineering*. 114(2):133–149.

Vucetic, M. & Dobry, R. 1991. Effect of soil plasticity on cyclic response. *Journal of Geotechnical Engineering*. 117(1):89–107.

Wagner, H. & Mathur, J. 2013. *Introduction to wind energy systems: basics, technology and operation*. 2nd ed. Heidelberg, Germany: Springer.

Warren-Codrington, C.J. 2013. Geotechnical considerations for onshore wind turbines: adapting knowledge and experience for founding on South African pedocretes. M.Sc. Dissertation. University of Cape Town.

WASA. 2013. *WAsP analysis of WASA stations (WASA-OWA-3y-default-fluxes.wwh) [Database]*. Available: wasa.csir.co.za.

WASA. 2014. *Complete set of wind atlas data sets (Version 2) (WASA_WRF_LIBS_V2.zip) [Database]*. Available: wasa.csir.co.za.

van der Westhuizen, V. 2015. The role of the geotechnical engineer on site. *SAICE Civil Engineering Magazine*. 23(3):50–51.

Wichtmann, T. & Triantafyllidis, T. 2012. Behaviour of granular soils under environmentally induced cyclic loads. In *Mechanical behaviour of soils under environmentally induced cyclic loads*. C. Di Prisco & D.M. Wood, Eds. Vienna, Austria: Springer. 1–136.

Wojtowitz, G. & Vorster, T.E.B. 2014. The design of gravity foundations for wind turbines for West Coast 1 Wind Farm. In *Proceedings of the 8th South African Young Geotechnical Engineers Conference*. 17-19 September 2014. Stellenbosch, South Africa.

Wood, D.M. 1991. Approaches to modelling the cyclic stress-strain response of soils. In *Cyclic loading of soils: from theory to design*. M.P. O'Reilly & S.F. Brown, Eds. Glasgow: Blackie and Son. 19–69.

Wood, D.M. 2004. *Geotechnical modelling*. Boca Raton, Florida: CRC Press.

Yu, H., Guzman, C. & Ntambakwa, E. 2016. Consideration of the cyclic degradation of cohesive soils in pile foundation design for onshore wind turbines. In *Geo-Chicago 2016: Geotechnics for Sustainable Energy*. 14-18 August 2016. Chicago, Illinois: American Society of Civil Engineers. 195–206.

Yu, L., Wang, L., Guo, Z., Bhattacharya, S., Nikitas, G., Li, L. & Xing, Y. 2015. Long-term dynamic behavior of monopile supported offshore wind turbines in sand. *Theoretical and Applied Mechanics Letters*. 5(2):80–84.

van Zyl, W. 2014. Aveng Ground Engineering's contribution to renewable energy in South Africa. *SAICE Civil Engineering Magazine*. 22(4):5–6.

Appendix A

CALCULATION METHOD FOR MASS GROUND MODULUS

Based on Fraser and Wardle (1976)

Fraser and Wardle (1976) proposed a weighting method that can be used to calculate an equivalent soil modulus for a multi-layered soil system. This equivalent modulus is referred to as the *mass ground modulus* in this study, in accordance with the notation adopted by Wojtowitz and Vorster (2014). Although Fraser and Wardle (1976) originally developed this weighting method with the intention of providing a means to calculate settlement of rectangular rafts on layered foundations, whereby the calculations are conducted using a homogenous soil layer with the equivalent elastic parameters, it was suggested by Wojtowitz and Vorster (2014) that this method can be used to calculate the mass shear modulus G_{mass} for purposes of wind turbine foundation design.

The basic premise of the method by Fraser and Wardle (1976) is that, by weighting the elastic parameters of each layer in a multi-layered system according to its influence on settlement, the mass ground modulus can be determined for the overall system. Specifically, the mass ground modulus is calculated according to Equation A.1, which is undertaken in combination with Equations A.2, A.3 and A.4. Note that the elastic parameter E^* is used, rather than the conventional E or G, to account for the difference in Poisson's ratio between the various soil layers. Furthermore, reference is made to Figure A.1 for a basic illustration of a multi-layered soil system and the characterisation of certain parameters.

It is evident from the equations below that an integral component of the weighting method is the influence factor I. This parameter is large near the surface and decreases with depth. Accordingly, the soil near founding level with a larger influence factor has a larger contribution to the mass ground modulus, and soil at a greater depth has a smaller contribution.

$$\frac{1}{E_{mass}^*} = \sum_{i=1}^{n} \frac{1}{E^*_i} \frac{\Delta I^i}{\Delta I^{total}} \qquad \text{Eqn. A.1}$$

$$E^* = E/(1-\nu^2) \qquad \text{Eqn. A.2}$$

$$\Delta I^i = I(z^i_{\text{top}}) - I(z^i_{\text{bottom}}) \qquad \text{Eqn. A.3}$$

$$\Delta I^{total} = I(0) - I(d) \qquad \text{Eqn. A.4}$$

Where E_{mass} = mass elastic modulus (Pa); E^*_i = elastic parameter for layer number i (Pa); E = elastic modulus (Pa); ν = Poisson's ratio; I = influence factor (unitless); z_{top}^i, z_{bottom}^i = depth below the surface of the top and bottom of layer number i (m); and d = depth of the base of the bottom layer (m).

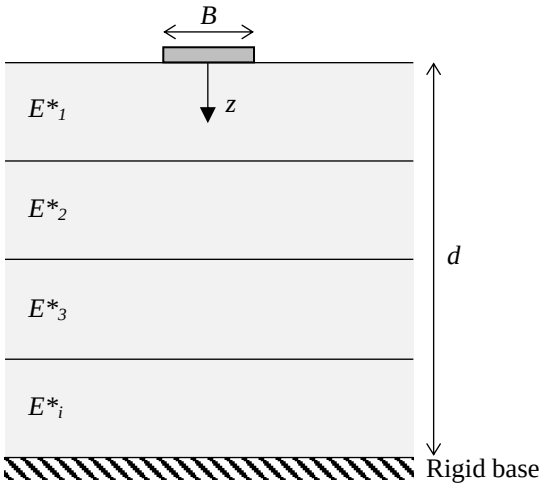

Figure A.1: Multi-layered system and parameters

Fraser and Wardle (1976) also proposed that the mass Poisson's ratio ν_{mass} can be calculated for a multi-layered soil system using the same weighting method. This is undertaken using Equation A.5 below.

$$\nu_{mass} = \sum_{i=1}^{n} \nu_i \frac{\Delta I^i}{\Delta I^{total}} \qquad \text{Eqn. A.5}$$

In the scenario that all Poisson's ratios within the multi-layered system are equal, Equation A.1 becomes equivalent to Equation A.6 (Fraser & Wardle, 1976), with the difference being that E^* is replaced by E. It follows that because E is proportional to G (see Equation 3.1) and the influence factor is independent of the elastic parameters, the mass shear modulus G_{mass} can be calculated similarly according to Equation A.7. This is again only in the case that all Poisson's ratios are equal.

$$\frac{1}{E_{mass}} = \sum_{i=1}^{n} \frac{1}{E_i} \frac{\Delta I^i}{\Delta I^{total}} \qquad \text{Eqn. A.6}$$

$$\frac{1}{G_{mass}} = \sum_{i=1}^{n} \frac{1}{G_i} \frac{\Delta I^i}{\Delta I^{total}} \qquad \text{Eqn. A.7}$$

Fraser and Wardle (1976) simplify the task of determining the equivalent modulus by suggesting that the values of $1/E^*_i$ (or $1/E_i$ or $1/G_i$) can be plotted using a horizontal scale that is linear with respect to $I(z)$, but for convenience is labelled with values of z/B. This particular scale is shown in Figure A.2. By plotting $1/E^*_i$ on this chart and calculating the area under the plotted curves, the calculations are simplified because this area represents the term $\Sigma(\Delta I^i/E^*_i)$ in Equation A.1, which can then be used to calculate the value of E_{mass}^* with the same equation. Similarly, if $1/E$

or $1/G$ is rather plotted in Figure A.2, then the area under the curves represents the term $\Sigma(\Delta I^i/E_i)$ or $\Sigma(\Delta I^i/G_i)$ in Equation A.6 or A.7, which can be used to calculate E_{mass} or G_{mass}. Finally, ν_{mass} can also be calculated using this horizontal scale. However, as can be inferred from Equation A.5, rather than plotting the reciprocal of ν as is the case for the various moduli, the actual value of ν is plotted.

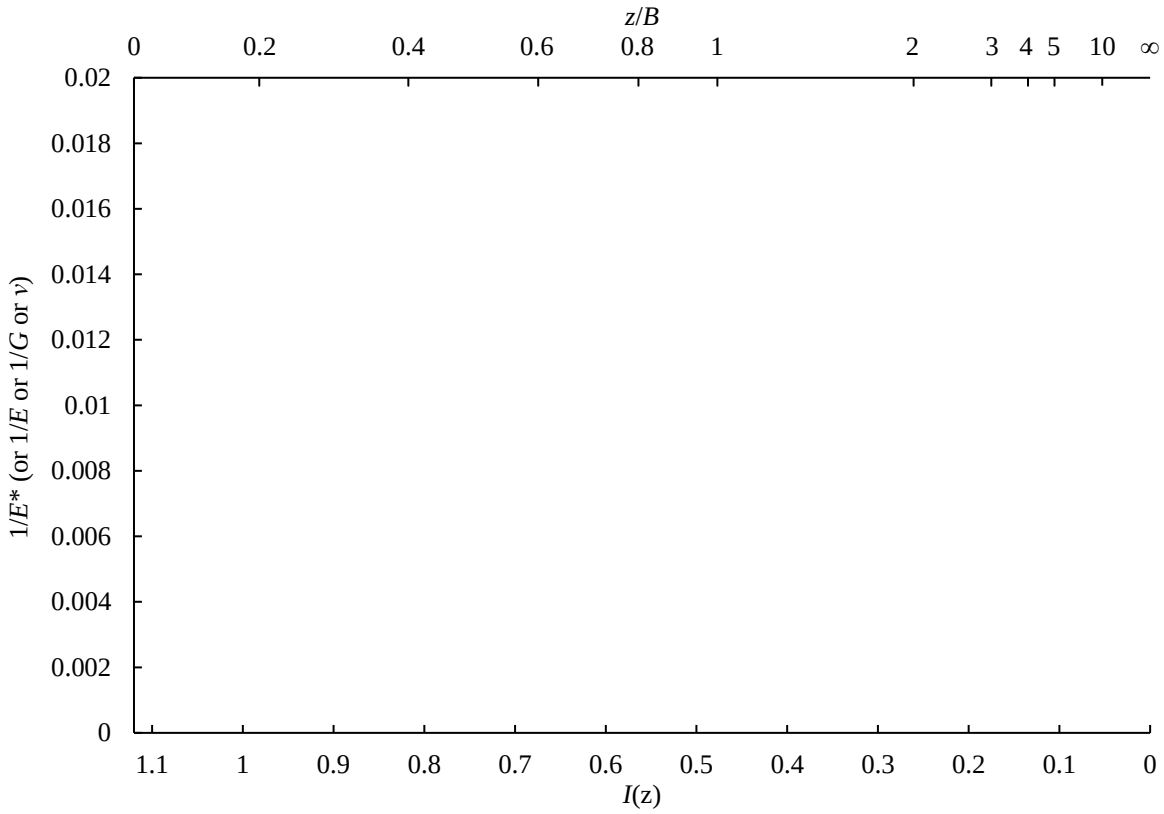

Figure A.2: Horizontal scale of *z*/*B* that produces a linear variation of *I*(z)

Adapted from Fraser and Wardle (1976)

Appendix B

CALCULATION OF MASS GROUND MODULI AND MINIMUM REQUIRED FOUNDATION DIAMETERS FOR CASE STUDY

The mass ground modulus and minimum required foundation diameter (based on the foundation stiffness requirements only) was calculated for each of the three ground profiles investigated in the case study. The former parameter was estimated using the method by Fraser and Wardle (1976), described in Appendix A, whereas the latter was determined in accordance with DNV/Risø (2002). In doing so, an upper and lower bound stiffness profile was analysed for each of the three ground profiles. The upper bound profile corresponded to the in-situ, undegraded stiffness profile as determined from the CSW testing. On the other hand, the lower bound profile corresponded to the degraded stiffness profile, whereby the modulus was reduced up to the depth of influence of cyclic degradation determined from the numerical modelling.

B.1 Ground Profile A

B.1.1 Upper bound stiffness profile

Ground Profile A was representative of a deep clayey soil profile at the wind farm site. The upper bound stiffness profile measured at this wind turbine location is presented in Figure 5.8(a). Using the specific G_0 values from this, G_{mass} was calculated using Equation A.7. This was used in preference to Equation A.1 because the Poisson's ratio was assumed to be uniform throughout this ground profile, with $\nu = 0.5$ due to all the soil being undrained.

To plot the variation of $1/G_0$ with z/B on the scale shown in Figure A.2, these quantities were calculated throughout the depth of the stiffness profile. These calculations were performed in a spreadsheet, with the resultant values shown in Table B.1. Each variation in G_0 was interpreted as a separate layer in these calculations. Further, note that the values of z used in the subsequent tables and figures were measured from founding level and not from the original ground surface. The data presented in Table B.1 was plotted in Figure B.1, and the remaining calculations performed to calculate G_{mass}.

Table B.1: Calculation of z/B and $1/G_0$ for upper bound profile of Ground Profile A

Layer	z_{top}	z_{bottom}	z_{top}/B	z_{bottom}/B	G_0 (MPa)	$1/G_0$
1	0	4.9	0	0.2722	60	0.01667
2	4.9	9.6	0.2722	0.5333	67	0.01493
3	9.6	17.7	0.5333	0.9833	72	0.01389
4	17.7	21	0.9833	1.167	230	0.004348

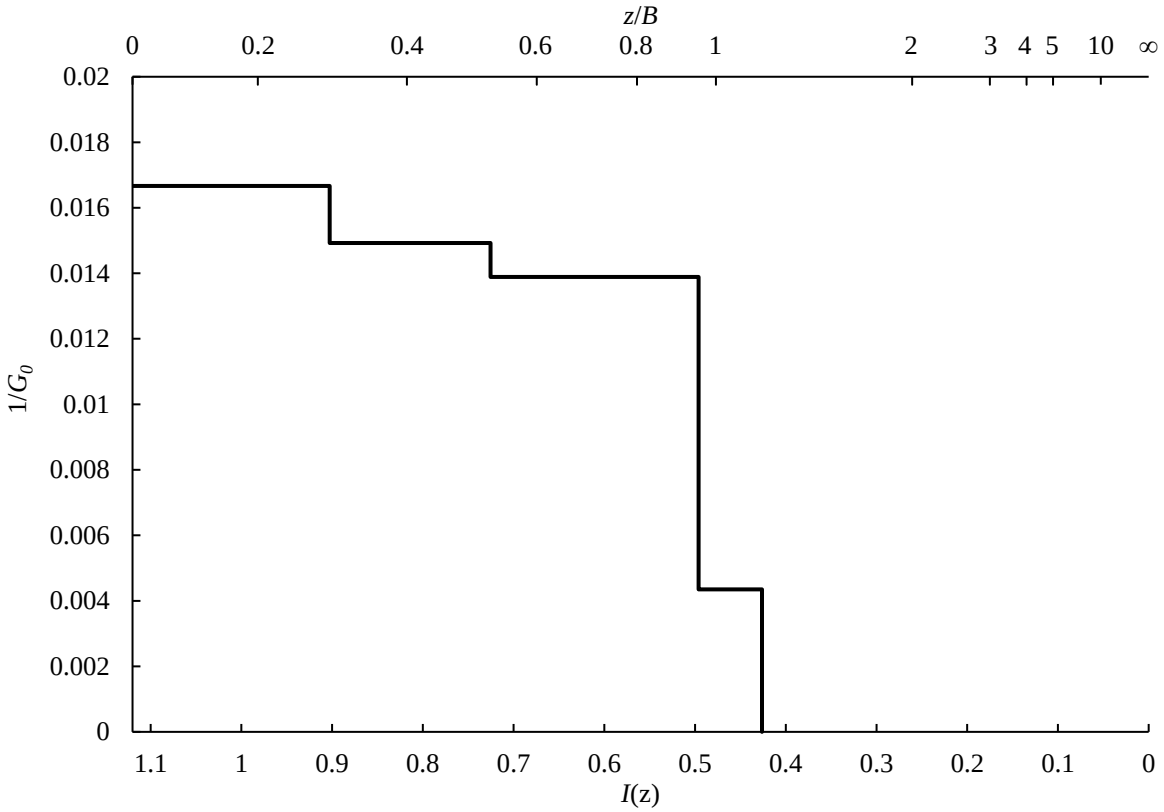

Figure B.1: Variation of $1/G_0$ with depth z/B for upper bound profile of Ground Profile A

By quantifying the values of I from Figure B.1, the area under the curve was calculated as:

$$\text{Area} = \sum_{i=1}^{n} \frac{\Delta I^i}{G_{0(i)}}$$
$$= \frac{1.12 - 0.903}{60} + \frac{0.903 - 0.725}{67} + \frac{0.725 - 0.496}{72} + \frac{0.496 - 0.426}{230}$$
$$= 0.009757$$

Therefore, $G_{0(mass)}$ was calculated using Equation A.7:

$$\frac{1}{G_{0(mass)}} = \sum_{i=1}^{n} \frac{1}{G_{0(i)}} \frac{\Delta I^i}{\Delta I^{total}}$$

$$\Rightarrow G_{0(mass)} = \frac{1.12 - 0.426}{0.009757}$$
$$= 71.1 \text{ MPa}$$

To calculate the minimum required foundation diameter from the stiffness requirements stipulated by the wind turbine manufacturer, the value of $G_{0(mass)}$ was reduced to a value of G_{mass} based on the anticipated level of shear strain induced in the soil. In this regard, DNV/Risø (2002)

suggests that the level of shear strain induced from wind loading for wind turbine foundation design is typically $\gamma = 0.001$. Using the modulus reduction curve by Vucetic and Dobry (1991) for a PI of 15% (Figure 3.4), this shear strain level coincided with a G/G_0 ratio of 0.41. However, based on experimental evidence, Clayton and Heymann (2001) found that for a variety of geomaterials including soft clay, G/G_0 ranged from 0.35 to 0.55 for the same strain level. Therefore, in the interest of conservatism, the lower bound value of this range was adopted for this study, as it was marginally less than that suggested by the chart by Vucetic and Dobry (1991). Thus, a G/G_0 ratio of 0.35 was used, and G_{mass} calculated as follows:

$$\begin{aligned} G_{mass} &= \frac{G}{G_0} G_{0(mass)} \\ &= 0.35 \times 71.1 \\ &= 24.9 \text{ MPa} \end{aligned}$$

Using Equation 2.12, the minimum foundation radius R was calculated as shown below. In doing so, the rotational stiffness K_R was equated to the lowest value stipulated by the turbine manufacturer that would not require a very high lateral stiffness K_H. For the wind turbine model in question, this was 68000 MNm/rad as shown in Table 2.3, which required an associated K_H value of 47.4 MN/m. Furthermore, the Poisson's ratio was equated to 0.5 for this calculation, which was based on the assumption that the soil was in an undrained state. Although it was acknowledged that partial drainage could occur in the long term, thus leading to a reduction in the Poisson's ratio for the upper bound stiffness profile, this assumption was implemented in order for a direct comparison to be made with the lower bound stiffness profile, which would inevitably be in an undrained state due to this being associated with the generation of pore water pressure, which is one of the mechanisms for cyclic degradation.

$$\begin{aligned} R &= \sqrt[3]{\frac{3K_R(1-\nu)}{8G_{mass}}} \\ &= \sqrt[3]{\frac{3(68000)(1-0.5)}{8(24.9)}} \\ &= 8.0 \text{ m} \end{aligned}$$

This radius was then used to calculate K_H with Equation 2.11, to verify if it exceeded the associated minimum value of 47.4 MN/m.

$$\begin{aligned} K_H &= \frac{8G_{mass}R}{2-\nu} \\ &= \frac{8(24.9)(8.0)}{2-0.5} \\ &= 1062 \text{ MN/m} > 47.4 \text{ MN/m} \therefore \text{Okay} \end{aligned}$$

Therefore, since the requirements for K_H were satisfied, the minimum required foundation radius was taken to be 8.0 m. Accordingly, the minimum required diameter was 16.0 m for the upper bound stiffness profile of Ground Profile A.

B.1.2 Lower bound stiffness profile

The lower bound stiffness profile of Ground Profile A is illustrated in Figure 5.8(b). As for the upper bound stiffness profile, G_{mass} was calculated using Equation A.7. The relevant calculations for each G_0 value in the stiffness profile were undertaken in a spreadsheet, with the resultant data shown in Table B.2. This data was plotted in the chart shown in Figure B.2.

Table B.2: Calculation of z/B and $1/G_0$ for lower bound profile of Ground Profile A

Layer	z_{top}	z_{bottom}	z_{top}/B	z_{bottom}/B	G_0 (MPa)	$1/G_0$
1	0	4.9	0	0.2722	36	0.02778
2	4.9	7.2	0.2722	0.4	40.2	0.02488
3	7.2	9.6	0.4	0.5333	67	0.01493
4	9.6	17.7	0.5333	0.9833	72	0.01389
5	17.7	21	0.9833	1.167	230	0.004348

The area under the curve in Figure B.2 was calculated as:

$$\begin{aligned}\text{Area} &= \sum_{i=1}^{n} \frac{\Delta I^i}{G_{0(i)}} \\ &= \frac{1.12-0.903}{36} + \frac{0.903-0.811}{40.2} + \frac{0.811-0.725}{67} + \frac{0.725-0.496}{72} + \frac{0.496-0.426}{230} \\ &= 0.01308\end{aligned}$$

Therefore, $G_{0(mass)}$ was calculated using Equation A.7:

$$\frac{1}{G_{0(mass)}} = \sum_{i=1}^{n} \frac{1}{G_{0(i)}} \frac{\Delta I^i}{\Delta I^{total}}$$

$$\begin{aligned}\Rightarrow G_{0(mass)} &= \frac{1.12-0.426}{0.01308} \\ &= 53.0 \text{ MPa}\end{aligned}$$

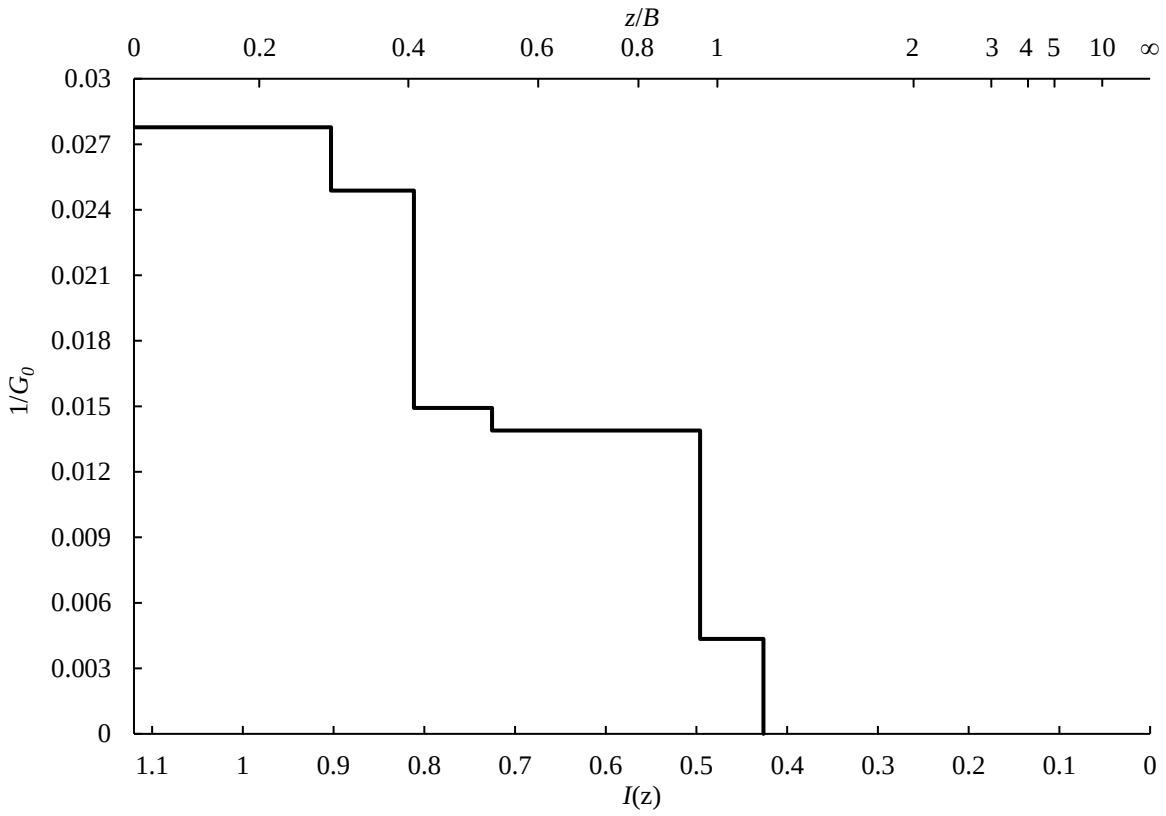

Figure B.2: Variation of $1/G_0$ with depth z/B for lower bound profile of Ground Profile A

The value of $G_{0(mass)}$ was reduced to a value of G_{mass} using the same assumption of $G/G_0 = 0.35$ as before:

$$G_{mass} = \frac{G}{G_0} G_{0(mass)}$$
$$= 0.35 \times 53.0$$
$$= 18.6 \text{ MPa}$$

The minimum R was then calculated using Equation 2.12 as:

$$R = \sqrt[3]{\frac{3K_R(1-\nu)}{8G_{mass}}}$$
$$= \sqrt[3]{\frac{3(68000)(1-0.5)}{8(18.6)}}$$
$$= 8.8 \text{ m}$$

This was cross-checked with the associated minimum value of K_H = 47.4 MN/m:

$$K_H = \frac{8G_{mass}R}{2-\nu}$$
$$= \frac{8(18.6)(8.8)}{2-0.5}$$
$$= 873.6\ \text{MN/m} > 47.4\ \text{MN/m} \therefore \text{Okay}$$

Therefore, the minimum required radius was 8.8 m and the diameter 17.6 m for the lower bound stiffness profile of Ground Profile A.

B.2 Ground Profile B

B.2.1 Upper bound stiffness profile

Ground Profile B consisted of a clayey profile with bedrock located at a depth below founding level equal to half of the foundation diameter. The upper bound stiffness profile for this ground model is presented in Figure 5.14(a). Using this stiffness profile, G_{mass} was calculated up to the level of the bedrock only, as the procedure for calculating the minimum required foundation diameter differed slightly in this case due to the presence of the bedrock, as shown later in this section. As the Poisson's ratio for the soil was uniform throughout, Equation A.7 was used for this calculation. In order to plot the stiffness profile on the horizontal scale suggested by Fraser and Wardle (1976), the relevant parameters were calculated in Table B.3, and subsequently plotted in Figure B.3.

Table B.3: Calculation of z/B and $1/G_0$ for upper bound profile of Ground Profile B

Layer	z_{top}	z_{bottom}	z_{top}/B	z_{bottom}/B	G_0 (MPa)	$1/G_0$
1	0	1.6	0	0.08889	80	0.01250
2	1.6	9	0.08889	0.5	60	0.01667

The area under the curve in Figure B.3 was calculated as:

$$\text{Area} = \sum_{i=1}^{n} \frac{\Delta I^i}{G_{0(i)}}$$
$$= \frac{1.12-1.05}{80} + \frac{1.05-0.746}{60}$$
$$= 0.005941$$

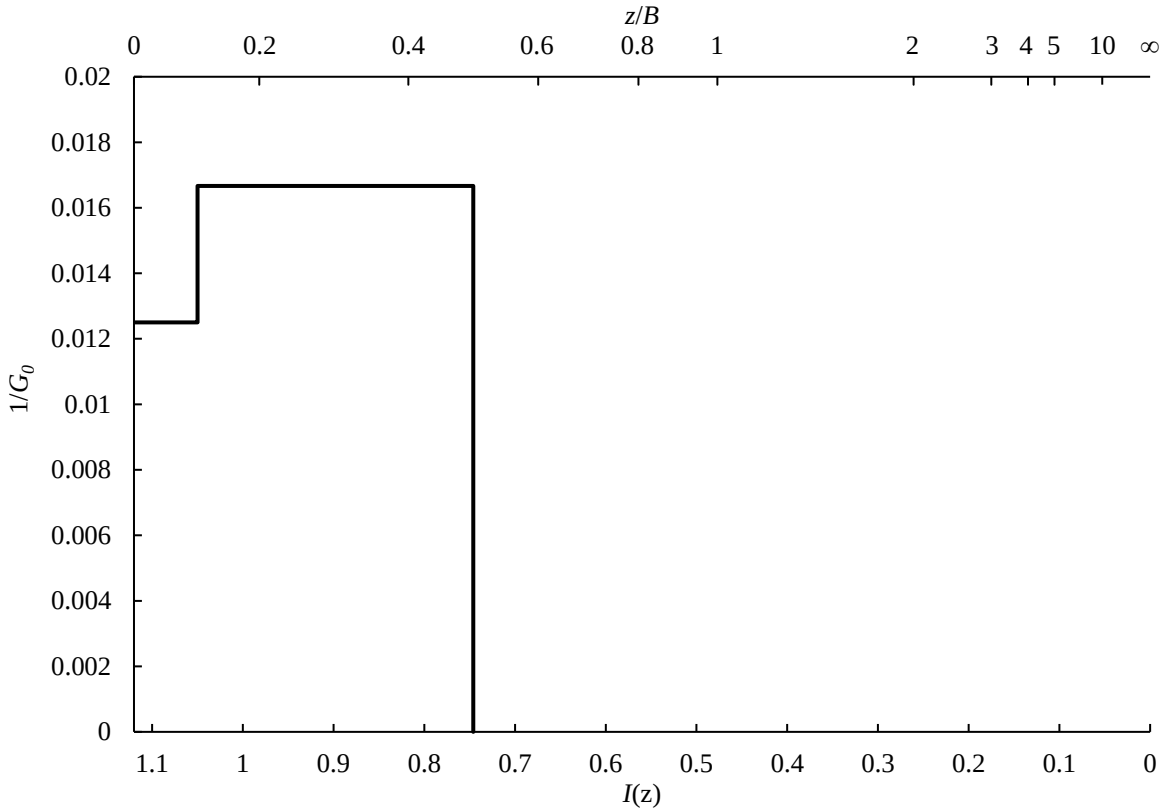

Figure B.3: Variation of $1/G_0$ with depth z/B for upper bound profile of Ground Profile B

The value of $G_{0(mass)}$ was subsequently calculated using Equation A.7:

$$\frac{1}{G_{0(mass)}} = \sum_{i=1}^{n} \frac{1}{G_{0(i)}} \frac{\Delta I^{i}}{\Delta I^{total}}$$

$$\Rightarrow G_{0(mass)} = \frac{1.12 - 0.746}{0.005941}$$

$$= 63.0 \text{ MPa}$$

This was reduced to a value of G_{mass} using the same assumption of $G/G_0 = 0.35$ as before:

$$G_{mass} = \frac{G}{G_0} G_{0(mass)}$$

$$= 0.35 \times 63.0$$

$$= 22.0 \text{ MPa}$$

With G_{mass} determined up to the level of the bedrock, the minimum foundation radius R was calculated. However, rather than using Equation 2.12 as for the previous ground profile, DNV/Risø (2002) presented a different set of equations for calculating foundation stiffness in the scenario that a circular footing is embedded in a soil stratum over bedrock. These equations

are shown below for K_R and K_H respectively, with an illustration of the relevant parameters presented in Figure B.4.

Rotational: $$K_R = \frac{8G_{mass}R^3}{3(1-\nu)}\left(1+\frac{R}{6H}\right)\left(1+2\frac{D}{R}\right)\left(1+0.7\frac{D}{H}\right) \quad \text{Eqn. B.1}$$

Lateral: $$K_H = \frac{8G_{mass}R}{2-\nu}\left(1+\frac{R}{2H}\right)\left(1+\frac{2}{3}\frac{D}{R}\right)\left(1+\frac{5}{4}\frac{D}{H}\right) \quad \text{Eqn. B.2}$$

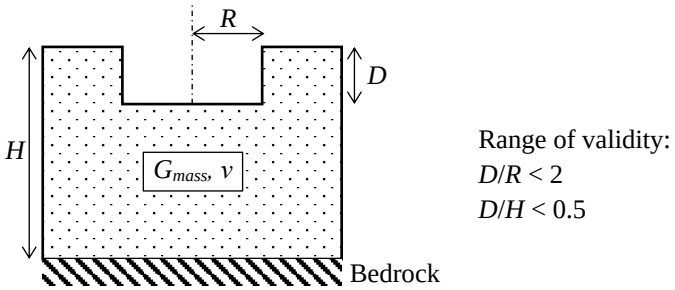

Figure B.4: Circular footing embedded in stratum over bedrock
Adapted from DNV/Risø (2002)

Using Equation B.1, and substituting in the relevant parameters, R was calculated as follows:

$$K_R = \frac{8G_{mass}R^3}{3(1-\nu)}\left(1+\frac{R}{6H}\right)\left(1+2\frac{D}{R}\right)\left(1+0.7\frac{D}{H}\right)$$

$$68000 = \frac{8(22.0)R^3}{3(1-0.5)}\left(1+\frac{R}{6(12)}\right)\left(1+2\frac{3}{R}\right)\left(1+0.7\frac{3}{12}\right)$$

$$\Rightarrow R = 6.1\,\text{m}$$

This foundation radius was then used to calculate K_H with Equation B.2, to verify if it exceeded the associated minimum value of 47.4 MN/m.

$$K_H = \frac{8G_{mass}R}{2-\nu}\left(1+\frac{R}{2H}\right)\left(1+\frac{2}{3}\frac{D}{R}\right)\left(1+\frac{5}{4}\frac{D}{H}\right)$$

$$= \frac{8(22.0)(6.1)}{2-0.5}\left(1+\frac{6.1}{2(12)}\right)\left(1+\frac{2}{3}\times\frac{3}{6.1}\right)\left(1+\frac{5}{4}\times\frac{3}{12}\right)$$

$$= 1571.7\ \text{MN/m} > 47.4\ \text{MN/m} \therefore \text{Okay}$$

Since the requirements for K_H were met, the minimum required foundation radius was taken to be 6.1 m. Therefore, the minimum required diameter was 12.2 m for the upper bound stiffness profile of Ground Profile B.

B.2.2 Lower bound stiffness profile

The lower bound stiffness profile of Ground Profile B is presented Figure 5.14(b). The same procedure as was used for the upper bound stiffness profile was followed to calculate G_{mass}, up to the level of the bedrock only. This initially involved calculating the various parameters in Table B.4, and plotting these values in Figure B.5.

Table B.4: Calculation of z/B and $1/G_0$ for lower bound profile of Ground Profile B

Layer	z_{top}	z_{bottom}	z_{top}/B	z_{bottom}/B	G_0 (MPa)	$1/G_0$
1	0	1.6	0	0.08889	48	0.02083
2	1.6	7.2	0.08889	0.4	36	0.02778
3	7.2	9	0.4	0.5	60	0.01667

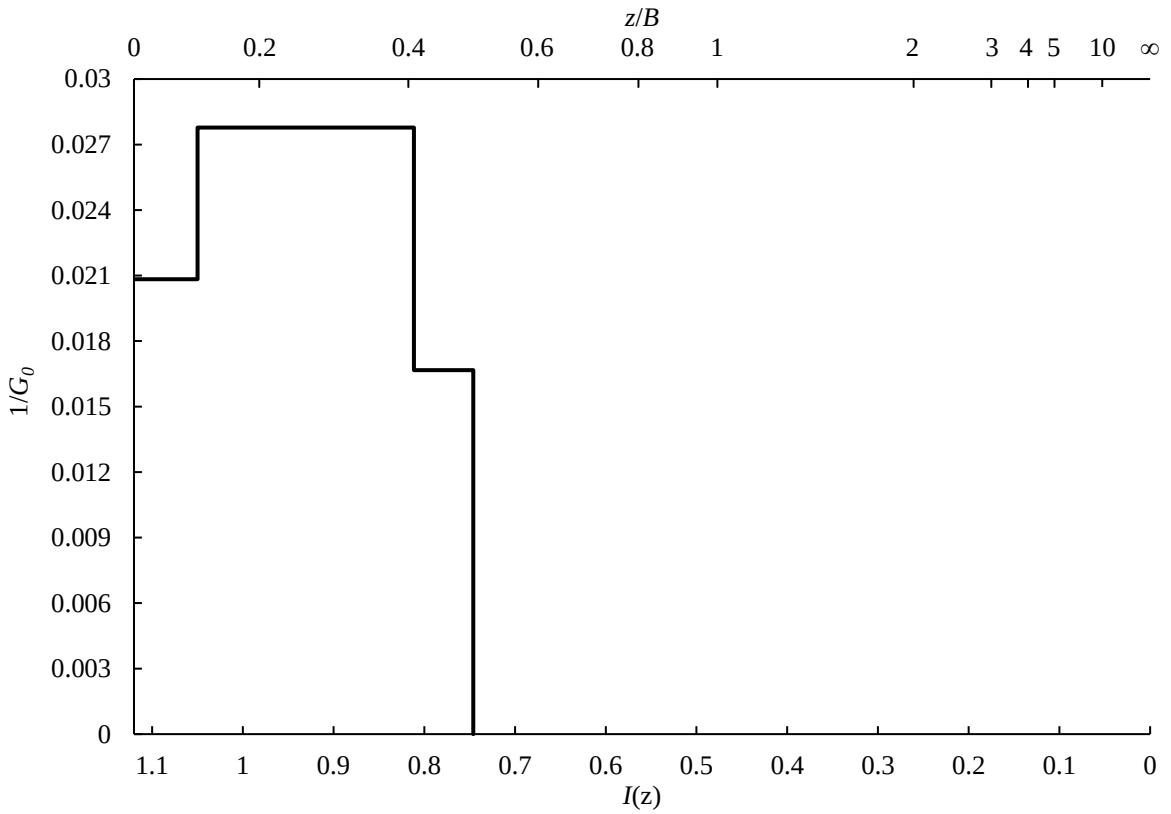

Figure B.5: Variation of $1/G_0$ with depth z/B for lower bound profile of Ground Profile B

The area under the curve in Figure B.5 was calculated as:

$$\begin{aligned}\text{Area} &= \sum_{i=1}^{n} \frac{\Delta I^i}{G_{0(i)}} \\ &= \frac{1.12-1.05}{48} + \frac{1.05-0.811}{36} + \frac{0.811-0.746}{60} \\ &= 0.009174\end{aligned}$$

Therefore, $G_{0(mass)}$ was calculated using Equation A.7:

$$\frac{1}{G_{0(mass)}} = \sum_{i=1}^{n} \frac{1}{G_{0(i)}} \frac{\Delta I^i}{\Delta I^{total}}$$

$$\begin{aligned}\Rightarrow G_{0(mass)} &= \frac{1.12-0.746}{0.009174} \\ &= 40.8 \text{ MPa}\end{aligned}$$

This was reduced to a value of G_{mass} using the same assumption of G/G_0 = 0.35 as before:

$$\begin{aligned}G_{mass} &= \frac{G}{G_0} G_{0(mass)} \\ &= 0.35 \times 40.8 \\ &= 14.3 \text{ MPa}\end{aligned}$$

The relevant parameters were substituted into Equation B.1, and R calculated as follows:

$$K_R = \frac{8G_{mass}R^3}{3(1-\nu)}\left(1+\frac{R}{6H}\right)\left(1+2\frac{D}{R}\right)\left(1+0.7\frac{D}{H}\right)$$

$$68000 = \frac{8(14.3)R^3}{3(1-0.5)}\left(1+\frac{R}{6(12)}\right)\left(1+2\frac{3}{R}\right)\left(1+0.7\frac{3}{12}\right)$$

$$\Rightarrow R = 7.2 \text{ m}$$

This foundation radius was then used to calculate K_H with Equation B.2, to verify if it exceeded the associated minimum value of 47.4 MN/m.

$$\begin{aligned}K_H &= \frac{8G_{mass}R}{2-\nu}\left(1+\frac{R}{2H}\right)\left(1+\frac{2}{3}\frac{D}{R}\right)\left(1+\frac{5}{4}\frac{D}{H}\right) \\ &= \frac{8(14.3)(7.2)}{2-0.5}\left(1+\frac{7.2}{2(12)}\right)\left(1+\frac{2}{3}\times\frac{3}{7.2}\right)\left(1+\frac{5}{4}\times\frac{3}{12}\right) \\ &= 1199.2 \text{ MN/m} > 47.4 \text{ MN/m} \therefore \text{Okay}\end{aligned}$$

Therefore, the minimum required foundation radius was taken to be 7.2 m and the diameter 14.5 m for the lower bound stiffness profile of Ground Profile B.

B.3 Ground Profile C

B.3.1 Upper bound stiffness profile

Ground Profile C comprised a clayey profile with a layer of very dense sand, of thickness 1.5 m, located at founding level. As the dense sand was drained, and thus had a different Poisson's ratio to the undrained clayey soil below, Equation A.7 could not be used to calculate G_{mass}. Rather, Equation A.1 had to be used, which accounted for the difference in Poisson's ratios with the use of the parameter E^*.

The upper bound stiffness profile for Ground Profile C is illustrated in Figure 5.20(a). As this stiffness profile was expressed in terms of G_0, it had to be converted to equivalent values of E_0^*. This was undertaken by first converting G_0 to E_0 using Equation 3.1, and subsequently converting E_0 to E_0^* using Equation A.2. The resultant values are shown in Table B.5 and plotted in Figure B.6.

Table B.5: Calculation of z/B and $1/E_0^*$ for upper bound profile of Ground Profile C

Layer	z_{top}	z_{bottom}	z_{top}/B	z_{bottom}/B	G_0 (MPa)	ν (-)	E_0 (MPa)	E_0^* (MPa)	$1/E_0^*$
1	0	1.5	0	0.08333	390	0.3	1014	1114.3	0.0008974
2	1.5	2.1	0.08333	0.1167	113	0.5	339	452	0.002212
3	2.1	9.8	0.1167	0.5444	60	0.5	180	240	0.004167
4	9.8	12.2	0.5444	0.6778	88	0.5	264	352	0.002841
5	12.2	17	0.6778	0.9444	190	0.5	570	760	0.001316

The area under the curve in Figure B.6 was calculated as:

$$\begin{aligned}\text{Area} &= \sum_{i=1}^{n} \frac{\Delta I^i}{{E_0}^*_i} \\ &= \frac{1.12-1.05}{1114.3} + \frac{1.05-1.03}{452} + \frac{1.03-0.719}{240} + \frac{0.719-0.642}{352} + \frac{0.642-0.512}{760} \\ &= 0.001792\end{aligned}$$

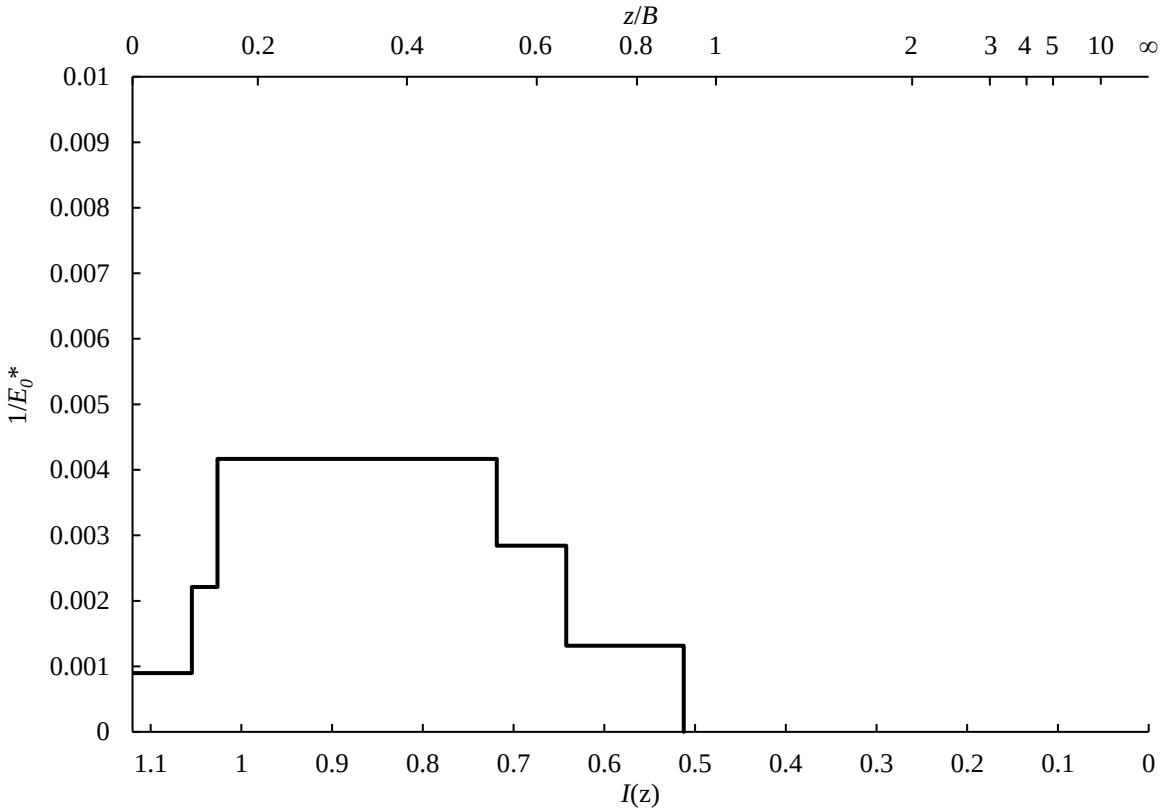

Figure B.6: Variation of $1/E_0^*$ with z/B for upper bound profile of Ground Profile C

The value of $E_{0(mass)}^*$ was subsequently calculated using Equation A.1:

$$\frac{1}{E_{0(mass)}^*} = \sum_{i=1}^{n} \frac{1}{E_0^*{}_i} \frac{\Delta I^i}{\Delta I^{total}}$$

$$\Rightarrow E_{0(mass)}^* = \frac{1.12 - 0.512}{0.001792}$$

$$= 339.1\,\text{MPa}$$

This mass ground modulus was then converted back to a value of $E_{0(mass)}$ using Equation A.2, and subsequently to $G_{0(mass)}$ using Equation 3.1. However, prior to doing so, ν_{mass} had to be calculated to account for the variation in ν within the soil profile. To assist in calculating this, the variation in ν was plotted in Figure B.7 using the scale proposed by Fraser and Wardle (1976).

The area under the curve in Figure B.7 was calculated as:

$$\text{Area} = \sum_{i=1}^{n} \nu_i \Delta I^i$$

$$= 0.3(1.12 - 1.05) + 0.5(1.05 - 0.512)$$

$$= 0.2907$$

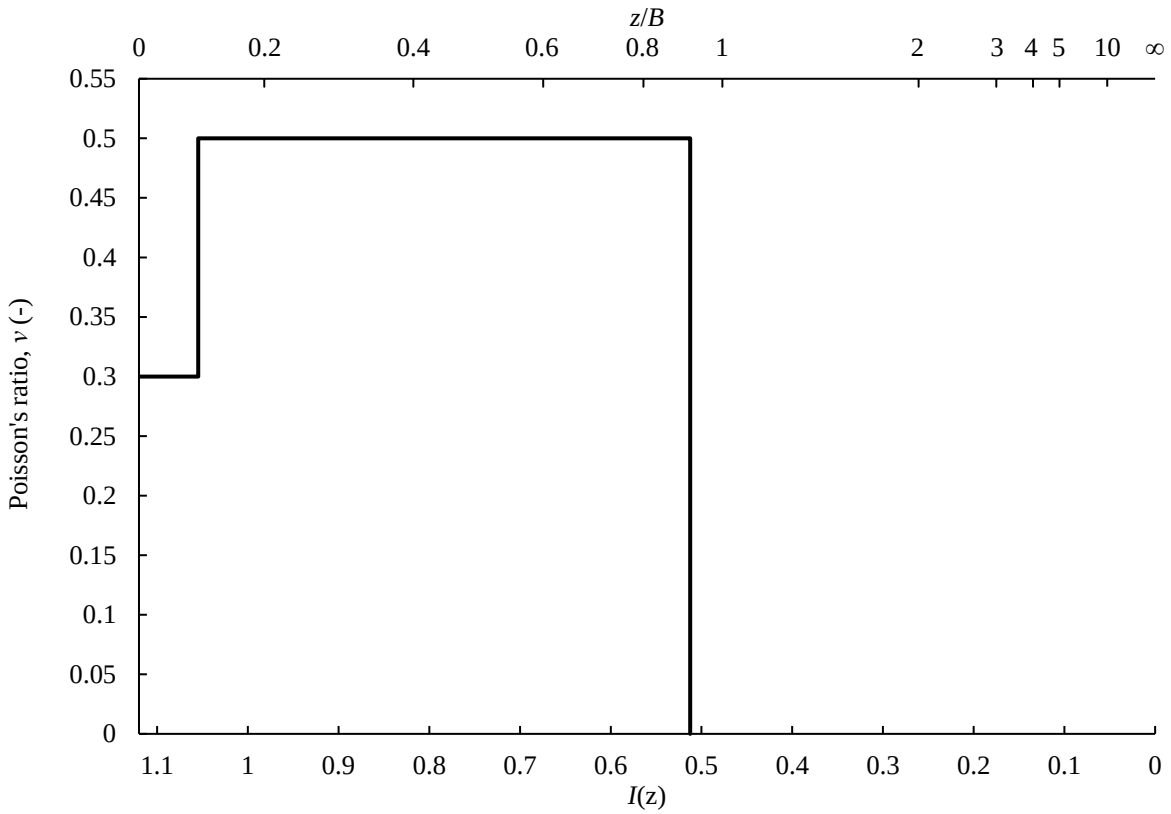

Figure B.7: Variation of *v* with *z*/*B* for Ground Profile C

Therefore, v_{mass} was determined using Equation A.5:

$$\begin{aligned} v_{mass} &= \sum_{i=1}^{n} v_i \frac{\Delta I^i}{\Delta I^{total}} \\ &= \frac{0.2907}{(1.12-0.512)} \\ &= 0.478 \end{aligned}$$

Using the calculated values of $E_{0(mass)}$* and v_{mass}, the value of $E_{0(mass)}$ was calculated using Equation A.2:

$$\begin{aligned} E_{0(mass)} &= (1-v^2)E_{0(mass)}\,* \\ &= \left[1-(0.478)^2\right](339.1) \\ &= 261.5\,\text{MPa} \end{aligned}$$

The value of $G_{0(mass)}$ was subsequently determined using Equation 3.1:

$$\begin{aligned} G_{0(mass)} &= \frac{E_{0(mass)}}{2(1+\nu)} \\ &= \frac{261.5}{2(1+0.478)} \\ &= 88.4\,\text{MPa} \end{aligned}$$

This was reduced to a value of G_{mass} using the same assumption of G/G_0 = 0.35 as before:

$$\begin{aligned} G_{mass} &= \frac{G}{G_0} G_{0(mass)} \\ &= 0.35 \times 88.4 \\ &= 30.9\,\text{MPa} \end{aligned}$$

The minimum R was calculated using Equation 2.12 as:

$$\begin{aligned} R &= \sqrt[3]{\frac{3K_R(1-\nu)}{8G_{mass}}} \\ &= \sqrt[3]{\frac{3(68000)(1-0.478)}{8(30.9)}} \\ &= 7.5\,\text{m} \end{aligned}$$

This was cross-checked with the associated minimum value of K_H = 47.4 MN/m:

$$\begin{aligned} K_H &= \frac{8G_{mass}R}{2-\nu} \\ &= \frac{8(30.9)(7.5)}{2-0.478} \\ &= 1228.0\,\text{MN/m} > 47.4\,\text{MN/m} \therefore \text{Okay} \end{aligned}$$

Therefore, since the requirements for K_H were satisfied, the minimum required radius was taken to be 7.5 m and the diameter 15.1 m for the upper bound stiffness profile of Ground Profile C.

B.3.2 Lower bound stiffness profile

The lower bound stiffness profile for Ground Profile C is shown in Figure 5.20(a). The same procedure as used for the upper bound stiffness profile was followed to calculated G_{mass}. This involved calculating the various parameters in Table B.6, and plotting these values in Figure B.8.

Table B.6: Calculation of z/B and $1/E_0$* for lower bound profile of Ground Profile C

Layer	z_{top}	z_{bottom}	z_{top}/B	z_{bottom}/B	G_0 (MPa)	ν (-)	E_0 (MPa)	E_0* (MPa)	$1/E_0$*
1	0	1.5	0	0.08333	390	0.3	1014	1114.3	0.0008974
2	1.5	2.1	0.08333	0.1167	67.8	0.5	203.4	271.2	0.003687
3	2.1	5.4	0.1167	0.3	36	0.5	108	144	0.006944
4	5.4	9.8	0.3	0.5444	60	0.5	180	240	0.004167
5	9.8	12.2	0.5444	0.6778	88	0.5	264	352	0.002841
6	12.2	17	0.6778	0.9444	190	0.5	570	760	0.001316

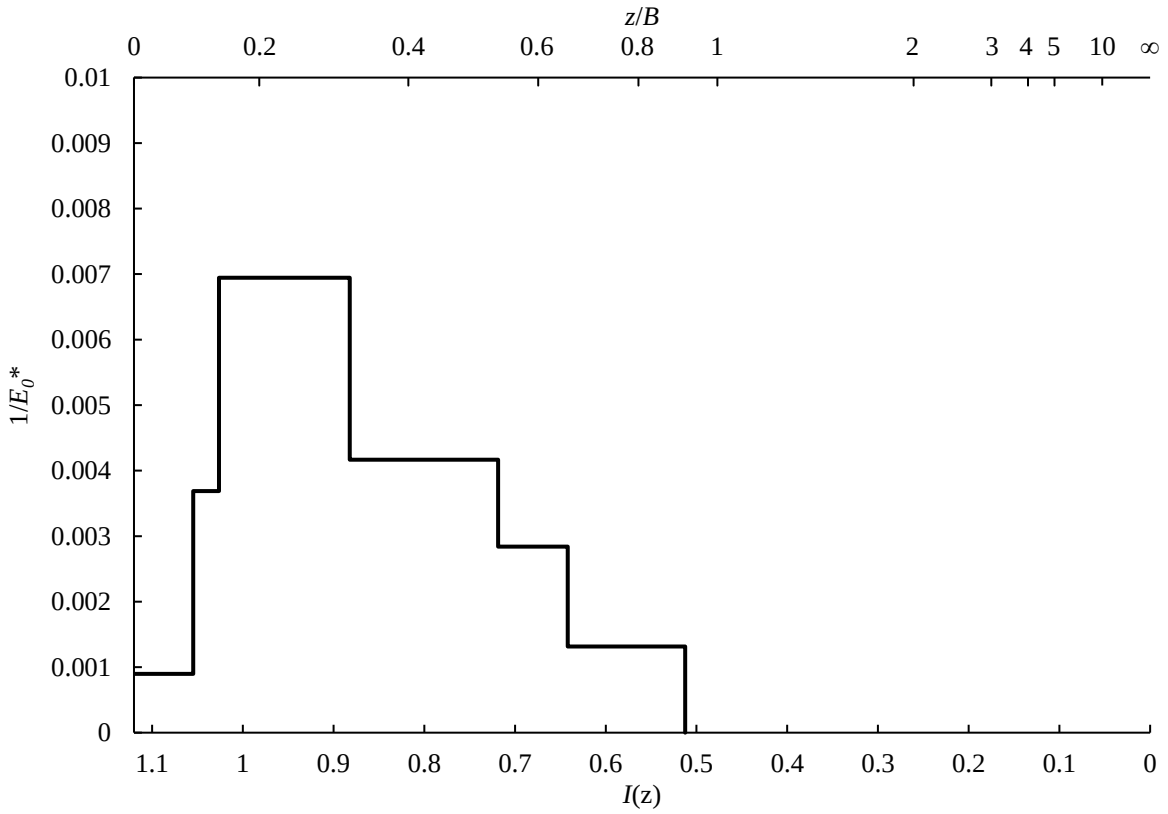

Figure B.8: Variation of $1/E_0$* with z/B for lower bound profile of Ground Profile C

The area under the curve in Figure B.8 was calculated as:

$$\begin{aligned}\text{Area} &= \sum_{i=1}^{n} \frac{\Delta I^i}{E_0{}^*_i} \\ &= \frac{1.12-1.05}{1114.3} + \frac{1.05-1.03}{271.2} + \frac{1.03-0.882}{144} + \frac{0.882-0.719}{240} + \frac{0.719-0.642}{352} \\ &\quad + \frac{0.642-0.512}{760} \\ &= 0.002234\end{aligned}$$

Therefore, $E_{0(mass)}$* was calculated using Equation A.1:

$$\frac{1}{E_{0(mass)}{}^*} = \sum_{i=1}^{n} \frac{1}{E_0{}^*_i} \frac{\Delta I^i}{\Delta I^{total}}$$

$$\begin{aligned}\Rightarrow E_{0(mass)}{}^* &= \frac{1.12-0.512}{0.002234} \\ &= 272.0 \text{ MPa}\end{aligned}$$

The value of ν_{mass} = 0.478 calculated for the upper bound stiffness profile was the same as that of the lower bound.

Using the values of $E_{0(mass)}$* and ν_{mass}, the value of $E_{0(mass)}$ was calculated using Equation A.2:

$$\begin{aligned}E_{0(mass)} &= (1-\nu^2)E_{0(mass)}{}^* \\ &= \left[1-(0.478)^2\right](272.0) \\ &= 209.7 \text{ MPa}\end{aligned}$$

The value of $G_{0(mass)}$ was subsequently calculated using Equation 3.1:

$$\begin{aligned}G_{0(mass)} &= \frac{E_{0(mass)}}{2(1+\nu)} \\ &= \frac{209.7}{2(1+0.478)} \\ &= 70.9 \text{ MPa}\end{aligned}$$

This was reduced to a value of G_{mass} using the same assumption of G/G_0 = 0.35 as before:

$$\begin{aligned} G_{mass} &= \frac{G}{G_0} G_{0(mass)} \\ &= 0.35 \times 70.9 \\ &= 24.8\,\text{MPa} \end{aligned}$$

The minimum R was calculated using Equation 2.12 as:

$$\begin{aligned} R &= \sqrt[3]{\frac{3K_R(1-\nu)}{8G_{mass}}} \\ &= \sqrt[3]{\frac{3(68000)(1-0.478)}{8(24.8)}} \\ &= 8.1\,\text{m} \end{aligned}$$

This was cross-checked with the associated minimum value of K_H = 47.4 MN/m:

$$\begin{aligned} K_H &= \frac{8G_{mass}R}{2-\nu} \\ &= \frac{8(24.8)(8.1)}{2-0.478} \\ &= 1060.0\,\text{MN/m} > 47.4\,\text{MN/m} \therefore \text{Okay} \end{aligned}$$

Therefore, the minimum required radius was 8.1 m and the diameter 16.2 m for the lower bound stiffness profile of Ground Profile C.